CONDUCTING DIBLOCK COPOLYMERS AS MULTIFUNCTIONAL BINDERS FOR LITHIUM-ION BATTERIES & SURFACE-AGNOSTIC HIGHLY STRETCHABLE AND BENDABLE CONDUCTIVE MXENE MULTILAYERS

A Dissertation

by

HYOSUNG AN

Submitted to the Office of Graduate and Professional Studies of
Texas A&M University
in partial fulfillment of the requirements for the degree of

DOCTOR OF PHILOSOPHY

Chair of Committee,	Jodie L. Lutkenhaus
Committee Members,	Perla B. Balbuena
	Yossef A. Elabd
	Sarbajit Banerjee
Head of Department,	M. Nazmul Karim

May 2018

Major Subject: Chemical Engineering

ABSTRACT

A conductive block copolymer binder P3HT-*b*-PEO was studied to form a flexible, tough, carbon-free hybrid battery cathode. Only 5 wt % polymer was required to triple the flexibility of V_2O_5, and electrodes comprised of 10 wt % polymer had unusually high toughness (293 kJ/m3) and specific energy (530 Wh/kg), both higher than reduced graphene oxide paper electrodes. Addition of P3HT-*b*-PEO increased lithium-ion diffusion, eliminated cracking during cycling, and enhanced cyclability relative to V_2O_5 alone.

We compared the P3HT-*b*-PEO block copolymer binders with P3HT, PEO, and a P3HT/PEO homopolymer blend in carbon-free V_2O_5. The electrode with P3HT-*b*-PEO binder showed the highest capacity of 190 mAh/g at a 0.1 C-rate after over 200 cycles, a 2.5-fold improvement of that of pure V_2O_5, whereas P3HT, PEO, and the blend exhibited capacities of 139, 130, and 70 mAh/g. The unique architecture of P3HT-*b*-PEO, wherein P3HT and PEO blocks are covalently bonded, improved the uniform distribution of the conductive binders within the V_2O_5 structure, whereas the analogous P3HT/PEO blend suffers from phase separation.

We presented the strong effects of regioregularity and molecular weight of the P3HT block in P3HT-*b*-PEO on molecular conformation and electrochemical properties by comparing four different P3HT-*b*-PEOs of varying P3HT regioregularity (86-97%) and molecular weight (8-19 kDa) while the PEO block was kept the same (7 kDa) to isolate the influence of the P3HT block. Our data show that, as increasing regioregularity, the capacity of P3HT-*b*-PEO significantly increase and, as increasing molecular weight, the redox potential decreases. The underlying reasons for this finding are revealed by the characterizations of P3HT backbone conformation and chain packing.

Also, we studied highly stretchable conductive titanium carbide (MXene) multilayer coatings that can undergo extreme deformation while maintaining their electrical conductivity. The conductive and conformal MXene multilayer coatings that can undergo large-scale mechanical deformation while maintaining a conductivity as high as 2,000 S/m. MXene multilayers were successfully prepared onto flexible polymer sheet, stretchable poly(dimethylsiloxane), nylon fiber, and glass. The coating showed a recoverable resistance response to bending (up to 2.5 mm bending radius) and stretching (up to 40% tensile strain).

ACKNOWLEDGEMENTS

I would like to thank my advisor, Professor Jodie L. Lutkenhaus for the guidance, encouragement, and support throughout my research. It was great luck for me to conduct the research under her guidance. Without her guidance, I could not have conducted meaningful research. I will be forever grateful for that. I would like to thank my committee members, Professor Perla B. Balbuena, Professor Yossef A. Elabd, and Professor Sarbajit Banerjee, for their guidance and support throughout the course of this research.

I would like to thank Lutkenhaus Group members past and present, Anish Patel, Pilar Suarez, Josh O'Neal, Yanpu Zhang, Matthew Bolen, Paraskevi Flouda, Alexandra Easley, Dimitrios Loufakis, Kasturi Sarang, Ian Echols, Jared Mike, Choonghyun Sung, Ju-Won Jeon, Dariya Reid, Se Ra Kwon, Souvik De, Sheng Luo, and Shaoyang Wang. I feel fortunate to have been part of such an energetic, collaborative, and compassionate team. I would like to especially thank to Anish Patel, Josh O'Neal, Pilar Suarez, and Yanpu Zhang for their friendship, consistent help, and advice.

I would like to express my appreciation for my "Aggieland" family, the Mike Green, Pam Green, Michael Green, and Cassie Green. They have "adopted" me. They show love beyond blood ties. Whenever I face problems, they help and guide me, and give their wisdom. They are my family, mentors, and friends.

I would like to thank my parents, parent-in-law, sister, and brother-in-law for their love, unlimited support, and unconditional encouragement. I would like to thank my lovely wife Chung Lee. She has supported and encouraged me throughout this journey. She has been an excellent wife, mother, friend, and researcher. All the extra time I dedicated to this work was discounted

from the precious time of being with her. For being with me during my PhD she sacrificed a lot of things in her career. I will return the favors. Also, I would like to thank my son Jace Aesop An for giving us a million reasons to be happy. All my life's troubles disappear when I see his smile. He is the best gift in my life.

CONTRIBUTORS AND FUNDING SOURCES

This work was supported by a dissertation committee consisting of Professor Jodie L. Lutkenhaus, Professor Perla B. Balbuena, and Professor Yossef A. Elabd of the Department of Chemical Engineering and Professor Sarbajit Banerjee of the Department of Chemistry.

The polymer synthesis and characterization for Chapter II, III, and IV were conducted by Professor Rafael Verduzco, Dr. Kendall A. Smith, Dr. Yen-Hao Lin, Xiaoyi Li, Stacy L. Pesek, and Lisa Swank at Rice University. The MAX phase and MXene synthesis and characterization for Chapter V were conducted by Professor Miladin Radovic, Professor Micah J. Green, Touseef Habib, Smit Shah, and Huili Gao at Texas A&M University. All other work conducted for the dissertation was completed by the student independently.

The study for Chapter II, III, and IV was supported in part by National Science Foundation Grant (1336716 and 1336073), Air Force Young Investigator Research Program (FA9550-13-1-0147), Welch Foundation (A-1766), and Kwanjeong Educational Foundation. The study for Chapter V was supported in party by the National Science Foundation Grant (1410983, 1057155, and 1049706) and Kwanjeong Educational Foundation.

TABLE OF CONTENTS

Page

LIST OF FIGURES

LIST OF TABLES

CHAPTER I

INTRODUCTION

1.1 INTRODUCTORY REMARKS

Polymeric binders are essential to battery electrodes, mechanically stabilizing the active materials. Most often, these binders are insulating, bearing no electrochemical activity nor ionic or electronic conductivity, and conductive carbons must be added to the electrode. Poly(vinylidene fluoride) (PVDF) is the most commonly used binder, followed by poly(tetrafluoroethylene) (PTFE) and carboxy methyl cellulose (CMC).[2, 3] It is desired to minimize amount of binders to maintain mechanical and electrochemical stability and of conductive additives to increase conductivity of the electrode without diluting the active material. Conductive polymer binders, those that transport both ions and electrons, could operate as both binder and conductor to eliminate the need for carbon additives and reduce the total amount of additives.

On the other hand, stretchable, bendable, and foldable conductive coatings are essential for emerging flexible technologies such as biometric sensors, adaptive displays, artificial skin, and wearable devices.[4, 5, 6, 7, 8] This brings the unique requirement of merging electronic performance with mechanical functionality. In this arena, graphene, carbon nanotubes, and metal nanowires have been explored, but it remains challenging to comprehensively address the disparate mechanical deformations in stretching, bending, and twisting while maintaining their electric conductivity. Furthermore, it is desired to engineer conductivity into a variety of unconventional surfaces (*e.g.*, cloth, fiber), but this is challenged by the need for harsh post-treatments to activate the conductive media (*i.e.*, graphene) that may damage the underlying substrate. These challenges

could be met to demonstrate surface-agnostic conductive coatings on flexible and stretchable media using layer-by-layer (LbL) assembly.

This chapter serves to provide background on lithium ion batteries, battery materials, MXene, and LbL assembly to better understand this thesis. The first half covers the working principle of lithium ion batteries and the properties of vanadium pentoxide (V_2O_5), and polythiophenes. In the second half, the general introduction of LbL assemblies and MXenes are provided. Finally, the outline and scope of this thesis are presented.

1.2 LITHIUM ION BATTERY

In 1800, Alessandro Volta first reported a battery consisting of a zinc metal and a copper metal separated by a paper soaked with NaCl electrolyte.[9] The battery mechanism was not understood until 1834 when Michael Faraday demonstrated the zinc metal oxidation during the reaction.[10] Faraday's discovery contributed to the creation of a new scientific field, Electrochemistry. In the 1970-1980s, the concept of a lithium-ion battery was demonstrated.[11, 12, 13] Whittingham presented a TiS_2-based cathode in a cell with a metallic lithium anode.[11] This pioneer study promoted research on other sulfides and chalcogenides during the 1970s and 1980s. However, such cathodes suffered from low cell voltages < 2.5 V. In 1980, the Goodenough group presented oxide cathode material $LiCoO_2$ with high cell voltage (V_{cell}> 4 V).[13] In 1991, Sony succeeded in the commercialization of the world's first high power density, light weight, portable size and long-life lithium ion battery based on a carbon anode and $LiCoO_2$ cathode. This battery exhibited an open circuit voltage of over 3.6 V, an energy density of 150 WH/kg.[14] These outstanding features made them the ideal energy sources for mobile electronic devices and electric vehicles.

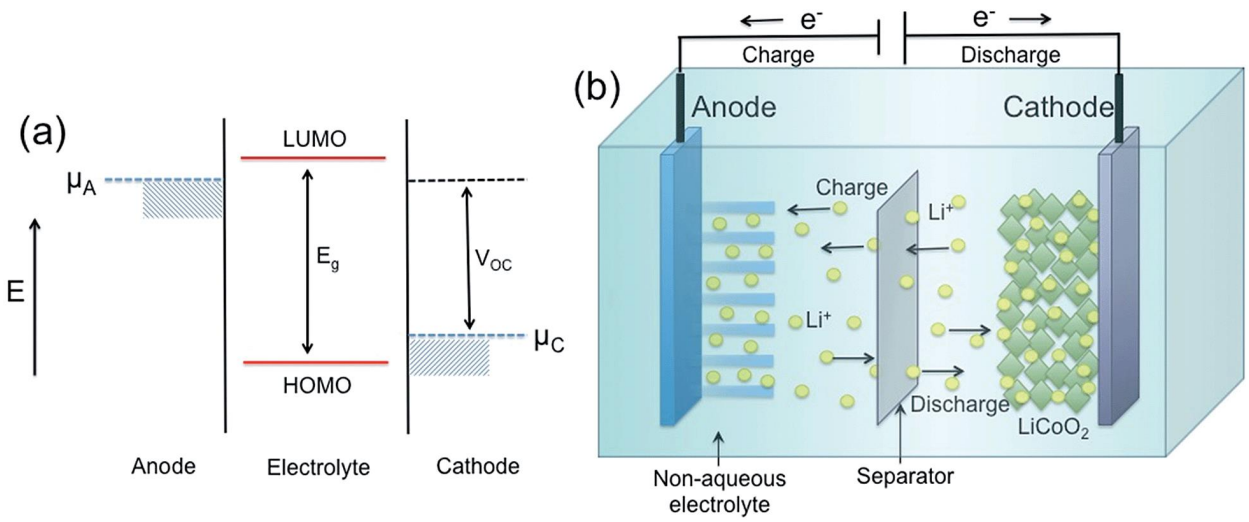

Figure 1.1 (a) Relative energy diagram of electrode potentials and electrolyte energy gap in lithium ion batteries. (b) Schematic diagram of the lithium intercalation–deintercalation mechanism in lithium ion batteries. Reprinted with permission from ref [15]. Copyright 2015 American Chemical Society.

In general batteries, negative and positive electrodes are separated by an ion-conducting and electronic-insulating electrolyte. A lithium ion battery works by converting chemical energy into electrical energy. For an electrochemically stable battery, anode must have lower electrochemical potential (μ_A) than the LUMO of the electrolyte, otherwise the electrolyte will be degraded, and cathode must have higher electrochemical potential (μ_C) than the HOMO of the electrolyte to prevent the oxidation of the electrolyte, as shown in Figure 1.1a.

As shown in Figure 1.1b, a conventional lithium ion battery consists of graphite anode and layered $LiCoO_2$ cathode as an intercalation host for lithium ion, separated by a porous membrane. On charging, $LiCoO_2$ cathode releases lithium ions, they pass through electrolyte, and are stored

in graphite anode. The lithium ion battery chemical redox reactions are shown the following equations:[15]

$$\text{Cathode: } LiCoO_2 \leftrightarrow Li_xCoO_2 + xLi^+ + xe^-$$

$$\text{Anode: } 6C + xLi^+ + xe^- \leftrightarrow Li_xC_6$$

The generated electrons move through the external electrical circuit to couple with the lithium ions in the electrode. In the case of discharge, the reverse redox reactions occur.

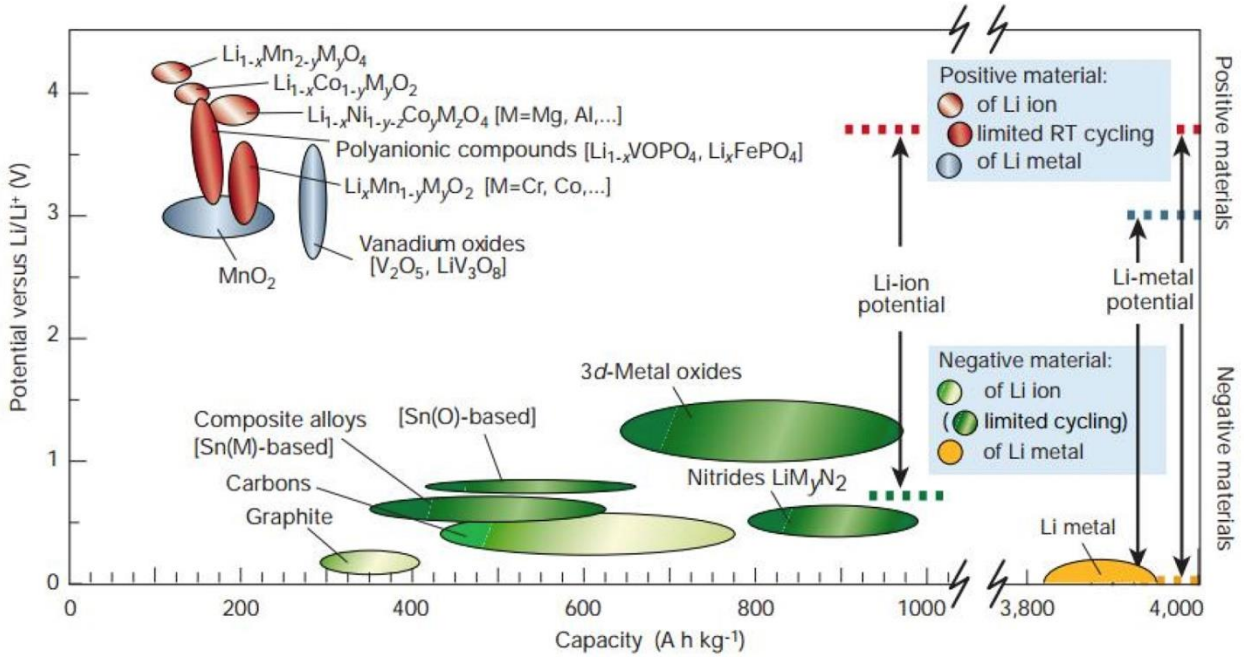

Figure 1.2 Currently available cathode and anode active materials with their potential and capacity. Reproduced with permission from ref [16]. Copyright 2001 Nature Publishing Group.

Figure 1.2 shows available cathode and anode electrode materials along with their performance metrics.[17, 18, 19, 20, 21] Cathode active materials include metal oxides such as lithium

cobalt oxide, lithium manganese oxide, lithium iron phosphate, and vanadium oxide. In the case of anodes, lithium metal, graphite, tin, and silicon have been used. Higher redox potential materials are utilized as cathodes, whereas lower redox potential ones are used as anodes.

In general, electrodes are prepared by mixing active materials with polymeric binders and conductive additives (e.g., super P, Cajun black), and then coated onto current collectors (*e.g.*, Al or Cu foils). As for the electrolyte, lithium salt (*e.g.*, $LiPF_6$ and $LiClO_4$) in a carbonate solvent (*e.g.*, dimethyl carbonate and ethylene carbonate) is used.[22] Electrical insulating separators are placed between anode and cathode to prevent electrical short circuits.[23]

Polymeric binders are ideal components to provide mechanical stability to the electrodes during cycling. Conventional binders include poly(vinylidene fluoride), PVDF poly(tetrafluoroethylene) (PTFE), and carboxyl methyl cellulose (CMC).[2, 3] However, they are usually insulating, bearing no ionic or electronic conductivity nor electrochemical activity.[24, 25, 26] Electroactive polymers are of interest because they can serve as both binder and conductor with the potential to eliminate the need for carbon additives.[27, 28, 29, 30, 31] Electroactive polymer binders includes polyaniline,[30, 32, 33, 34, 35, 36, 37, 38, 39, 40] polypyrol,[32, 41, 42] PEDOT:PSS,[28, 29, 30, 43, 44, 45] polyfluorene,[31, 45] polydopamine,[46, 47, 48] and polythiophene.[49, 50, 51]

Conductive block copolymers are promising for multifunctional binders that can simultaneously improve mechanical adhesion and flexibility with tolerance to large volume changes of the active material during cycling, promote suitable electrode–electrolyte contacts, and increase electronic and ionic conductivity. For example, the Yang group demonstrated a graft copolymer binder, PVDF-*graft*-poly(*tert*-butyl acrylate) (PVDF-*g*-PtBA), for silicon electrodes with improved cyclability (84% of the initial capacity after 50 cycles) compared to Si with PVDF (34% after 50 cycles).[45] The Wei group also showed a poly(acrylic acid sodium)-*graft*-CMC

(NaPAA-*g*-CMC) copolymer binder for Si anodes with improved capacity retention (80%) compared to CMC, PAA, and a NaPAA/CMC mixture showed 39, 46, and 43% retention, respectively.[52] The Balsara group demonstrated a poly(3-hexylthiophene)-*block*-PEO (P3HT-*b*-PEO) binder enabling both electron and ion conductions (10^{-2} and 10^{-4} S/cm, respectively).[1, 53] They reported that the P3HT-*b*-PEO binder enhanced the capacity to a near-theoretical value (about 140 mAh/g) without carbon additives.[53] The multifunctional block copolymer binders successfully replaced both the PVDF binder and carbon additive, promoting efficient use of the active material. Thus, there is great interest in investigating "beyond-PVDF" binders that simultaneously address ion and electron transport in the pursuit of carbon-free electrodes.

Also, selecting a suitable electrolyte for both electrodes is another important aspect. Commonly, aprotic organic solvents such as ethylene carbonate (EC), propylene carbonates (PC), diethyl carbonate (DEC) mixed with lithium salts are used as electrolytes.[54] Lithium salts include hexafluorophosphate ($LiPF_6$) or lithium perchlorate ($LiClO_4$).[55] Electrolyte's viscosity, dielectric constants, side reaction with electrodes are other important parameters for stability of lithium ion batteries.[56, 57, 58, 59, 60, 61, 62]

1.3 VANADIUM PENTOXIDE (V_2O_5)

Vanadium oxides, typical layered structure materials with high theoretical capacity (294 mAh/g assuming two lithium ions were exchanged) and earth abundance, have been extensively studied as a cathode material.[63, 64, 65, 66, 67, 68, 69] Orthorhombic V_2O_5 (or crystalline V_2O_5) has ordered structure with an interlayer spacing of ~4.37 Å (Figure 1.3).[70] The crystalline structure of V_2O_5 has series of distorted VO_6 octahedra. The oxygen atom at the apices of a pyramid has a weak V-O interaction with the vanadium atom in the adjacent layer whereas there is a strong V-O

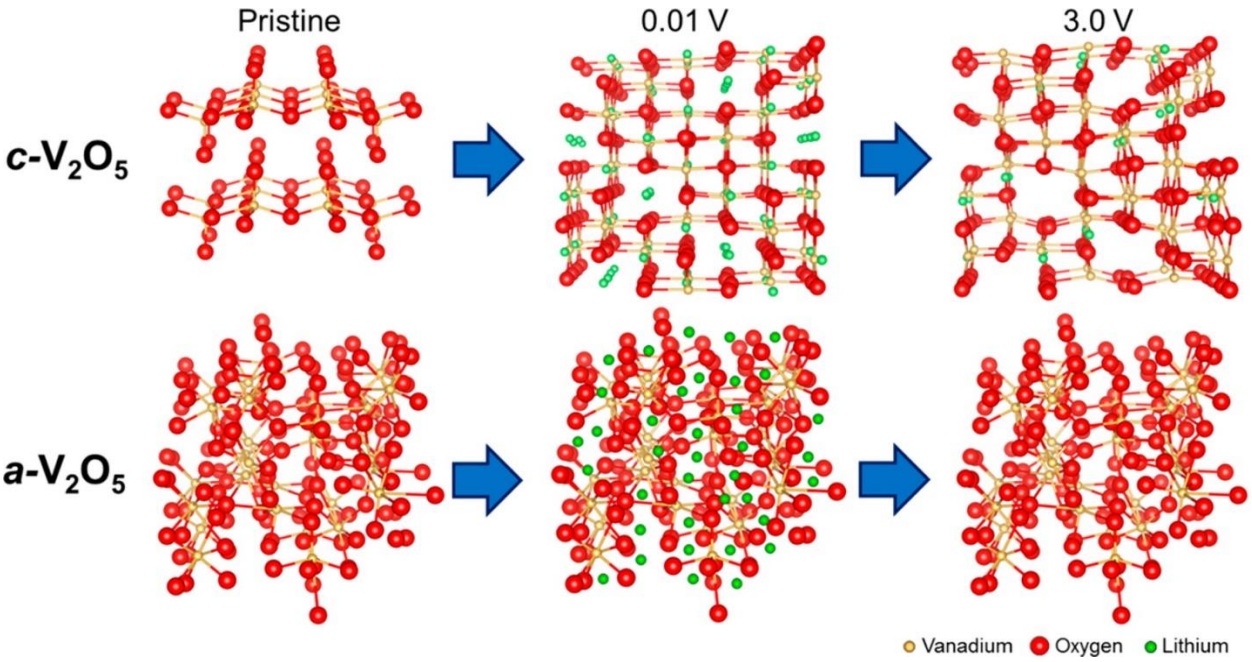

Figure 1.3 Schematic diagrams of structural changes upon lithiation down to 0.01 V and delithiation up to 3.0 V for crystalline V_2O_5 (*c*-V_2O_5) and amorphous V_2O_5 (*a*-V_2O_5). Reproduced with permission from ref [71]. Copyright 2014 American Chemical Society.

interaction between the oxygen atoms at the pyramid base and the vanadium atom in the same layer.[63] In other words, the interlayer interaction is relatively weaker compared the intralayer interaction. The weak V–O interaction provides the layered character of the V_2O_5. The lithium ion intercalation reactions in V_2O_5 is shown the following equations:

$$V_2O_5 + xLi^+ + xe^- \leftrightarrow Li_xV_2O_5$$

Inserting lithium ions into the interlayered spaces of crystalline V_2O_5 results in a series of the phase change: α-$Li_xV_2O_5$ ($0 < x < 0.01$); ε-$Li_xV_2O_5$ ($0.35 < x < 0.7$); δ-$Li_xV_2O_5$ ($0.7 < x < 1$);

γ-$Li_xV_2O_5$ ($1 < x < 2$); ω-$Li_xV_2O_5$ ($2 < x < 3$).[71, 72, 73, 74] The formation of ω-$Li_xV_2O_5$ phase is irreversible.[75, 76]

Amorphous V_2O_5 was prepared as xerogels or aerogels with a large surface area (Figure 1.4).[77, 78, 79, 80] Ambiently dried V_2O_5 xerogels usually has n = 1.8 water in the formula $V_2O_5 \cdot nH_2O$ resulting in an interlayer distance of 11.5 Å.[81] Vacuum-dried V_2O_5 xerogels show n = 0.5 water and an interlayer distance of 8.8 Å.[82] This amorphous V_2O_5 xerogels exhibited a large capacity of ~300 mAh/g compared to crystalline V_2O_5.[83] It is probably because a considerable amount of lithium ions/electrons are stored at the surface.[71]

The implementation of V_2O_5 in practical battery applications has been hindered by low Li^+-diffusion coefficient (~10^{-13} cm^2/s),[84] low electronic conductivity (~10^{-3} S/cm),[67] a loss of structural stability (e.g., pulverization and cracking) during cycling,[85, 86, 87, 88, 89, 90] and irreversible phase formation upon deeper discharge.[91] To address the electrochemical limitations of V_2O_5, conductive polymers were incorporated.[92, 93, 94] Conjugated polymers enhanced the electronic conductivity of V_2O_5 electrodes,[92, 93] and ion-conductive polymers (e.g., poly (ethylene oxide) (PEO)) demonstrated improved ionic conductivity.[94]

1.4 POLYTHIOPHENE

In solid state applications (*e.g.*, photovoltaic cells,[95, 96, 97, 98] and field-effect transistors[99, 100, 101, 102]), poly(3-alkylthiophene)s (P3ATs) have been extensively studied because their thermal and environmental stability, and solution processability. Due to the asymmetricity of the 3-alkylthiophene monomer, it is important to consider the P3ATs' regioregularity—the percentage of a head-to-tail configuration of the hexyl side chains (Figure 1.4).[99, 103, 104, 105, 106, 107, 108, 109, 110, 111] The 3-alkylthiophene monomer are polymerized by coupling between the 2 and 5 positions.

Regiorandom structures induce twisted backbone due to steric hindrance of the alkyl side chains, resulting in the reduction of the conjugation length, poor π-π stacking of the polymer backbone.[112] This increases the bandgap leading to a lower conductivity.[112] On the other hand, P3ATs with a high regioregularity (>90%) have fewer twists in the its backbone providing a planar conformation.[103, 113] This increases a conjugation length and enhance π-π stacking allowing a decrease in the bandgap and an enhanced electronic conductivity.[103, 113]

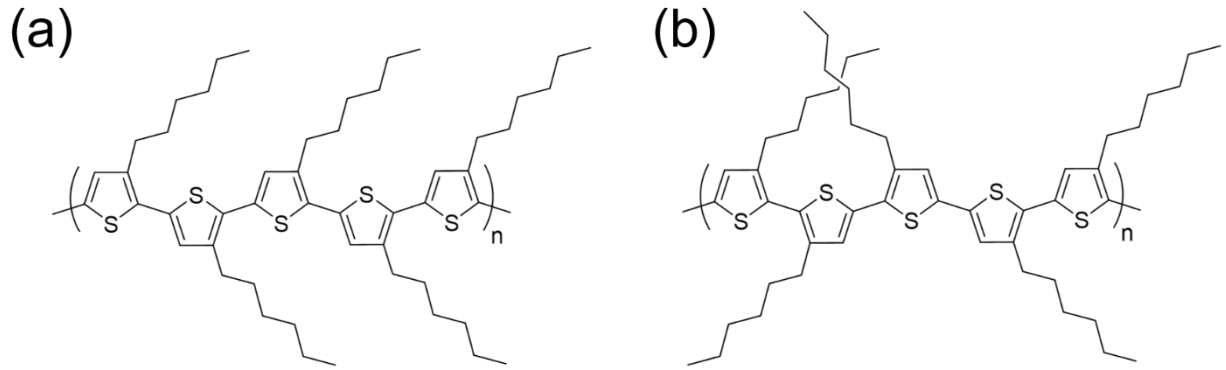

Figure 1.4 Schematic diagrams of regioisomers. (a) Regioregular and (b) regiorandom Poly(3-hexylthiophene)s (P3HTs).

Doping also is important for conductivity of P3ATs. Pristine P3ATs have very low electrical conductivity (10^{-5}~10^{-8} S/cm) due to a very low charge carrier density.[114, 115, 116, 117, 118, 119] To increase charge carriers, P3ATs can be doped chemically or electrochemically.[120] In the case of chemical doping, introduction of an oxidizing agent (*e.g.,* 2,3,5,6-Tetrafluoro-tetracyanoquinodimethane (F4TCNQ)) leads to a spontaneous oxidation of the P3ATs.[121, 122, 123, 124] As for electrochemical doping, an applied potential is used and the dopant counterion in the electrolyte diffuses to stabilize the oxidized P3ATs.[125, 126, 127]

Researcher demonstrated that molecular weight[98, 102, 128, 129, 130, 131, 132, 133] and regioregularity[99, 104, 105, 106, 107, 108, 109, 110, 111] strongly influence on the solid state electronic properties of P3HT. For example, higher molecular weight (30 kDa) of P3HT increased charge-carrier mobility (6×10^{-3} cm^2 V^{-1} s^{-1}) compared to that of lower molecular weight P3HT (4 kDa, 4×10^{-6} $cm^2V^{-1}s^{-1}$).[128] Higher regioregularity (96% vs. 70%) increased charge-carrier mobility (5×10^{-2} $cm^2V^{-1}s^{-1}$ vs. 2×10^{-5} $cm^2V^{-1}s^{-1}$).[99] Although the importance of regioregularity and molecular weight on solid state electronic performance was recognized, such an understanding of the effects on electrochemical property is lacking.

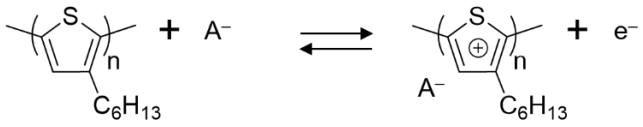

Figure 1.5 P3HT doping/depoing mechanism. A^- is a counter anion.

Unlike the solid state electronic process, the electrochemical process occurs in the presence of a liquid electrolyte in which both electrons and ions simultaneously transport. In an electrochemical system, P3HT exhibits a pseudocapacitive behavior (Figure 1.5): when P3HT is being doped, it loses electrons and becomes positively charged, causing anions in the electrolyte to approach the positively charged polymer backbone for electroneutrality. There have been few reports on the regioregularity effect of P3HT homopolymers on electrochemical performance: high regioregularity (96% vs. 58%) increased specific capacitance (134.5 F/g vs. 71.8 F/g).[134]

1.5 MXENE

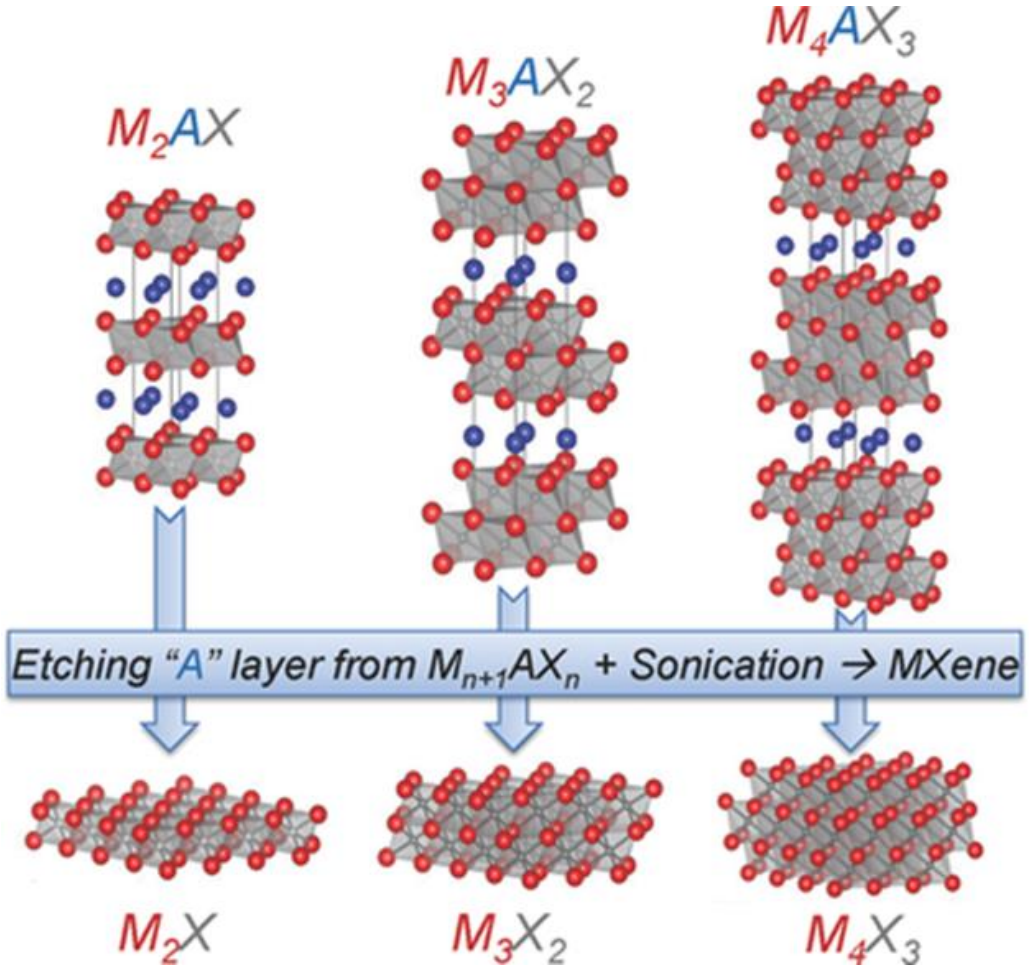

Figure 1.6 Schematics of the preparation of MXenes from the corresponding MAX phases. Reproduced with permission from ref [135]. Copyright 2013 Advanced Materials.

Two-dimensional transition metal carbides (called MXenes) were discovered in 2011 by Naguib and co-workers.[136] In general, MXenes are derived from the parent MAX phases (Figure 1.6) consisting of layered carbides with the formula $M_{n+1}AX_n$, where M is an early transition metal (Sc, Ti, V, Cr, Zr, Nb, Mo, Hf, or Ta), A is mainly groups 13 or 14 (Cd, Al, Si, P, S, Ga, Ge, As, In, Sn, Tl, Pb, or S), X is C and/or N, and n = 1, 2, or 3.[137, 138, 139, 140, 141] General chemical formula

of MXene is $M_{n+1}X_nT_x$, where surface terminal groups (T) are -F, -OH, -O, etc., and where "x" denotes the number of terminal groups.[135] In Ti_3AlC_2, the Al atoms could be selectively removed from the MAX structure in a 50 wt.% aqueous hydrofluoric acid (HF) solution at room temperature for 2 h.[136] To separate the solid from the supernatant, the mixture was centrifuged and/or filtrated followed by washing of the solid with deionized water.[135] MXene exhibited a loosely packed accordion-like structure (Figure 1.7).[142] The accordion-like multilayered MXene were isolated into single flakes via sonication, showing a layered morphology similar to that of exfoliated graphite (Figure 1.7).[142]

MXenes have received considerable attention due to their hydrophilic surfaces,[143] metallic-like conductivities (~600,000 S/m),[144, 145] high surface area,[135] structure tunability[135] and a wide range of applications including energy storage devices,[140, 146, 147, 148] electromagnetic interference shielding,[149] transparent, conductors,[144, 150, 151] water desalination,[152] and catalysis.[137] MXenes are of particular interest due to their high conductivity. For example, the Gogotsi group demonstrated conductive MXene papers with a modulus of 3.5 GPa and ultimate strain of 1%.[153] Adding polymers (e.g., polyvinyl alcohol, polyacrylamide, polyethylene, polydiallyldimethylammonium chloride) to the MXene papers enhanced mechanical robustness.[153, 154, 155] However, these MXene papers were not stretchable, and their integration into complex surfaces (such as fiber and fabric) was not demonstrated.

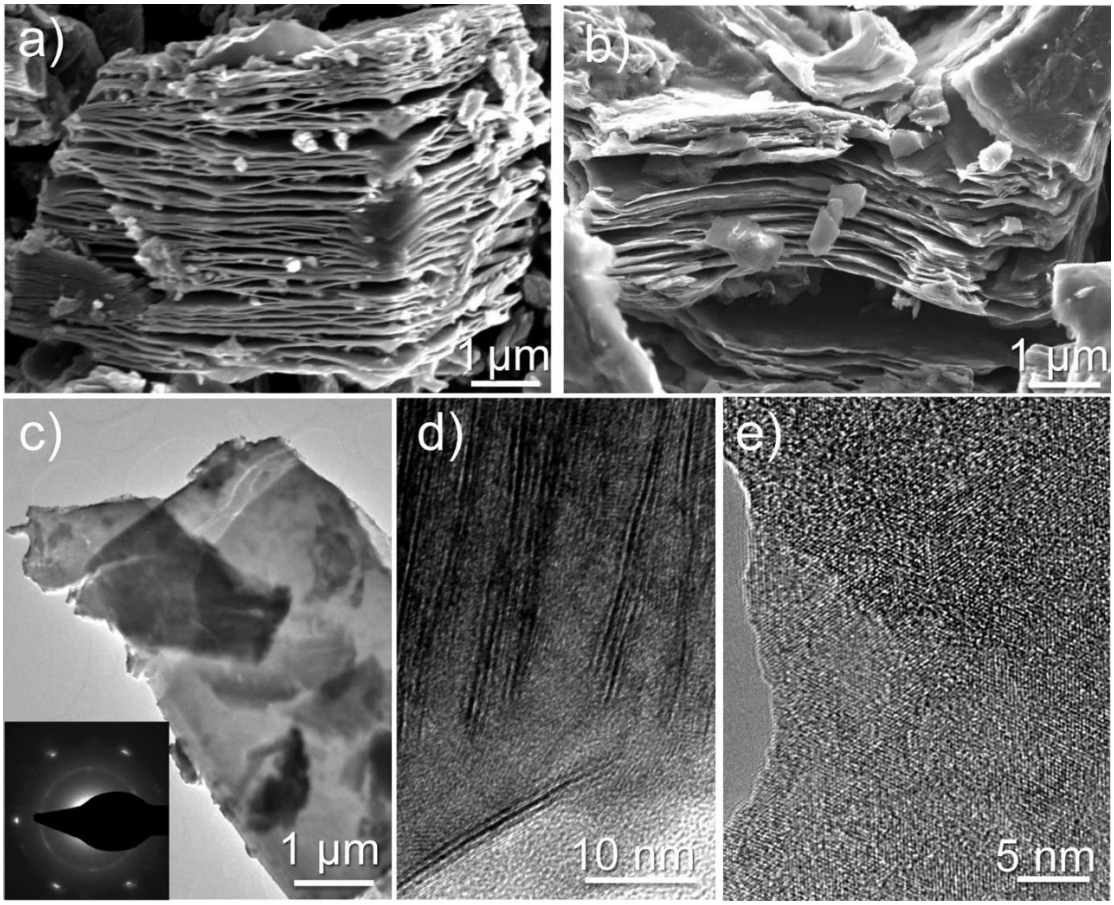

Figure 1.7 Scanning electron microscope (SEM) images of (a) Nb_2CT_x and (b) V_2CT_x and (c) Transmission electron microscope (TEM) image of a Nb_2CT_x flake. Inset of the SAED shows the hexagonal basal plane symmetry, which is identical to that of the parent MAX phase. (d) Cross-sectional TEM image of Nb_2CT_x and (e) in-plane TEM image of a V_2CT_x flake. Reproduced with permission from ref [142]. Copyright 2013 American Chemical Society.

1.6 LAYER-BY-LAYER ASSEMBLY

The layer-by-layer (LbL) assembly technique has been of considerable interest because it offers superior control and versatility compared to other available thin-film deposition techniques. Iler and later Decher first demonstrated LbL assembly.[156, 157] LbL assemblies are built up by the

sequential deposition of oppositely charged materials (Figure 1.8) through various forces such as electrostatic interactions, hydrogen bonding, charge transfer, hydrophobic interactions, and enthalpic and entropic driving forces.[158, 159, 160, 161, 162]

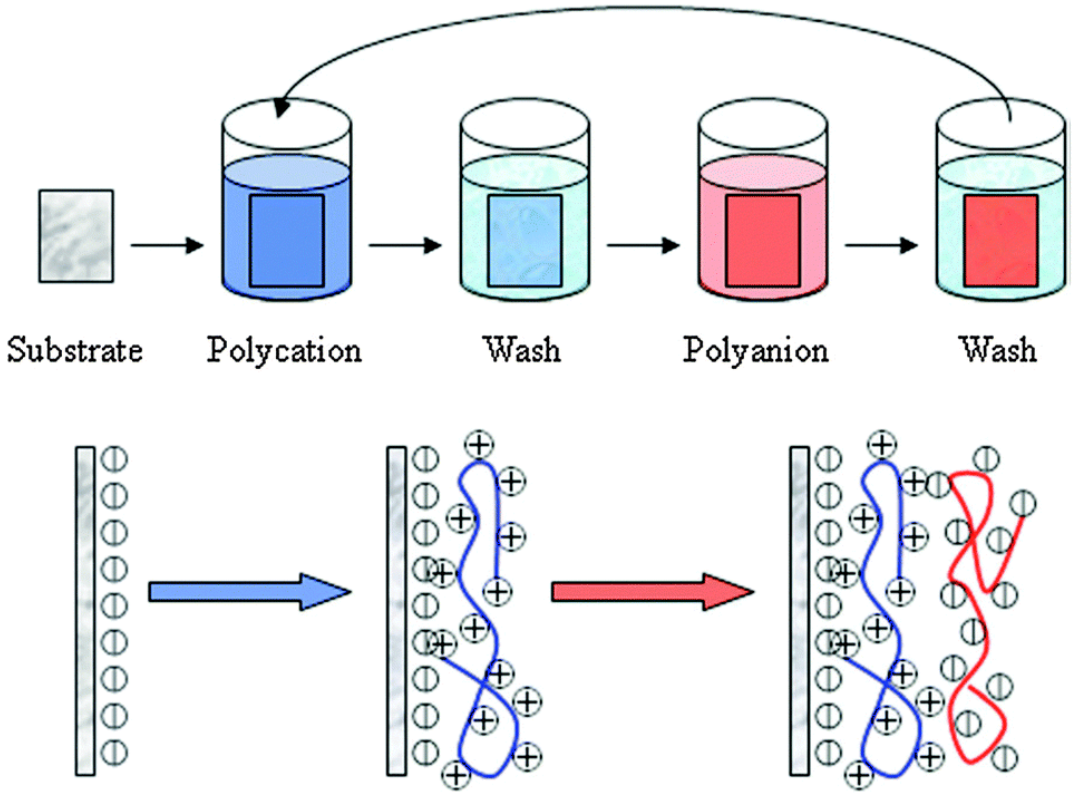

Figure 1.8 Schematic diagram of layer-by-layer assembly technologies. Reproduced with permission from ref [163]. Copyright 2012 The Royal Society of Chemistry.

The standard LbL assembly is dipping-assisted assembly, whereby the substrate is sequentially immersed into oppositely charged material solutions for deposition, with rinsing steps between the deposition steps to remove weakly bound materials. We can control film thickness easily by controlling the number of deposition cycles. Also, it allows conformal coatings on three-dimensional objects with tailored balance among multiple functional properties through

meticulous controlled of material structure and coating uniformity. A number of materials can be used to fabricate LbL films including polymers, clays, graphene oxide, nanoparticles, dendrimers, proteins, DNA, colloids, quantum dots, metal oxides, and carbon nanotubes.[164, 165, 166, 167, 168, 169, 170, 171, 172]

LbL assemblies have been extensively explored for diverse applications in a wide range of fields including separations,[173, 174] optics,[175, 176] flexible electronics,[177] energy,[177, 178, 179, 180, 181, 182] anticorrosions,[182, 183] sensors,[184, 185] and biomedicine.[186, 187] For example, the Kotov group successfully demonstrated stretchable conductors of polyurethane containing spherical gold nanoparticles deposited by layer-by-layer assembly.[177] The polyurethane/gold nanoparticle composites can conduct electricity even when stretched (3500 S/m at $\varepsilon = 480\%$). These materials also exhibited the electro-tunability of their viscoelastic properties, which result from the dynamic self-organization of the nanoparticles as the material is stretched. The Hammond group demonstrated multiwall carbon nanotube nanoporous thin films with interpenetrating network structure.[179] This thin film showed high electronic conductivity and high capacity with precise control of capacity.

1.7 DISSERTATION OVERVIEW

Polymeric binders are important to battery electrodes, mechanically and electrochemically stabilizing the electrode structures. Most often, these binders are insulating, and conductive carbons must be added to the electrode structure. Conductive polymer binders, those that transport both ions and electrons, are of primary interest because they have the potential to reduce or potentially eliminate the need for carbon additives. However, it is challenging to incorporate both ion- and electron-conducting polymeric binders into electrode systems because of differences in

physical affinities among the two polymer types and the electroactive material. Chapters II and III deal with conductive block copolymer binders for lithium ion batteries, and Chapter IV presents the characteristics of conductive block copolymers.

Stretchable, bendable, and foldable conductive coatings are crucial for wearable electronics and biometric sensors. Such coatings should maintain their conductivity while simultaneously interfacing with different types of surfaces undergoing mechanical deformation. MXene sheets as conductive 2D nanomaterials are promising for the conductive coatings, but it is challenging to form surface-agnostic MXene coatings that can withstand extreme mechanical deformation. In Chapter V, we present surface-agnostic highly stretchable and bendable conductive MXene multilayers.

Chapter II presents the water-based self-assembly approach that incorporates electron- and ion-conducting P3HT-*b*-PEO block copolymer binders into V_2O_5 to form a flexible, tough, carbon-free hybrid battery cathode. V_2O_5 is a promising cathode material, but it remains limited by its poor conductivity and mechanical stability. Our approach led to a unique electrode structure consisting of interlocking V_2O_5 layers held together by the block copolymer binder in a brick-and mortar-like fashion. This structure resulted in robust mechanical properties, far exceeding those obtained from conventional fluoropolymer binders. Only 5 wt % polymer was required to triple the flexibility of V_2O_5, and electrodes comprised of 10 wt % polymer had unusually high toughness (293 kJ/m3) and specific energy (530 Wh/kg), both higher than reduced graphene oxide paper electrodes. Addition of P3HT-*b*-PEO increased lithium-ion diffusion, eliminated cracking during cycling, and enhanced cyclability relative to V_2O_5 alone.

Chapter III presents the comparison of block copolymer binders and homopolymer binders. P3HT-*b*-PEO binder was compared to P3HT, PEO, and a blend of P3HT/PEO homopolymers in

carbon-free V_2O_5. The electrode with P3HT-*b*-PEO binder showed the highest capacity of 190 mAh/g at a 0.1 C-rate after over 200 cycles, a 2.5-fold improvement of that of pure V_2O_5, whereas P3HT, PEO, and the blend exhibited capacities of 139, 130, and 70 mAh/g. The unique architecture of P3HT-*b*-PEO, wherein P3HT and PEO blocks are covalently bonded, improved the uniform distribution of the conductive binders within the V_2O_5 structure, whereas the analogous P3HT/PEO blend suffers from phase separation.

Chapter IV presents the strong effects of regioregularity and molecular weight of the P3HT block in P3HT-*b*-PEO on molecular conformation and electrochemical properties. We compared four different P3HT-*b*-PEO block copolymers—various P3HT regioregularities and molecular weights while the PEO block molecular weight was kept the same. Under sonication, the P3HT-*b*-PEO block copolymers formed micellar aggregates, in which hydrophilic PEO forms a corona around hydrophobic P3HT. The self-assembled P3HT domains had a disordered structure (over 90 wt% is quasi-ordered or even amorphous). The regioregularity and molecular weight of P3HT block strongly affected its backbone conformation and chain packing structure, correlating with the P3HT redox properties. We also found that backbone planarity was most important for affecting capacity.

Chapter V show the conductive and conformal MXene multilayer coatings that can undergo large-scale mechanical deformation while maintaining a conductivity as high as 2,000 S/m. MXene multilayers were successfully fabricated onto flexible polymer sheet, stretchable poly(dimethylsiloxane), nylon fiber, and glass. The coating showed a recoverable resistance response to bending (up to 2.5 mm bending radius) and stretching (up to 40% tensile strain), which was leveraged for detecting human motion and topographical scanning.

Finally, Chapter VI summarizes the results and suggests possible directions for future work.

CHAPTER II

HIGHLY FLEXIBLE SELF-ASSEMBLED V_2O_5 CATHODES ENABLED BY CONDUCTING DIBLOCK COPOLYMERS*

2.1 INTRODUCTION

There is a growing need for low-cost, flexible, and rugged energy storage devices compatible with emerging flexible energy conversion devices and structural energy and power.[153, 188, 189, 190] Recent work has demonstrated electrode materials with both mechanical robustness and electrochemical functionality, including carbon nanotube Buckypaper,[182, 191, 192, 193] reduced graphene oxide paper,[194, 195] graphite on super-aligned CNTs,[196] TiO_2 on activated carbon fabric, [196] and vanadium pentoxide (V_2O_5) wires.[197] Of these, V_2O_5 is particularly promising because it offers higher specific energy and because it has the ability to form paper-like electrodes very similar to Bucky paper. Unfortunately, the application of V_2O_5 in practical batteries has been hindered by a low Li^+-diffusion coefficient (10^{-12} –10^{-13} cm^2/s),[67] low electronic conductivity (10^{-2} –10^{-3} S/cm)[67] and volumetric changes[86] during cycling.

Past approaches sought to address the electrochemical limitations of V_2O_5 by incorporation of conductive polymers, but little has been achieved by way of mechanical enhancement. Conjugated polymers can improve the electronic conductivity of V_2O_5electrodes,[93, 198] and ethylene oxide-containing polymers have demonstrated improved

*Reprinted with permission from "Highly flexible self-assembled V_2O_5 cathodes enabled by conducting diblock copolymers" by Hyosung An, Jared Mike, Kendall A. Smith, Lisa Swank, Yen-Hao Lin, Stacy L. Pesek, Rafael Verduzco and Jodie L. Lutkenhaus, *Sci. Rep.* **2015**, 5, 14166. Copyright 2015 Nature Publishing Group.

ionic conductivity.[94] Besides the materials themselves, the manner in which the blend is prepared can have a huge impact on electrode structure and mechanical properties. Large-scale phase separation between different components can result in poor mechanical properties, so intimate mixing and good interfacial adhesion is important.

To demonstrate a viable route to mechanically robust V_2O_5 electrodes, we propose the implementation of block copolymers, in which two polymers are covalently attached to each other preventing mascroscopic phase separation.[199] There exist only a handful of studies that incorporate block copolymers into hybrid electrodes, highlighting that the largest challenge for these hybrid electrodes is to balance the benefits of the added conductivity from the polymer without diluting the active material. For instance, the Balsara group reported the use of poly(3-hexylthiophene)-*block*-poly(ethyleneoxide) P3HT-*b*-PEO block copolymer as a conductive binder for a $LiFePO_4$ cathode.[1, 53] $LiFePO_4$performed at near-theoretical capacity, but a block copolymer loading of 50 wt% was required; mechanical properties were not reported. The Mayes group reported the synthesis of V_2O_5aerogel within a block copolymer matrix.[94] This resulted in significantly improved mechanical properties, but the V_2O_5 content was only 34 wt%, resulting in a very low capacity. In both of these approaches, the loading of the active material was prohibitively low.

Here, our approach centers on a V_2O_5 hybrid electrode, in which we balance a high active material content with the benefits afforded by the P3HT-*b*-PEO block copolymer. The electrodes are prepared in a straightforward and scalable water-based process, and the addition of just 5 wt % block copolymer produces electrodes with excellent mechanical flexibility. We present the electrochemical and mechanical properties of the hybrid electrodes as a function of

composition, for which a trade-off between polymer content and electromechanical properties is revealed. Specifically, we demonstrate that small amounts of a (P3HT-*b*-PEO) block copolymer can bring about significant improvements in mechanical flexibility, toughness, and lithium ion diffusion. The enhanced mechanical properties are attributed to the self-assembled layering of V_2O_5 with P3HT-*b*-PEO micellar aggregates. A proof-of-concept flexible half-cell is also shown. These results confirm that these ion- and electron-conducting block copolymers are excellent binders, bringing about not only conductivity but also mechanical flexibility.

2.2 EXPERIMENTAL METHOD

Materials. Vanadium pentoxide, lithium bis(trifluoromethanesulfonyl)imide (LiTFSI), poly(vinylidene fluoride) (PVDF, molecular weight = 534,000 g/mol), N-methyl-2-pyrrolidone (NMP), and propylene carbonate (PC) were purchased from Sigma Aldrich. Lithium ribbon was purchased from Alfa Aesar. All chemicals were used as received. 316 stainless steel coins used as substrates were purchased from MTI Corporation. Water was purified to 18.2 MΩ-cm (Milli-Q, Millipore). PEO-OH was purchased from from Aldrich (lot# BCBB1016, 7.17 kg mol^{-1} by ^1H NMR).

Synthesis of V_2O_5 xerogel. Vanadium pentoxide xerogel was synthesized using hydrogen peroxide according to previously reported procedures.[200] Briefly, V_2O_5 (3.0 g) was dissolved into 300 mL of 10% aqueous H_2O_2 solution. This solution was aged for three days, after which the water was removed and the solid xerogel was dried in the oven under air overnight at 100°C. After synthesis, the V_2O_5 xerogel was resuspended in water at a concentration of 16.7 mg/mL.

Synthesis of P3HT-*b*-PEO block copolymer. Isopropyl magnesium chloride with lithium chloride complex (^{i}PrMgCl·LiCl, 1.3M), tetrakis(triphenylphosphine)nickel(0) ($Ni(PPh_3)_4$), 4-

chloro-3-methylphenol, 1,3-bis(diphenylphosphino)propane (dppp), tetra-*n*-butylammonium fluoride (TBAF) (1.0 M in THF), 5-hexynoic acid (112.13 g/mol), 4-dimethylaminopyridine (DMAP) (122.17 g/mol), N,N,N′,N″,N″-pentamethyldiethylenetriamine (PMDETA) , 3-hexylthiophene, drisolve dichloromethane, p-Toluenesulfonyl chloride, azidotrimethylsilane, ethylene carbonate, imidazole, and copper (I) bromide, and *tert*-butyldimethylsilane were purchased from Sigma-Aldrich and used as received. 2,5-dibromo-3-hexylthiophene and 2-(4-chloro-3-methylphenoxy)ethanol[201] (1) were synthesized as previously reported. N-(3-dimethylaminopropyl)-N′-ethylcarbodiimide hydrochloride (EDC) was purchased from TCI America. All other solvents and reagents were purchased from VWR and used as received unless stated otherwise.

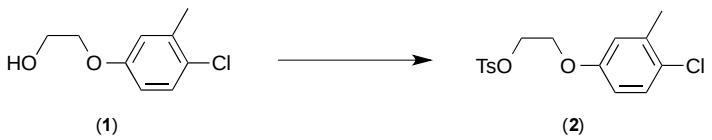

(**1**) (**2**)

Figure 2.1 Synthesis scheme of 2-(4-chloro-3-methylphenoxy)ethyl tosylate.

2-(4-chloro-3-methylphenoxy)ethyl tosylate (2). A dry flask was charged with 2-(4-chloro-3-methylphenoxy)ethanol (1) (3.3 g, 17.7 mmol), p-Toluenesulfonyl chloride (6.8g, 35.7 mmol), dry dichloromethane (15ml), and pyridine (2.7 ml) and stirred overnight with a precipitate forming. The organic phase was dried over magnesium sulfate and purified by column chromatography (SiO_2, 25% EtOAc/hexanes). Solvent was removed under reduced pressure and the product was stored under vacuum overnight as a white solid. Yield (recovered): 3.47 g, 60%. ^{1}H NMR (500 MHz, $CDCl_3$), δ (ppm): 7.81 (d, 2H, Ar-*H*), 7.34 (d, 2H, Ar-*H*), 7.18 (d, 1H, Ar-*H*),

6.65 (d, 1H, Ar-*H*), 6.55 (q, 1H, Ar-*H*), 4.35 (t, 2H, Ar-O-CH_2-C*H*$_2$-O-), 4.10 (t, 2H, Ar-O-C*H*$_2$-CH_2-O-), 2.45 (s, 3H, Ar-C*H*$_3$), 2.31 (s, 3H, Ar-C*H*$_3$).

Tosylate-functionalized Ni(dppp) catalyst (3). In a nitrogen-filled glovebox, $Ni(PPh_3)_4$ (54 mg, 0.049 mmol) was dissolved in 1 mL anhydrous tetrahydrofuran (THF). 2-(4-chloro-3-methylphenoxy)ethyl tosylate **(2)** (100 mg, 0.332 mmol) was added and the solution was allowed to stir overnight, at least 16 h. In a separate flask, 1,3-bis(diphenylphosphino)propane (80 mg, 0.192 mmol) was dissolved in 1 mL THF and added to the crude reaction solution of **(2)**, and the reaction mixture was stirred at room temperature for 2h. The crude product was removed from the glovebox and used to initiate the polymerization of P3HT, as described below.

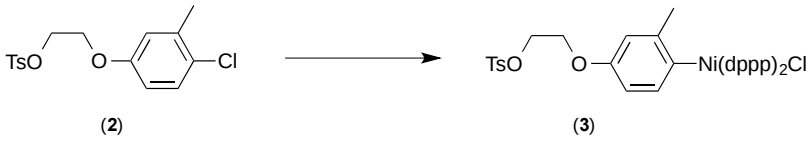

(**2**) (**3**)

Figure 2.2 Synthesis scheme of Tosylate-functionalized Ni(dppp) catalyst.

Tosylate end-functionalized P3HT. 2,5-dibromo-3-hexylthiophene (1.91g, 5.86 mmol) was dissolved in anhydrous THF (4.5 mL) in a 100 mL round-bottom flask, and the solution was stirred at 0 ^oC for 15 minutes. A solution of isopropyl magnesium chloride with LiCl (1.3 M) in THF (4.51 mL, 5.86 mmol) was added, and the mixture was stirred for 2 hours at 0 ^oC. Next, 40 mL of THF was added to the reaction flask followed by the crude reaction solution containing (**3**) (0.049 mmol, 2mL). The solution was stirred for an hour and a half before quenching with 5M HCl (2 mL, 10 mmol). The polymer was recovered by precipitation in ethanol and dried under

vacuum. ^{1}H NMR (500 MHz, $CDCl_3$), δ (ppm): 7.83 (d, 2H, Ar-*H*), 7.35 (d, 2H, Ar-*H*), 7.30 (d, 1H, Ar-*H*), 6.68 (d, 1H, Ar-*H*), 6.64 (q, 1H, Ar-*H*), 4.41 (t, 2H, Ar-O-C*H*$_2$-CH$_2$-O-), 4.19 (t, 2H, Ar-O-CH$_2$-C*H*$_2$-O-), 2.45 (s, 3H, Ar-C*H*$_3$), 2.47 (s, 3H, Ar-C*H*$_3$), 7.00 (s, n·1H, Ar-*H*), 2.82 (t, n·2H,Ar-C*H*$_2$-), 1.72 (q, n·2H, -C*H*$_2$-), 1.46 (b, n·2H, -C*H*$_2$-), 1.37 (b, n·4H, -C*H*$_2$-), 0.93 (t, n·3H, -C*H*$_3$).

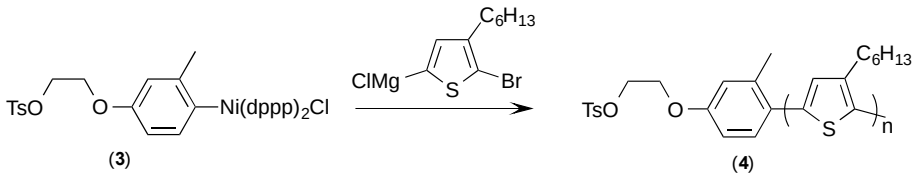

Figure 2.3 Synthesis scheme of Tosylate end-functionalized P3HT.

Azide end-functionalized P3HT. In a typical procedure, tosylate functionalized P3HT (473 mg, 0.049 mmol) was dissolved in 20 ml of anhydrous THF and heated to dissolve the polymer before returning to room temperature. Azidotrimethylsilane (0.4 ml, 3mmol), 2ml of 1M TBAF (2mmol) were added to the flask and the solution was heated overnight at 35°C. Solution was precipitated in methanol, collected by filtration, and washed with acetone before drying overnight in a vacuum oven. Molecular weight and polydispersity was determined relative to polystyrene standards (M_N = 9.7 kg mol^{-1}, PDI = 1.22). Molecular weight was also determined by integration of aromatic hydrogens relative to end group hydrogens (M_N = 13.3 kg mol^{-1}). ^{1}H NMR (500 MHz, $CDCl_3$), δ (ppm): 7.38 (d, 1H, Ar-*H*), 6.84 (s, 1H, Ar-*H*), 6.80 (q, 1H, Ar-*H*), 4.20 (t, 2H, Ar-O-CH$_2$-C*H*$_2$-O-), 3.63 (t, 2H, Ar-O-C*H*$_2$-CH$_2$-O-), 7.00 (s, n·1H, Ar-*H*), 2.82 (t, n·2H,Ar-C*H*$_2$-), 1.72 (q, n·2H, -C*H*$_2$-), 1.46 (b, n·2H, -C*H*$_2$-), 1.37 (b, n·4H, -C*H*$_2$-), 0.93 (t, n·3H, -C*H*$_3$)

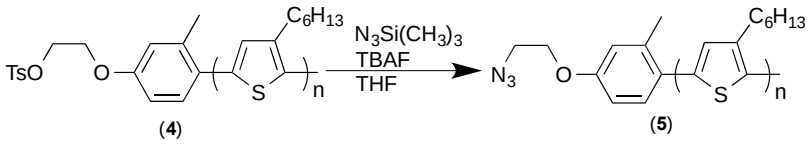

Figure 2.4 Synthesis scheme of Azide end-functionalized P3HT.

Synthesis of alkynyl-PEO. PEO-OH (5.07 g, 0.71 mmol), 5-hexynoic acid (1 g, 8.9 mmol), EDC (0.28 g, 1.466), DMAP (0.05 g, 0.42 mmol), and dichloromethane (30 ml) were added to a flask and stirred overnight. Solution washed with brine and DI water in a separation funnel. Organic fraction collected, dried over magnesium sulfate, filtered and concentrated under reduced pressure. Cold ether was added (80ml) and the material collected by filtration and dried overnight under vacuum. Molecular weight and polydispersity was determined relative to polystyrene standards (M_N = 5.5 kg mol^{-1}, PDI = 1.06). Molecular weight was also determined by integration of aromatic hydrogens relative to end group hydrogens (M_N = 7.2 kg mol^{-1}). Yield 3.3 g (65%). ^{1}H NMR (500 MHz, $CDCl_3$), δ (ppm): 4.24 (t,2H,O-CH_2-CH_2-OCO), 3.64 (b, 652H, -O-CH_2-CH_2-O-), 3.78 (t,2H,O-CH_2-CH_2-OCO), 2.48 (t, 2H, OCO-CH_2-CH_2-CH_2-C-CH), 2.27 (t, 2H, OCO-CH_2-CH_2-CH_2-C-CH), 1.99 (s, 1H, C-CH), 1.85 (m, 2H, OCO-CH_2-CH_2-CH_2-C-CH)

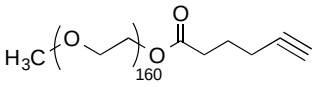

Figure 2.5 Chemical structure of alkynyl-PEO.

P3HT-*b*-PEO block copolymers. In a typical reaction, azide functionalized P3HT (403mg, 0.049 mmol), alkyne functionalized PEO (377 mg, 0.05 mmol), and CuBr (7.7mg, 54 mmol) where mixed with 20ml of THF in a dry flask. Oxygen was removed by bubbling with

nitrogen for 20 min, after which PMDETA was added (0.2 ml). Reaction was allowed to proceed overnight at 40°C after which the raw product was passed through a short basic alumina column which was washed with copious amounts of THF, concentrated under reduced pressure, and washed with cold methanol to remove excess PEO. Sample is 76% P3HT by integration of backbone hydrogens from ^{1}H NMR. Molecular weight and polydispersity was determined relative to polystyrene standards (M_N = 9.35 kg mol^{-1}, PDI = 1.24). ^{1}H NMR (500 MHz, $CDCl_3$), δ (ppm): 7.53 (s, 1H, CH triazole), 7.34 (d, 1H, Ar-*H*), 6.79 (s, 1H, Ar-*H*), 6.74 (m, 1H, Ar-*H*), 4.74 (t, 2H, Ar-O-C*H*$_2$-CH$_2$-O-), 4.37 (t, 2H, Ar-O-CH$_2$-C*H*$_2$-O-), 4.23 (t,2H,O-CH$_2$-C*H*$_2$-OCO), 3.78 (t,2H,O-C*H*$_2$-CH$_2$-OCO), 2.61 (t, 2H, OCO-C*H*$_2$-CH$_2$-CH$_2$-C-CH), 2.42 (t, 2H, OCO-CH$_2$-CH$_2$-C*H*$_2$-C-CH), 2.03 (m, 2H, OCO-CH$_2$-C*H*$_2$-CH$_2$-C-CH), 7.00 (s, n·1H, Ar-*H*), 2.82 (t, n·2H,Ar-C*H*$_2$-), 1.72 (q, n·2H, -C*H*$_2$-), 1.46 (b, n·2H, -C*H*$_2$-), 1.37 (b, n·4H, -C*H*$_2$-), 0.93 (t, n·3H, -C*H*$_3$) , 3.64 (b, m·H, -O-C*H*$_2$-C*H*$_2$-O-).

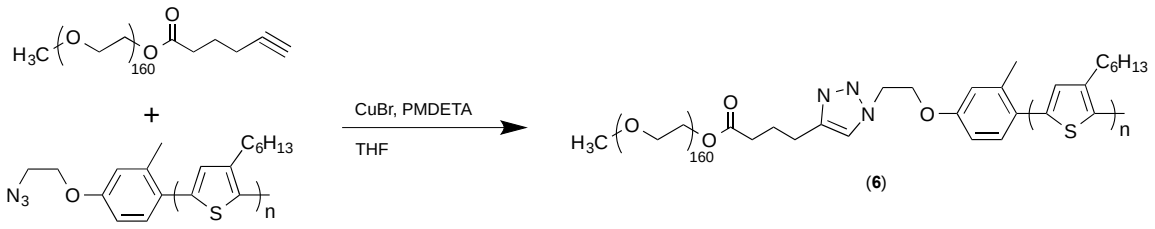

Figure 2.6 Synthesis scheme of P3HT-*b*-PEO block copolymers.

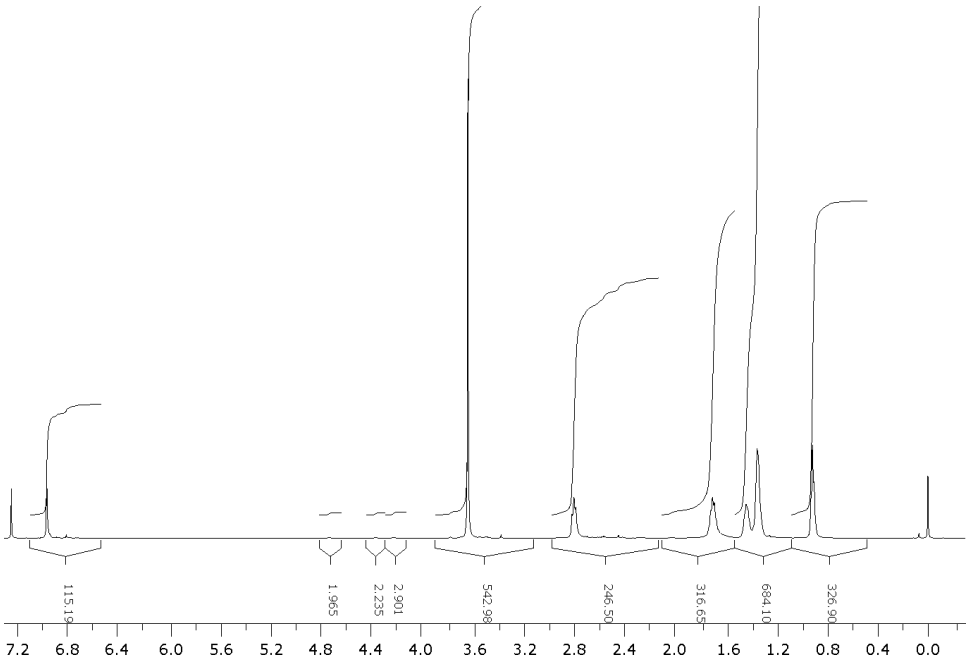

Figure 2.7 ^{1}H NMR of P3HT-*b*-PEO

Preparation of polymer suspensions. A VWR Symphony ultrasonic cleaner (VWR Model 97043-936, 35 kHz) was used to prepare the polymer dispersion. P3HT-*b*-PEO suspensions were made by sonicating the polymer and LiTFSI in Milli-Q water at 0 °C to make a 4 mg/mL stock solution. The molar ratio of ethylene oxide units to lithium ions was 0.085. Before making composites, aliquots of 4 mg/mL P3HT-*b*-PEO solutions were diluted to 1 mg/mL. Hydrodynamic diameter was determined using dynamic light scattering (DLS) (ZetasizerNano ZS90, Malvern) at 25 °C. For DLS, the P3HT-*b*-PEO solution was diluted to 0.05 mg/ml.

Cathode preparation. Before use, 316 stainless steel coins (15.8 mm diameter × 1.6 mm thickness) were cleansed *via* sonication for 15 minutes each in dichloromethane, acetone, water, and isopropanol, followed by drying under vacuum overnight at room temperature. Composites were made by mixing together appropriate volumes of 1 mg/mL P3HT-*b*-PEO (diluted from

4 mg/mL solutions) and 16.7 mg/mL V_2O_5 xerogel solutions in Milli-Q water. These solutions were drop-cast on stainless steel coins by depositing 0.97–1.12 mg worth of material (polymer + V_2O_5) onto the surface. Hereafter, electrodes containing X wt% polymers will be called "PX". After drying in air, the cathodes were held under vacuum at 90 °C for 16 hours. For the electrodes containing PVDF, these were prepared by mixing V_2O_5 with PVDF in NMP. The mixture was cast as before and allowed to dry at 70 °C for three hours, and then 90 °C overnight under vacuum.

Cathode morphologies were investigated using scanning electron microscopy (SEM, JEOL JSM-7500F). Grazing incidence wide angle x-ray scattering measurements were carried out on Sector 8-ID-E at Advanced Photon Source, Argonne National Laboratory.[202] Beamline 8-ID-E operates at an energy of 7.35 keV and images were collected from a Pilatus 1MF camera (Dectris), with two exposures for different vertical position of the detector. After flatfield correction for detector non-uniformity, the images are combined to fill in the gaps for rows at the borders between modules, leaving dark only the columns of inactive pixels at the center. Using the GIXSGUI package[203] for Matlab (Mathworks), data are corrected for x-ray polarization, detector sensitivity and geometrical solid-angle. The beam size is 200 μm (h) × 20 μm (v). Sample detector distance is 204 mm. Sample measurement and thermal annealing were carried out under vacuum which is in the range of $2 \sim 3 \times 10^{-6}$ bar, with the sample stage interfaced with a Lakeshore 340 unit.

Cell assembly and measurement. Electrochemical measurements were performed in two electrode cells (Tomcell Japan Co., Ltd.) assembled in a water-free, oxygen-free, argon-filled glovebox (MBraun) using lithium metal anodes. 1.0 M LiTFSI in propylene carbonate was used as the electrolyte and Celgard 3501 was used as the separator. Cyclic voltammetry, galvanostatic

measurements, and impedance spectroscopy were performed using a Gamry Interface 1000, Solartron SI 1287, and Solartron 1470E.

Free-standing film preparation and mechanical testing. P3HT-*b*-PEO/V_2O_5 mixtures were cast onto polystyrene weigh-boats (VWR), followed by air-drying. Following isolation from the weigh-boat, the hybrid electrodes were cut into rectangular strips of approximately $1\,\text{mm} \times 18\,\text{mm}$ for testing. Static mechanical tensile tests were performed using a dynamic mechanical analyzer (DMA-Q800, TA Instruments). All tensile tests were conducted in controlled-force mode with a strain rate of 0.2 %/min and preload of 0.02 N.

2.3 RESULTS AND DISCUSSION

Our approach to flexible hybrid battery electrodes was to combine P3HT-*b*-PEO block copolymer with V_2O_5. The block copolymer contains electron- and ion-conducting P3HT and PEO blocks, respectively, whereas V_2O_5 has a high capacity for lithium ions. The challenge is to combine the two materials in such a manner so as to leverage the conductivity and flexibility of the polymer without compromising the electroactivity of the V_2O_5. Thus processing and blending were key considerations.

P3HT-*b*-PEO was synthesized using a modified approach based upon our prior publication.[201] Briefly, reactive, end-functionalized P3HT and PEO macroreagents were synthesized separately and coupled through a copper-catalyzed azide-alkyne click coupling reaction (see Figure 2.8). The P3HT macroreagent was prepared through an externally-initiated polymerization reaction, which provided a higher degree of end-group functionality compared with conventional methods.[204] The catalyst contained a tosylate functionality, which was then

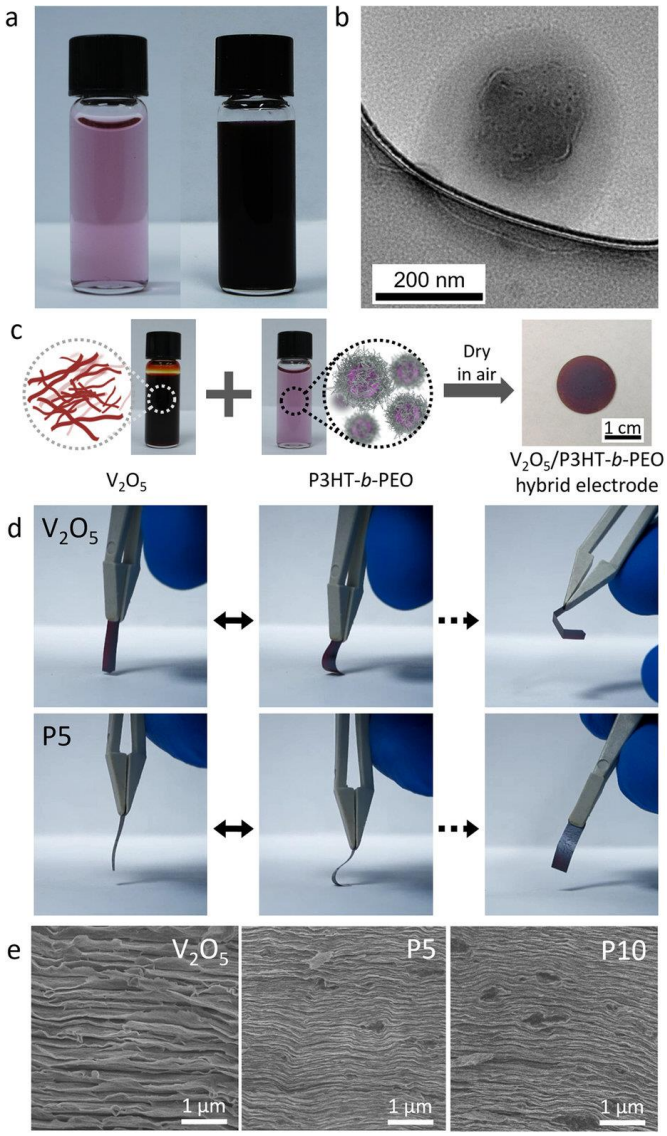

Figure 2.8 (a) P3HT-*b*-PEO dispersions at low concentration (0.05 mg/ml, left) and high concentration (1 mg/ml, right) with LiTFSI (the molar ratio of Li^+ to PEO repeat units was 0.085) in water, (b) transmission electron micrograph of a drop-cast P3HT-*b*-PEO micellar aggregate. (c) Schematic of P3HT-*b*-PEO/V_2O_5/LiTFSI cathode preparation (drawn by H.A.). (d) Digital images of a V_2O_5/LiTFSI cathode (V_2O_5) (24 µm thick) and P5 (36 µm thick) in flexure. (e) Cross-sectional SEM images of V_2O_5, P5, and P10 cathodes after failure during dynamic mechanical analysis. Micellar aggregates (black dots) were arranged between V_2O_5 layers in hybrid electrodes.

converted to an azide in a single post-polymerization reaction step. The PEO-alkyne macroreagent was prepared through Steglich esterification of commercially available monomethoxy-poly(ethylene oxide) and hexynoic acid. The P3HT prepared for this study had a M_n of 13.3 kDa, as measured by NMR end-group analysis and multi-angle laser light scattering. The PEO block had a M_n of 7.1 kDa. The polydispersity of the final block copolymer was 1.24, as measured by gel-permeation chromatography (GPC).

We next desired to combine P3HT-*b*-PEO and V_2O_5 so as to obtain an intimately mixed, flexible, and electroactive electrode. Inspired by earlier approaches,[41, 94, 198, 200, 205, 206] we first attempted *in situ* synthesis of V_2O_5 in the block copolymer as well as direct mixing of the two components in various solvents or as dry powders. However, none of these approaches yielded electrodes with appreciable electrochemical activity. This result might be explained by considering prior reports on polyaniline/V_2O_5 hybrid electrodes, where it was observed that polyaniline reduced V^{5+} to $V^{4+}$and the overall electrochemical activity was reduced.[93] In comparison, it is possible that similar interactions between P3HT and V_2O_5 might have led to the observed negligible electrochemical activity.

An alternative water-based approach met with much greater success. First, P3HT-*b*-PEO and lithium bis(trifluoromethanesulfonyl)imide (LiTFSI) were dispersed in water using sonication. The molar ratio of Li^+ to ethylene oxide repeat units was kept at 0.085,[207] which has been reported to be an optimal ratio for lithium-ion conduction.[208] Although P3HT-*b*-PEO is insoluble in water, after 1 h sonication, a uniform dispersion was formed (Figure. 2.8a). The block copolymer dispersion was stable for up to a week, after which large aggregates precipitated. The dispersion itself was purple in color and transparent. Other groups have used mixed solvents or dialysis to

disperse P3HT-*b*-PEO block copolymers in water,[209, 210, 211] but our approach centers upon only sonication. From heareafter, hybrid electrodes containing *x* wt% polymer are called "Px".

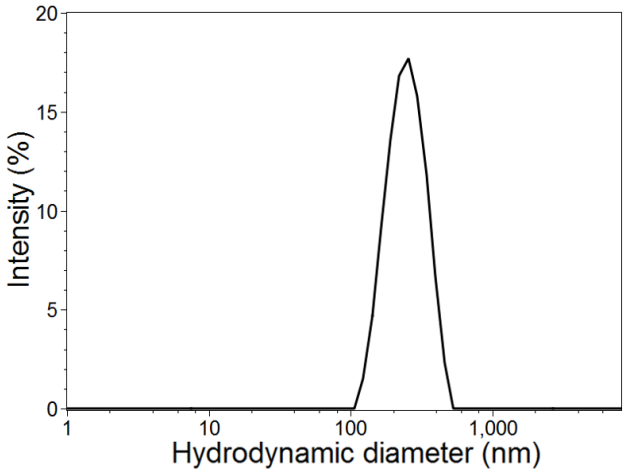

Figure 2.9 Dynamic light scattering of P3HT-*b*-PEO micelles in water.

We propose that a micellization and aggregation process, in which hydrophilic PEO forms a corona around hydrophobic P3HT, is responsible for the dispersion's stability. In support of this, TEM images of the drop-cast dispersion revealed a micellar aggregate diameter of ~320 nm, Figure 2.8b. The dark core (~200 nm diameter) is likely the hydrophobic P3HT block, and the lighter shell (~60 nm in thickness) is likely the hydrophilic PEO block. The exact structure of the micellar aggregate remains a topic of future study. Dynamic light scattering (DLS) of the dispersion yielded an average aggregate diameter 250 nm (Figure 2.9), consistent with TEM results.

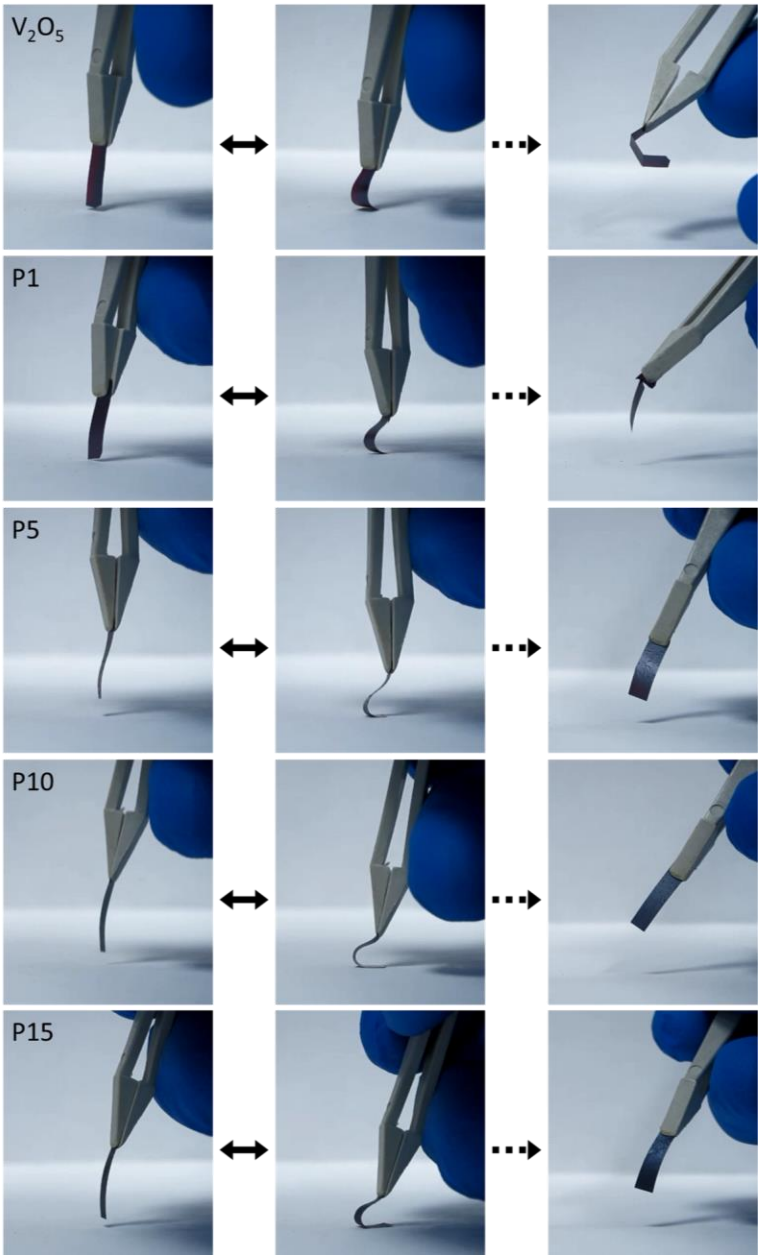

Figure 2.10 Images of free-standing hybrid electrodes demonstrating the flexibility of the films. Mechanical properties of hybrid electrodes improved with increasing P3HT-*b*-PEO content. A V_2O_5 film broke while bending several times. A P1 film broke after bending dozens of times. P5, P10, and P15 could be flexed hundreds of times. Thickness of V_2O_5, P1, P5, P10, and P15: 24, 25, 36, 36, and 31 μm, respectively.

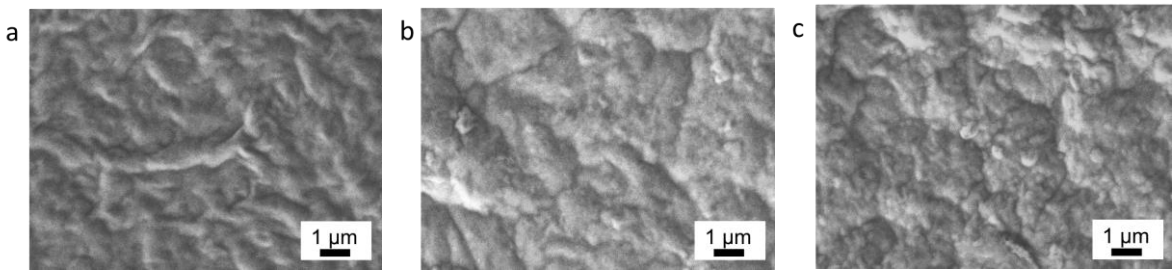

Figure 2.11 SEM images of (a) V_2O_5, (b) P5, and (c) P15 surfaces.

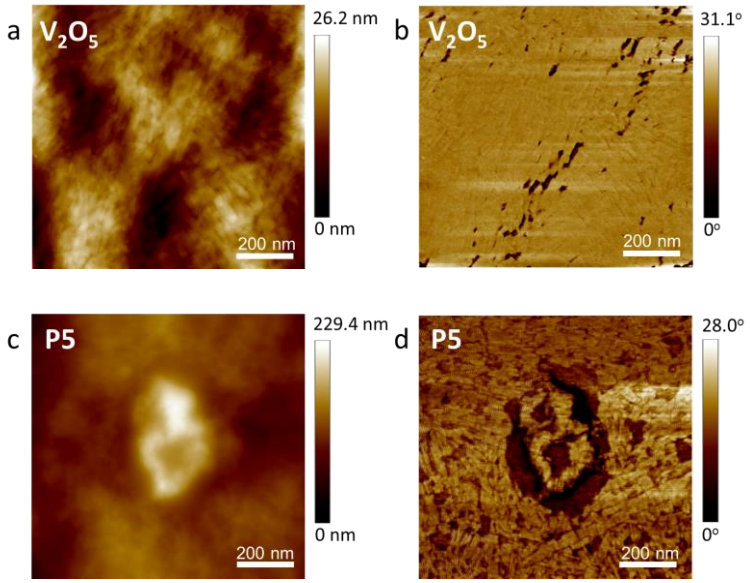

Figure 2.12 AFM images of (a-b) V_2O_5 xerogel and (c-d) of P3HT-b-PEO/V_2O_5/LiTFSI cathode with 5 wt% P3HT-*b*-PEO. Height (a,c) and phase (b,d) images are shown.

Having successfully made the P3HT-*b*-PEO dispersion, it was next mixed with aqueous V_2O_5xerogel and sonicated, Figure 2.8c. The mixture was then drop-cast, air-dried, and annealed at 90 °C. We prepared cathodes with total polymer content ranging from 1–50 wt % to assess the effect of block copolymer content on mechanical and electrochemical properties. Whereas neat V_2O_5 cathodes were brittle and failed under modest flexure, all hybrid cathodes were found to be

flexible, (Figure. 2.8d and 2.10). Cross-sectional SEM images reveal the fractured edges of neat V_2O_5, P5, and P10 cathodes. Well-packed V_2O_5 layers were visible throughout, Figure 2.8e. The dark regions observed for P5 and P10 hybrid electrodes are likely micellar aggregates sandwiched between layers or locations at which aggregates had been pulled out during the fracturing process. SEM of the surface reveals a rough but uniform morphology, indicating that there is no large-scale phase separation (Figure 2.11). AFM images of the V_2O_5 and P5 cathode surfaces showed some evidence of micellar aggregates on the P5 electrode's surface, Figure 2.12.

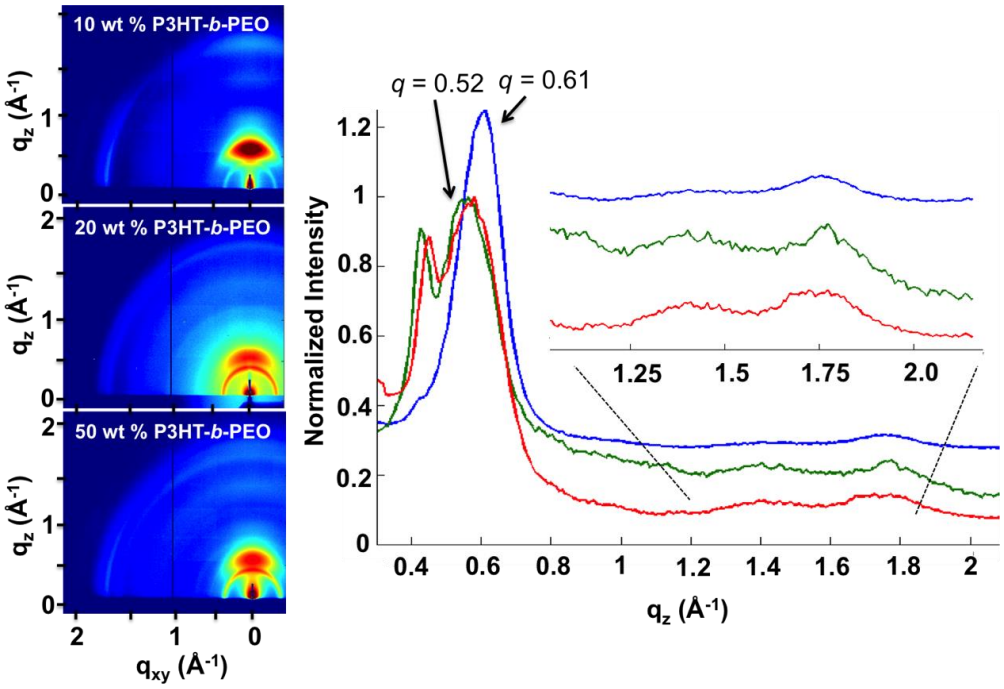

Figure 2.13 Grazing-incidence wide-angle X-ray scattering (GIWAXS) analysis of P3HT-*b*-PEO hybrid electrodes. 2-D GIXS scattering plots are shown on the left for P10, P20, and P50 hybrid cathodes. The plot on the right shows linecuts along the q_z direction, which corresponds to the direction perpendicular to the substrate.

The microstructure of the P3HT-*b*-PEO/LiTFSI/V_2O_5 cathodes was analyzed using grazing-incidence wide-angle X-ray scattering (GIWAXS). Films for GIWAXS analysis were prepared by drop-casting onto glass slides followed by air-drying and vacuum annealing at 70 °C, similar to the procedure used for cathode preparation. As shown in Figure 2.13, P3HT-*b*-PEO/LiTFSI/V_2O_5 films exhibited wide-angle scattering peaks at $q = 0.38$ Å^{-1} and 0.64 Å^{-1}, corresponding to primary scattering peaks for regioregular P3HT[212] and $V_2O_5 \cdot nH_2O$ xerogels,[191] respectively. The most intense peak at 0.64 Å^{-1}corresponds to quasi-ordered $V_2O_5 \cdot nH_2O$.[213] An additional peak at 1.70 Å^{-1} was also apparent from linecut analysis along the q_z direction, corresponding to the (003) plane of $V_2O_5 \cdot nH_2O$.[191] Peaks at 0.38, 0.8, and 1.2 Å^{-1} correspond to regioregular P3HT crystallization in the edge-on orientation. An in-plane peak at $q_y = 1.66$ Å^{-1} was evident by linecut analysis and corresponds to face-to-face π-π stacking of P3HT chains.

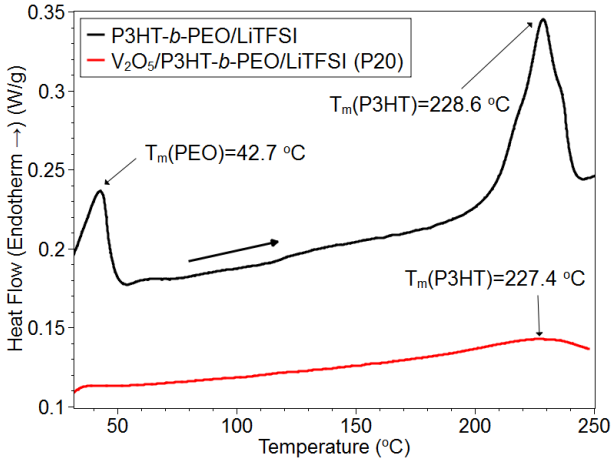

Figure 2.14 The second heating DSC scan of P3HT-*b*-PEO/LiTFSI and P20. (scan rate = 10 °C/min, 1.64 mg and 8.78 mg, respectively)

These measurements reveal crystallization of P3HT and $V_2O_5 \cdot nH_2O$ in the composite cathodes. Scattering peaks match those for pure P3HT and $V_2O_5 \cdot nH_2O$, suggesting phase segregation and crystallization of each component within discrete domains. Additionally, crystallites for P3HT and $V_2O_5 \cdot nH_2O$ are oriented in the out-of-plane direction, as commonly observed for thermally annealed thin films.[212] Differential scaning calorimetry revealed only a P3HT crystallization peak (Figure 2.14), which suggests phase segregation and crystallization of P3HT blocks but not of PEO, consistent with the GIWAXS. This indicates that PEO crystallization was restricted since polymer chains were intercalated into V_2O_5 layers.

We next sought to quantify the mechanical properties using tensile testing and collapsing radius experiments. Figure 2.15a shows stress-strain curves for V_2O_5, P5, and P10 electrodes in triplicate, and Table 2.1 summarizes the average and standard deviation values of tensile strength, ultimate strain, Young's modulus, and toughness (see also Table 2.2). Both V_2O_5 and hybrid electrodes exhibited tensile behavior very similar to that of graphene oxide paper, in which three regimes (straightening, elastic, and plastic) successively occur during elongation. P10 exhibited the highest ultimate strain and toughness, whereas the Young's modulus decreased and the tensile strength remained unchanged. It is noteworthy that only 10 wt% polymer (P10) is required to obtain a 320% increase in toughness and a 250% increase in ultimate strain relative to polymer-free V_2O_5; this enhancement in mechanical properties does not come at the cost of tensile strength, but does cause a decrease in Young's modulus. SEM images suggest that the enhanced ultimate strain and toughness enhancements come from well-dispersed P3HT-*b*-PEO micelles between V_2O_5slabs, improving the flexibility of hybrid electrodes, Figure 2.8e.

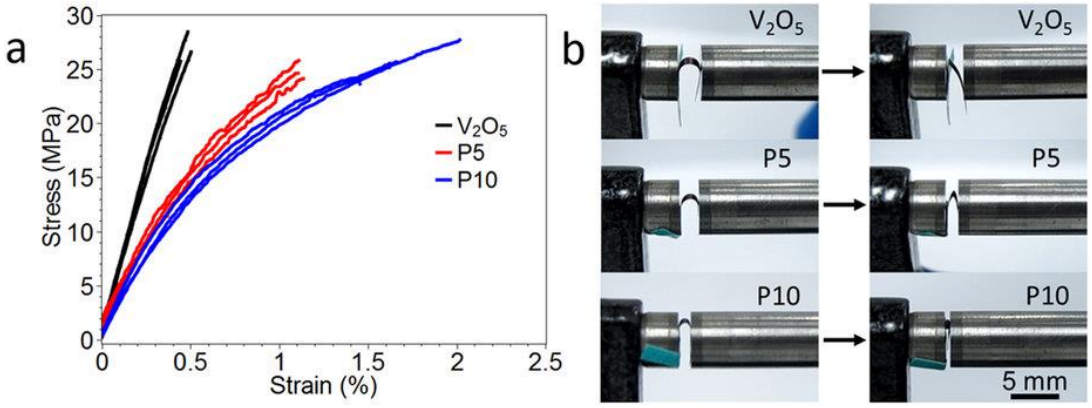

Figure 2.15 (a) Representative tensile profiles of hybrid electrodes in dependence of P3HT-*b*-PEO content and (b) digital images of collapsing radius test of hybrid electrodes. The collapsing radii of V_2O_5, P5, and P10 are 1.70, 0.40, and 0.30 mm, respectively. (Thickness of V_2O_5, P5, and P10: 26.9, 26.0, and 33.3 µm, respectively).

Table 2.1 Mechanical properties of hybrid electrodes derived from the stress-strain curves under tensile loading[a] and from the collapsing radius test[b] respectively.

Sample	Tensile strength[a] σ (MPa)	Ultimate strain[a] ε (m/m)	Normal strain[b] $\lvert\varepsilon_x\rvert$ (m/m)	Young's modulus[a] E (GPa)	Toughness[a] W (kJ/m^3)
V_2O_5	27 ± 2	0.0048 ± 0.0004	0.008 ± 0.003	6.0 ± 0.7	70 ± 8
P5	25 ± 1	0.011 ± 0.002	0.034 ± 0.13	3.7 ± 0.9	171 ± 5
P10	26 ± 2	0.017 ± 0.003	0.056 ± 0.006	3.5 ± 0.3	293 ± 73
PVDF10[c]	24.1 ± 0.3	0.0078 ± 0.0006	0.010 ± 0.001	2.9 ± 0.6	99 ± 9

[a]Values obtained are an average of three samples for each tensile test. [b]Values obtained are an average of three samples for each collapsing radius experiment. [c]PVDF10 consists of 10 wt% PVDF and 90 wt% V_2O_5.

Table 2.2. Tensile testing results.

Sample_#	Length (mm)	Width (mm)	Thickness (μm)	Tensile strength σ (MPa)	Ultimate strain ε (m/m)	Young's modulus E (Gpa)	Toughness W (kJ/m^^{3})
V_2O_5_1	8.1792	0.726	24.1	25.72	0.0044	6.4	61.5
V_2O_5_2	7.7357	0.604	23.8	26.62	0.0050	5.2	73.2
V_2O_5_3	6.0937	0.77	34.0	28.46	0.0048	6.3	73.9
P5_1	10.911	0.888	14.3	25.81	0.0111	4.6	176.7
P5_2	5.892	0.804	11.2	24.17	0.0114	3.1	169.3
P5_3	9.5914	1.054	13.9	24.66	0.0110	3.4	168.1
P10_1	8.816	0.956	25.0	24.2	0.0146	3.8	235.7
P10_2	8.8212	0.848	29.6	27.73	0.0202	3.4	366.4
P10_3	9.195	0.918	28.5	25.7	0.0166	3.2	277.9

Tensile strength σ is stress at fracture. Ultimate strain ε is strain at fracture. Young's modulus E was determined by fitting the stress-strain curves ranging from initial point of strain to 0.05%. Toughness W is the total work of extension to fracture, meaning total energy absorbed to fracture. Toughness was determined by taking the integral under the strain-stress curve.

The mechanical properties of the hybrid electrodes are comparable, and in some cases higher, than that of graphene oxide paper and carbon nanotube sheets. For example the tensile strength of the P10 electrode was about four times higher than that of single-walled carbon nanotube Buckypaper (6.3 MPa), whereas the Young's modulus was only slightly higher (3.5 vs. 2.3 GPa, respectively).[214] In comparison, P10's tensile strength and modulus was 66% and 16% that of graphene oxide paper of similar thickness (22–25 μm, average values of 39 MPa and 22 GPa, respectively). Notably, P10's toughness was within range of that of graphene oxide paper (293 vs. 251 kJ/m^3, respectively).[195] On the other hand, the ultimate strain of P10 was far greater than that of graphene oxide paper (5.6% vs. 0.31%, respectively).[195, 215] These results show that the similarities in the mechanical properties between V_2O_5 hybrid electrodes, Buckypaper, and

graphene oxide paper, which are largely attributed to the interlocking nature of the nanomaterials, similar to the morphology shown in Figure 2.8e. A comparison with poly(vinylidene difluoride) (PVDF, Table 2.1) binder shows no remarkable improvement relative to P10, which suggests that the unique block copolymer structure is responsible for the enhanced mechanical properties.

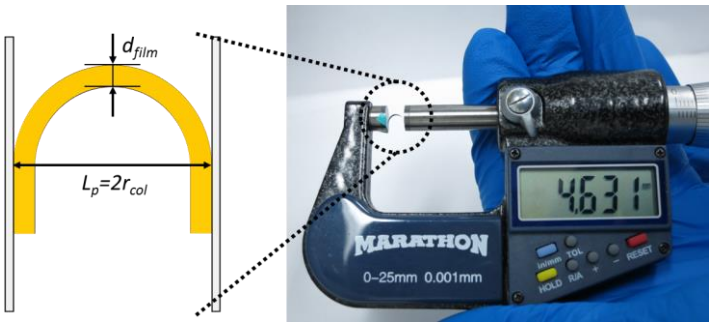

Figure 2.16 Digital image of collapsing radius test, and schematic diagram of thin film bent between plates.

Table 2.3 Mechanical properties of hybrid electrodes derived from the collapsing radius test

Sample	Collapsing radius R_{col} (mm)	Average thickness d_{film} (μm)	Normal strain $\lvert\varepsilon_x\rvert$ (m/m)
V_2O_5	1.70±0.85	26.9±9.1	0.8±0.3
P5	0.40±0.09	26.0±3.3	3.4±1.3
P10	0.30±0.04	33.3±8.3	5.6±0.6

Bending experiments were also conducted with hybrid electrodes, Figure. 2.15b, Table 2.1, and Table 2.3. A strip of a hybrid electrode with thickness d_{film} was bent so that a simple curve was formed and then compressed between two parallel plates, Figure 2.16. The radius of curvature R_{col} was taken at the first sign of kink formation. The normal strain ε_x at the surface was calculated by $|\varepsilon_x| = 0.5 d_{film}/R_{col}$.[216] The images in Figure 2.15b clearly show that the samples

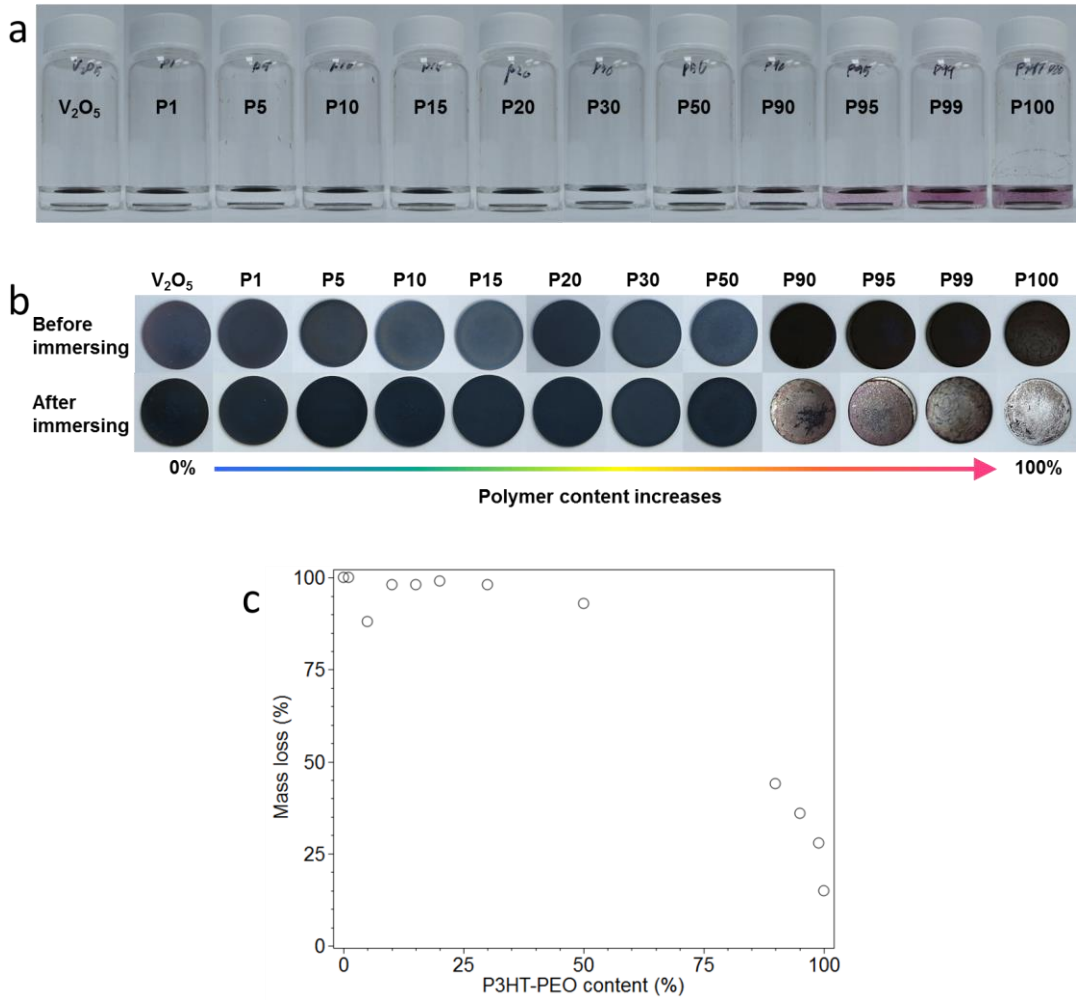

Figure 2.17 (a) Images showing solvent-resistance of hybrid electrodes with increasing P3HT-PEO concentration in propylene carbonate solvent after 1 week of soaking. (b) Hybrid electrodes immersed in propylene carbonate solution after 1 week. (From left, V_2O_5, P1, P5, P10, P15, P20, P30, P50, P90, P95, P99 and P100) (c) Plot of the mass loss of the hybrid electrodes in propylene carbonate as a function of P3HT-PEO concentration.

sustained a greater collapsing radius as polymer content increased. This enhancement is attributed to the polymer, which acts as a glue, holding the V_2O_5 sheets together. Here too, PVDF binder showed no remarkable enhancement relative to P10. This result emphasizes that the P3HT-*b*-PEO

polymer and the self-assembled structure is superior to conventional fluoropolymer binders in terms of mechanical performance.

We next turn to the electrochemical properties of hybrid electrodes. Both V_2O_5 and P3HT are capable of storing energy, but V_2O_5 is expected to dominate charge storage behavior because P3HT has a near-negligible capacity (less than 10 mAh/g).[1, 53] We found that for up to 50 wt% P3HT-*b*-PEO, the electrode showed no signs of dissolution into the electrolyte. However at higher polymer content, the electrolyte turned purple, suggestive of some amount of P3HT-*b*-PEO dissolution, Figure 2.17. Therefore, we investigated only hybrid electrodes containing up to 15 wt% polymer. At and above this concentration, the electrochemical performance was very poor, which we attribute to the low V_2O_5 content. A half-cell was assembled, and the hybrid electrode was used as the cathode, lithium foil as the anode, and 1 M LiTFSI in propylene carbonate as the electrolyte. Typical electrode thicknesses were in the range of 1.5 to 5 μm.

Cyclic voltammetry of the P3HT-*b*-PEO/V_2O_5|Li half-cell was carried out in the range of 2–3.8 V vs. Li/Li^+ at a scan rate 0.1 mV/s for various polymer loadings, Figure 2.18a. For V_2O_5, two distinct redox peaks appear at around 3.0 and 2.5 V in the cathodic/anodic scans consistent with insertions at a- and b-sites.[200, 217, 218] For compositions above 10 wt% P3HT-*b*-PEO, the current decreased significantly, suggesting diminished electrochemical activity. For V_2O_5 alone (Figure 2.18b), as the scan rate increased, the V_2O_5 voltammogram became distorted, obscuring the higher voltage peak. On the other hand for P10 (Figure 2.18c), little distortion was observed, suggestive of reduced Ohmic overpotential and increased accessibility of lithium ions into the xerogel.[83] The P3HT redox peak was observed only at very high polymer loadings; in Figure 2.19, P50 exhibited a small P3HT redox peak at 3.3 V.[1]

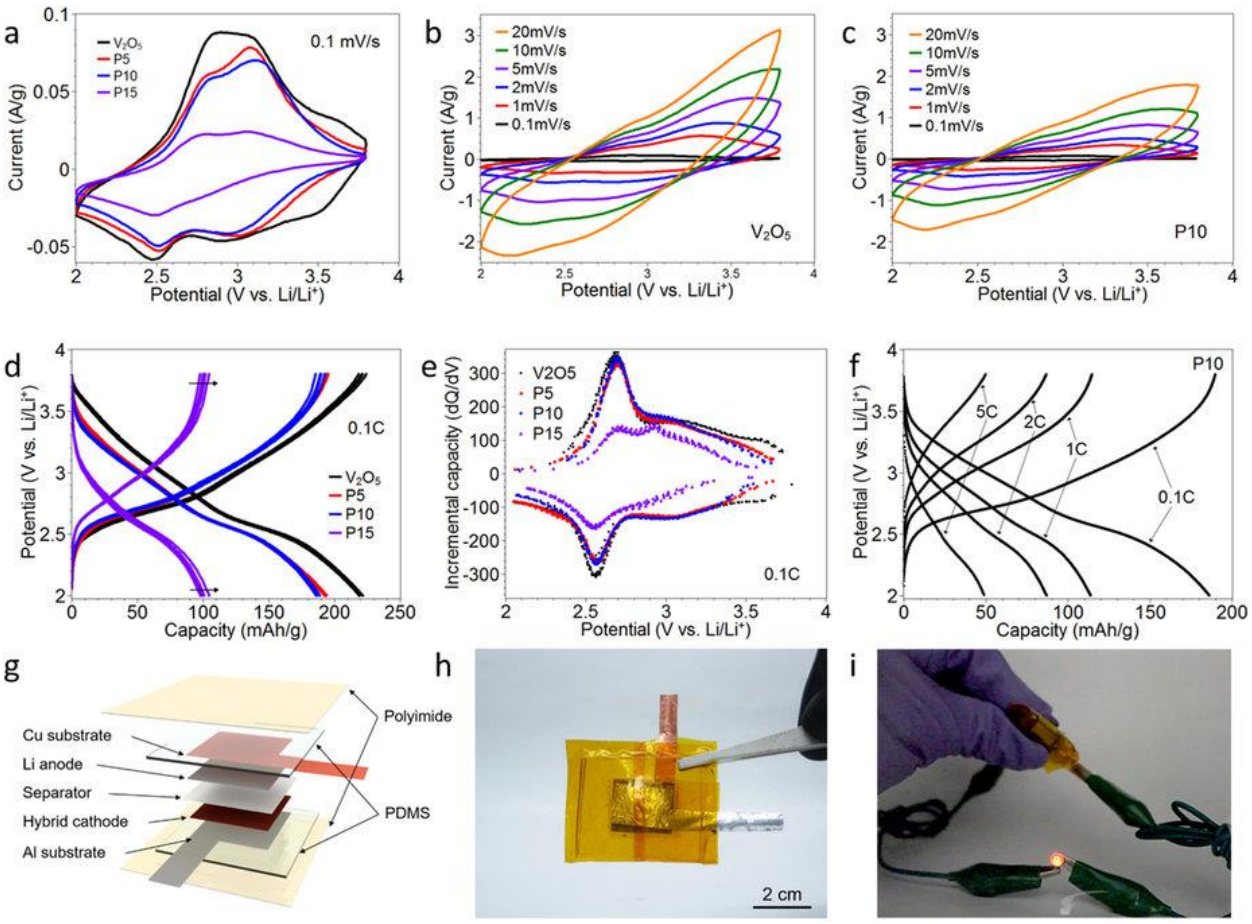

Figure 2.18 Cyclic voltammograms of (a) all compositions at 0.1 mV/sec, (b) V_2O_5 at various scan rates, and (c) P10 at various scan rates. All samples were approximately 4 μm in thickness. (d) Charge-discharge behavior of V_2O_5, P5, P10, and P15 electrodes at 0.1 C-rate and (e) incremental capacity (dQ/dV) taken from Fig. 2.18d. (f) Charge-discharge behavior at varying C-rates (0.1 to 5C) for a P10 cathode. For panels a–f, data were obtained from a two-electrode half-cell with lithium metal anode and 1 M LiTFSI in propylene carbonate. The capacity is based on mass of V_2O_5. (g) A schematic illustration of the assembled flexible half-cell using the P5 hybrid cathode and digital images of (h) the flexible battery as-assembled. (i) The flexible half-cell lights an LED while bending.

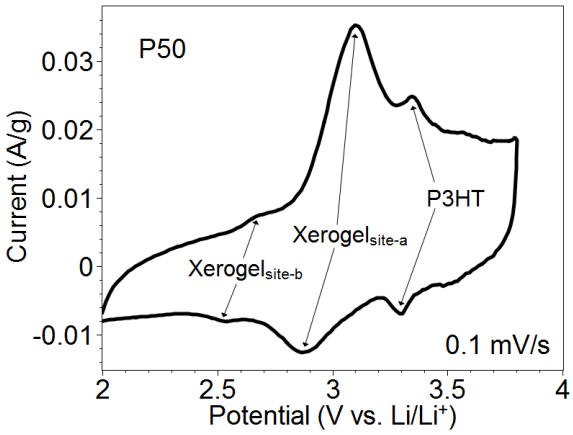

Figure 2.19 Cyclic voltammogram of P50 at 0.1mV/s. For the P50 hybrid electrode, a small P3HT redox peak was observed at 3.3V.[1] Due to its relatively small content in a cathode, P3HT redox peak was rarely observed in other hybrid electrodes containing less than 50 wt% of P3HT-*b*-PEO.

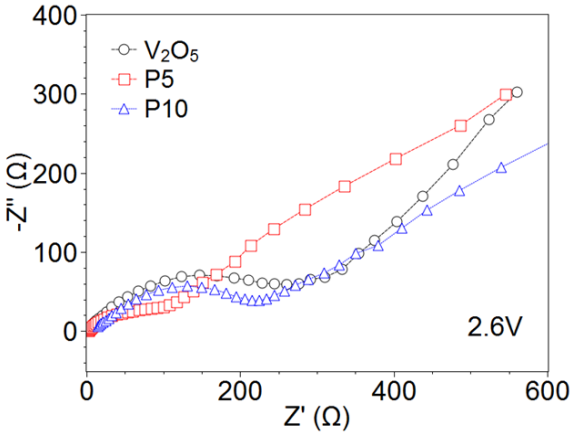

Figure 2.20 Electrochemical impedance spectroscopy (EIS) of V_2O_5, P5 and P10 at 2.6V. The amplitude was 10 mV. The frequency range was from 100,000 Hz to 0.05 Hz.

Figure 2.18d shows five galvanostatic charge-discharge cycles for P3HT-*b*-PEO/V_2O_5 hybrid electrodes of various compositions at a discharge rate of 0.1 C. From 3.8 to 2.0 V, a sloping discharge profile was obtained, typical of V_2O_5xerogels.[69, 219, 220, 221] The b-site

Li^+ intercalation reaction (at ~2.5 V) was also observed during cycling. V_2O_5 alone exhibited an average discharge capacity and Coulombic efficiency of 220.9 mAh g^{-1} and 99.4%, respectively. As the polymer content increased, the capacity decreased (P5: 193.3 mAh g^{-1} and P10: 187.2 mAh g^{-1}) and the Coulombic efficiency decreased only slightly (P5: 99.5% and P10: 98.8%). The P5 electrode exhibited only a slight decrease in capacity relative to the pure V_2O_5 electrode, whereas the P15 exhibited a much larger decrease (100.2 mAh g^{-1}). We also examined a thicker P10 electrode, where it was found that capacity dropped from 187.2 mAh g^{-1} to 40 mAh g^{-1} (5 μm vs. 50 μm, respectively), which we attribute to diffusion limitations in thicker electrodes. The derivative of the galvanostatic cycle was taken with respect to voltage to obtain the incremental capacity, Figure 2.18e. The peaks displayed were similar to those observed in cyclic voltammograms. Cycling was also conducted at various C-rates, in which a drop in capacity with increasing C-rate was observed, Figure 2.18f. From electrochemical impedance spectroscopy at 2.6 V vs. Li/Li^+, where V_2O_5 is particularly active, the diffusion coefficients (D_{Li^+}) were calculated for V_2O_5, P5, and P10 cathodes,[64, 222, 223] Figure 2.20. The diffusion coefficient increased with polymer content, suggesting that lithium ion diffusion was enhanced by the P3HT-*b*-PEO diblock copolymer (D_{Li^+} of V_2O_5, P5 and P10: 0.85×10^{-11}, 1.64×10^{-11}, and 2.09×10^{-11} cm^2/s, respectively). A full study of the charge storage mechanism as a function of polymer content is underway.

To demonstrate the union of good mechanical properties with energy storage, we constructed a prototype flexible half-cell, Figure 2.18h and 18i. The flexible battery was assembled with lithium ribbon as the anode and a P5 hybrid electrode as the cathode. Celgard film and 1 M LiTFSI in propylene carbonate were used as the separator film and electrolyte. Polydimethylsiloxane film with 1 mm thickness was used as packaging. To seal the cell more

firmly, a polyimde film was used. The battery was repeated bent and flexed, and the LED light maintained its illumination, Figure 2.18i.

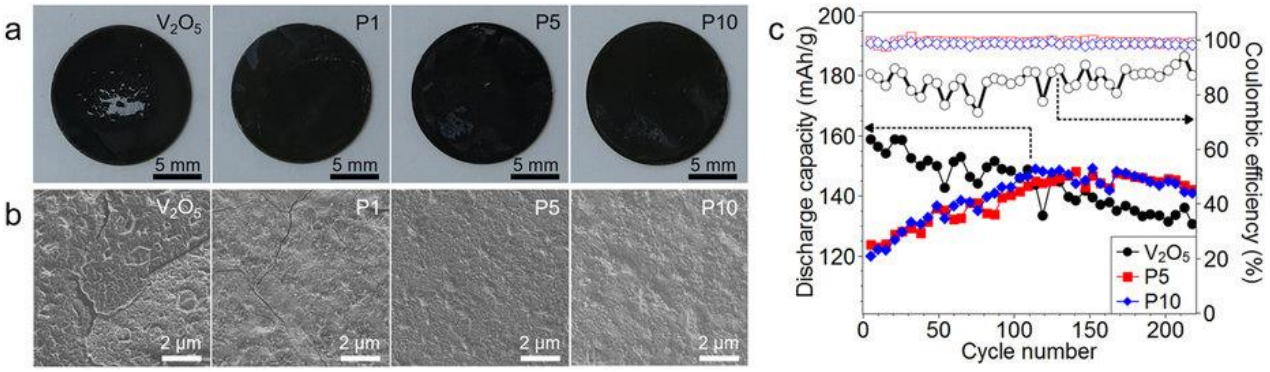

Figure 2.21 (a) Digital images of hybrid electrodes and (b) SEM images of hybrid electrodes after CV test. (c) Cycling behavior of V_2O_5, P5, and P10 electrodes at a discharge rate of 1C.

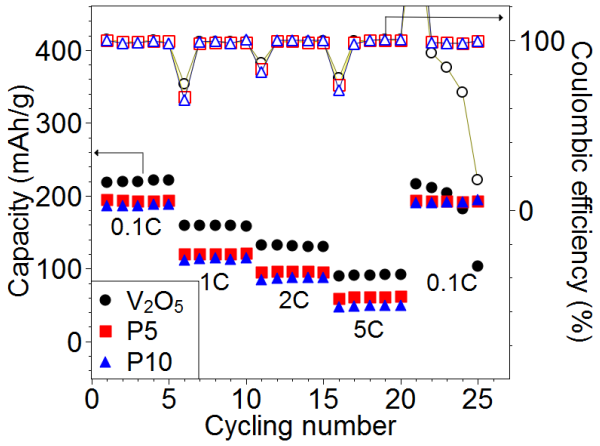

Figure 2.22 Half-cell capacities and Coulombic efficiencies under various C-rates for V_2O_5, P5, and P10.

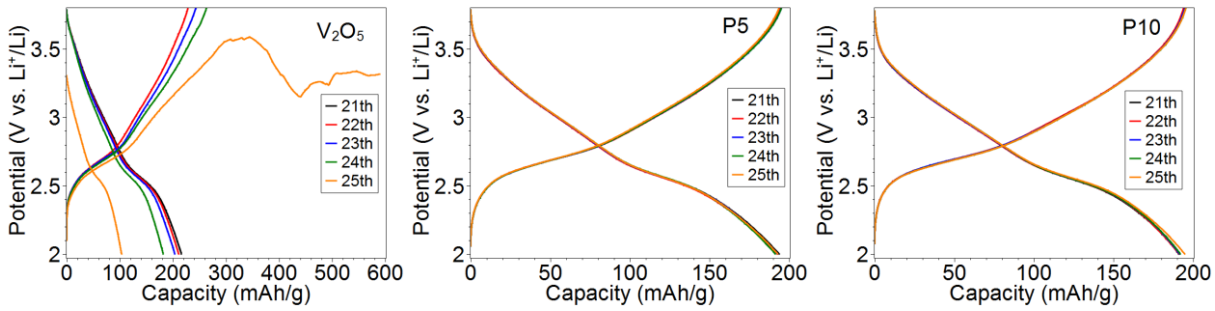

Figure 2.23 Charge-discharge profiles of V_2O_5, P5, and P10 during rate performance test. It should also be noted that V_2O_5 samples had difficulty in reaching the upper voltage cutoff of 3.8V in the 25^{th} charge step at 0.1 C-rate.

V_2O_5 is very sensitive to cycling, in which changes in volume have led to reduced cycle life and irreversible damage to the electrode. Post-mortem SEM analysis of our electrodes after cycling illustrate cracks, and digital images show large-scale flaking of the electrode, Figure 2.21a and 21b. However with just 5 wt% polymer, the formation of cracks and flakes appears to be completely arrested. Accelerated cycling (Figure 2.21c, Figure 2.22 and Figure 2.23) demonstrates a gradual capacity fade for V_2O_5, but P5 and P10 do not. Instead, the capacity of P5 and P10 gradually increases as electrolyte penetrates into the film with each cycle. After 100 cycles, the discharge capacity P5 and P10 electrodes exceeds that of V_2O_5. Furthermore, the Coulombic efficiency is enhanced for the P5 and P10 electrodes. These results demonstrate that the polymer acts as a good binder, and only a small amount is required to achieve good cyclability.

Table 2.4 Ashby plot data from Figure 2.24. Values are for the electrode alone.

Materials	Energy density (Wh/kg)	Tough-ness (kJ/m^3)	Fabrication method	
			Electrochemical performance	Mechanical performance
SWNT buckypaper[191, 192]	95.0	174.0	Filtration of CNT with Triton X-100 as a surfactant[191]	Filtration of CNT with Triton X-100 as a surfactant [192]
MWNT buckypaper[182, 193]	410.0	30.0	LbL method using MWNT-COOH/MWNT-NH_2 [182]	Electrophoretic deposition of MWNT with a surfactant [193]
Graphene[194, 195]	7.4	177.5	Filtration of rGO[194]	Filtration of rGO with poly(sodium 4-styrenesulfonate) as a surfactant[195]
Graphene[195, 224]	350.0	177.5	Filtration of rGO with CTAB as a surfactant[224]	Filtration of rGO with poly(sodium 4-styrenesulfonate) as a surfactant[195]
TiO_2 / activated carbon fabric (ACF)[196]	340.7	43.6	Hydrothermal reaction of TiO_2 onto ACF	
Graphite / CNT[196]	54.3	5.8	Casting mixture of Graphite/Super-P/PVDF (=8:1:1 wt. ratio) onto super-aligned carbon nanotube	
SnO_2 / CNT / carboxyl methyl cellulose (CMC)[225]	176.3	613.0	Casting mixture of SnO_2/CMC/MWCNT (= 3:1:1 wt. ratio) on Cu foil and then drying in the air followed by delamination	
V_2O_5 wire[197]	989.0	13.2	Filtration of V_2O_5 with Triton X-100 as a surfactant	
V_2O_5 wire/ polypropyrrole (ppy)[197]	704.0	23.2	Filtration of ppy-coated V_2O_5 with Triton X-100 as surfactant	
V_2O_5 (this study)	631.1	69.5	Casting V_2O_5 xerogel	
P5 (this study)	546.4	171.4	Casting mixture of V_2O_5/P3HT-*b*-PEO (=95:5 wt. ratio)	
P10 (this study)	529.5	293.4	Casting mixture of V_2O_5/P3HT-*b*-PEO (=90:10 wt. ratio)	

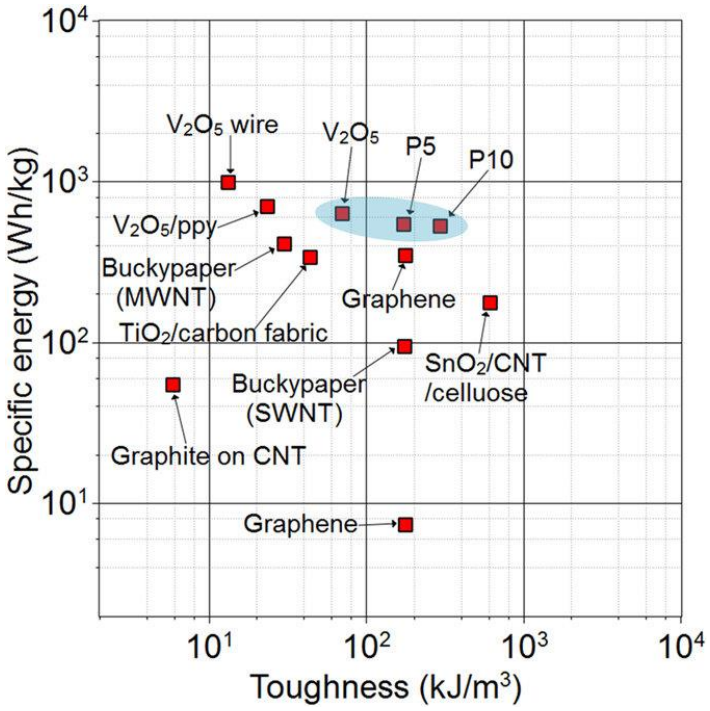

Figure 2.24 An Ashby plot of specific energy vs. toughness. Specific energy is reported as per mass of electrode. Data are taken from literature, discussed in main text, and data presented herein.

Figure 2.24 shows an Ashby plot of specific energy vs. toughness, summarizing data from the literature and data presented here. Since our focus in this study is the electrode, we present electromechanical properties for the electrode alone. Our electrodes show a good combination of both mechanical and electrochemical properties as compared to Buckypaper (SWNT[191, 192] and MWNT[182, 193]), reduced graphene oxide paper,[194, 195] graphite on super-aligned CNTs,[196] TiO_2 on activated carbon fabric, [12] V_2O_5 wires[197] and polypyrrole (ppy)-coated V_2O_5 wires,[197] Table 2.4. In the context of structural energy, it is important to note that one desires to maximize both mechanical and electrochemical properties. From the results, it is clear that it is very difficult to get both exceptional mechanical properties and electrochemical performance in one single electrode. One property often comes at the cost of another. One example of this here is with

polymer content, in which increasing the polymer content enhances mechanical properties at the cost of capacity or energy. Still, for applications where both properties are desired it is more practical to find an electrode that marries the two even if there exists a trade-off.

2.4 CONCLUSIONS

This paper outlines a simple, water-based route to self-assemble diblock copolymers bearing electron- and ion-conducting blocks with $V_2O_5$to form a flexible hybrid battery cathode. Only a small amount of the diblock copolymer is required to realize significant gains in mechanical properties without significantly sacrificing electrochemical properties. Further, this polymer halted the progression of mechanical failure, a common problem for V_2O_5 electrodes, which suffer from severe volume expansion. In the context of structural energy and power, in which one must balance mechanical with electrochemical properties, these electrodes are particularly interesting. They are far more flexible than V_2O_5 alone, and they exhibit mechanical properties comparable with that of Bucky paper and reduced graphene oxide paper.

CHAPTER III

CONDUCTING BLOCK COPOLYMER BINDERS FOR CARBON-FREE HYBRID VANADIUM PENTOXIDE CATHODES WITH ENHANCED PERFORMANCE*

3.1 INTRODUCTION

Polymeric binders, a necessary component in battery electrodes, provide mechanical integrity to the electrodes but are usually inactive, bearing no ionic or electronic conductivity nor electrochemical activity.[24, 25, 26] Poly(vinylidene fluoride) (PVDF) is the most commonly used binder, followed by poly(tetrafluoroethylene) (PTFE) and carboxy methyl cellulose (CMC).[2] Electroactive polymers are of interest because they can operate as both binder and as conductor, and because they have the potential to reduce or eliminate the need for carbon additives.[27, 28, 29, 30, 31, 226] Therefore, there is great interest in investigating "beyond-PVDF" binders that simultaneously address ion and electron transport in the pursuit of carbon-free electrodes.

Recent work has demonstrated that π-conjugated polymers have the potential to accomplish these various functions *simultaneously*. Binders consisting of poly(3-hexylthiophene)-*block*-poly(ethylene oxide) (P3HT-*b*-PEO) boosted the capacity of $LiFePO_4$ to near-theoretical values at block copolymer loadings as high as 50 wt%.[53] In work recently reported by us, we found that P3HT-*b*-PEO improved the mechanical flexibility and toughness of V_2O_5 cathodes.[85] In another example, conjugated poly(fluorene)s were tuned to provide both mechanical integrity and

*Reprinted with permission from "Conducting block copolymer binders for carbon-free hybrid vanadium pentoxide cathodes with enhanced performance" by Hyosung An, Xiaoyi Li, Cody Chalker, Maria Stracke, Rafael Verduzco, and Jodie L. Lutkenhaus, *ACS Appl. Mater. Interfaces* **2016**, 8 (42), 28585. Copyright 2016 American Chemical Society.

example, conjugated poly(fluorene)s were tuned to provide both mechanical integrity and electronic conductivity in silicon anodes.[227] These prior studies point to examples of π-conjugated polymers and block copolymers that allow one to synergistically combine aspects of conductivity, electrochemical activity, and mechanical properties into a single multifunctional polymeric binder. However, π-conjugated polymeric binders are still poorly understood, and there is a fundamental lack of knowledge regarding their mechanical, electronic, and electrochemical properties in the context of electrochemical energy storage.

V_2O_5 is a promising candidate as a cathode material in next-generation lithium-ion batteries because of its high specific energy, earth-abundance, and cost-effectiveness.[67, 68, 69, 228] However, the implementation of V_2O_5 in practical lithium-ion batteries has been impeded by low Li^+-diffusion coefficient (10^{-12} - 10^{-13} cm^2/s),[84] low electronic conductivity (10^{-2} - 10^{-3} S/cm),[67] volumetric expansion[229] and pulverization during cycling,[86] and irreversible phase transitions upon deeper discharge.[23] The addition of a multi-functional polymeric binder can potentially address these limitations.

Additives have been explored as an approach to boost V_2O_5 performance and capacities. As a recent example, a V_2O_5 xerogel electrode with only 2 wt% graphene demonstrated outstanding cyclability.[230] In another example, a block copolymer was added to produce flexible V_2O_5 xerogel electrodes at 5-10 wt%.[26] Other additives include PEO, polypyrrole, and conducting polymers.[32, 41, 231, 232, 233, 234] These examples demonstrate that properly designed additives can enhance both electrochemical and mechanical properties, even at very low additive contents.

Here, we present a systematic investigation of how P3HT-*b*-PEO interacts with V_2O_5 in the context of carbon-free hybrid electrodes for electrochemical energy storage as compared to P3HT, PEO, and a P3HT/PEO homopolymer blend. Most prior studies focus upon a single polymer (either

electron conducting or ion conducting), yet there remains an open question as to whether a simple blend can yield the same performance as a block copolymer analogue. Further, it is not clear how conductive block copolymer binders interact with electroactive materials and what type of morphology results from these interactions. Our approach uses X-ray photoelectron spectroscopy (XPS), Fourier transform infrared (FT-IR) spectroscopy, cyclic voltammetry, galvanostatic cycling, and electrochemical impedance spectroscopy (EIS). From these experiments, we probe morphology, capacity retention, the origins of electrochemical degradation, and chemical interactions in the carbon-free hybrid electrode to probe the performance of block copolymer vs homopolymer binders in carbon-free V_2O_5 electrodes.

3.2 EXPERIMENTAL METHOD

Materials. Vanadium pentoxide (V_2O_5), lithium bis(trifluoromethanesulfonyl)imide (LiTFSI), poly(ethylene oxide) (PEO, molecular weight = 8,000 g/mol), poly(vinylidene fluoride) (PVDF, molecular weight = 534,000 g/mol), N-methyl-2-pyrrolidone (NMP), and propylene carbonate (PC) were purchased from Sigma Aldrich. Lithium ribbon was purchased from Alfa Aesar. All chemicals were used as received. 316 stainless steel coin cells were purchased from MTI Corporation. Water was purified to 18.2 MΩ-cm (Milli-Q, Millipore). PEO-OH was purchased from Aldrich (lot# BCBB1016, 7.17 kg mol^{-1} by ^1H NMR).

Synthesis of V_2O_5 xerogel. Vanadium pentoxide (V_2O_5) xerogel was prepared using hydrogen peroxide (H_2O_2) according to previously reported procedures.[200] Briefly, V_2O_5 (3.0 g) was dissolved into 300 mL of 10% aqueous H_2O_2 solution. This solution was aged for three days, after which the water was removed and the solid xerogel was dried in the oven under air overnight

at 100°C. After synthesis, the V_2O_5 xerogel was suspended again in water at a concentration of 16.7 mg/mL. V_2O_5 xerogel was confirmed using XPS and X-ray diffraction (XRD).

Synthesis of P3HT-*b*-PEO block copolymer. P3HT-*b*-PEO was synthesized according to our previous report.[85] The molecular weight and PDI of P3HT-*b*-PEO were 9.35 kDa and 1.24, respectively. The weight ratio of P3HT to PEO was 0.76:0.24, confirmed by ^{1}H-NMR.

Synthesis of P3HT homopolymer. 2,5-dibromo-3-hexylthiophene (3.63 g, 11.1 mmol) was dissolved in anhydrous THF (4.8 mL) in a 100 mL round-bottom flask, and the solution was stirred at 0 ^{o}C for 20 minutes. A solution of isopropyl magnesium chloride with LiCl (1.3 M) in THF (8.31 mL, 10.8 mmol) was added, and the mixture was stirred for 2 hours at 0 ^{o}C. In a nitrogen-filled glovebox, [1,3-Bis(diphenylphosphino)propane]dichloronickel(II), Ni(dppp)Cl_2 (62.82 mg, 0.11 mmol), was dissolved in 1 mL of THF, and this solution was transferred out via syringe. 15 mL of THF was then added to the reaction mixture, following by Ni(dppp)Cl_2 solution. The flask was removed from ice and stirred for additional 40 minutes before quenching with 5M HCl (5 mL). The polymer was recovered by precipitation in methanol and dried under vacuum. The molecular weight and PDI of P3HT are 7.4 kDa and 1.386, respectively.

Preparation of polymer suspensions. P3HT-*b*-PEO suspensions were made by sonicating the polymer and LiTFSI in Milli-Q water at 0^{o}C to make a 4 mg of polymer + salt/mL stock solution.[85] The molar ratio of ethylene oxide units to Li^+ was 0.085. Before preparing hybrid cathodes, aliquots of 4 mg/mL P3HT-*b*-PEO dispersion were diluted to 1 mg/ml. For the PEO solution, PEO was dissolved in water with LiTFSI to make 1 mg of polymer + salt/ml. For water-dispersible P3HT, P3HT (1 mg) was dissolved in chloroform (1 ml) using sonication. Water (6 ml) was added into the P3HT mixture, followed by sonication with the lid open until the solution color changed from bright yellow to purple.

Cathode preparation. Hybrid electrodes were prepared according to our previous work.[85] Briefly, 316 stainless steel coins (15.8 mm diameter x 0.5 mm thickness) were cleaned *via* sonication for 15 minutes each in water, isopropanol, and acetone followed by purging with nitrogen gas and drying at 75°C. Aqueous mixtures were made by mixing together appropriate volumes of 1 mg/mL P3HT-*b*-PEO and 16.7 mg/mL V_2O_5 xerogel dispersions in Milli-Q water. These solutions were drop-cast onto cleaned stainless steel coins by depositing 0.97 – 1.12 mg of material (polymer + V_2O_5) onto the surface and drying in air. Hereafter, hybrid electrodes (called P3HT-*b*-PEO/V_2O_5) containing *x* wt% P3HT-*b*-PEO copolymer will be called "*Px*". After drying in air, the cathodes were held under vacuum at 90°C for 16 hours.

To investigate individual contributions of polymer blocks, we prepared four other types of hybrid electrodes: (1) V_2O_5 with 2.4 wt% PEO (called PEO/V_2O_5); (2) V_2O_5 with 7.6 wt% P3HT (called P3HT/V_2O_5); (3) V_2O_5 with both 2.4 wt% PEO and 7.6 wt% P3HT (called PEO+P3HT/V_2O_5) to mimic the polymer composition present in a P10 electrode; and (4) 10 wt% PVDF (called PVDF/V_2O_5). For the PEO homopolymer/V_2O_5 hybrid electrode, 1 mg/ml PEO solution and 16.7 mg/ml V_2O_5 xerogel dispersion were mixed to make a 2.4 wt% PEO-containing electrode. For the P3HT homopolymer/V_2O_5 hybrid electrode, 1 mg/ml P3HT dispersion and 16.7 mg/ml V_2O_5 xerogel dispersion were mixed to make 7.6 wt% P3HT-containing electrode. For the PEO and P3HT blend/V_2O_5 hybrid electrode, 1 mg/ml PEO solution, 1 mg/ml P3HT dispersion, and 16.7 mg/ml V_2O_5 xerogel dispersion were mixed to yield 2.4 wt% of PEO and 7.6 wt% of P3HT. All mixtures were cast and then air-dried and annealed at 90°C under vacuum for 16 hours. For the PVDF/V_2O_5 electrode, V_2O_5 xerogel in water and PVDF in NMP were mixed. The mixture was cast and dried at 70°C for three hours, and then dried at 90°C overnight under vacuum. Pure

V_2O_5 electrodes were prepared by drop-casting of V_2O_5 dispersion on stainless steel substrate. It should be noted that pure V_2O_5 has no other carbon additives and polymer binders.

Electrode characterization. Cathode morphologies were investigated using scanning electron microscopy (SEM, JEOL JSM-7500F). Attenuated total reflection Fourier transformation infrared (ATR FT-IR) spectroscopy (Nicolet 6700 FT-IR ATR, Thermo Scientific) was utilized with a germanium crystal. The IR spectra were obtained at a wave number range of 650-4000 cm^{-1} at a resolution of 1 cm^{-1}. XPS (Omicron) was performed using Mg Kα X-ray (source energy of 1253.6 eV) and a charge neutralizer (Omicron CN10). Ar ion sputtering (5 keV) for 10 min was conducted before measuring XPS to remove the top surface. All spectra were collected at a pass energy of 20 eV and at an energy step size of −0.05 eV. A linear-type background subtraction was applied to the photoemission lines. For curve fitting, a combined Gaussian-Lorentzian line shape (CasaXPS) was used with the same full-width-half-maximum of all components. XRD was carried out using a Rigaku Ultima II vertical θ-θ powder diffractometer using Cu Kα radiation (λ = 1.5418 Å) with Bragg-Brentano para-focusing optics. The operating power was 40 kV and 40 mA. The 2-theta angle varied from 3° to 70°.

Cell assembly and measurement. Electrochemical measurements were performed in two-electrode cells (Tomcell Japan Co., Ltd.) assembled in a water-free, oxygen-free, argon-filled glovebox (MBraun) using lithium metal anodes. 1.0 M LiTFSI in propylene carbonate was used as the electrolyte and Celgard 3501 was used as the separator. Cyclic voltammetry, galvanostatic measurements, and electrochemical impedance spectroscopy (EIS) were performed using a Gamry Interface 1000, Solartron 1287/1260, and Solartron 1470E. For EIS, the frequency range was from 100 kHz to 50 mHz with 10 mV AC amplitude.

3.3 RESULTS AND DISCUSSION

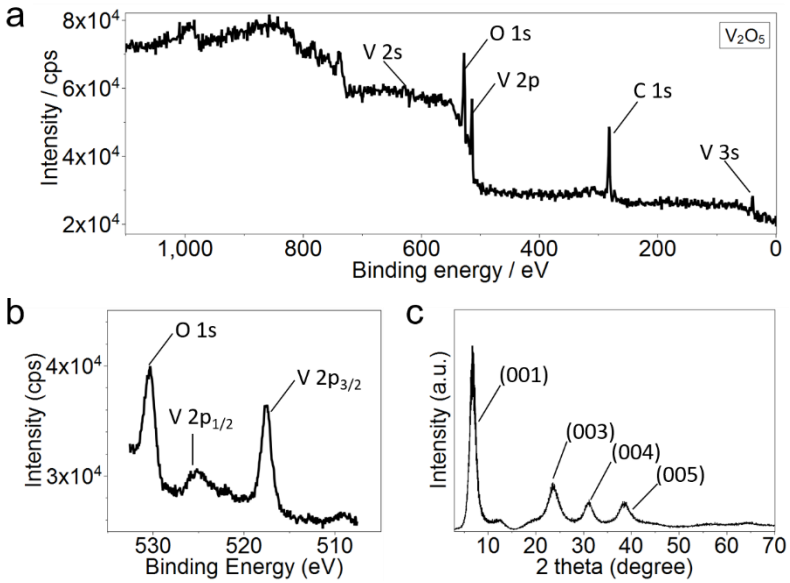

Figure 3.1 XPS spectra of (a) as-prepared V_2O_5 xerogel and (b) O 1s and V 2p core peaks. (c) XRD patterns of as-prepared V_2O_5 xerogel.

We have characterized the as-prepared V_2O_5 xerogel using X-Ray Photoelectron Spectroscopy (XPS) and X-ray diffraction (XRD). XPS spectra of as-prepared V_2O_5 xerogel (Figure 3.1a and 2.1b) shows the peaks attributed to the core levels of V 2p, V 2s, V 3s, O 1s, and C 1s. The binding energy of V 2p3/2 is 516.9 eV corresponding to V^{5+} valance state.[235] The XRD shows clearly a hydrated layered structure with (*00l*) reflection peaks for V_2O_5 synthesized by H_2O_2 method, Figure 3.1c. The major peak is located at 6.88° and the d-spacing is calculated to be about 12.8 Å. This XRD plot is consistent with JCPDS No. 40-1296 hydrated layer-structured V_2O_5. These XPS and XRD data of V_2O_5 xerogel are in good agreement with the reported studies.[235, 236, 237]

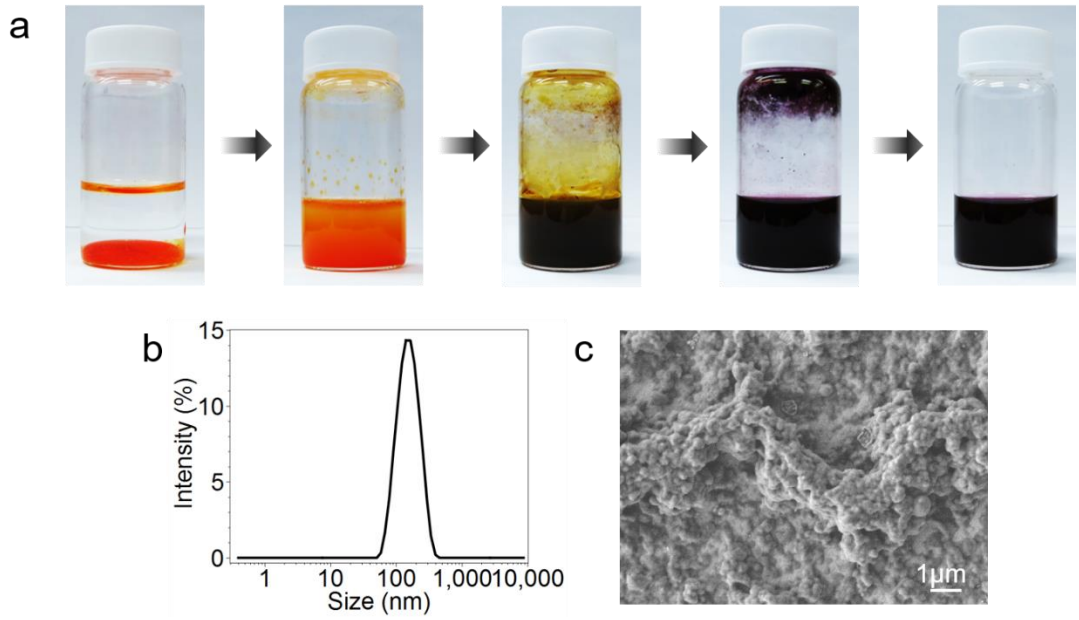

Figure 3.2 (a) Preparation of water-dispersible P3HT. (b) Dynamic light scattering (DLS) of 0.05 mg/ml of dispersed P3HT shows that the average diameter is 151 nm. (c) SEM image of P3HT drop-cast from dispersion.

The 1 ml P3HT solution in chloroform (1 mg/ml) with 6 ml Milli-Q water was sonicated at room temperature with the lid open in order to evaporate the chloroform. At the beginning of sonication, the chloroform layer (orange layer seen in Figure 3.2a) and the water layer were partially mixed. As the chloroform evaporated, the solution changed from a bright orange color to a purple color. In order to remove the residual chloroform, the solution was sonicated for another 10 minutes after the color change. After sonication, the P3HT dispersion was transferred to new vial (last digital images of Figure 3.2a). The solution was stable for 2 days.

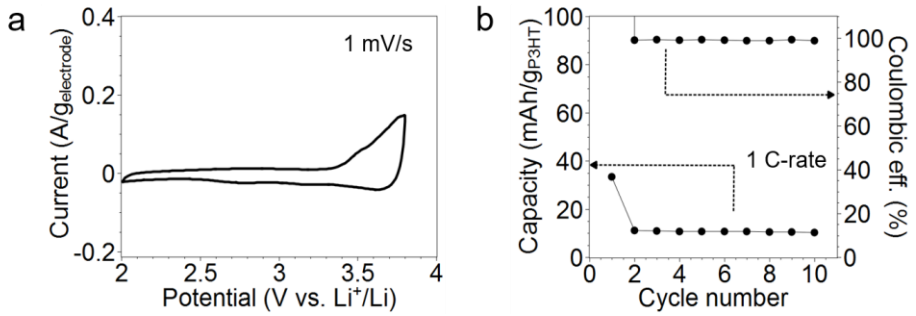

Figure 3.3 (a) Cyclic voltammetry and (b) discharge capacity and coulombic efficiency of pure P3HT-*b*-PEO.

We analysed a series of polymeric binders in V_2O_5 to understand individual contributions of polymer blocks and the role of copolymer architecture. In all cases, the polymeric binder and V_2O_5 were blended in water and subsequently dried to produce the hybrid cathode. In addition to pure V_2O_5 cathodes, we analysed cathodes with 5 and 10 wt % block copolymer binders (P5 and P10, respectively) and V_2O_5 cathodes with PEO, P3HT, and a blend of PEO and P3HT. The same weight fraction of PEO and/or P3HT homopolymer with similar molar mass as for the block copolymer was added to mimic the P10 case. No other conducting additives (such as carbon black) were present. The theoretical capacities of V_2O_5 and P3HT are 147 mAh/g and 161 mAh/g, respectively, assuming one Li-ion exchanged and one doping event. Considering that the weight ratio of P3HT-*b*-PEO is 0.76:0.24 P3HT:PEO, the theoretical capacities of P5 and P10 electrodes are 146 and 145 mAh/g, respectively. Experimentally, P3HT homopolymer exhibited a practical capacity 11 mAh/g, Figure 3.3. Therefore, we expect that the block copolymer mainly contributes through enhanced conductivity and mechanical robustness.

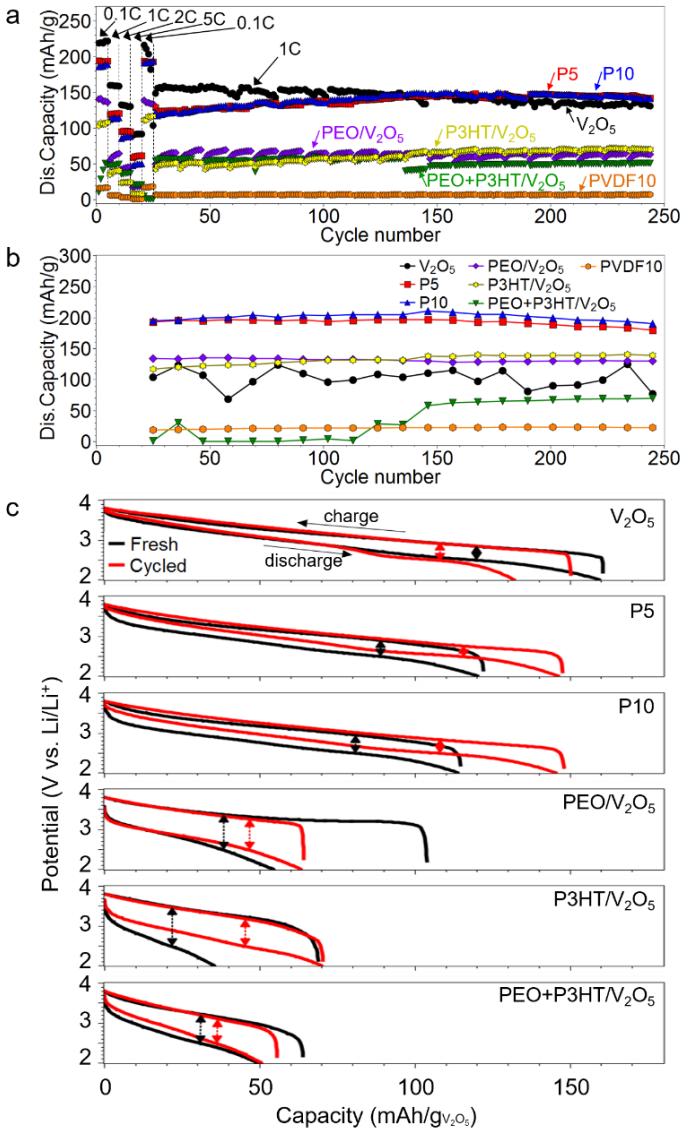

Figure 3.4 (a) Cycling properties of V_2O_5, PEO/V_2O_5, P3HT/V_2O_5, PEO+P3HT/V_2O_5, P3HT-*b*-PEO/V_2O_5 (P5 and P10), and PVDF/V_2O_5 electrodes at various C-rates. Charge-discharge cycling was conducted for five cycles each at 0.1, 1, 2, 5, and 0.1 C-rates, followed by accelerated cycling, which consisted of 10 charge-discharge cycles at 1 C-rate and 1 charge-discharge cycle at 0.1 C-rate (11 total). 20 sets were performed (total 220 cycles). The accelerated cycling data at 1 C-rate was plotted in panel (a) and that at 0.1 C was plotted in panel (b). (c) Charge-discharge behavior of electrodes at 1 C-rate before (black) and after (red) cycling. The double-headed arrows indicated hysteresis at 2.5 V discharge voltage. All capacities are based on V_2O_5 mass and a cut-off voltage range of 2.0-3.8 V or 30 h. (In Figure 3.4b, V_2O_5 often reached the 30 h cut-off and could not discharge completely).

Galvanostatic charge-discharge curves for these cathodes in a lithium half-cell configuration are shown in Figure 3.4. Each sample was analysed for 10 cycles at 0.1 C, followed by 10 cycles at 1 C, 2 C, 5 C, 0.1 C, and finally 20 sets of cycling at 1 C for 10 cycles and 0.1 C for one cycle. For V_2O_5, the discharge capacity at 1 C-rate decreased from 160 to 131 mAh/g over 200 cycles (-0.08% per cycle). For both P5 and P10, the discharge capacities increased from 120 to 142 mAh/g (+0.08% per cycle) and from 112 to 141 mAh/g (+0.11% per cycle), respectively. The initial capacities of P5 and P10 electrodes were lower than that of pure V_2O_5, yet they increased with cycling and were comparable to pure V_2O_5 after long term cycling due to electrolyte penetration as is common with electroactive polymers.[238] The discharge capacities of all other cathodes (PEO/V_2O_5, P3HT/V_2O_5, and PEO+P3HT/V_2O_5) were significantly lower than that of pure V_2O_5 and the hybrid block copolymer electrodes. We also examined a conventional non-conductive polymer binder, poly(vinylidene difluoride) (PVDF), but this yielded a low discharge capacity (~6 mAh/g) probably because of poor conductivity, and was not investigated further.

Figure 3.4b shows discharge capacities at 0.1 C, which were excerpted from the accelerated cycling process shown in Figure 3.4a; P5 and P10 have dramatically higher capacities (180 and 190 mAh/g, respectively) than V_2O_5 (77 mAh/g) because V_2O_5 failed to discharge completely over the 30 hr allotted time, probably due to steady degradation of V_2O_5 during cycling. These studies show that the cathode performance is dramatically improved in the case of the block copolymer binder and are potentially suitable binders for carbon-free electrodes.

The reversibility of the redox reaction was next explored by examining the voltage hysteresis,[239] illustrated in Figure 3.4c by the double-headed arrow at a discharge voltage of 2.5 V before (black) and after (red) cycling. For V_2O_5, the voltage hysteresis increased after cycling from 0.35 V to 0.42 V. However, the voltage hysteresis for P5 (0.4 → 0.27 V) and P10 (0.47 → 0.35

V) decreased after cycling. On the other hand, the hysteresis for PEO/V_2O_5, P3HT/V_2O_5, and PEO+P3HT/V_2O_5 was large both before and after cycling. Only P3HT-*b*-PEO-containing hybrid electrodes exhibited hysteresis smaller than that of than pristine V_2O_5. The reduced hysteresis in P3HT-*b*-PEO-containing hybrid electrodes is beneficial to electrode performance and efficiency, demonstrating enhanced reversibility.[240, 241]

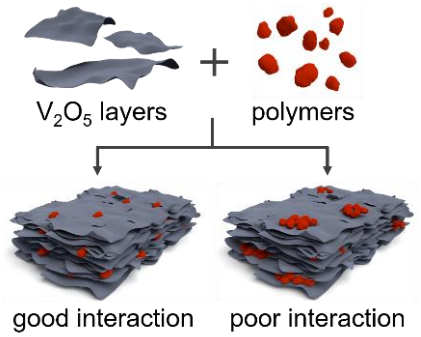

Figure 3.5 Schematic diagram of hybrid electrode preparation and two expected electrode structures.

We hypothesized that the different cathode performances shown in Figure 3.4 were a result of the nature of the interactions between the polymer binder and V_2O_5, leading to different electrode morphologies. This is shown schematically in Figure 3.5. Favorable interactions between additive and V_2O_5 result in more homogeneous electrodes and improved performance attributes.[242, 243, 244, 245] In contrast, poor interactions can cause large-scale phase separation, reducing the performance attributes.

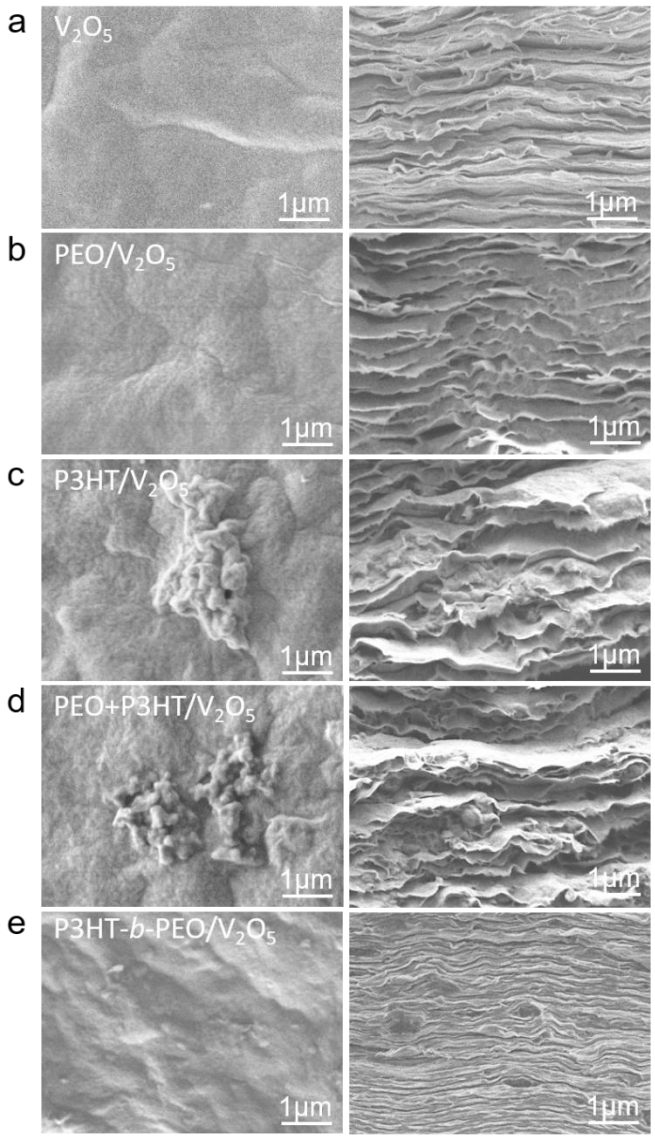

Figure 3.6 Surface (left) and cross-sectional (right) SEM images of (a) V_2O_5, (b) PEO/V_2O_5, (c) P3HT/V_2O_5, (d) PEO+P3HT/V_2O_5, and (e) P3HT-*b*-PEO/V_2O_5 (P10) electrodes. For the P3HT/V_2O_5 and PEO+P3HT/V_2O_5 electrodes, macroscopic phase segregation of P3HT particles was observed. Micellar aggregates (black dots) were arranged between V_2O_5 layers and on the surface in the P3HT-*b*-PEO/V_2O_5 (P10) electrode.

SEM images shown in Figure 3.6 support this idea; only the P3HT-*b*-PEO/V_2O_5 cathode shows both a uniform surface and tightly packed V_2O_5 sheets, indicating that there is no large-scale phase separation, Figure 3.6e. During processing, the block copolymer likely forms a micellar aggregate with a hydrophilic PEO shell and hydrophobic P3HT core. The PEO interacts favorably with the V_2O_5 sheets and the P3HT acts as a physical crosslink or anchor. In comparison, both V_2O_5 and PEO/V_2O_5 cathodes show smooth surfaces with loosely packed and buckled V_2O_5 sheets, Figure 3.6a and 3.6b. Both P3HT/V_2O_5 and PEO+P3HT/V_2O_5 cathodes show surface-deposits (Figure 3.6c and 3.6d), which we attribute to poor interactions and phase separation.

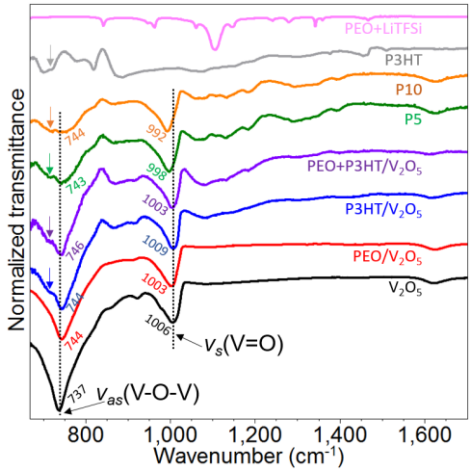

Figure 3.7 FT-IR spectra of as-prepared V_2O_5, PEO/V_2O_5, P3HT/V_2O_5, PEO+P3HT/V_2O_5, P3HT-*b*-PEO/V_2O_5 (P5, P10), pure P3HT, and PEO+LiTFSI.

FTIR spectroscopy provides additional evidence for favorable PEO-V_2O_5 interactions, as shown in Figure 3.7 and Table 3.1. Pure V_2O_5 exhibited bands at 737 and 1006 cm^{-1}, which we attribute to the asymmetric stretching mode for V-O-V and the terminal oxygen symmetric stretching mode for V=O, respectively.[41, 231, 246, 247] With the addition of polymeric binders that

contain PEO, the ν_{as}(V-O-V) band shifted to lower wavenumber and the ν_{s}(V=O) band to higher wavenumber. The peak shifts result from an increase in the V=O bond length and a decrease in the V-O-V bond length and reflect interactions between ether oxygens and terminal oxygen atoms on V_2O_5.[246] The largest shift in these bands is observed for block copolymer additives, and no shift is observed in the case of P3HT additive. This is consistent with a more homogeneous and stronger interaction between V_2O_5 and the block copolymer additive compared with the other binders studied.

Table 3.1 Characteristic absorption bands and assignment of FTIR spectra of PEO homopolymer with LiTFSI and P3HT homopolymer.[248, 249, 250]

Material	Wavenumber (cm^{-1})	Functional group	Material	Wavenumber (cm^{-1})	Functional group
PEO+ LiTFSI	1467 1360, 1342 1280, 1242	-CH2- bending (scissoring) -CH2- bending (wagging) -CH2- bending (twisting)	P3HT	1510	C=C thiophene ring asymmetric stretching
				1455	C=C thiophene ring symmetric stretching
	1148, 1107, 1061	C-O-C asymmetric stretching		1377	Aliphatic -CH_3 bending
	963	-CH2- asymmetric stretching and -CH2- bending (rocking)		820	Aromatic C-H bending out of plain
	842	C–O-C symmetric stretching		716	Aliphatic -CH2- bending (rocking)

We investigated the impact each binder had on electrical conductivity and ion diffusivity through electrochemical impedance spectroscopy (EIS) measurements. Figure 3.8 displays electrochemical impedance spectra for each of the cathodes at 3.6 V vs. Li/Li^+. Typical impedance plots consist of a semi-circle at the high frequency region and a long diffusion tail at the low frequency region. An equivalent circuit was fit to the spectra.[251] V_2O_5, PEO+P3HT/V_2O_5, and P10 all exhibited similarly sized semi-circles (~200 Ω), suggestive of similar overall cathode resistances and conductances. The other electrodes were more resistive or less conductive, with

the semi-circle for P3HT/V_2O_5 being slightly larger (~300 Ω) than that of V_2O_5 likely due to its non-uniform morphology.[244] PEO/V_2O_5 had the biggest semi-circle (~1000 Ω) because of PEO's insulating nature. Also, ion diffusion (mainly Li^+) can be discussed qualitatively by comparing the phase angle of the diffusive tail in the low-frequency region.[251, 252] An increase of the angle can be indicative of enhanced diffusion and ion transport. The angle of V_2O_5 (37°) was lower than that of PEO+P3HT/V_2O_5 (51°) and P10 (66°). The angle for PEO/V_2O_5 was similar to that of V_2O_5. P3HT+V_2O_5 showed the lowest angle at 28°. Therefore, ion transport in the electrodes can be ordered from highest to lowest as: P3HT-*b*-PEO/V_2O_5 (P10) > PEO+P3HT/V_2O_5 > V_2O_5 > PEO/V_2O_5 > P3HT/V_2O_5.

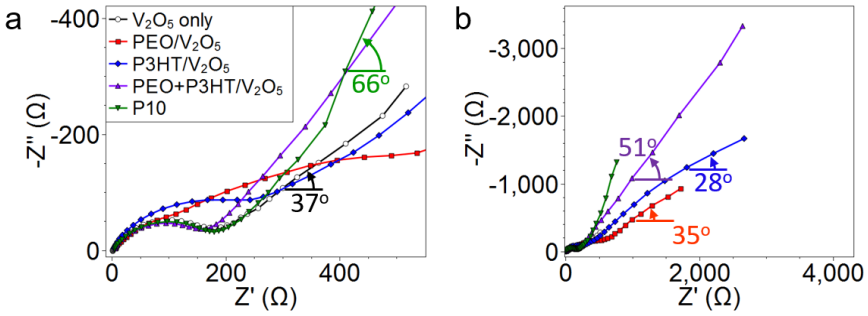

Figure 3.8 Nyquist plots of V_2O_5, PEO/V_2O_5, P3HT/V_2O_5, PEO+P3HT/V_2O_5, and P10 (P3HT-*b*-PEO/V_2O_5) electrodes at 3.6 V vs. Li^+/Li. The AC amplitude was 10 mV. The frequency range of 100 kHz to 5 mHz. Panel (a) is an expanded view of the high frequency region from panel (b). The labelled angles indicate the phase angles at 0.03Hz.

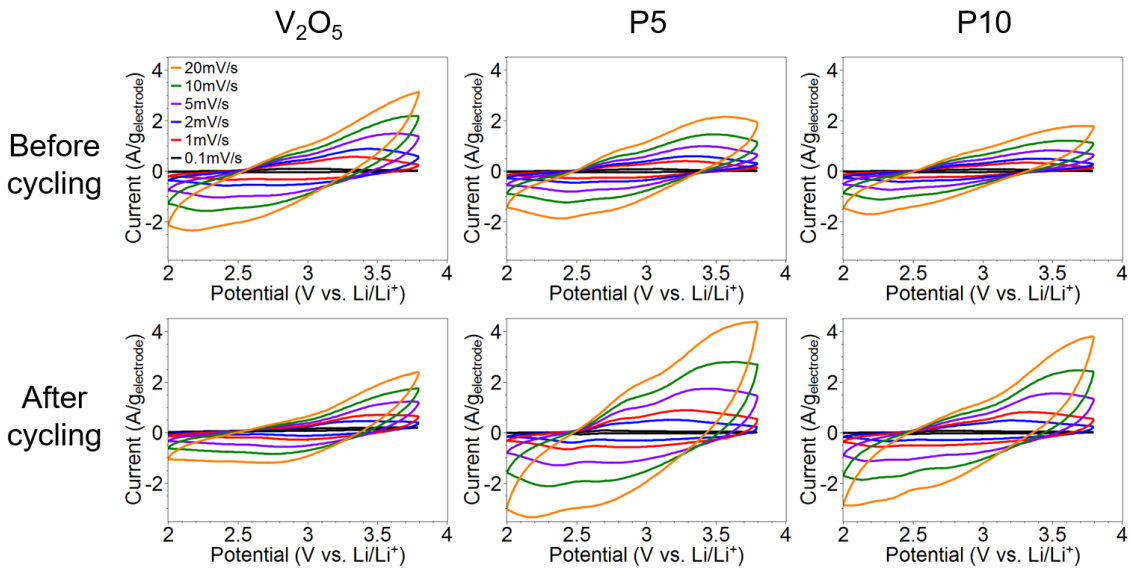

Figure 3.9 Cyclic voltammograms of V_2O_5, P5, and P10 before and after cycling at various scan rates.

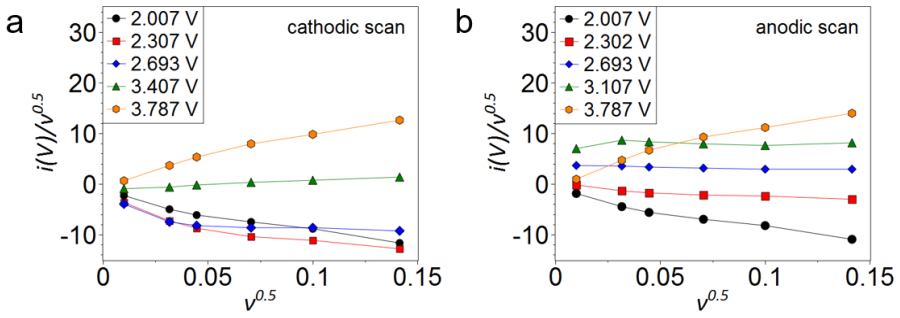

Figure 3.10. Plots of $v^{0.5}$ vs. $i(V)/v^{0.5}$ from (a) cathodic and (b) anodic scans in cyclic voltammetry, which were used for determining a_1 and a_2 from $i(V)/v^{0.5} = a_1 + a_2 v^{0.5}$ at given potentials. The current responses were obtained from cyclic voltammetry at various scan rates of 0.1 to 20 mV/s.

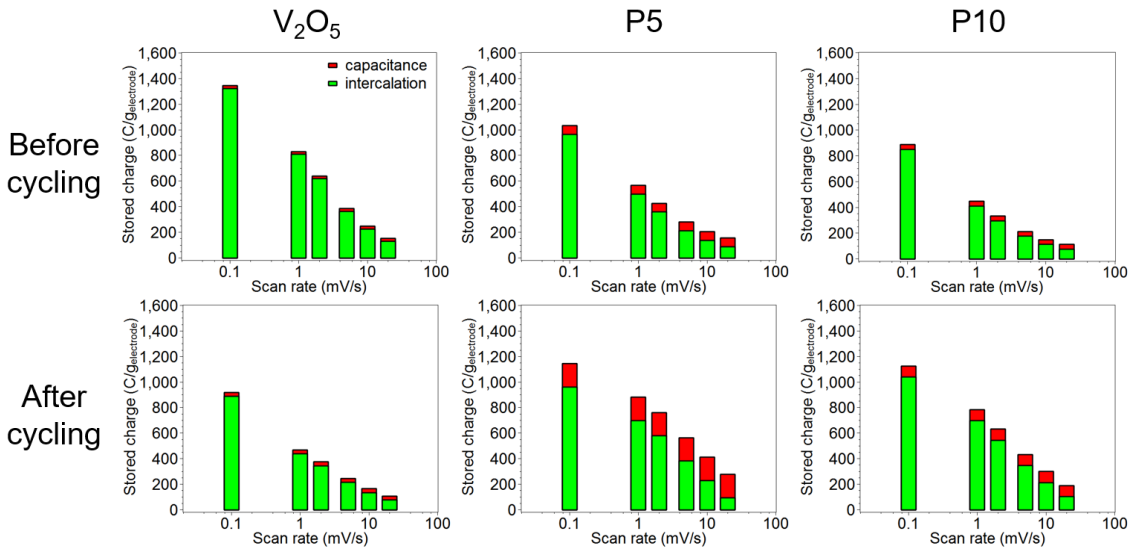

Figure 3.11 Total stored charge for V_2O_5, P5, and P10 before and after cycling as a function of scan rate.

We investigated the charge storage contribution attributed to intercalation and capacitive behaviors. In cyclic voltammetry, the current response *i(V)* as a function of given potential *V* at different scan rates can be expressed as the sum of both intercalation ($a_1 v^{0.5}$) and capacitive contributions ($a_2 v$) as shown below:

$$i(V) = a_1 v^{0.5} + a_2 v$$

where *i*(*V*) is the current response at a given potential in the CV curve, *v* is the scan rate, and a_1 and a_2 are adjustable constants. $i(V) = a_1 v^{0.5} + a_2 v$ was rearranged into $i(V)/v^{0.5} = a_1 + a_2 v^{0.5}$, and then plots of $i(V)/v^{0.5}$ vs. $v^{0.5}$ were drawn at various potentials and scan rates using CV data (Figure 3.9), yielding Figure 3.10. a_1 (y-axis intercept) and a_2 (slope) were determined by linear fitting. Based on the calculated a_1 and a_2 values, intercalation ($a_1 v^{0.5}$) and capacitive contributions ($a_2 v$) can be calculated at a given scan rate and a given potential, Figure 3.10. Figure 3.11 shows the

total charge stored and both capacitive and intercalation contributions calculated by integrating CV curves from Figure 3.9.

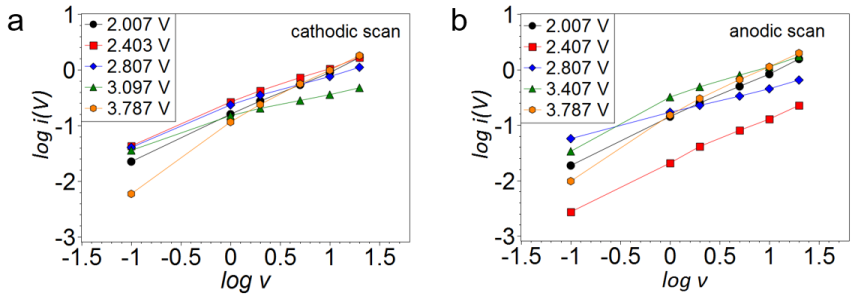

Figure 3.12 Plots of *log v* vs. *log i(V)* from (a) cathodic and (b) anodic scans in cyclic voltammetry, which were used for determining *a* and *b* of *log i(V) = b log v + log a* at given potentials. The current responses were obtained from cyclic voltammetry at various scan rates from 0.1 to 20 mV/s.

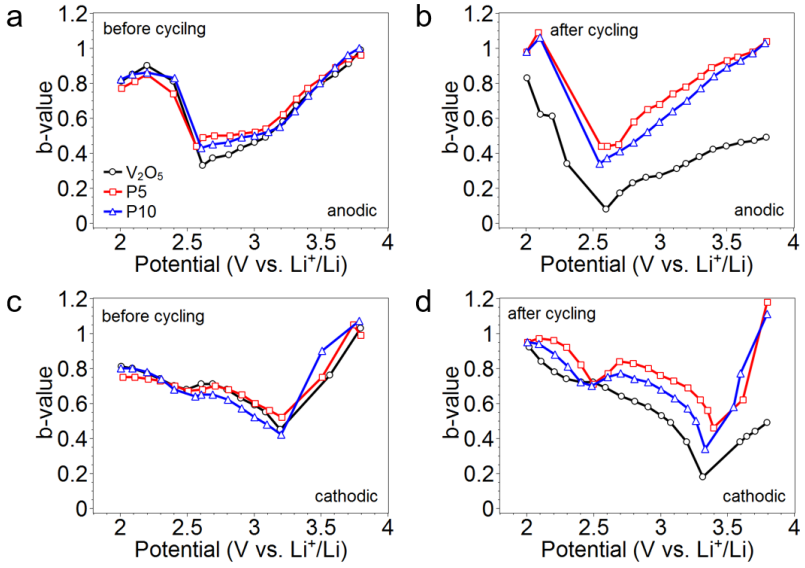

Figure 3.1 b-values for V_2O_5, P5, and P10 plotted as a function of voltage for anodic and cathodic sweeps before cycling and after cycling.

The b-value calculation provides information on whether the current response *i(V)* from cyclic voltammetry is controlled by faradaic (intercalation) and/or non-faradaic processes (capacitive) processes.[221, 253, 254] The current response *i(V)* can be expressed using the power law as shown below:

$$i(V) = a\, v^b$$

where *i*(*V*) is the current response at a given potential in the cyclic voltammogram, *v* is the scan rate, and *a* and *b* are adjustable constants. $i(V) = a\, v^b$ was rearranged into $\log i(V) = b \log v + \log a$, and then plots of *log v* vs. *log i(V)* were drawn at various potentials and scan rates using CV data (Figure 3.9), Figure 3.12. *log a* (y-axis intercept) and *b* (slope) were determined by linear fits. Figure 3.13 shows the determined b-values as a function of potential. In the case of *b*=1, the redox process is an ideal non-diffusion-limited process (such as pseudocapacitance). When *b*=0.5, $i(V) = a\, v^{0.5}$ satisfies the Cottrell equation. The redox process is an ideal diffusion-limited faradaic reaction (such as intercalation). For V_2O_5 in the anodic scan, the b-values of fresh electrodes were close to unity around 2V. The b-value decreased to around 0.5 around 2.6V and 3.2V, and then the b-value increased toward unity above 3.2V. This trends corresponds with the range of the Li^+ intercalation reaction for V_2O_5 xerogel electrode.[200, 217, 218] Fresh P5 and P10 electrodes exhibit the same trend. After cycling, P5 and P10 electrodes had a higher b-value due to their faster response.

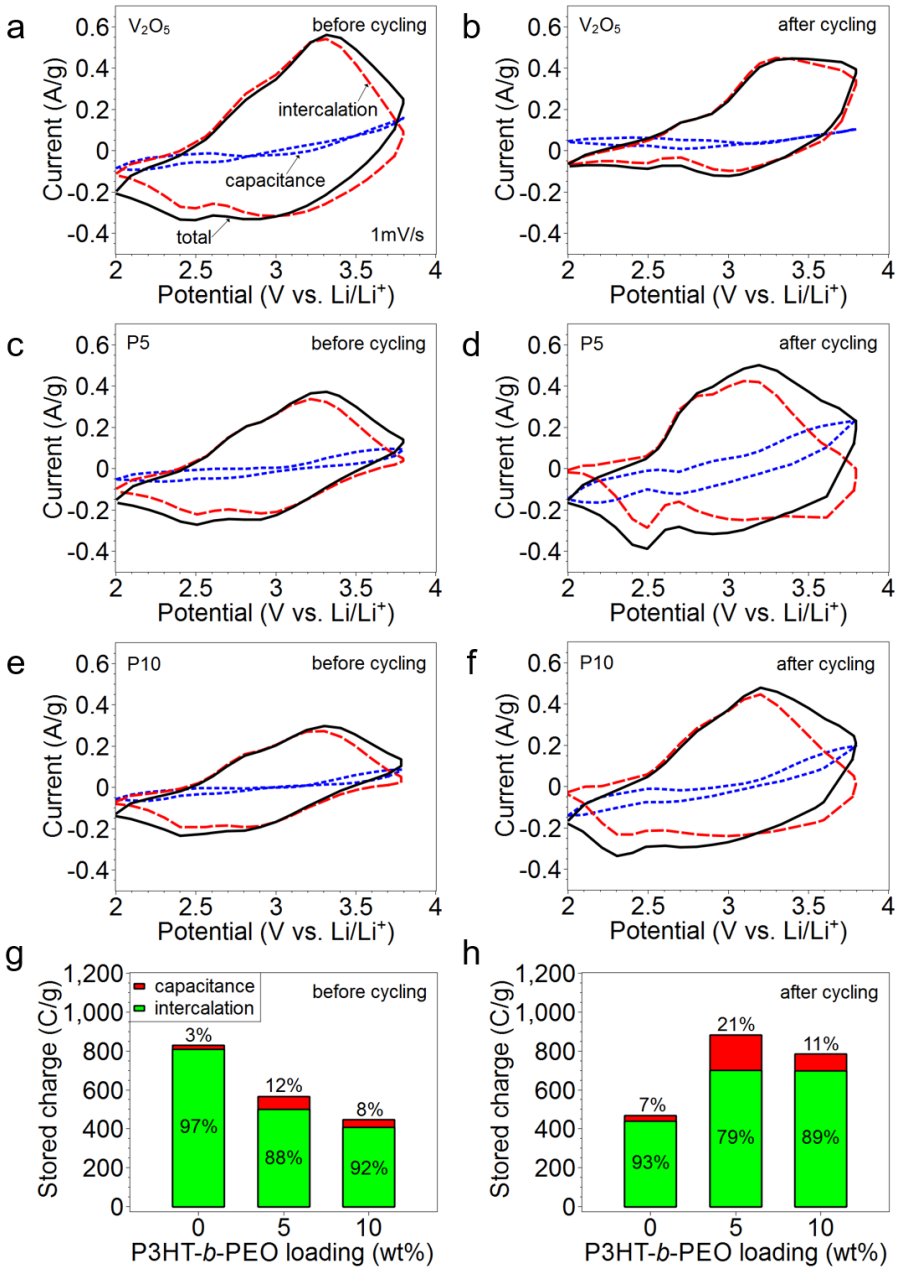

Figure 3.14 Cyclic voltammetry for (a, b) V_2O_5, (c, d) P5, and (e, f) P10 before and after cycling at a scan rate of 1 mV/s. The capacitive and intercalation charge storage contributions to the total current (black) are blue and red, respectively. (g, h) Total charge stored with capacitive and intercalation contributions as a function of P3HT-*b*-PEO loading before and after cycling. The scan rate is 1 mV/s.

Integration of the curves at 1 mV/s provides contributions from the capacitive and diffusion-controlled (intercalation) mechanisms, Figure 3.14 The intercalation mechanism is primarily attributed to V_2O_5 while P3HT is responsible for capacitive storage. For fresh V_2O_5, P5, and P10 electrodes, intercalation is the main contribution to the total stored charge. After cycling of V_2O_5, intercalation is still dominant, but the total area *(i.e.,* the capacity) decreased. On the other hand, P5 and P10 show improved capacitive and intercalation charge storage. The total charge stored as a result of both mechanisms was calculated, Figure 3.14g, 14h and Figure 3.11. For V_2O_5, the charge stored at 1 mV/s decreased from 829 C/g to 468 C/g after cycling. However, the charge stored for P5 (564C/g → 880C/g) and P10 (447 C/g → 783C/g) significantly increased. This trend confirms the results obtained in galvanostatic cycling and is attributed to gradual electrolyte penetration (Figure 3.4). This result is further confirmed using b-values analysis for each electrode, Figure 3.13. Interestingly, these analyses show that V_2O_5 electrodes lose their intercalation ability after repeated cycling, but just 5 or 10 wt% of polymer can prevent this loss.

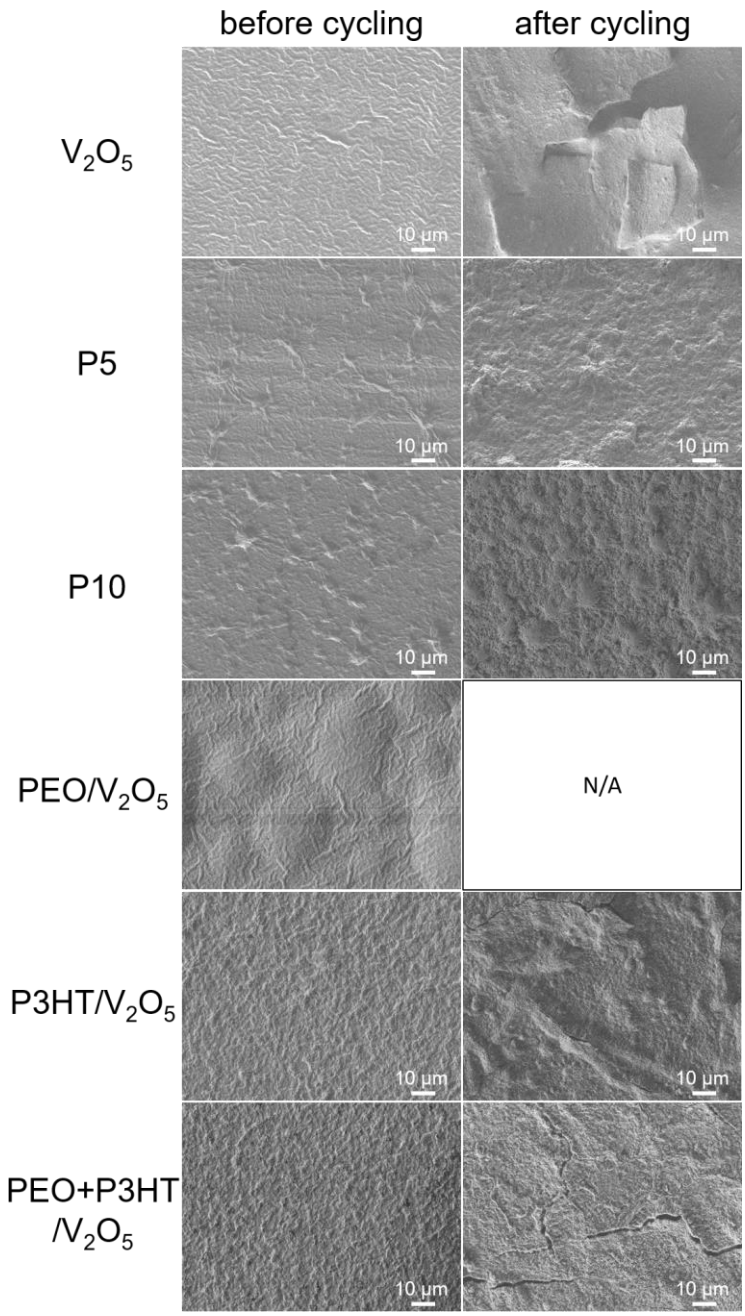

Figure 3.15 SEM images of V_2O_5, P5, P10, PEO/V_2O_5, $P3HT/V_2O_5$, and $PEO+P3HT/V_2O_5$ electrode surfaces before accelerated cycling (left) and after accelerated cycling (right). One set of accelerated cycling consists of 10 charge-discharge cycles at 1 C-rate and 1 charge-discharge cycle at 0.1 C-rate (11 total). 20 sets were performed (total 220 cycles).

Besides the electrochemical properties, we also investigated mechanical degradation post-mortem. Figure 3.15 shows SEM images of the electrode surface before and after cycling. After cycling, large cracks on the surface of V_2O_5, P3HT/V_2O_5 and PEO+P3HT/V_2O_5 electrodes were observed. However, P5 and P10 electrodes displayed no significant cracking on the surface. The SEM images for PEO/V_2O_5 electrodes were not available due to severe pulverization and possible PEO dissolution.

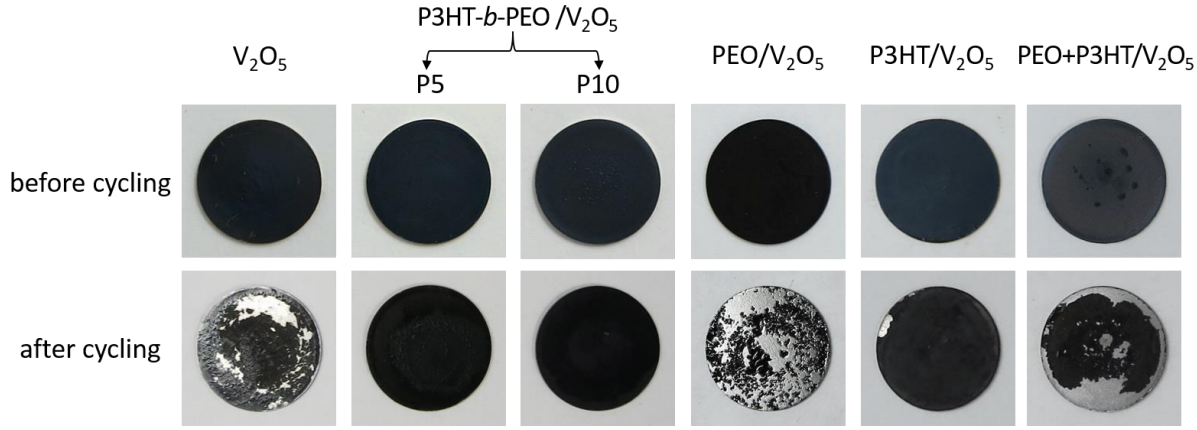

Figure 3.16 Digital images of V_2O_5, P5, P10, PEO/V_2O_5, P3HT/V_2O_5, and PEO+P3HT/V_2O_5 after cycling.

Digital images of these electrodes show similar results, Figure 3.16. This supports that the loss of intercalation capacity in V_2O_5 is attributed to mechanical degradation and crack formation. Other studies have also reported a loss of structural stability for V_2O_5 during cycling, resulting in capacity fade.[85, 86, 87, 89, 90] It is observed here that P3HT-*b*-PEO effectively prevents mechanical degradation of the V_2O_5 system, allowing excellent cycling stability of hybrid electrodes (P5 and P10).

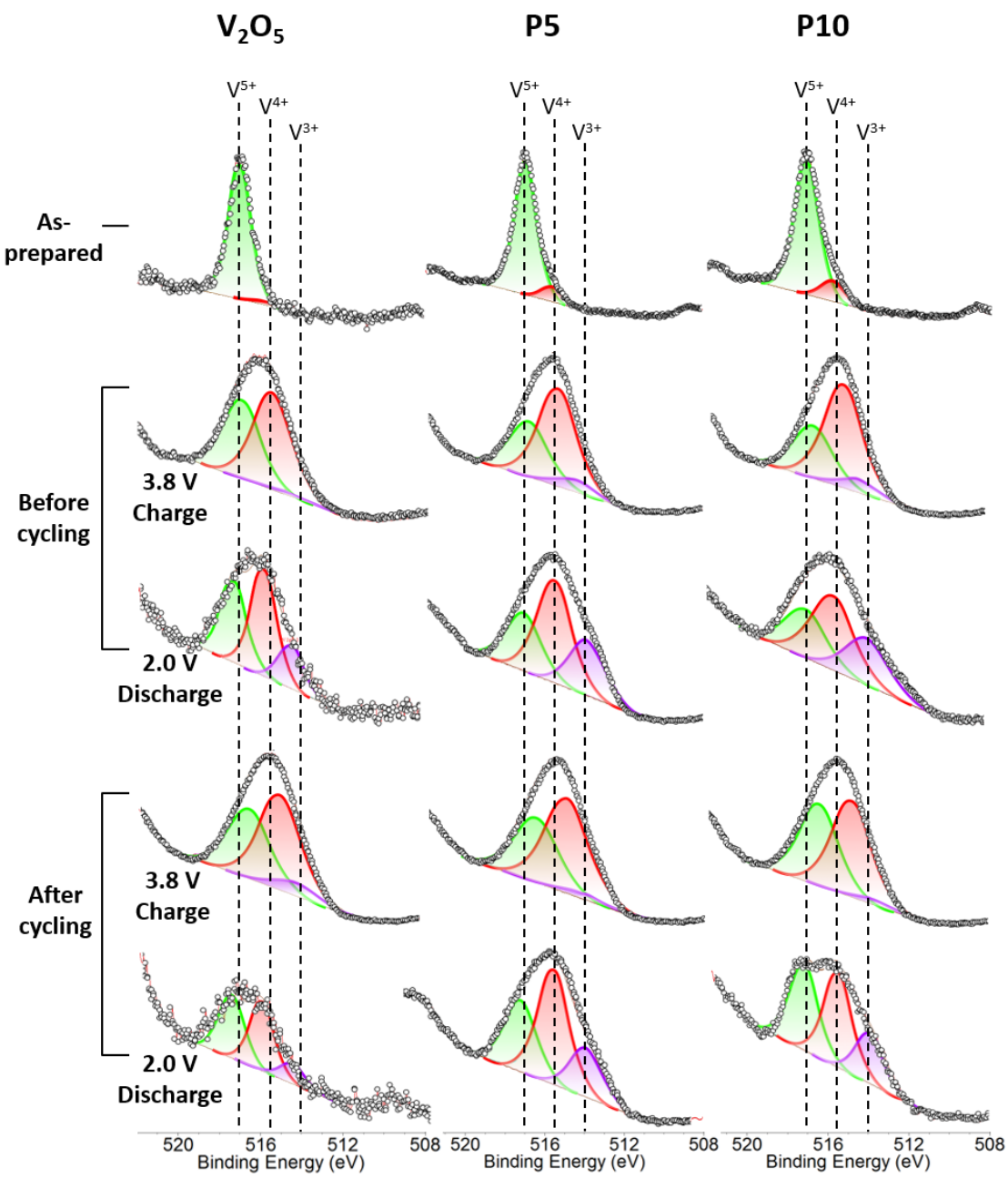

Figure 3.17 XPS of the V2p region if as-prepared electrodes before and after cycling at charged (3.8 V) and discharged (2.0 V) states. For curve fitting, a combined Gaussian-Lorentzian line shape (CasaXPS) and linear-type background was used with the same full-width-half-maximum (FWHM) for all components.

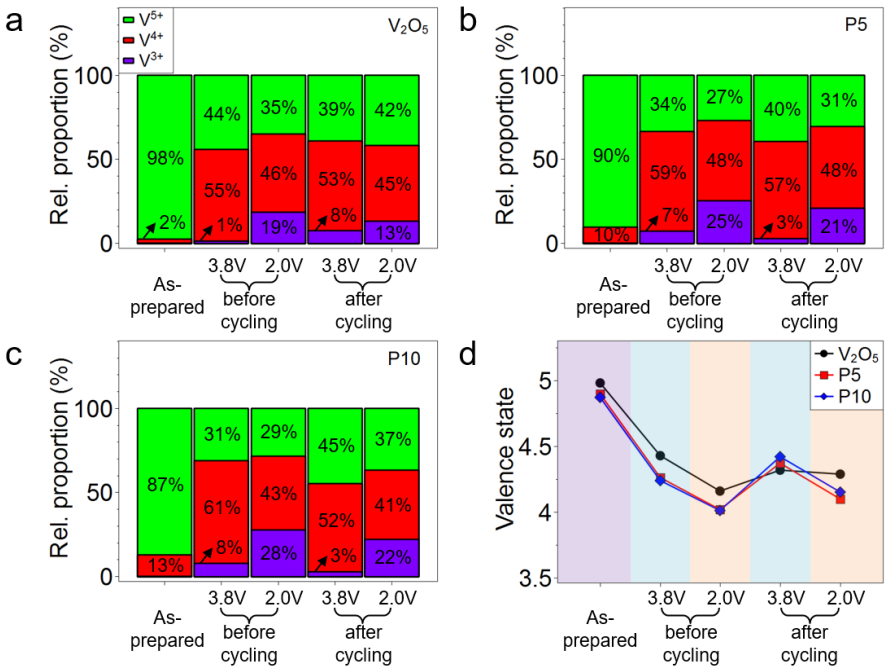

Figure 3.18 The relative proportion of V^{3+}, V^{4+}, and V^{5+} in (a) V_2O_5, (b) P5, and (c) P10 hybrid electrodes as determined by XPS before and after cycling and at 2.0 and 3.8 V. (d) The average vanadium valence of the three electrodes form panels (a-c).

Finally, the chemical stability of the electrode was investigated using XPS after Ar-ion milling, Figure 3.17 and Figure 3.18. These measurements interrogate the electrode's surface and thus do not represent the state of the bulk electrode. However, they can capture the relative changes of vanadium's valency during cycling. The V2p peak was fitted with three peaks for V^{5+}, V^{4+}, and V^{3+} at 516.9 eV, 515.4 eV, and 514.2 eV, respectively.[235] As prepared, all electrodes were rich in V^{5+}, as expected. The general observation was that upon discharge from 3.8 to 2.0 V, there was a decrease in the V^{5+} and V^{4+} populations and an increase in the V^{3+} population, consistent with lithium intercalation.[255, 256] On charging from 2.0 to 3.8 V, the relative fraction of V^{5+} and V^{4+} increased, whereas that of V^{3+} decreased with lithium de-intercalation. Another important point to

note is that after cycling, the average vanadium valency showed greater changes (*i.e.* more electrochemical activity) upon discharge from 3.8 to 2.0 as compared to V_2O_5. The average valence states of vanadium of the hybrid electrodes were calculated from the V2p spectra using the equation below:

$$V^{n+} = \frac{5 \times V^{5+} + 4 \times V^{4+} + 3 \times V^{3+}}{V^{5+} + V^{4+} + V^{3+}}$$

where V^{5+}, V^{4+}, and V^{3+} are the integrated peak areas for V^{5+}, V^{4+}, and V^{3+}, respectively. Overall analysis of the electrode surface shows that the block copolymer maintains and facilitates the electoactivity of V_2O_5. V_2O_5 alone shows a loss of electrochemical activity upon cycling, which we believe is caused by mechanical degradation.

3.4 CONCLUSIONS

We compared a series of polymeric binders based on P3HT and PEO for carbon-free V_2O_5 electrodes, and we found significant differences in performance. The use of block copolymer additives produced superior electrodes, and morphological studies suggest this is due to enhanced mixing between V_2O_5 and the polymeric binder. For a cathode containing 10 wt% P3HT-*b*-PEO and a discharged at 0.1 C-rate, the capacity after cycling was 190 mAh/g, whereas that of V_2O_5 was 77 mAh/g (a 2.5 fold difference). Also, the capacity of P3HT/V_2O_5, and PEO+P3HT/V_2O_5 was very low due to macroscopic phase segregation. PEO/V_2O_5 cathodes also showed no improvement because of the presence of the non-conducting polymer. These results show that block copolymers are potentially a powerful means to create "beyond PVdF" binders that simultaneously address ion and electron conduction, mechanical properties, and stability in the pursuit of carbon-free battery cathodes.

CHAPTER IV

EFFECTS OF REGIOREGULARITY AND MOLECULAR WEIGHT OF SELF-ASSEMBLED CONJUGATED POLYMER BLOCK ON ELECTROCHEMICAL PERFORMANCE OF POLY(3-HEXYLTHIOPHENE)-BLOCK-POLY(ETHYLENE OXIDE)

4.1 INTRODUCTION

In solid state applications (photovoltaic cells,[95, 96, 97, 98] and field-effect transistors[99, 100, 101, 102]), conjugated polymers such as poly(3-hexylthiophene) (P3HT) have demonstrated considerable promise as active materials. P3HT polymer chains have many degrees of conformational freedom, resulting in complex self-organizing structures in the solid state.[257] In such systems, which have ordered and amorphous domains with various degrees of order, understanding the doping/dedoping process and charge carrier transport is difficult because of the complex self-organizing properties. The growing technological appeal of these semiconductors makes the fundamental understanding of the self-assembled structure effect extremely important for rational design of device functionalities and engineering breakthroughs. It has been demonstrated that molecular weight[98, 102, 128, 129, 130, 131, 132, 133] and regioregularity[99, 104, 105, 106, 107, 108, 109, 110, 111]—the percentage of a head-to-tail configuration of the hexyl side chains as shown in Figure 4.1—strongly affects the solid state electronic properties of P3HT. For example, higher molecular weight (30 kDa) of P3HT showed faster charge-carrier mobility (6×10^{-3} cm^2 V^{-1} s^{-1}) compared to lower molecular weight P3HT (4 kDa, 4×10^{-6} $cm^2V^{-1}s^{-1}$).[128] Higher regioregularity (96% vs. 70%) improved charge-carrier mobility (5×10^{-2} $cm^2V^{-1}s^{-1}$ vs. 2×10^{-5} $cm^2V^{-1}s^{-1}$).[99] Despite the recognized importance of regioregularity and molecular weight on solid state electronic performance, a detailed understanding of the effects on electrochemical property is lacking.

The electrochemical process differs from the solid state electronic process because the electrochemical process occurs in the presence of a liquid electrolyte in which both electrons and ions simultaneously transport. In an electrochemical system, P3HT shows a pseudocapacitive behavior (Figure 4.1c): when P3HT is being charged, it loses electrons and becomes positively charged, causing anions in the electrolyte to approach the positively charged polymer backbone to ensure electroneutrality. There have been few reports on the regioregularity effect of P3HT homopolymers on electrochemical performance: high regioregularity (96% vs. 58%) enhances specific capacitance (134.5 F/g vs. 71.8 F/g) as reported by Sivaraman and coworkers.[134]

Meanwhile, in electrochemical systems, amphiphilic block copolymers bearing a conjugated P3HT block and an ion-conducting block are particularly interesting due to being able to conduct electrons and ions simultaneously and prevent large-scale phase segregation.[1, 53, 85, 208, 227, 258, 259, 260, 261] For example, Balsara and coworkers demonstrated that P3HT-*b*-PEO block copolymers form P3HT-rich and PEO-rich nanoscale domains, showing simultaneous conduction of electrons and ions (approximately 10^{-5} S/cm and 10^{-4} S/cm, respectively).[208] Recently, our group reported a P3HT-*b*-PEO micellar aggregate—having a PEO-shell and P3HT-core—as conductive polymeric binders for lithium-ion batteries.[85, 261] The P3HT-*b*-PEO micellar aggregate showed a pseudocapacitive behavior but the relationship between its self-organizing structures and desired functions (e.g., capacity and redox potentials) has not yet been examined, and is of utmost importance to the future design of these promising materials.

Here, we demonstrate the strong effects of regioregularity and molecular weight of the P3HT block in P3HT-*b*-PEO on molecular conformation and electrochemical properties (e.g., redox property and capacity). We compared four different P3HT-*b*-PEO block copolymers—various P3HT regioregularities and molecular weights while the PEO block

molecular weight was kept the same. The P3HT-*b*-PEO block copolymers formed micellar aggregates, in which hydrophilic PEO forms a corona around hydrophobic P3HT. The self-assembled P3HT domains had a disordered structure (over 90 wt% is quasi-ordered or even amorphous). We showed that P3HT regioregularity and molecular weight strongly affected its backbone conformation and chain packing structure, correlating with the redox properties of P3HT block. We also found that backbone planarity was most important for affecting capacity. This molecular conformational-electrochemical correlation study opens up a wide range of novel technological solutions for conjugated polymer-based materials in electrochemical systems.

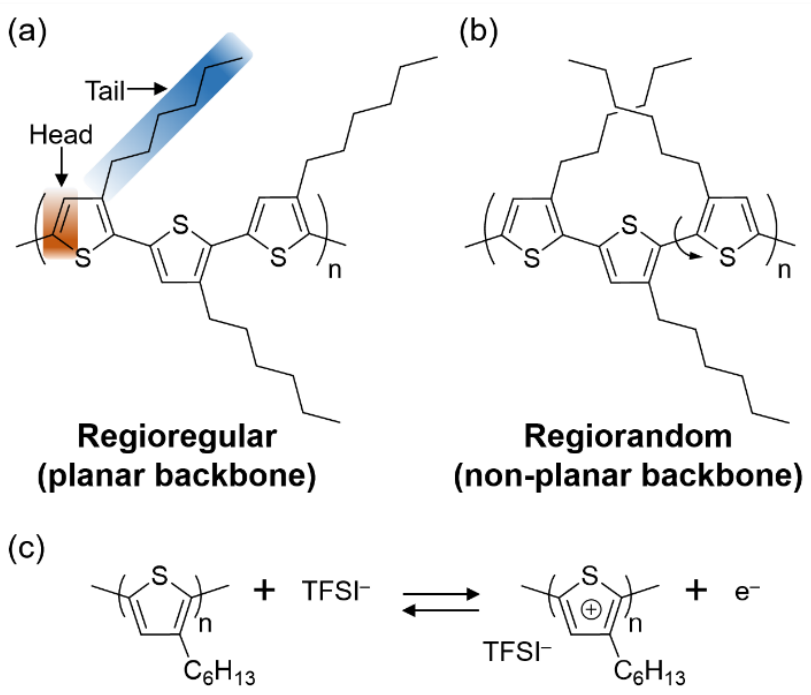

Figure 4.1 Schematic diagrams of (a) regioregular and (b) regiorandom P3HTs. (c) P3HT doping/depoing mechanism.

4.2 EXPERIMENTAL METHOD

Materials. Isopropyl magnesium chloride with lithium chloride complex (1.3M), Ni(PPh3)4), 4-chloro-3-methylphenol, 1,3-bis(diphenylphosphino)propane, tetra-n-butylammonium fluoride (TBAF) (1.0 M in THF), 5-hexynoic acid, 4-dimethylaminopyridine (DMAP), PMDETA , 3-hexylthiophene, drisolve dichloromethane, p-Toluenesulfonyl chloride, azidotrimethylsilane, ethylene carbonate, imidazole, copper (I) bromide, and tert-butyldimethylsilane were purchased from Sigma-Aldrich. N-(3-dimethylaminopropyl)-N'-ethylcarbodiimide hydrochloride (EDC) was purchased from TCI America. Lithium bis(trifluoromethanesulfonyl)imide (LiTFSI), and propylene carbonate were purchased from Sigma Aldrich. Lithium ribbon was purchased from Alfa Aesar. All chemicals were used as received, unless stated otherwise. 316 stainless steel coin spacers (15.8 mm diameter × 0.5 mm thickness) were purchased from MTI Corporation. Water was purified to 18.2 MΩ-cm (Milli-Q, Millipore). Celgard 3501 polypropylene separator was obtained from Celgard.

Synthesis of P3HT-*b*-PEO block copolymers. 2,5-dibromo-3-hexylthiophene was dissolved in anhydrous THF and the solution was stirred in an ice bath for 15 minutes. A solution of isopropyl magnesium chloride with LiCl (1.3 M) in THF was added, and the mixture was stirred for another 2 hours at 0 C. Next, 40 mL of THF was added to the reaction flask followed by a solution containing the functionalized linker and catalyst. This catalyst solution was made by dissolving Ni(PPh3)4 and 2-(4-chloro-3-methylphenoxy)ethyl tosylate in 1 mL anhydrous THF inside a glove-box. After it was stirred overnight, this solution was added to the reaction mixture in ice bath directly to produce the regiorandom P3HT. On the other hand, for the more regioregular P3HT, 1,3-bis(diphenylphosphino)propane (dppp) was dissolved in 1 mL of dry THF and added to the catalyst solution to stir for additional 2 hours, before being added to the reaction mixture.

The final polymer product was recovered by precipitation in ethanol and dried under vacuum. P3HT-*b*-PEO was then synthesized by click chemistry with azide-functionalized P3HT and alkyne-functionalized PEO. A more detailed, step-to-step description to the overall procedure can be found in our previous paper.[201] In NMR, Regio-regularity of each P3HT-b-PEO copolymer can be obtained from the two peaks at 2.80 ppm and 2.57 ppm (Figure 4.2), which represent the regio-regular (H-T bonds) part and regio-random (H-H bonds) part of the copolymer respectively.[262] By comparing the integrated area under the peaks, we are able to calculate the percentage of regio-regular P3HT in a block copolymer.

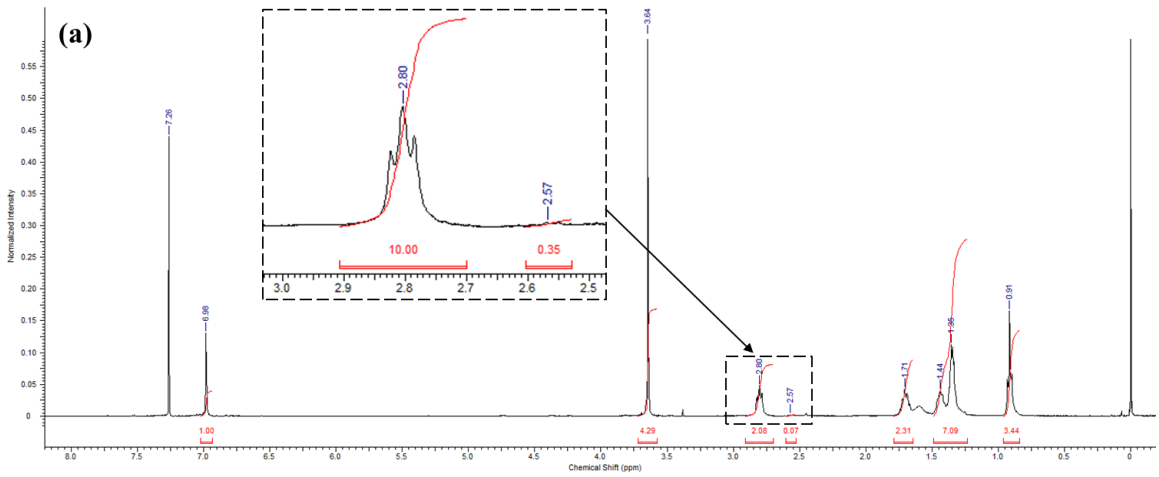

Figure 4.2 ^{1}H-NMR of (a) P3HT-*b*-PEO (97%/14 kDa), (b) P3HT-*b*-PEO (93%/12 kDa), (c) P3HT-*b*-PEO (94%/19 kDa), (d) P3HT-b-PEO (86%/8 kDa). ^{1}H NMR (500 MHz, $CDCl_3$), δ (ppm): 7.53 (s, 1H, CH triazole), 7.34 (d, 1H, Ar-H), 6.79 (s, 1H, Ar-H), 6.74 (m, 1H, Ar-H), 4.74 (t, 2H, Ar-O-CH_2-CH_2-O-), 4.37 (t, 2H, Ar-O-CH_2- CH_2-O-), 4.23 (t,2H,O-CH_2-CH_2-OCO), 3.78 (t,2H,O-CH_2-CH_2-OCO), 2.61 (t, 2H, OCO-CH_2-CH_2-CH_2-C-CH), 2.42 (t, 2H, OCO-CH_2-CH_2-CH_2-C-CH), 2.03 (m, 2H, OCO-CH_2-CH_2-CH_2-C-CH), 7.00 (s, n*1H, Ar-H), 2.82 (t, n*2H,Ar-CH_2-), 1.72 (q, n*2H, - CH_2-), 1.46 (b, n*2H, -CH_2-), 1.37 (b, n*4H, -CH_2-), 0.93 (t, n*3H, -CH_3) , 3.64 (b, m*H, - O-CH_2-CH_2-O-).

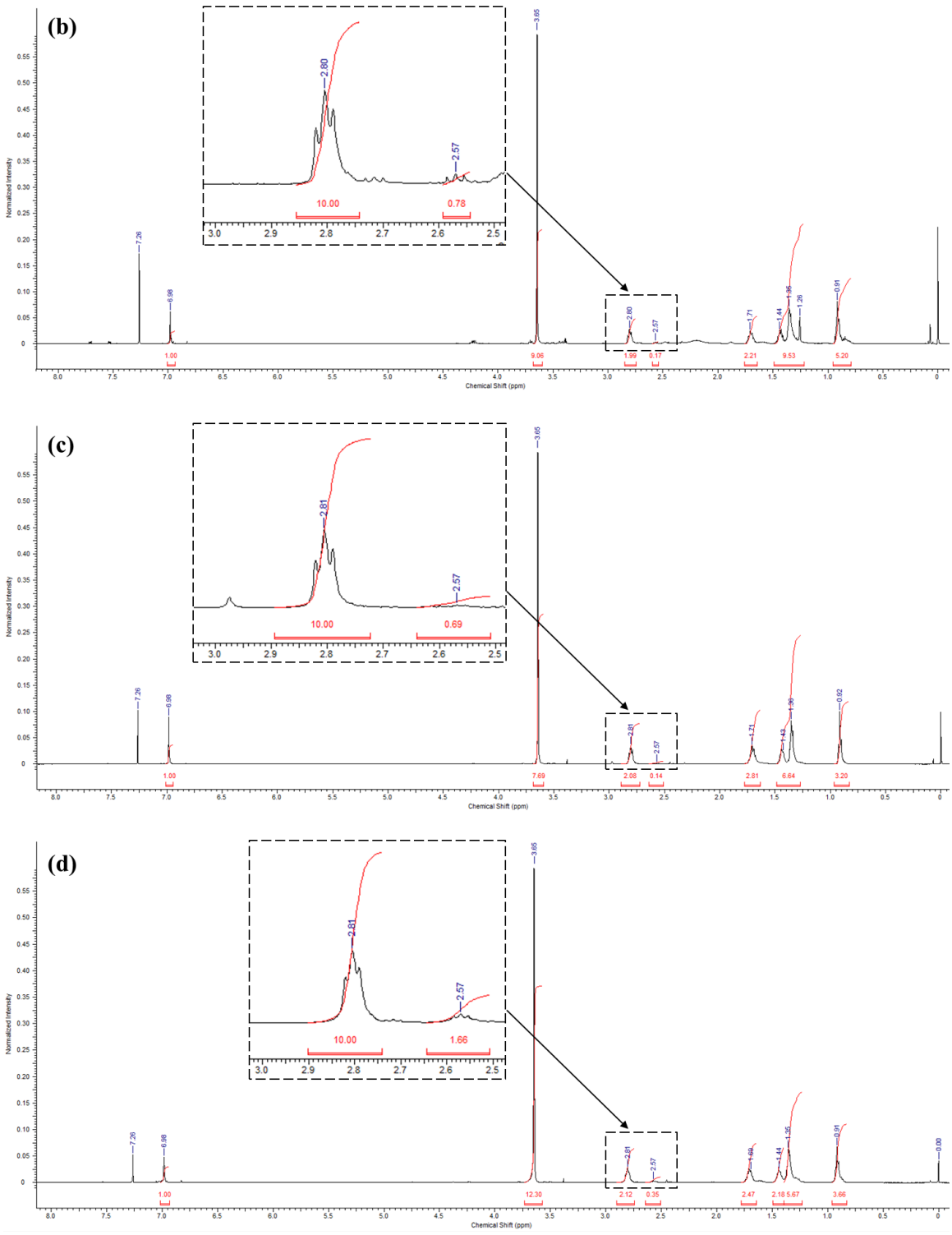

Figure 4.2 Continued.

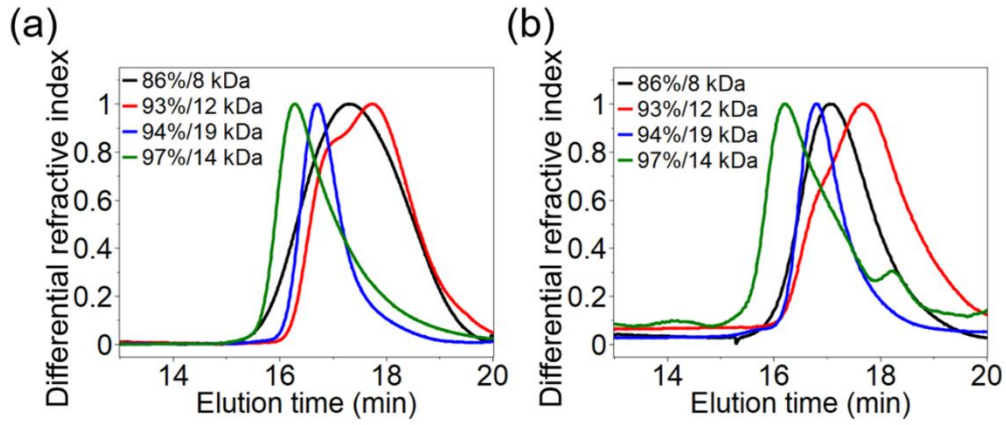

Figure 4.3 GPC analysis of (a) P3HT polymers, before "click" reaction and (b) P3HT-*b*-PEO block copolymers.

Preparation and characterization of polymer dispersions. P3HT-*b*-PEO dispersions were made by sonicating the polymer and LiTFSI in Milli-Q water at 0 ^{o}C to make a 1 mg of polymer + salt/mL of stock solution. The molar ratio of ethylene oxide units to Li^{+} was 0.085. Hydrodynamic diameter was determined using dynamic light scattering (DLS) (ZetasizerNano ZS90, Malvern) at 25 °C. For DLS, the P3HT-*b*-PEO dispersions were diluted to 0.05 mg/mL. Atomic force microscopy (AFM) measurements were carried out using a Bruker Dimension Icon AFM under tapping mode. UV-vis spectra were measured using a Hitachi U-4100 UV-Vis-NIR spectrophotometer (341-F). P3HT-*b*-PEO morphologies were investigated using scanning electron microscopy (SEM, JEOL JSM-7500F). For AFM, UV-vis spectroscopy, and SEM, about 0.1 - 0.3 mg of P3HT-*b*-PEO dispersions were drop-cast on glass (1 cm × 1 cm), air-dried for three hours, and then annealed at 90 °C for 12 hours under vacuum. XRD was carried out using a Rigaku Ultima II vertical θ-θ powder diffractometer using Cu Kα radiation (λ = 1.5418 Å) with Bragg-Brentano para-focusing optics. The operating power was 40 kV and 40 mA. The 2-theta angle was

varied from 3° to 30°. Differential scanning calorimetry (DSC, Q200, TA Instruments) was performed on approximately 2 mg samples of P3HT-*b*-PEOs using a heat-cool method. Dried samples were loaded into a Tzero aluminium pan (TA Instruments) and annealed at 90 °C for 12 hours under vacuum. The dried samples were heated up to 250 °C from 25 °C at a rate of 10 °C/min followed by cooling at the same rate for three heat–cool cycles.

Electrode preparation. 316 stainless steel coins (15.8 mm diameter × 0.5 mm thickness) were cleaned via sonication for 15 min each in water, isopropanol, and acetone followed by purging with nitrogen gas and drying at 75 °C. P3HT-*b*-PEO dispersions (1 mg/mL) were drop-cast onto cleaned stainless steel coins by depositing about 0.30 mg of P3HT-b-PEO onto the surface and then air drying and annealing at 90 °C for 12 hours under vacuum.

Cell assembly and measurement. Electrochemical measurements were performed using two-electrode cells (Tomcell Japan Co., Ltd.) assembled in a water-free, oxygen-free, argon-filled glovebox (MBraun) using lithium metal anodes. 1.0 M LiTFSI in propylene carbonate was used as the electrolyte and Celgard 3501 was used as the separator. Cyclic voltammetry and galvanostatic charge-discharge measurements were performed using a Solartron 1470E.

4.3 RESULTS AND DISCUSSION

The aims of this study were: (1) to study the effects of P3HT block's regioregularity and molecular weight on self-organizing structure; and (2) to find a correlation between the self-organizing structure and electrochemical properties (i.e., capacity, redox property) of P3HT-*b*-PEO block copolymers. We first synthesized four P3HT-*b*-PEO block copolymers with different regioregularities (86 %–97 %) and molecular weights (8–19 kDa) of the P3HT block while the PEO block was kept the same (7 kDa) using a modified approach based upon our prior

publication.[201] The P3HT-*b*-PEO block copolymers' regioregularity and molecular weight are listed in Table 4.1. Hereafter, P3HT-*b*-PEO having regioregularity of XX% and number average molecular weight of YY kDa will be called "P3HT-*b*-PEO (XX%/YY kDa)". High regioregular block copolymers were synthesized with the addition of 1,3-bis(diphenylphosphino)propane (dppp) during P3HT polymerization, which made the reaction more favorable towards a head-to-tail configuration. The three P3HT-*b*-PEOs (93%/12 kDa, 94%/19 kDa, and 97%/14 kDa) are more region-regular (Figure 4.2) and have a higher region-regularity ranging from 93% to 97%. Low regioregular P3HT-*b*-PEO (86%/8 kDa) was synthesized using a very similar approach, but without use of dppp in the catalyst solution; thereby it has a lower regioregularity of 85.8%. PEO was purchased from Sigma-Aldrich and therefore has the same molecular weight in all four block copolymers. The molecular weight of P3HT was controlled mostly by varying the reaction time. However, due to the lack of dppp in the synthesis of low regioregular P3HT, the reaction is more uncontrolled and results in a low degree of polymerization of regiorandom P3HT. Hence, P3HT-*b*-PEO (86%/8 kDa) has the smallest P3HT block among all four samples.

Table 4.1 Characteristics of P3HT-*b*-PEO Block Copolymers.

Polymer	Regioregularity[a] (%)	$M_{n,P3HT}$[b] (kDa)	$M_{n,PEO}$[b] (kDa)	PDI[c]
P3HT-*b*-PEO (86%/8 kDa)	86	8	7	1.38
P3HT-*b*-PEO (93%/12 kDa)	93	12	7	1.47
P3HT-*b*-PEO (94%/19 kDa)	94	19	7	1.12
P3HT-*b*-PEO (97%/14 kDa)	97	14	7	1.37

[a]Determined using ^{1}H-NMR. [b]*M*n = number-average molecular weight, determined using ^{1}H-NMR. [c]PDI = polydispersity index of the P3HT polymer determined by gel permeation chromatography with polystyrene standards (Figure 4.3).

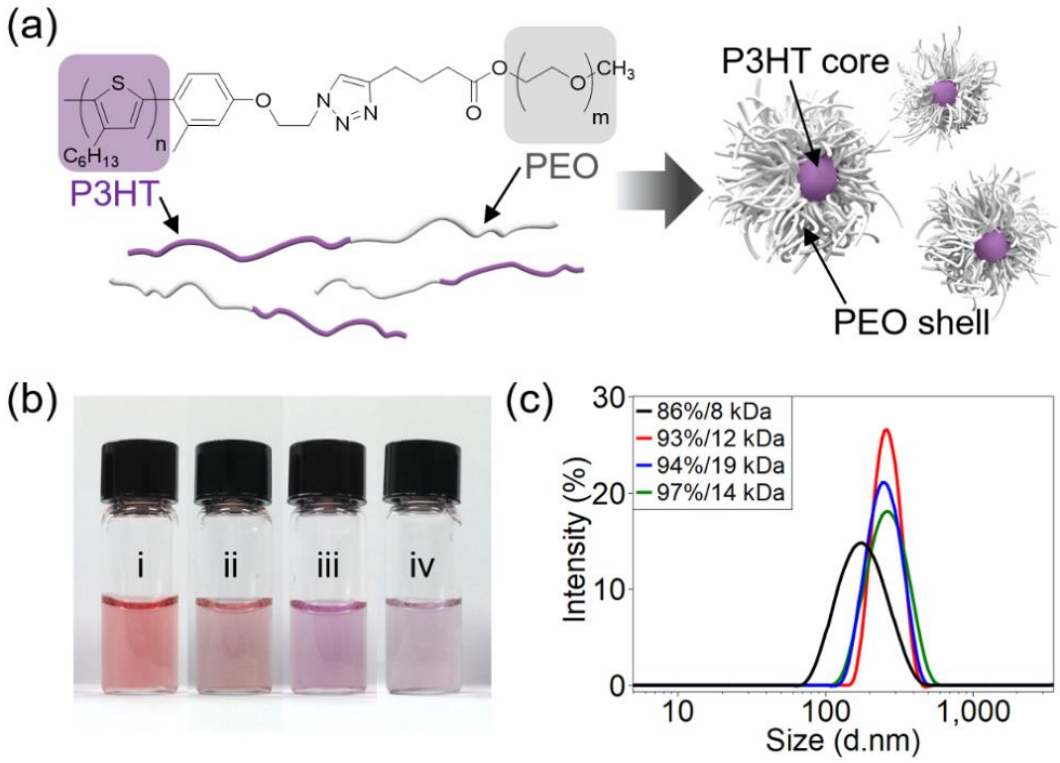

Figure 4.4 (a) Schematic of P3HT-*b*-PEO micellar aggregate preparation. (b) P3HT-*b*-PEO dispersions at a concentration of 0.05 mg/mL with LiTFSI (the molar ratio of Li^+ to PEO repeat units was 0.085) in water. Roman numerals (i, ii, iii, and iv) denote P3HT-*b*-PEO (86%/8 kDa), P3HT-*b*-PEO (93%/12 kDa), P3HT-*b*-PEO (94%/19 kDa), and P3HT-*b*-PEO (97%/14 kDa), respectively. (c) Size distribution profiles for all P3HT-*b*-PEO dispersions in water obtained by dynamic light scattering (DLS).

We next prepared P3HT-*b*-PEO dispersions in water. All P3HT-*b*-PEOs were dispersed in water using 1h sonication (Figure 4.4a and 4.4b). Under sonication, lithium bis(trifluoromethanesulfonyl)imide (LiTFSI) was added for optimum lithium-ion conduction.[207] The molar ratio of Li^+ to ethylene oxide repeat units was kept at 0.085. The P3HT-*b*-PEO dispersions were stable for over 6 months, after which large aggregates precipitated. The

dispersion's stability is due to the micellization process, in which hydrophilic PEO forms a corona around hydrophobic P3HT core confirmed by TEM in our previous study.[85] DLS study revealed that the average dimeters of P3HT-*b*-PEO (93%/12 kDa, 94%/19 kDa, and 97%/14 kDa) were similar (274 nm, 258 nm, and 266 nm, respectively) whereas an average dimeter of P3HT-*b*-PEO (86%/8 kDa) was smaller (189 nm) (Figure 4.4c). These sizes were consistent with the AFM results (Figure 4.5).

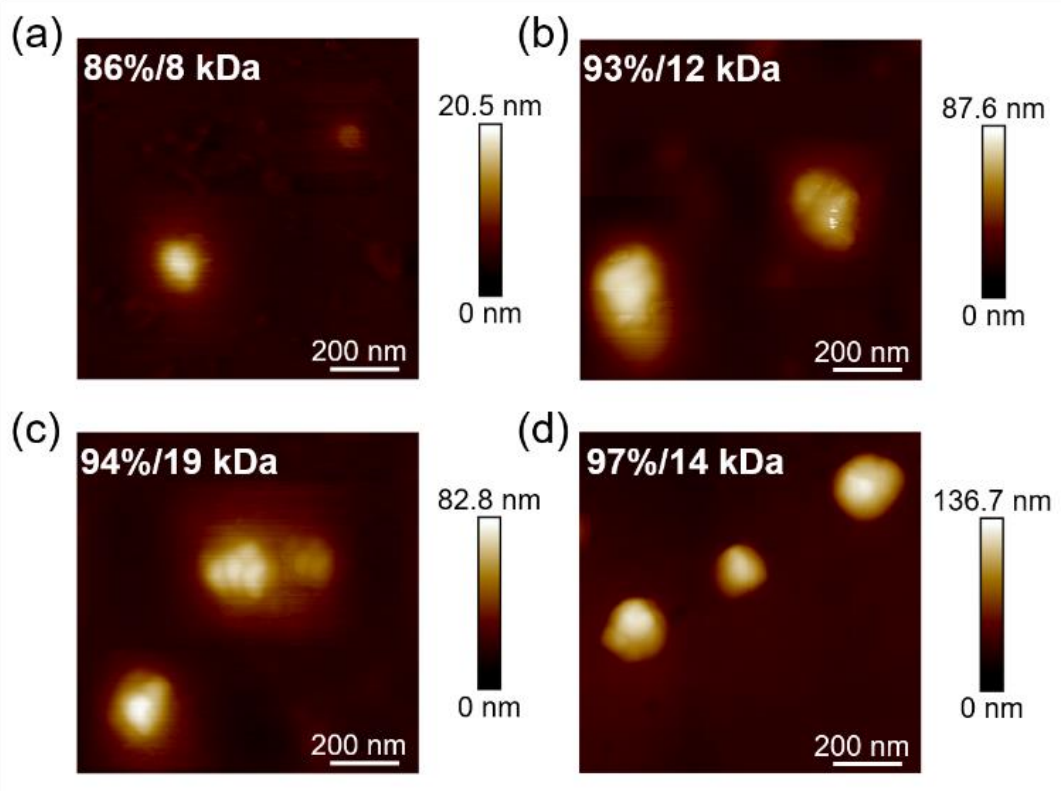

Figure 4.5 (a-d) AFM height images of individual micellar aggregates coated onto glass substrate.

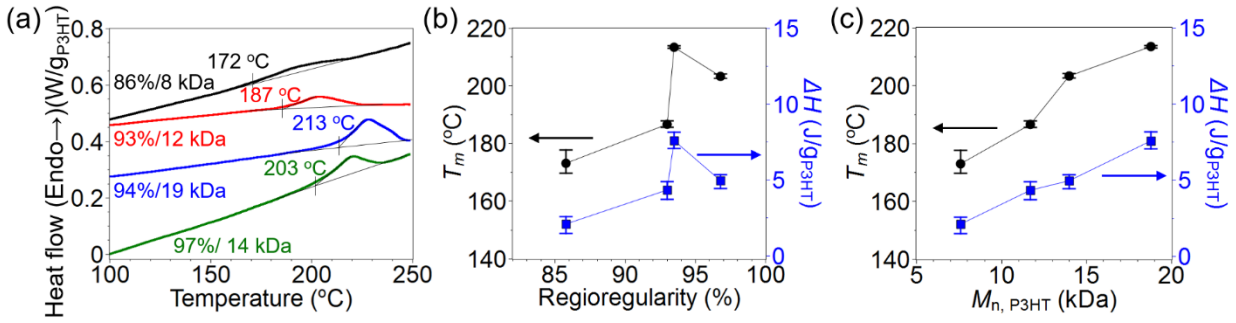

Figure 4.6 (a) The second heating DSC scan of a P3HT block of the block copolymers. A scan rate was 10 °C/min. (b) Melting temperatures and enthalpy of fusions (ΔH) of a P3HT block as a function of regioregularity. (c) Melting temperatures and enthalpy of fusions (ΔH) of a P3HT block as a function of molecular weight (M_n).

We evaluated thermal properties of dried P3HT-*b*-PEO micellar aggregates as a function of the regioregularity and molecular weight of the P3HT block (Figure 4.6). T_m increased as molecular weight increased. The molecular weight dependent results were consistent with the published study.[263] For enthalpy of fusion (ΔH)— area under the endotherm, regioregularity had no trend but ΔH increased with increasing molecular weight. Malik et al. reported the heat of fusion ($\Delta H°$) for 100% crystalline P3HT of 99 J/g.[264] The degrees of P3HT block crystallinity—determined from $\Delta H/\Delta H°$, were very low (2.1-7.6%) (Table 4.2), indicating that quasi-ordered or amorphous regions take a majority portion in the P3HT domains.

Table 4.2 Characteristics of the P3HT-*b*-PEO micellar aggregates.

Polymer	ΔH (J/g)	Crystallinity, $\Delta H/\Delta H°$ (%)	Band gap[a] (eV)	Cathodic peak (V vs. Li/Li^+)	Discharge capacity[b] (mAh/g_{P3HT})	Doping level
P3HT-*b*-PEO (86%/8 kDa)	2.1	2.1	1.9	3.4	9.4 ± 1.2	0.06 ± 0.01
P3HT-*b*-PEO (93%/12 kDa)	4.3	4.4	1.8	3.5	23.2 ± 4.5	0.15 ± 0.03
P3HT-*b*-PEO (94%/19 kDa)	7.6	7.6	1.8	2.8	24.1 ± 5.3	0.15 ± 0.03
P3HT-*b*-PEO (97%/14 kDa)	4.9	5.0	1.7	2.8, 3.4	37.3 ± 5.6	0.23 ± 0.04

[a]Calculated from UV-vis absorption spectra, Figure 4.6a. [b]Measured at 1 C-rate.

Figure 4.7a shows UV-vis absorption spectra of dried P3HT-*b*-PEOs on glass. These spectra resembled those of typical P3HT homopolymers.[95] λ_{max} decreased as regioregularity decreased. This blue-shifted absorption originates from steric hindrance of head-head configuration inducing twisted backbone and disordered structure, decreasing the π-overlap along the backbone.[265] On the other hand, no distinct trend in molecular weight was observed throughout all samples. Band gap increased as regioregularity decreased, whereas no trend in molecular weight was observed.

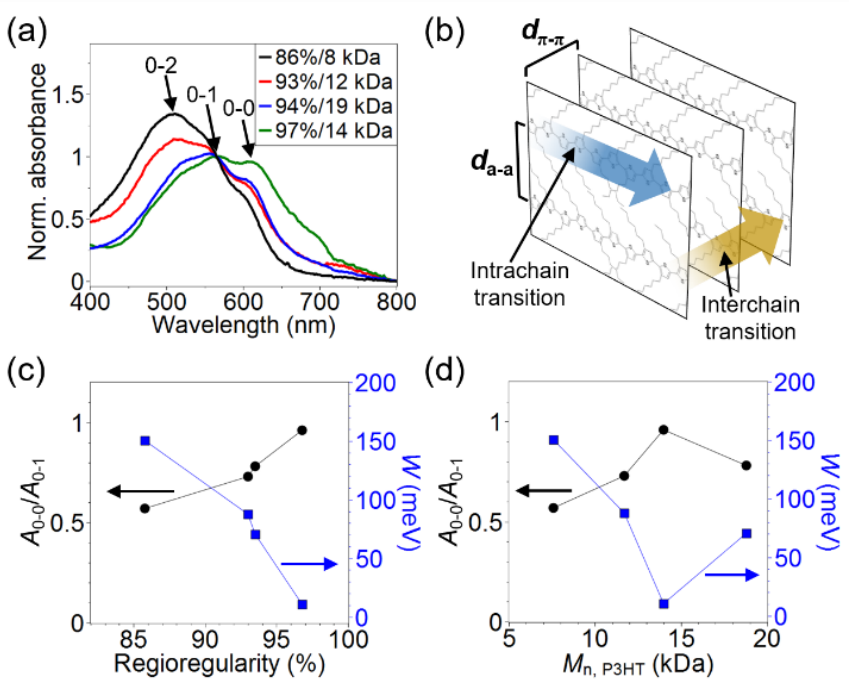

Figure 4.7 (a) Representative UV-vis absorption spectra of dried P3HT-*b*-PEO dispersions on glass. (b) A schematic diagram of P3HT chain packing conformation and competitive charge transports (intrachain vs. interchain). (c) The ratio of the 0-0 and 0-1 peak absorbance ($A_{0\text{-}0}/A_{0\text{-}1}$) and exciton bandwidth (W) as a function of regioregularity. (d) $A_{0\text{-}0}/A_{0\text{-}1}$ and W as a function of molecular weight.

To further understand P3HT chain conformation, we used HJ-aggregate model developed by Spano and co-workers.[266, 267] The HJ-aggregate model clarifies the competitive effects of interchain (H-like aggregate) vs. intrachain (J-like aggregate) transition, which are governed by the polymer chain conformation; thus, the HJ-aggregate model allows for insights in both the charge transport directions within the polymer aggregates and the polymer chain conformation. Typically, J-like aggregate is desirable because intrachain charge transport along polymer backbone is two orders of magnitude faster than interchain charge transport through the π-π

interaction packing direction.[99, 268, 269] Generally, P3HT aggregate shows three distinct absorption peaks at 612 nm, 562 nm, and 512 nm, indicating intrachain transition (0-0 transition) and interchain transitions (0-1 transition and 0-2 transition).[270, 271, 272, 273] The intensity ratio of A_{0-0}/A_{0-1} identifies the interchain and intrachain transitions:[266, 267]

$$A_{0-0}/A_{0-1} = \left[(1 - 0.24\ W/E_p)/(1 + 0.073\ W/E_p)\right]^2$$

where $A_{0\text{-}0}/A_{0\text{-}1}$ is the intensity ratio of the 0-0 and 0-1 peak absorption, W is exciton bandwidth (the nearest-neighbor interchain Coulombic coupling), E_p is the C=C stretching mode energy (0.18 eV).[267, 274] Intrachain transition (J-like aggregate) exhibits A_{0-0}/A_{0-1} slightly larger than 1, while interchain transition (H-like aggregate) shows A_{0-0}/A_{0-1} in the region of $\sim 0.5-0.8$.[273, 275, 276] A_{0-0}/A_{0-1} increased as regioregularity increased (Figure 4.7c), whereas molecular weight had no trend (Figure 4.7d). The highest regioregularity P3HT-*b*-PEO (97%/14 kDa) showed intrachain transition (J-like aggregate) whereas the other P3HT-*b*-PEOs had interchain transition (H-like aggregate).

We next determined exciton bandwidth W using eq. (1). Exciton bandwidth W decreased as regioregularity increased; however, no distinct trend in molecular weight was observed. This implies that the higher regioregularity suppresses interchain transport due to the long-range intrachain order (planarity). Conversely, in the lower regioregularity, the twisted backbone interrupts intrachain transport, showing higher W.[275, 277] These suggest that regioregularity has strong impact on chain conformation.

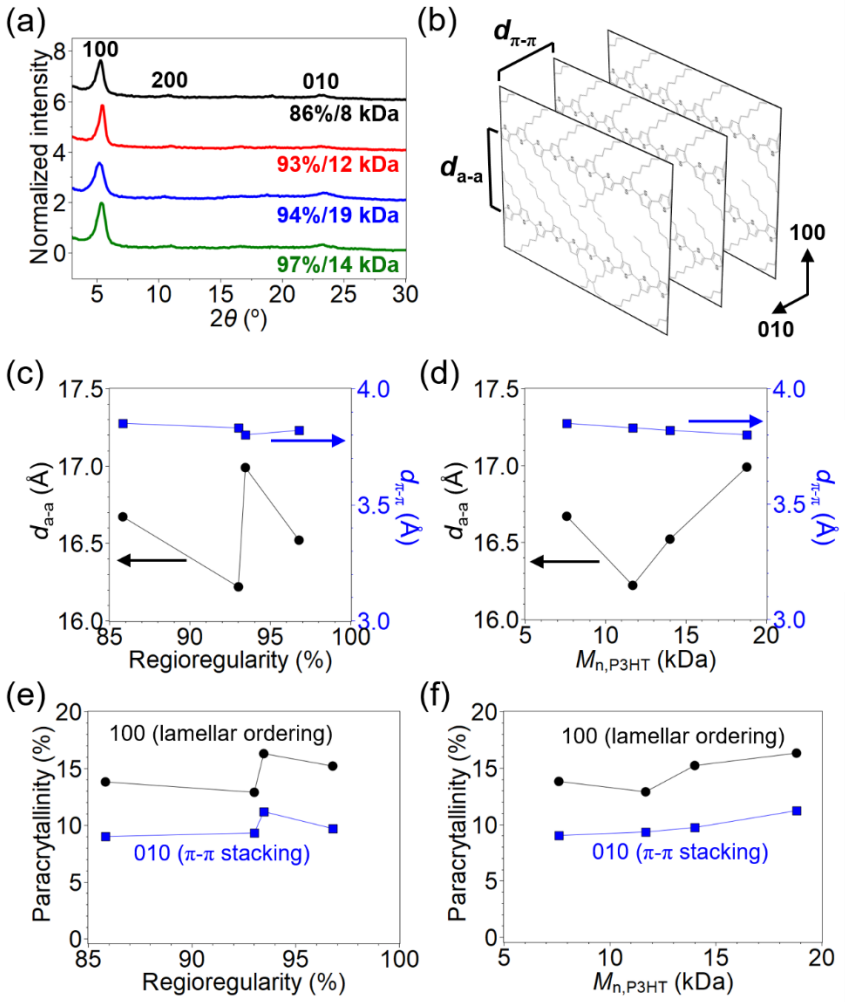

Figure 4.8 (a) X-ray diffraction (XRD) patterns of P3HT-*b*-PEO micellar aggregates. (b) A schematic diagram of crystalline region of P3HT. $d_{a\text{-}a}$ and $d_{\pi\text{-}\pi}$ are lamellar spacing and π-π stacking spacing distance, respectively. $d_{a\text{-}a}$ and $d_{\pi\text{-}\pi}$ are parallel and perpendicular to the chain backbone. (c) $d_{a\text{-}a}$ and $d_{\pi\text{-}\pi}$ as a function of regioregularity. (d) $d_{a\text{-}a}$ and $d_{\pi\text{-}\pi}$ as a function of $M_{n,P3HT}$. (e) Paracrystallinity of as a function of regioregularity. (f) Paracrystallinity of as a function of $M_{n,P3HT}$.

The influence of regioregularity and molecular weight on self-organizing structure is demonstrated with X-ray diffraction (XRD) measurements. Figure 4.8a showed P3HT

characteristic peaks, (100) peak and (010) peak—diffraction angle 2θ of 5.3° and 23.3°—indicating lamellar spacing distance ($d_{a\text{-}a}$) and π-π interaction staking distance ($d_{\pi\text{-}\pi}$) (Figure 4.8b).[95] Whereas regioregularity had no trend in chain packing distance, molecular weight had a trend (Figure 4.8c-d): as $M_{n,P3HT}$ increased, $d_{a\text{-}a}$ increased and $d_{\pi\text{-}\pi}$ decreased. The lowest molecular weight's $d_{a\text{-}a}$ is an exception probably because its lowest regioregularity induces packing hindrance (Figure 4.8d). Moreover, we quantify paracrystallinity parameter to determine degree of structural disorder in an imperfect crystallite. The paracrystallinity parameter, *g*, is a measure of the statistical deviation of local static lattice fluctuations normalized by the average lattice spacing distance:[257, 278, 279]

$$g \approx \sqrt{\Delta_q d_{hkl}}/2\pi$$

where Δ_q is the full width at half maximum (FWHM) of the diffraction peak, d_{hkl} is interplanar spacing. For reference, g = 0% for a perfect crystal, g = 5% for a moderately paracrystalline lattice, and g = 10-15% for a strongly disordered lattice (e.g., amorphous silicon dioxide glass).[278, 279] g increased with increasing molecular weight; regioregularity, however, had no trend in g. The determined g values ($g_{a\text{-}a}$ ~ 13-16% and $g_{\pi\text{-}\pi}$ ~ 9-11%) indicate the P3HT domains in the micellar aggregates are largely disordered (Figure 4.8e-f). Thus, the P3HT core domains are more accurately described as "disordered polymer aggregates" rather than as "polymer crystals". We, however, could not observe a strong correlation between XRD data and UV-vis analysis. We note that the X-ray diffraction data only reflect a minor portion (ordered, 2-8wt%) of the bulk material; its majority is quasi-ordered or even amorphous, which is supported by the DSC data. Unlike XRD, their optical properties reflect the backbone conformation and chain packing in this less-ordered matrix. This model could explain the lack of any clear correlation between the UV-vis studies and the X-ray data for our P3HT-*b*-PEO samples.

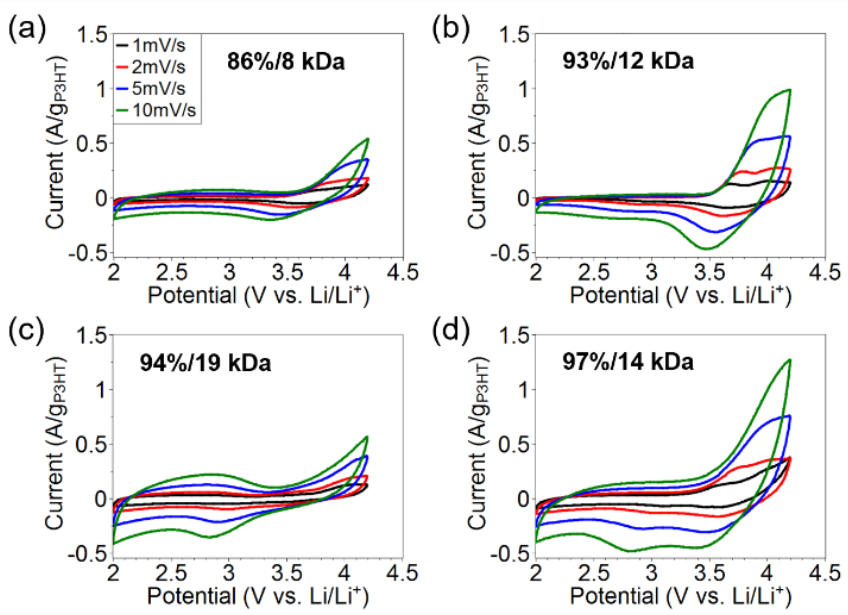

Figure 4.9 (a-d) Representative cyclic voltammetry for P3HT-*b*-PEO block copolymers at various scan rates. Sample masses of P3HT-*b*-PEOs (86%/8 kDa, 93%/12 kDa, 94%/19 kDa, and 97%/14 kDa) were 0.29mg, 0.31 mg, 0.29, and 0.31 mg, respectively. A lithium metal and 1 M LiTFSI/propylene carbonate were used as an anode and electrolyte. All currents were based on the mass of a P3HT block.

We used cyclic voltammetry to evaluate electrochemical active properties (i.e., redox reaction as shown in Figure 4.1c) of P3HT-*b*-PEO block copolymers (Figure 4.9). Relatively low regioregularity P3HT-*b*-PEO (86%/8 kDa) had a weak redox peak and rectangular shape curve at 2-3.5 V (capacitive behavior); higher regioregularity P3HT-*b*-PEOs (93%/12 kDa, 94%/19 kDa, and 97%/14 kDa) showed distinct redox peaks. The highest regioregularity P3HT-*b*-PEO (97%/14 kDa) showed two cathodic peaks (reduction) at 2.8 V and 3.4 V whereas the other P3HT-*b*-PEOs showed one cathodic peak (86%/8 kDa: 3.4V, 93%/12 kDa: 3.5 V, and 94%/19 kDa: 2.8 V). Interestingly, P3HT-*b*-PEO (93%/12 kDa) and P3HT-*b*-PEO (94%/19 kDa) which have similar

regioregularity showed different cathodic peaks (3.5 V vs 2.8 V): increasing the redox potential for the low molecular weight results from short-conjugated segments[134] supported by the blue-shifted λ_{max} in the UV-vis study (Figure 4.7a). This suggests that both regioregularity and molecular weight have significant impact on their redox properties of P3HT block.

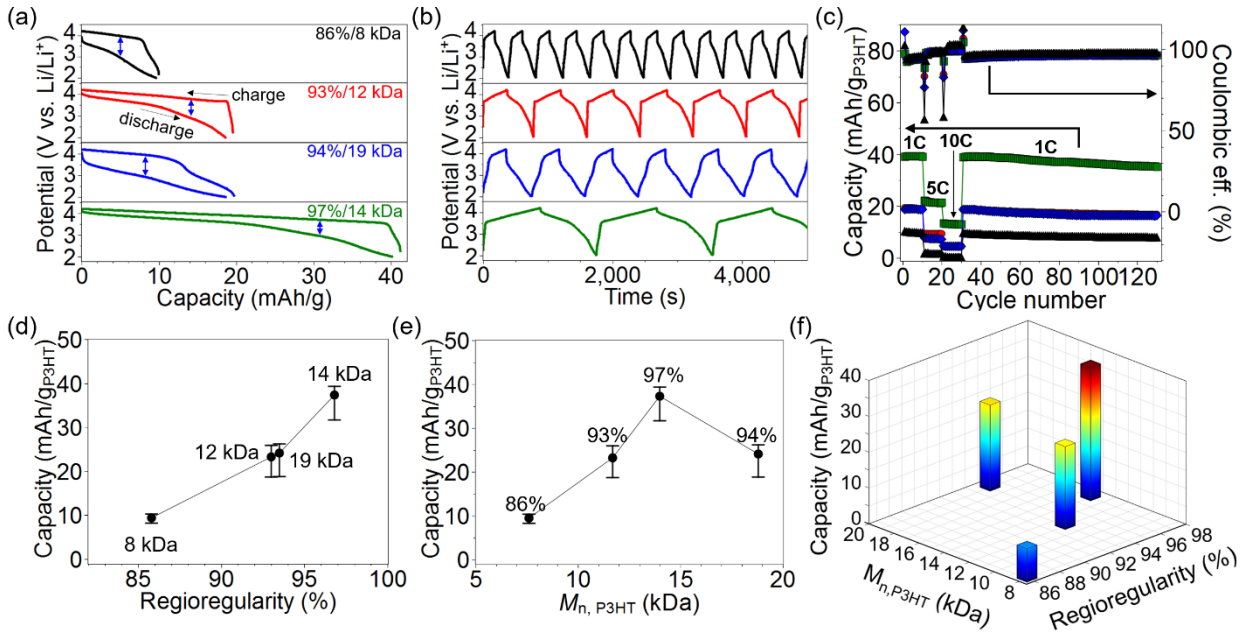

Figure 4.10 (a) Initial charge-discharge profiles of P3HT-*b*-PEO block copolymers at 1 C-rate. The double-headed arrows (blue) indicated hysteresis at 3.0 V discharge voltage. The color code applies to panels a-c. (b) Charge-discharge behaviour at 1 C-rate. (c) Representative cycling properties at various C-rates. (d) Discharge capacities as a function of regioregularity of P3HT block. C-rate was 1C. (e) Discharge capacities as a function of molecular weight of P3HT block ($M_{n,\,P3HT}$). C-rate was 1C. (f) Discharge capacities as a function of both regioregularity and $M_{n,P3HT}$. All capacities were based on a P3HT block mass. At least three samples were tested.

To evaluate the regioregularity and molecular weight effects on capacity, we conducted galvanostatic charge–discharge test of P3HT-*b*-PEOs in a lithium half-cell. Figure 4.10a-b shows galvanostatic charge–discharge profiles for P3HT-*b*-PEO block copolymers at 1 C-rate. From the discharge curve, we first calculated the specific capacities because the P3HT-*b*-PEO (97%/14 kDa) was used in a lithium ion battery electrode in our previous study. The specific capacities for P3HT-*b*-PEOs (86%/8 kDa, 93%/12 kDa, 94%/19 kDa, and 97%/14 kDa) were 10, 19, 19, and 40 mAh/g_{P3HT}, respectively. The calculated specific capacitances were 19, 35, 33, and 67 F/g, respectively (Figure 4.11). We also examined voltage hysteresis to study the redox reaction reversibility, illustrated in Figure 4.10a by the double-headed arrow (blue) at a discharge voltage of 3.0 V. The lowest regioregularity P3HT-*b*-PEO (86%/8 kDa) showed the highest voltage hysteresis (0.99 V); however, the highest regioregularity (97%) showed the lowest voltage hysteresis (0.78 V). The reduced hysteresis is beneficial to electrode performance and efficiency, demonstrating enhanced reversibility.[240, 241, 261] Figure 4.10c shows cycling properties of the P3HT-*b*-PEOs. Each sample was analysed for 10 cycles at 1 C-rate, followed by 10 cycles at 5 and 10 C-rates, and finally 100 cycles at 1 C-rate. Higher regioregularity P3HT-*b*-PEO's the specific capacity was more stable: the specific capacity of the P3HT-*b*-PEOs (86%/8 kDa, 93%/12 kDa, 94%/19 kDa, and 97%/14 kDa) retained 78, 87, 87, and 91% of the initial capacity after 130 cycles. Also, higher regioregularity P3HT-*b*-PEO resulted in higher discharge capacity at all C-rates. We plot the specific capacity as functions of regioregularity and molecular weight (Figure 4.10d-f). The specific capacity increased as regioregularity increased (Figure 4.10d), whereas molecular weight had no trend (Figure 4.10e). Figure 4.10f shows the summarized data, showing the strong effect of regioregularity on capacity clearly. This strong effect of regioregularity on capacity is because, in lower regioregularity P3HT, twisted chain conformations leads to charge localization

and charge carrier trapping,[280] resulting in poor doping efficiency and low capacity. Conversely, in higher regioregularity P3HT, planar backbone conformations delocalize polarons along P3HT backbones and minimize charge carrier trapping,[280] resulting in high doping efficiency and high capacity.

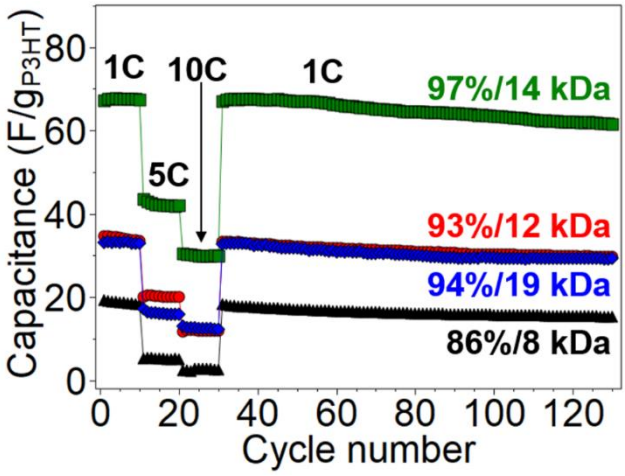

Figure 4.11 Specific capacitance of P3HT-*b*-PEOs as a function of galvanostatic charge-discharge cycles at various C-rates.

Next, we determined the doping level of P3HT blocks from a ratio of experimental capacity to theoretical capacity (i.e., 159 mAh/g) (Table 2). The doping levels for P3HT-*b*-PEOs (86%/8 kDa, 93%/12 kDa, 94%/19 kDa, and 97%/14 kDa) were 0.06, 0.15, 0.15, and 0.23, respectively. The achieved highest doping level (0.23) in this study was comparable with reported doping levels of poly(thiophene)s and poly(alkylthiophene).[126, 281, 282, 283] Other conjugated polymers such as poly(aniline) showed higher doping levels (0.3~0.5).[27] Therefore, increasing doping level is still challenging and future studies should explore how to increase doping level (over 0.5) to make P3HT more promising for energy storage applications.

4.4 CONCLUSIONS

We demonstrated the strong effects of regioregularity and molecular weight of P3HT block in P3HT-*b*-PEO on molecular conformation and electrochemical properties (i.e., redox property, capacity) by comparing four different P3HT-*b*-PEO block copolymers—different regioregularity (86-97%) and molecular weight (8-19 kDa) of P3HT block while the PEO block was kept the same (7 kDa). The specific capacity of P3HT-*b*-PEOs significantly increased with increasing regioregularity. The redox potential increased with decreasing molecular weight and the redox current response decreased with decreasing regioregularity. The changes in capacity and redox properties are accompanied by P3HT's degree of backbone conformation, backbone planarity and chain packing structure. The new insights obtained here may bridge the gap between conjugated polymer properties and their energy storage performance.

CHAPTER V

SURFACE-AGNOSTIC HIGHLY STRETCHABLE AND BENDABLE CONDUCTIVE MXENE MULTILAYERS*

5.1 INTRODUCTION

Stretchable, bendable, and foldable electronics are powerful enablers for emerging technologies such as adaptive displays, artificial skin, and wearable devices [4, 5, 6, 7, 8]. This brings the unique requirement of merging electronic performance with mechanical functionality. In this arena, graphene, carbon nanotubes, and metal nanowires have been explored, but it remains difficult to comprehensively address the disparate mechanical deformation modes of stretching, bending, and twisting while maintaining acceptable electronic conductivity. Further, it is desired to engineer conductivity into a variety of unconventional surfaces (cloth, fiber, plastic), but this is hindered by the need for harsh post-treatments to activate the conductive media (i.e. graphene) that may damage the underlying substrate. With the advent of water-processable two-dimensional MXene nanosheets [135], we hypothesized that these challenges could be met to demonstrate surface-agnostic conductive coatings on flexible and stretchable media.

Two-dimensional metal carbides (referred to as MXenes) are very promising candidates for these applications because of their metallic-like conductivity (ca. 2×10^5 S/m or sheet resistance of 1×10^{-3} kΩ/sq) [284]. MXenes have the chemical formula $M_{n+1}X_nT_x$, and consist of an

*Reprinted with permission from "Surface-agonistic highly stretchable and bendable conductive MXene multilayers" by Hyosung An, Touseef Habib, Smit Shah, Huili Gao, Miladin Radovic, Micah J. Green, and Jodie L. Lutkenhaus, *Sci. Adv.* **2018**, 4 (3), eaaq0118. Copyright 2018 The American Association for the Advancement of Science.

early transitional metal (M), carbon or nitrogen (X), and surface terminal groups (T) such as -F, -OH, -O, etc., where "x" denotes the number of terminal groups while "n" can be any number from 1-3. Using vacuum filtration, the Gogotsi group demonstrated conductive MXene papers with a modulus of 3.5 GPa and ultimate strain of 1% [153]. A polymer may be added to the MXene papers to enhance mechanical robustness [153, 154, 155]. While extremely promising, these MXene papers were not stretchable and their integration into complex surfaces (such as fabric) was not demonstrated.

5.2 EXPERIMENTAL METHOD

Materials. Poly(diallyldimethylammonium chloride) (PDAC, Mw = 200 000–350 000 g/mol, 20 wt% in water), linear poly(ethyleneimine) (Mw = 50,000 g/mol), hydrochloric acid (HCl, ACS reagent, 37% w/w), and dimethyl sulfoxide (DMSO, ReagentPlus, >99.5%) were purchased from Sigma-Aldrich. Ti (44 μm average particle size, 99.5% purity), Al (44 μm average particle size, 99.5% purity), TiC powders (2 – 3 μm average particle size, 99.5% purity), lithium fluoride (LiF, 98+% purity) were purchased from Alfa Aesar. Substrates for layer-by-layer (LbL) deposition included slide glass (VWR), indium-tin oxide (ITO)-coated glass (resistance < 20 ohm/sq, Delta Technologies), In_2O_3/Au/Au-coated PET (R < 10 ohm/sq, Delta Technologies), nylon fiber (Artiste), PDMS (Sylgard 184, Dow Corning) and PET (Melinex ST505, Tekra).

Synthesis of Ti_3AlC_2 MAX phase. Commercial Ti, Al and TiC powders were used as starting raw materials to synthesize Ti_3AlC_2 MAX phase. To prepare homogeneous powder mixtures, Ti, Al and TiC powders were first weighed to achieve Ti:Al:C=3.0:1.2:1.8 ratio and mixed together using ball-milling with zirconia beads in a glass jar at the speed of 300 rpm for 24 hours [285]. Then, the bulk high-purity Ti_3AlC_2 samples were sintered at temperature of 1510 °C for

15 mins with a loading of 50 MPa using Pulsed Electric Current System (PECS). To fabricate high-purity Ti_3AlC_2 powder, the PECSed sample was first drill-milled and sieved to obtain powder with particle sizes below 44 μm.

Synthesis of $Ti_3C_2T_x$ MXene clay. $Ti_3C_2T_x$ MXene clay was synthesized by etching aluminum from the MAX phase using the technique described by Ghidiu et.al . Concentrated HCl (37% w/w) was diluted with deionized (DI) water to obtain 30 mL of 6 M HCl solution. This solution was transferred to a polypropylene (PP) beaker and 1.98 gm of LiF was added to it. This dispersion was stirred for 5 minutes using a Teflon (PTFE) magnetic stirrer at room temperature. Ti_3AlC_2 MAX phase powder was slowly added to the HCl+LiF solution to prevent overheating as the reaction is highly exothermic. The PP beaker was capped to prevent evaporation of water and a hole was made in the cap to avoid buildup of gases. The reaction mixture was stirred at 40 ºC for about 45 hours. The slurry product was filtered and washed with DI water in a polyvinyl-difluoride (PVDF) filtration unit with pore size of 0.22 μm (Millipore® SCGVU10RE Stericup™ GV) to remove the unreacted HF and water soluble salts. This washing process was repeated until the pH of the filtrate reached a value of about 6. Reaction product collected over the PVDF filter was extracted as $Ti_3C_2T_x$ MXene clay.

Intercalation and delamination of $Ti_3C_2T_x$ MXene clay. $Ti_3C_2T_x$ MXene clay was intercalated with DMSO and subsequently bath sonicated to obtain an aqueous dispersion of delaminated $Ti_3C_2T_x$ MXenes. DMSO was added to $Ti_3C_2T_x$ MXene clay (dried in vacuum oven for about 24 hours at 40 °C) to form a 60 mg/ml suspension followed by about 18 hours of stirring at room temperature. After intercalation, excess DMSO was removed by several cycles of washing with DI water and centrifugation at 5000 rpm for 4 hours. The intercalated $Ti_3C_2T_x$ MXene suspension in DI water was bath sonicated for 1 hour at room temperature followed by

centrifugation at 3500 rpm for 1 hour to separate the heavier components. The supernatant contained the stable $Ti_3C_2T_x$ nanosheet dispersion.

Preparation of dip-assisted MXene-based multilayers. Multilayers were deposited at the surface of various substrates, slide glass, ITO-coated glass, pure PET, In_2O_3/Au/Au-coated PET, PDMS, and nylon fiber. The PDAC and MXene sheets were diluted to a concentration of 1.0 mg/ml in deionized water (18.2 MOhm). The pH values of the PDAC solution and MXene dispersion were 5.00 and 5.03, respectively and both solutions were used without adjusting the pH. For PDAC/MXene LbL film on bare glass, slide glass was cut into 1.25 cm × 5.00 cm and then cleaned by sequential sonication in isopropyl alcohol, water, and acetone for 15 min in each. After washing, the glass was dried with nitrogen. Plasma treatment (Harrick PDC-32G) was conducted for 5 min. Plasma treated glass substrates were immersed in PDAC solution for 15 min, and rinsed with deionized water for 2, 1, and 1 min each. Then, the substrates were immersed in MXene dispersion for 15 min, and rinsed with deionized water for 2, 1, and 1 min each. The same procedure was repeated until the desired thickness was obtained. For deposition onto ITO glass and PDMS, all procedures were identical. For LbL deposition onto pure PET, In_2O_3/Au/Au-coated PET, and nylon fiber, isopropyl alcohol and water were used to clean the substrates, while all other processing steps were the same is in the case of deposition on slide glass. For mechanical-electrical tests, the films were cut into 50 mm × 3.15 mm.

Preparation of spray-assisted MXene-based multilayers. The identical PDAC and MXene solution-dispersions were used for spray-assisted LbL deposition. A slide glass was cut into 1.25 cm × 1.25 cm. Cleaning and drying process were identical to those used in the dip-assisted method. Plasma treatment (Harrick PDC-32G) was conducted for 5 min. One layer of linear poly(ethyleneimine) was deposited by immersing substrates into the 1 mg/ml

poly(ethyleneimine) solution for 1 min, followed by rinsing with DI water three times. After washing, the glass was dried with nitrogen. PDAC solution was sprayed onto the substrates for 5 s at a flow rate of 0.4 ml/s, followed by spraying of deionized water for 20 s. Air was blown for 30 sec. Subsequently, MXene dispersion was sprayed for 5 s at a flow rate of 0.4 ml/s, followed by spraying of deionized water for 20 s. Air was blown for 30 sec. The procedure was repeated until the desired number of layer pairs was obtained.

Preparation of U-shaped patterned PDAC/MXene multilayers. To make a U-shaped pattern, a 1 mm wide tape was put on PET substrate prior to LbL assembly. After LbL coating, the tape was removed. Other procedures were identical to the dip-assisted LbL preparation.

Characterization. Transmission electron microscope (TEM, FEI Tecnai F20) was used to investigate morphologies of the Ti_3C_2 MXene nanosheet. The Ti_3C_2 MXene dispersion was diluted down to 0.01 mg/ml. Then a portion of the dispersion was collected in a dropper and poured onto a holey carbon grid. The grid was allowed to dry in air before it was examined under TEM. Scanning electron microscopy (SEM, JEOL JSM-7500F) was used to investigate morphologies of the multilayer films. A 3 nm of platinum/palladium alloy was sputter-coated onto samples prior to imaging. Profilometry (P-6, KLA-Tencor) was used to measure the thickness of the MXene-based multilayers. The thickness was measured in at least five different locations. The mass of the multilayer was measured using quartz crystal microbalance (QCM). First, plasma treatment was carried out on a 5 MHz Ti/Au quartz crystal for 5 min. The multilayer was deposited onto the quartz crystal using the LbL assembly procedure described above. The composition of the multilayer was determined by monitoring the frequency changes during each layer deposition from 10 to 15 layer pairs. Mass was calculated from the measured frequency using the Sauerbrey equation. UV-vis spectroscopy was conducted using a Shimadzu UV-2401 PC spectrometer over

a wavelength range of 300-900 nm. X-ray photoelectron spectroscopy (XPS) was performed using Mg Kα X-ray (energy source of 1253.6 eV) and a charge neutralizer (Omicron CN10). For the survey scan, a pass energy of 100 eV and energy step size of -1.0 eV were used. A linear-type background subtraction was used to the photoemission lines. A manual four-point resistivity probe (Lucas Labs S-302-4) was used to measure and calculate the conductivity of the multilayer. Multimeter (Velleman DVM890F) was used to measure the resistance under various deformations (bending, stretching, twisting, and folding). Attenuated total reflection Fourier transformation infrared (ATR FT-IR) spectroscopy (Nicolet 6700 FT-IR ATR, Thermo Scientific) was utilized with a germanium crystal. The IR spectra were obtained at a wavenumber range of 650–4000 cm^{-1} at a resolution of 1 cm^{-1}. Mechanical-electrical property characterization of the multilayer was performed on a homemade actuating tester. A multimeter (Velleman DVM890F) was used to measure the resistance of the LbL films.

Fabrication of an object scanner. 5-layer pair multilayers (50 mm × 3.15 mm) with U-shaped patterning were used. Copper wires were connected to both ends of the U-shaped patterned LbL film using silver paste. The object scanner was fixed between two metal frames with Kapton tape (VWR) for electrical insulation. For object scanning, the copper wires were connected to multimeter.

Fabrication of a human motion sensor. 20-layer pair multilayers (30 mm × 3.15 mm) was used. Aluminum ribbons were connected to both ends of the multilayer using an electrical tape (VWR). The human motion sensor was fixed on a finger using electrical tape. For human motion sensing, the aluminum ribbons of the sensors were connected to the multimeter.

5.3 RESULTS AND DISCUSSION

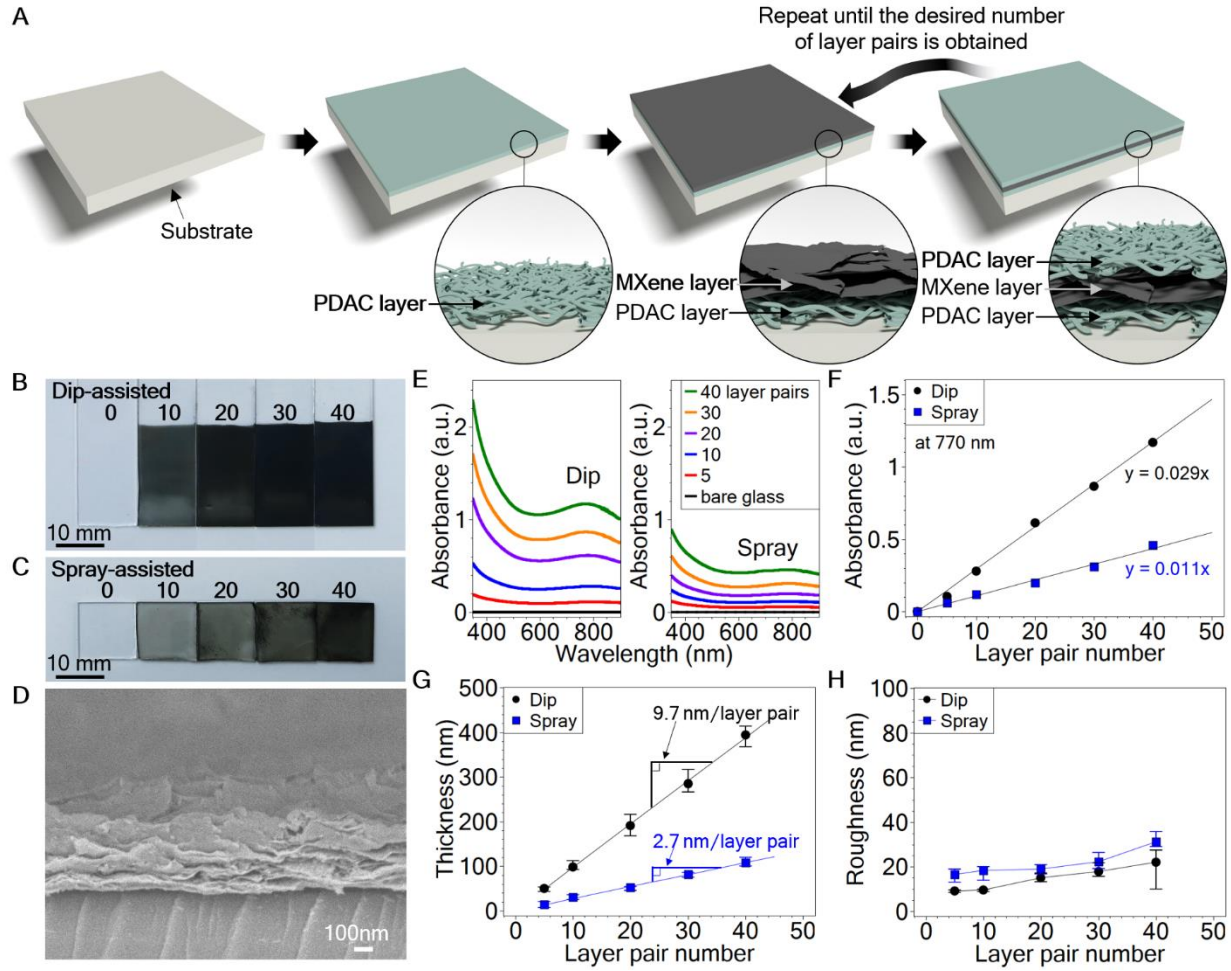

Figure 5.1 Structural and morphological characterizations of MXene multilayers. (a) Schematic of the PDAC/MXene layer-by-layer assembly process. Images of (b) immersion and (c) spray-assembly of multilayer coatings of varying number of layer pairs on glass. (d) A cross-sectional scanning electron microscope image of the multilayer coating. (e) UV-vis spectra of MXene multilayers on glass. (f) Absorbance values at 770 nm *vs.* number of layer pairs. (g) Growth profile of the multilayers on glass. (h) Root-mean-square roughness *vs.* number of layer pairs.

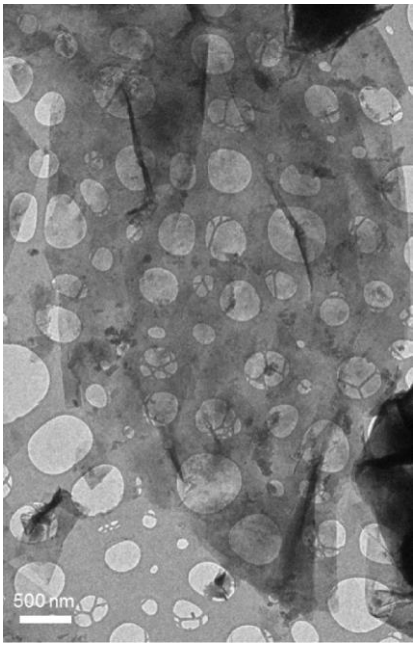

Figure 5.2 TEM image of a Ti_3C_2 MXene nanosheet on a perforated carbon grid. The nanosheet is several microns wide.

We produced conductive, stretchable, bendable, surface-agnostic MXene coatings through the sequential adsorption of negatively charged MXene sheets and positively charged polyelectrolytes using an aqueous assembly process known as layer-by-layer (LbL) assembly (Figure 5.1a)[177, 286, 287]. In this study, we used $Ti_3C_2T_x$ nanosheets, derived from the parent Ti_3AlC_2 MAX phase [288]. This type of MXene has been utilized in applications ranging from water desalination to catalysis [152, 289, 290]. MXene sheets in a stable aqueous dispersion at pH = 5 had a negative charge (-32 mV by zeta potential). A transmission electron microscopy (TEM) image of a drop-cast MXene nanosheet showed a slightly wrinkled morphology and a lateral size of the of several microns (Figure 5.2) [291]. The complementary species chosen for LbL assembly was poly(diallyldimethylammonium chloride) (PDAC) because of its positive charge (+18 mV by zeta potential).

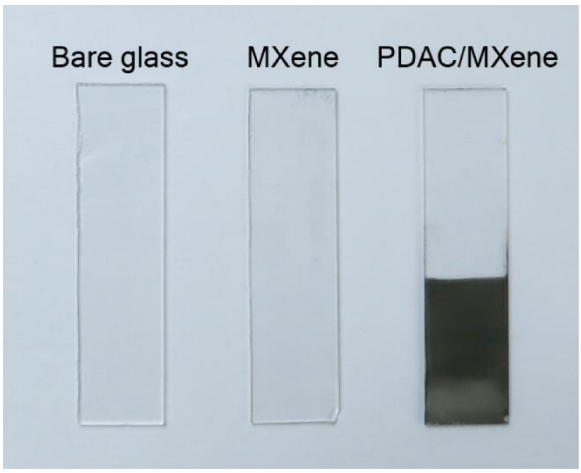

Figure 5.3 Digital images of (left) bare glass, (middle) the result of LbL assembly using only MXene sheets (without PDAC solution), (right) 10-layer pair MXene/PDAC multilayer coating. There was no observable growth for the LbL assembly with only the MXene sheet dispersion.

The MXene multilayers were first assembled either by alternate immersion (Figure 5.1b) or spraying (Figure 5.1c) of the two components onto glass. The color of the coating, which arises from the MXene nanosheets, became successively darker as the number of layer pairs or LbL cycles increased from 0 to 40. This confirms that MXenes may be directly incorporated into multilayer coatings with PDAC using electrostatic interactions. In contrast, when the PDAC adsorption step was removed from the assembly process, no MXene deposition was observed (Figure 5.3). Further, the MXene multilayer exhibited strong mechanical integrity during tape adhesion tests, whereas a comparable drop-cast MXene film did not (Figure 5.4). This result further emphasizes the influence of the attractive electrostatic interactions to the multilayer coating's good adhesion to the underlying surface.

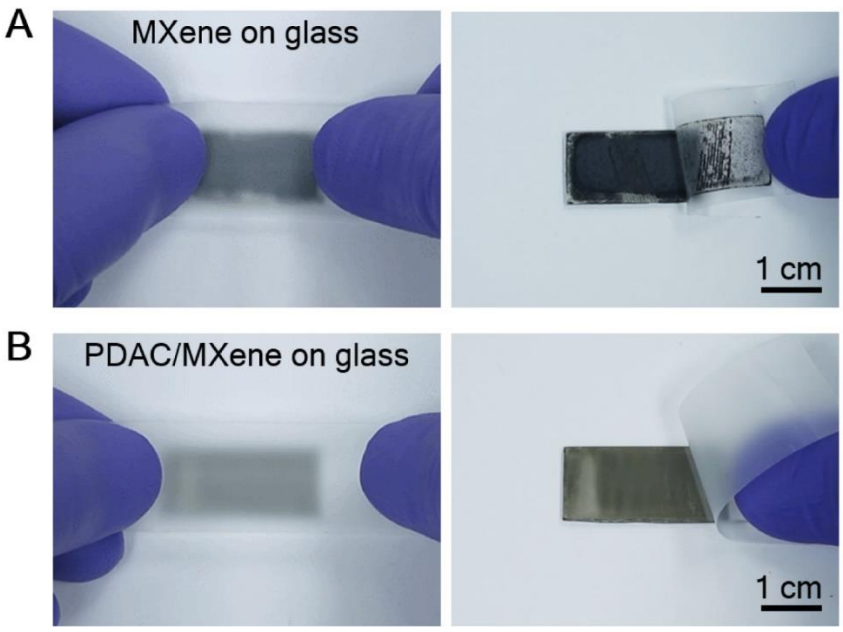

Figure 5.4 Digital images of adhesion testing with 3M Scotch tape on (a) drop-cast MXene sheets and (b) a MXene-based multilayer coating on glass substrates. The adhesion tests were carried out by strongly attaching the tape, and subsequently peeling it off. The drop-cast MXene sheets showed very poor adhesion, and the multilayer showed excellent adhesion.

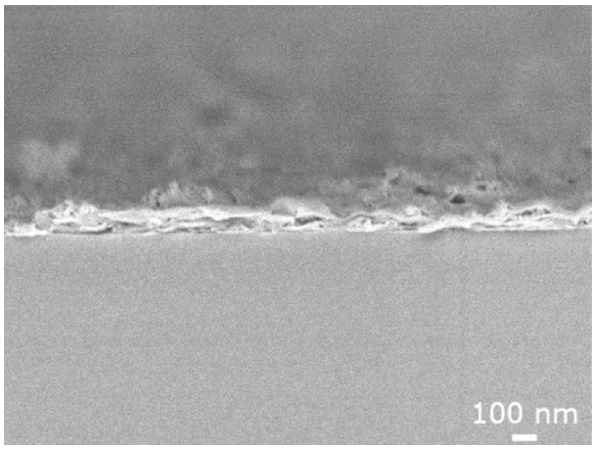

Figure 5.5 cross-sectional SEM image of the MXene multilayer prepared by spray-assisted LbL assembly on glass.

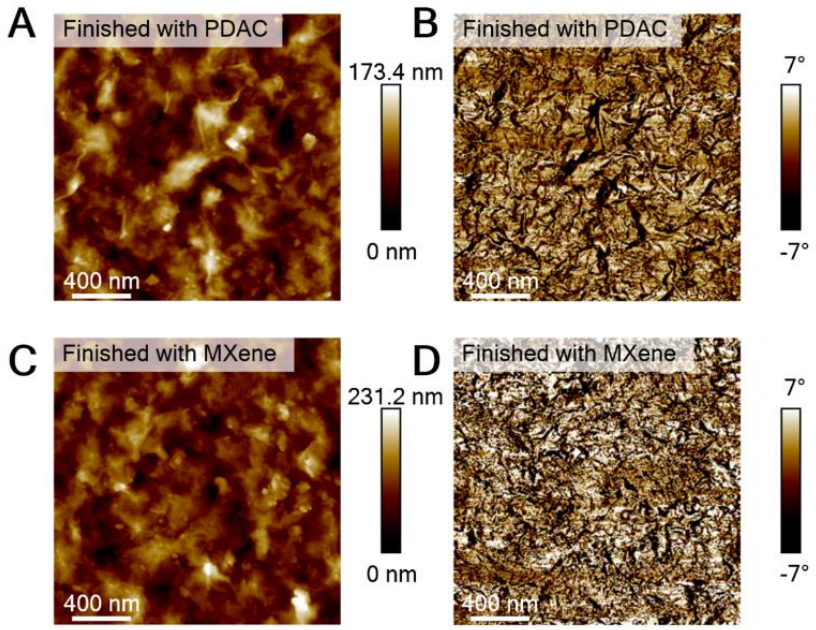

Figure 5.6 AFM height and phase images (2 μm × 2 μm) of (a, b) a $(PDAC/MXene)_{50.5}$ LbL film finished with PDAC and (c, d) a $(PDAC/MXene)_{50}$ LbL film finished with MXene.

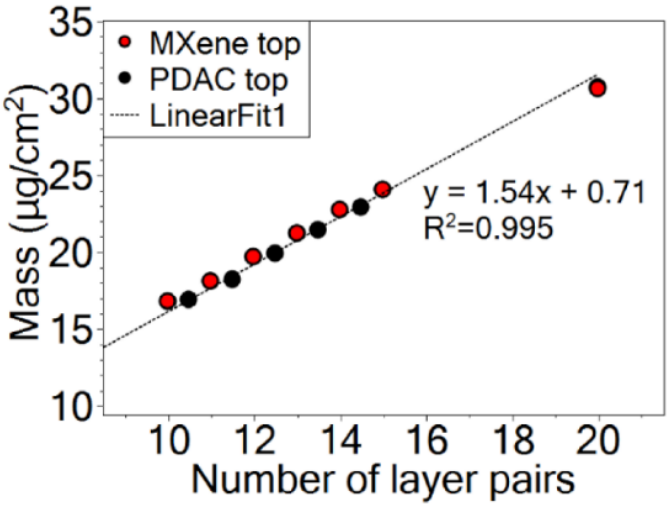

Figure 5.7 Thickness of the multilayers as a function of the number of layer pairs. Mass change was measured using QCM and the Sauerbrey equation. Average increases in mass for PDAC and MXene were 10.0 wt% and 90.0 wt%, respectively.

The structure and morphology of the multilayer coating was next examined. Scanning electron microscopy (SEM) and tapping-mode atomic force microcopy (AFM) verified dense coverage of the MXene nanosheets on the surface, as well as a nacre-like brick-and-mortar cross-section, (Figure 5.1D, 5.5 and 5.6). Figure 5.6 shows tapping-mode AFM height and phase images of the MXene multilayer on glass. Both multilayers that were finished with MXene as the last layer and PDAC as the last layer possessed similar surface morphologies. RMS roughness values measured by profilometry of PDAC on top (25 ± 2 nm) and MXene on top (29 ± 3 nm) coatings were similar. In the AFM phase images (Figure 5.6B and 5.6D), the MXene-finished multilayer showed a higher phase angle (brighter color) than the PDAC-finished multilayer because MXene sheets are more rigid. The subscripts 50 and 50.5 refer to the number of layer pairs.

For a 40-layer pair coating made by immersion, the thickness was 378 ± 33 nm. UV-vis spectroscopy, profilometry, and quartz crystal microbalance (QCM) measurements were conducted to assess the growth behavior (Figure 5.1e-g and 5.7). The coating's UV-vis spectra demonstrate broad adsorption at 770 nm, consistent with MXene nanosheets [150, 151]. The adsorption at 770 nm increased linearly with the number of layer pairs (Figure 5.1e and 5.1f), which is consistent with the linear increase in film thickness (9.7 nm/layer pair for immersion and 2.7 nm/layer pair for spraying, Figure 5.1g). QCM also confirmed linear growth and yielded a coating composition of 90 wt% MXene and 10 wt% PDAC (Figure 5.7). Assuming that the average thickness of a MXene sheet is ~1 nm [292] and that the coated polymer's contribution to thickness is negligible, then each MXene adsorption step deposits 10 layers of MXene nanosheets. The root-mean-square (RMS) roughness measured using profilometry was consistently less than 40 nm (Figure 5.1h). Attenuated total reflection Fourier transform infrared (ATR-FTIR) spectroscopy and X-ray photoelectron spectroscopy (XPS) studies support the successful growth of the MXene

multilayer (Figure 5.8 and 5.9, and Table 5.1), which displayed characteristic features of both PDAC and MXene sheets. Figure 5.10 shows X-ray powder diffraction (XRD) plots of freeze-dried Ti_3C_2 MXene nanosheets and a MXene multilayer coating prepared on glass. In Figure 5.10a, the peak at around 7˚ corresponds to MXene Ti_3C_2 nanosheets (as distinct from the parent MAX phase), in agreement with prior studies *(19)*. This peak shifted to 11˚ and broadened significantly in the multilayer (Figure 5.10b). XRD analysis shows a decrease in MXene sheet spacing upon inclusion in the multilayer (Figure 5.10).

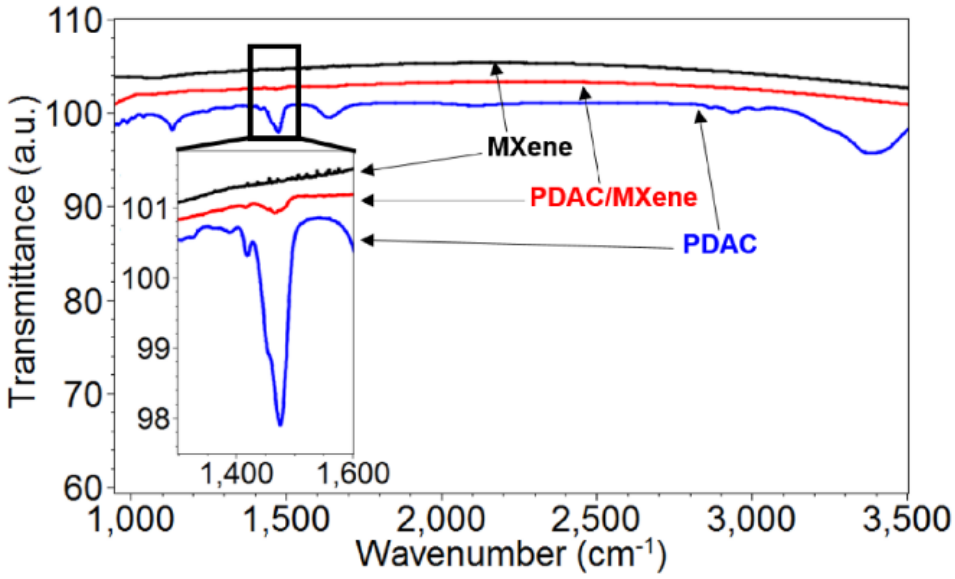

Figure 5.8 ATR FTIR spectra of MXene, PDAC, and 20-layer pair MXene multilayer coating. For the multilayer, a peak appeared at 1467 cm^{-1} (CH_2 bending), indicating the presence of PDAC.

Table 5.1 Atomic composition at the surface of cast MXene sheets, $(PDAC/MXene)_{20}$ multilayer terminated with MXene, and $(PDAC/MXene)_{20.5}$ multilayer terminated with PDAC from XPS survey spectra (Figure 5.9). Calculated atomic composition of MXene multilayers obtained using both QCM and XPS data. We assume that atomic ratio of C and N of PDAC is 8:1.

	MXene	$(PDAC/MXene)_{20}$ finished with MXene	$(PDAC/MXene)_{20.5}$ finished with PDAC	Calculated (PDAC/MXene = 10:90 w/w)
C	44.5	58.1	64.0	51.7
Ti	22.8	18.0	12.6	19.0
O	25.3	20.0	18.6	21.1
F	6.9	3.0	1.8	5.8
N	0.6	0.9	3.1	2.3

* Both $(PDAC/MXene)_{20}$ and $(PDAC/MXene)_{20.5}$ multilayers have higher carbon content than that of MXene due to presence of PDAC. We calculated atomic ratio of PDAC/MXene (=10:90 w/w) composite using QCM and XPS data. We assume that atomic ratio of C and N of PDAC is 8:1. The calculation result is in good agreement with XPS data.

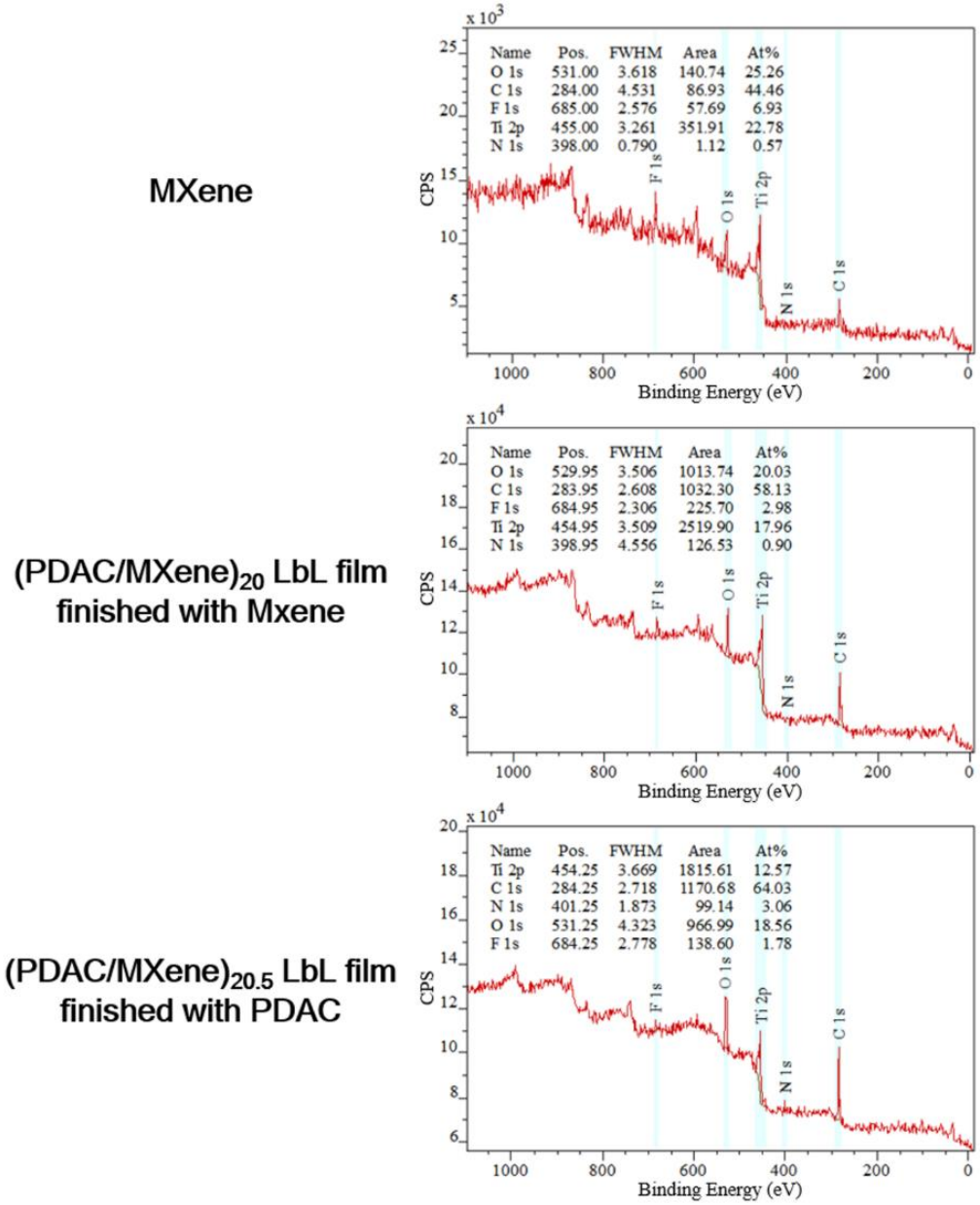

Figure 5.9 XPS survey spectra of MXene, $(PDAC/MXene)_{20}$ multilyaer finished with MXene, and $(PDAC/MXene)_{20.5}$ multilayer finished with PDAC.

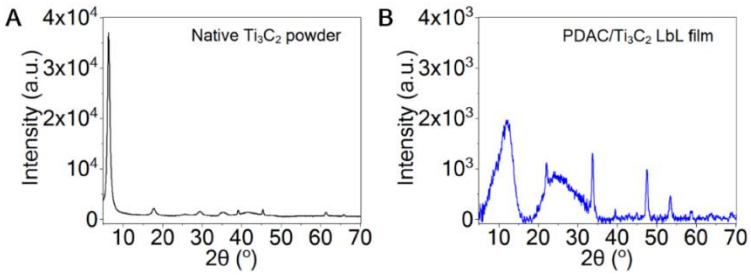

Figure 5.10 XRD of (a) freeze-dried Ti_3C_2 MXene powder and (b) a PDAC/MXene LbL film (MXene multilayer) on glass.

To demonstrate the surface-agnostic nature of the MXene multilayers, coatings were assembled by alternate immersion onto ITO-coated glass, poly(ethylene terephthalate) (PET) film, In_2O_3/Au/Ag-coated PET, kirigami-patterned PET, poly(dimethylsiloxane) (PDMS), and nylon fibers (Figure 5.11a-c). These surfaces span different chemistries (oxide, organic, hydrophilic, hydrophobic) and different geometries (flat *vs.* textured fiber). Figure 5.11a and 11b show the successful deposition of the multilayer onto all of these surfaces, which is impressive considering that this could not have been achieved by other means (e.g., vacuum filtration, dip-coating). It is also demonstrated that these coatings retain their conductive nature. Figure 5.11c shows that the nylon fiber was rendered conductive by the multilayer coating. Figure 5.11d quantifies the sheet resistance with the number of layers pairs. A 5-layer pair multilayer had a sheet resistance of 17 kΩ/sq, which decreased and stabilized to 5-8 kΩ/sq as more layer pairs were deposited. This is because more continuous pathways for charge transport developed as additional layer pairs were added. The sheet resistance values here were higher than that of pure Ti_3C_2 MXene sheets [153, 284] because of the presence of insulating PDAC in the multilayer coatings. To demonstrate conductivity, the multilayer coating on PET operated an LED even under extreme bending and folding from 180° to 0° (Figure 5.11e).

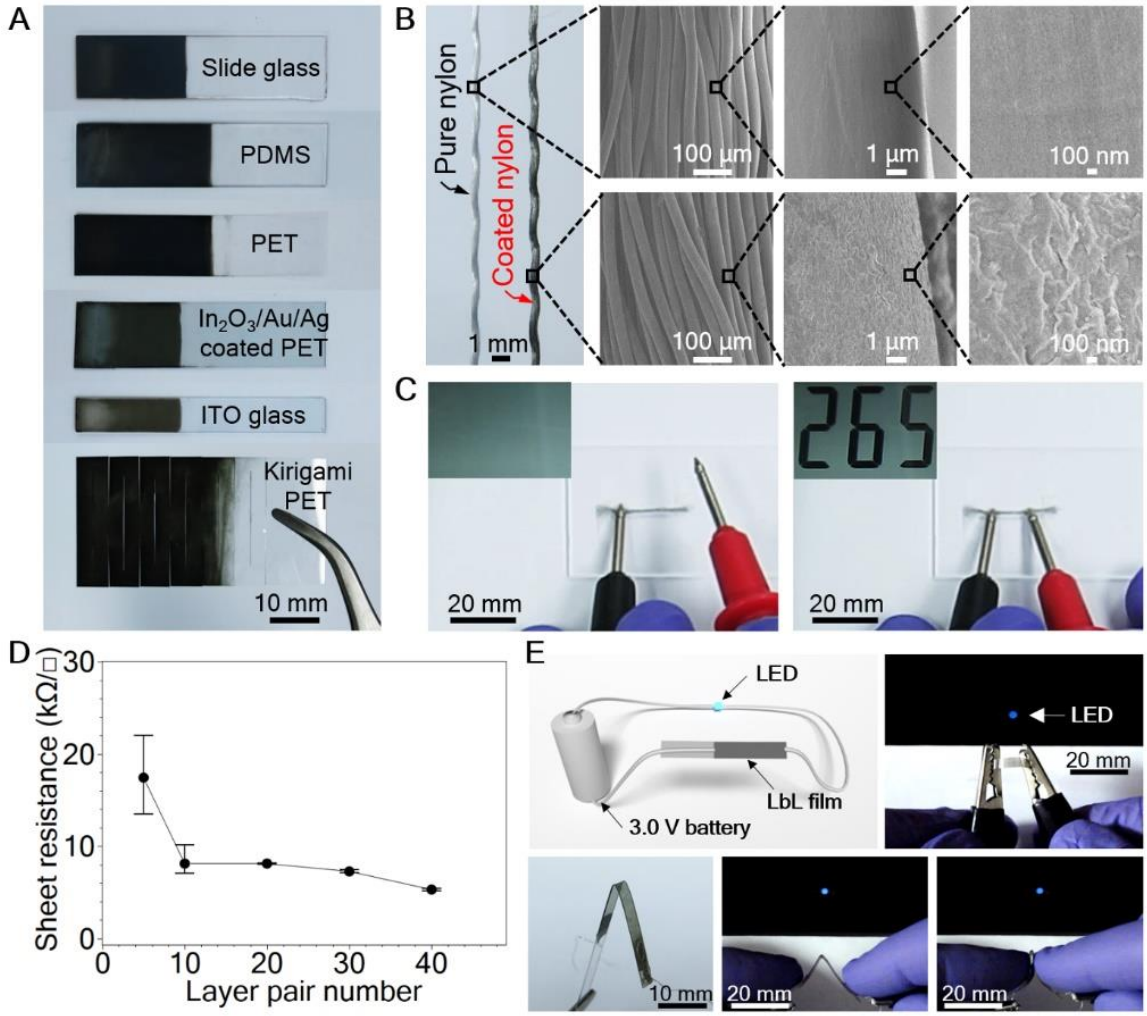

Figure 5.11 Surface-agnostic conductive coatings. (a) Digital images of 40-layer pair coatings on various substrates (sheet resistance of coatings on slide glass, PDMS, PET and kirigami PET: 7 kΩ/sq, 7 kΩ/sq, 4 kΩ/sq and 4 kΩ/sq, respectively). (b) A digital image and SEM images of bare nylon fiber and 20-layer pair coated nylon fiber. (c) Photographs to demonstrate conductive coating on nylon fiber (resistance = 26.5 MΩ). (d) Sheet resistance of the MXene multilayers on glass. (e) Schematic illustration of an electric circuit with a battery, a light emitting diode (LED), and the MXene multilayer (LbL film). Digital images to demonstrate the conductive coating on PET under bending and folding.

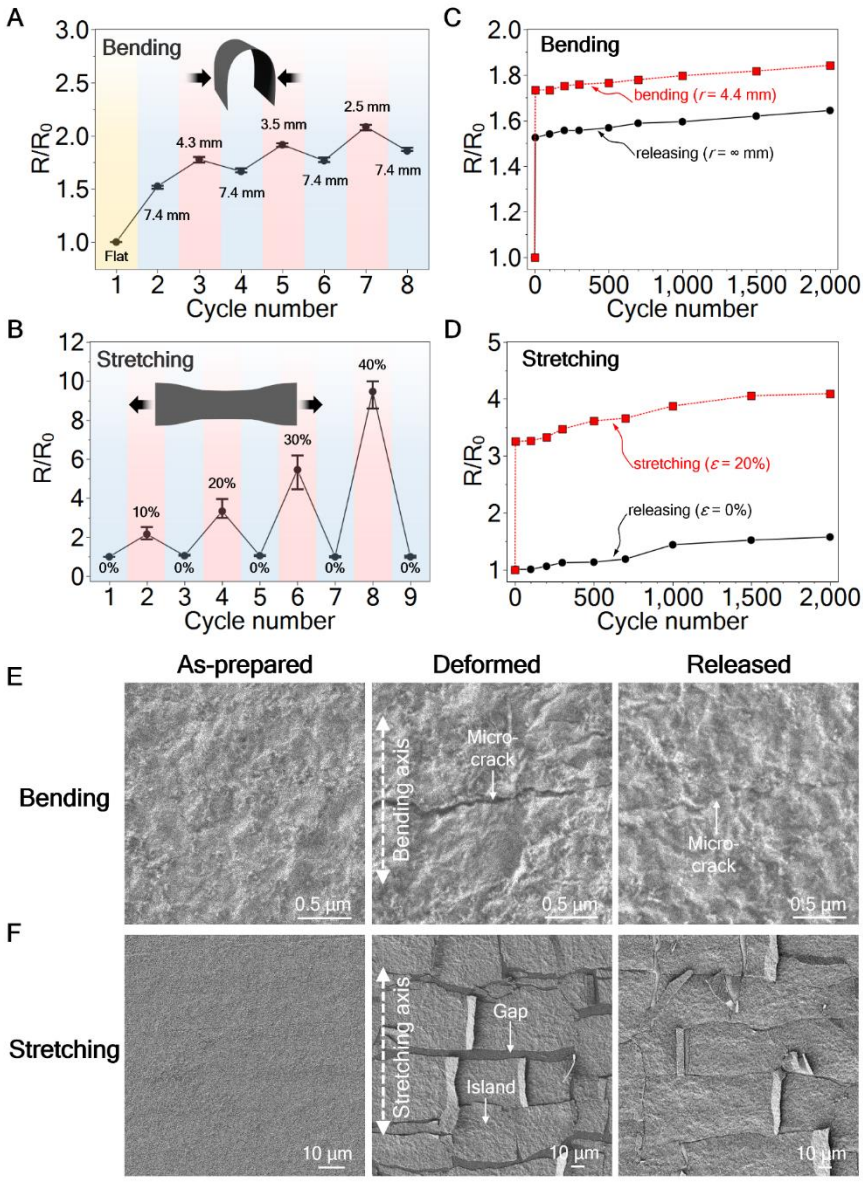

Figure 5.12 Strain sensor behavior under bending and stretching. (a) Normalized resistance (R/R_0) *vs.* bending radius for 20-layer pair MXene multilayer on PET and (b) *vs.* strain for 20-layer pair MXene multiilayer on PDMS. R_0 = 22.4 kΩ (bending) and 1.66 MΩ (stretching). Cycling performance under (c) bending and (d) stretching. SEM images of the surface structure of the 20-layer pair MXene multilayer on (e) PET (bending) and (f) PDMS (stretching). The deformed coatings on PET and PDMS are under bending (r = 4.4 mm) and stretching (ε = 20 %), respectively.

To understand the stability of resistance with mechanical cycling, both MXene-coated PET and PDMS were repeatedly bent and stretched, respectively (Figure 5.12c-d). Over the course of 2,000 cycles of bending from a radius of 4.4 mm to a flattened state, the resistance was fairly stable (increasing by 0.05% R/R_0 per cycle) (See Table 5.3 and Figure 5.15a in Supporting Information). There was some initial non-recoverable change in resistance in the first cycle, which we attribute to the initial formation of defects. We observed similar stability (0.03% R/R_0 per cycle) for MXene-coated PDMS with repeated stretching (See Table 5.4 and Figure 5.15b in Supporting Information). These MXene-based coatings endured other types of deformations, such as twisting and kirigami-stretching, reversibly responding to strain without forming large-scale visible cracks (Figure 5.16).

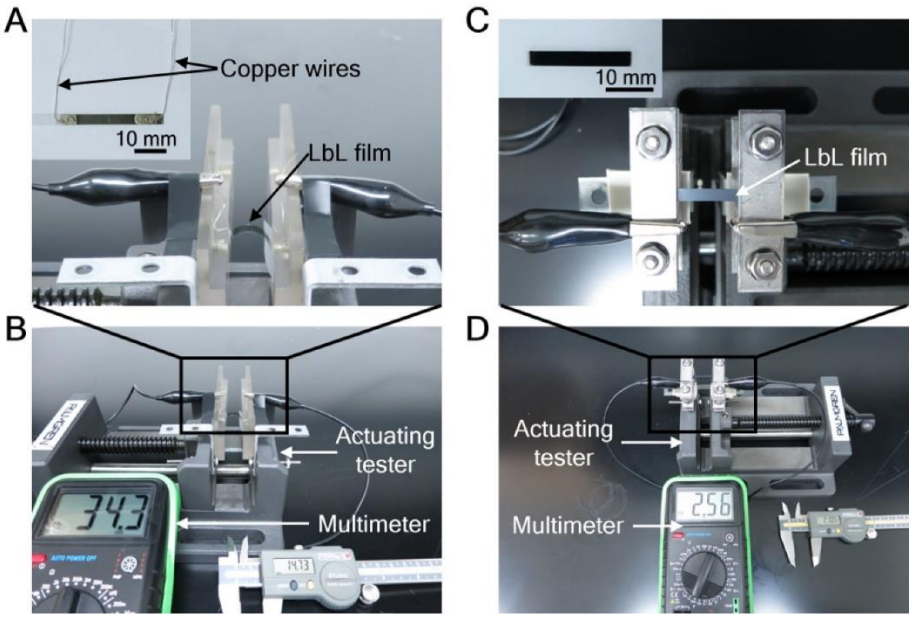

Figure 5.13 Photographs of (a, b) bending of the MXene multilayer on PET (inset of a) and (c, d) stretching of the MXene multilayer on PDMS (inset of c). For bending, copper wires were connected to both ends of the multilayer using silver paste.

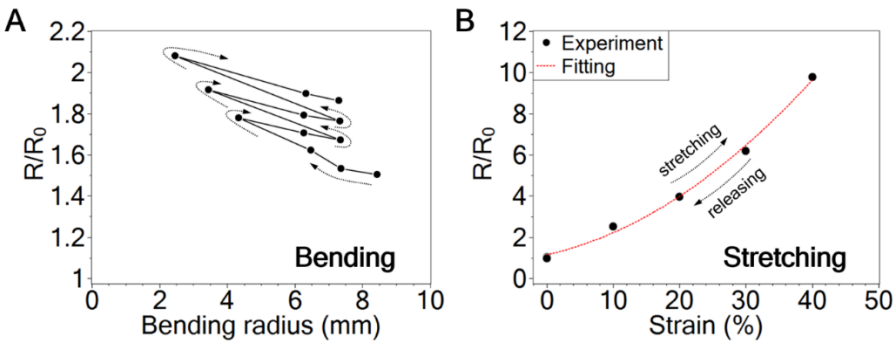

Figure 5.14 (a) Normalized resistance (R/R_0) versus bending radius for MXene multilayers on PET for multiple stages of bending at radii ranging from 8.4 mm to 2.5 mm. The resistance is normalized against the resistance of the flattened sample. (b) Normalized resistance versus strain for MXene multilayers on PDMS for multiple stages of tensile strain. R_0 = 22.4 kΩ (bending) and 1.66 MΩ (stretching).

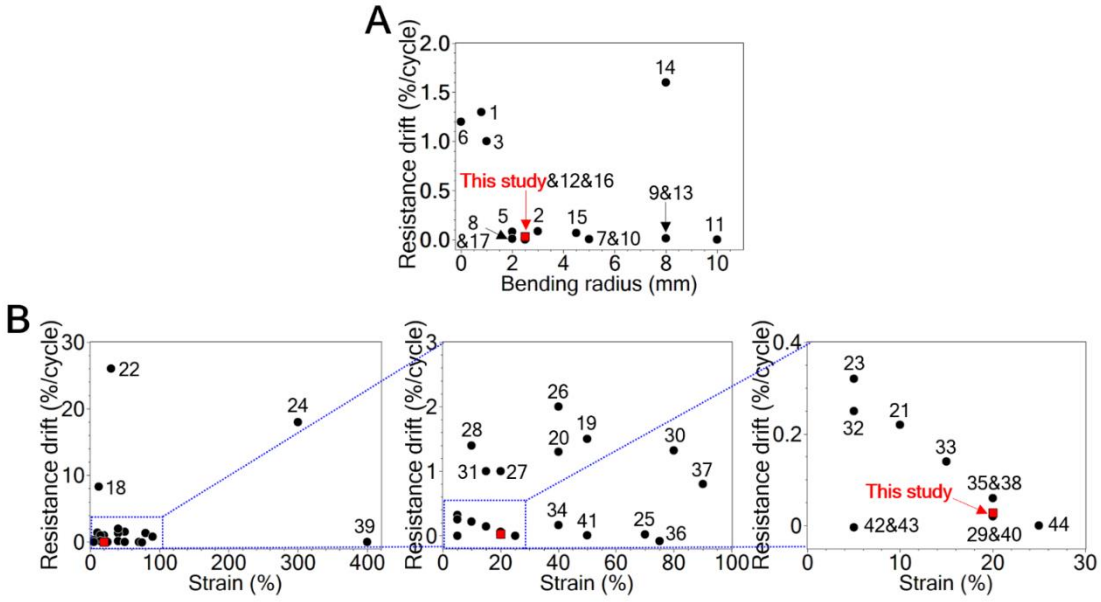

Figure 5.15 (a) Comparison of resistance drift between the bendable MXene coatings herein and other bendable conductors. (b) Comparison of resistance drift between the stretchable MXene coatings and other stretchable conductors.

As the conductive MXene multilayers can be incorporated into flexible (PET) and stretchable (PDMS) objects, we next examined how the resistance changes during extreme bending and stretching (Figure 5.13). There is a general increase in resistance upon bending to smaller radii, for which resistance doubled at a bending radius of 2.5 mm *vs.* the flattened state (Figure 5.12A and Figure 5.14a). A similar result was obtained for the case of stretching MXene-coated PDMS, where increasing tensile strain resulted in up to a 9-fold increase in resistance at 40% strain (Figure 5.12b and Figure 5.14b). This result is remarkable in that the film maintains its conductance at such extreme deformations; for comparison, MXene-based papers made by vacuum filtration cannot withstand such high strains (only 1.0%) [153]. To our knowledge, this is the one of the first reports of extremely stretchable surface agnostic MXene composites (See Table 5.2 in Supporting Information).

Table 5.2 Characteristics of flexible MXene-based films or coatings.

Sample[a)]	Substrate	Preparation method	Max. strain [%]	Max. bending radius [mm]	Sheet resistance[b)] [kΩ/sq]	Conduc-tivity [S/m]	Flexure type	Ref.
MXene	(free-standing)	Vacuum-assisted filtration (VAF)	1	-	1×10^{-3}	2×10^{5}	Rolling /folding	[153]
MXene/PVA = 90:10	(free-standing)	VAF	2	-	1×10^{-2}	2×10^{4}	Rolling /folding	[153]
MXene/PVA = 40:60	(free-standing)	VAF	4	-	2×10^{3}	4×10^{-2}	Rolling /folding	[153]
MXene/ polyacrylamide = 75:25	(free-standing)	Casting	-	-	-	3×10^{0}	N/A	[154]
MXene/PAM = 31:69	(free-standing)	Casting	-	-	-	1×10^{0}	N/A	[154]
MXene	(free-standing)	VAF	-	-	4×10^{-2}	1×10^{4}	Rolling	[293]
Mixed MXene/SWCNT = 50:50	(free-standing)	VAF	-	-	2×10^{-2}	3×10^{4}	Rolling	[293]
Sandwich-like MXene/SWCNT = 50:50	(free-standing)	VAF	-	-	1×10^{-2}	4×10^{4}	Rolling	[293]
Mixed MXene/MWCNT = 50:50	(free-standing)	VAF	-	-	3×10^{-2}	2×10^{4}	Rolling	[293]
Sandwich-like MXene/MWCNT = 50:50	(free-standing)	VAF	-	-	2×10^{-2}	2×10^{4}	Rolling	[293]
Sandwich-like MXene/onion-like carbon = 50:50	(free-standing)	VAF	-	-	6×10^{-2}	1×10^{4}	Rolling	[293]
Sandwich-like MXene/reduced graphene oxide = 50:50	(free-standing)	VAF	-	-	1×10^{-2}	4×10^{4}	Rolling	[293]
MXene[b)]	Polyester	Spray Coating	-	3.8	$1\sim8\times10^{0}$	6×10^{3}	Bending	[151]
MXene	Polyether-imide	Spin coating	-	5.1	1×10^{0}	7×10^{5}	Bending	[144]
MXene/PDAC multilayers = 90:10	PDMS[c)]	Layer-by-layer coating	50	-	5×10^{0}	2×10^{3}	Stretching	This study
MXene/PDAC multilayers = 90:10	PET[d)]	Layer-by-layer coating	-	2.5	5×10^{0}	2×10^{3}	Bending	This study

[a)]Based on weight ratio; [b)]Sheet resistance was calculated using Sheet resisatance [ohm sq^{-1}] = 1/(conductivity [S m^{-1}] × thickness [m]) where sq is unitless; [c)]Polyethylene terephthalate; and [d)]Polydimethylsiloxane.

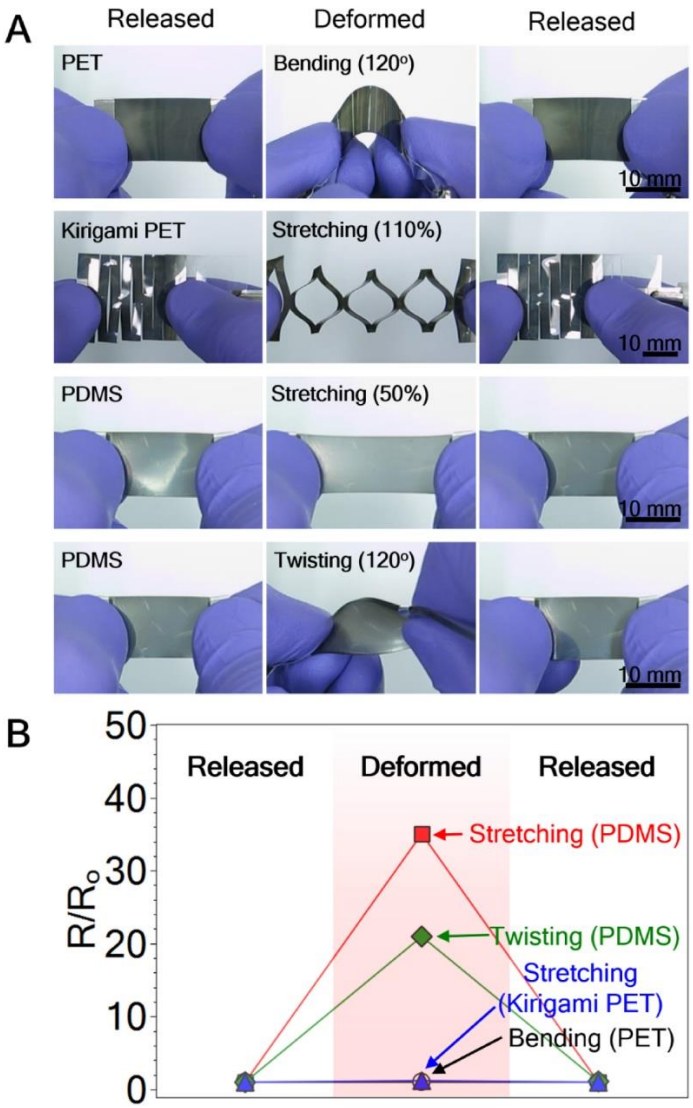

Figure 5.16 (a) Digital images and (b) normalized resistance (R/R_0) of MXene multilayers on PET, kirigami patterned PET, and PDMS under bending, stretching, and twisting. All samples were pre-deformed.

Table 5.3 Characteristics of reported bendable conductors.

No.	Sample	Sub-strate	Preparation method	Max. bending radius [mm]	Sheet resistance[a] [kΩ/sq]	Con-ductivity [S/m]	Cycle num-ber	Cycle bending radius [mm]	Resistance change per cycle [%/cycle]	Ref.
This study	MXene/PDAC	PET	Layer-by-layer coating	2.5	5	2×10^3	2000	2.5	0.05	This study
1	Graphene foams/PDMS	-	Template-directed CVD	0.8	-	1×10^3	10	0.8	1.3	[294]
2	Graphene	PMMA[b]	CVD	1.0	0.4	-	100	3.0	0.09	[295]
3	Graphene	PMMA	CVD	1.0	0.4	-	100	1.0	1	[295]
4	MWCNT/reduced graphene oxide	PET	Layer-by-layer coatings	90° bending angle	60	-	100	90° bending angle	-	[296]
5	Glassy graphene	PDMS	Laser direct writing method	2.0	1	1×10^4	250	2.0	0.08	[297]
6	Ag nanowire /PVA[c]	PET	Wet-chemical fabrication	0.0	0.003~0.2	-	250	0	1.2	[296]
7	Ag nanowire /graphene	PET	Vacuum filtration	5.0	0.0001~3	1×10^5	500	5.0	0.01	[289]
8	Graphene/Ag nanowire foam/PDMS	-	Polymer-assisted assembly /PDMS infiltration	2.0	-	1×10^3	500	2.0	0.005	[298]
9	PEDOT:PSS /graphene oxide	PEN[o]	Spin-coating	8.0	0.1	8×10^4	1000	8.0	0.01	[298]
10	PEDOT:PSS /graphene oxide	PET	Spin-coating	5.0	~0.1	-	1000	5.0	0.005	[299]
11	PEDOT:PSS	PET	Spin-coating	10.0	0.4	-	2000	10.0	-0.0005	[300]
12	Ag nanowire	PET	Transfer onto PET	2.5	0.01	1×10^6	2000	2.5	0.013	[301]
13	PEDOT:PSS	PET	Spin-coating	8.0	0.5	1×10^5	2500	8.0	0.012	[302]
14	Indium tin oxide (ITO)	PET	CVD	8.0	0.01	1×10^5	2500	8.0	1.6	[302]
15	Ag particle attached MWCNT	PET	Drop-casting	4.5	0.3	3×10^6	3000	4.5	0.07	[303]
16	Graphene foams/PDMS	-	Template-directed CVD	2.5	-	1×10^3	10000	2.5	0.0003	[294]
17	Graphene oxide /Ag nanowire	PET	Bar- or spray-coating	2.0	0.03	-	10000	2.0	0.007	[304]

[a] Conductivity was calculated using Conductivity [$S\,m^{-1}$] = 1/(sheet resistance [$ohm\,sq^{-1}$] × thickness [m]) where sq is unitless; [b]PMMA: poly(methyl methacrylate); and [c]PVA: poly(vinyl alcohol); and [o]PEN: poly(ethylene naphthalate).

Table 5.4 Characteristics of reported stretchable conductors.

No.	Sample	Sub-strate	Preparation method	Max. strain [%]	Sheet resis-tance[a] [kΩ/sq]	Con-ductivity [S/m]	Cycle num-ber	Cycle strain [%]	Resistance change per cycle [%/cycle]	Ref.
This study	MXene/PDAC[b]	PDMS[c]	Layer-by-layer coating	50	5	2×10^3	2000	20%	0.03	This study
18	Graphene	PDMS or PET[d]	CVD[e] method /transfer	30	~1	-	3	12%	8.3	[305]
19	Graphene foams/PDMS	-	Template-directed CVD	100	-	$\sim1\times10^3$	10	50%	1.5	[294]
20	CNT /dimethacrylate crosspolymer	Dimeth-acrylate cross-polymer	Photo-crosslinked polymeri-zation	50	0.2	-	14	40%	1.3	[306]
21	3D PEDOT:PSS[f] aerogel/PDMS	-	Aerogel embedment into PDMS	43	0.002	-	15	10%	0.2	[307]
22	Graphene/ polyurethane	-	Compression molding	300	2000	1×10^{-3}	20	30%	26	[308]
23	Graphene/ polyurethane	-	Compression molding	300	2000	1×10^{-3}	100	5%	0.3	[308]
24	Carbon nanofiber /paraffin wax–polyolefin thermoplastic	Natural rubber	Spray coating	600	~0.1	1×10^3	50	300%	18	[309]
25	Cu	Pre-strained PDMS	Metal electroless deposition	100	0.16	2×10^7	50	70%	0.02	[310]
26	Ag nanowire /graphene oxide	PUA[g]	Solution-based coating	100	0.01	-	100	40%	2	[311]
27	Ag nanowire /graphene oxide	PUA	Solution-based coating	100	0.01	-	100	20%	1	[311]
28	Graphene /PEDOT:PSS	Cotton fabrics	Spray coating	45	0.06	~100	100	10%	1.4	[312]
29	MWCNT[h] /Polyurethane (PU)	PU	Drop-casting	1400	-	~100	100	20%	0.06	[313]
30	MWCNT /Polyurethane (PU)	PU	Drop-casting	1400	-	50-100	100	80%	1.3	[313]
31	Positively- and negatively-charged SWCNT[i]s	PDMS	Layer-by-layer coating	80	0.6	-	100	15%	1	[261]
32	Graphene/ polyvinyl alcohol	-	Bidirectional freezing method	8.2	-	~250	100	5%	0.3	[314]
33	Super-aligned CNT/PDMS	PDMS	Embedding method	30	-	6×10^3	200	15%	0.14	[315]
34	Graphene/Ag nanowire/PDMS	-	Polymer-assisted assembly /PDMS infiltration	40	-	1×10^3	500	40%	0.16	[298]

Table 5.4 Continued.

No.	Sample	Sub-strate	Preparation method	Max. strain [%]	Sheet resis-tance[a] [kΩ/sq]	Con-ductivity [S/m]	Cycle num-ber	Cycle strain [%]	Resistance change per cycle [%/cycle]	Ref.
35	Graphene/Ag nanowire/PDMS	-	Polymer-assisted assembly	40	-	1×10^3	500	20%	0.06	[298]
36	Graphene/natural rubber	natural rubber	Solution-based coating	~800	-	~0.1	920	75%	-0.08	[316]
37	Graphene /graphene scrolls	SEBS[j]	CVD	100	0.1	-	1000	90%	0.8	[317]
38	SWCNT	PUA[k]	Drop-casting	50	0.02	-	1000	20%	0.06	[318]
39	Super-aligned CNT	PDMS	Transfer onto PDMS	600	-	-	5000	400%	0.0012	[319]
40	Ag/MWCNT	NBR	Drop-casting	140	-	6×10^5	5000	20%	0.02	[320]
41	SWCNT /fluorinated copolymer	PDMS	Drop-casting	134	-	6×10^3	10000	50%	0.007	4
42	Au nanoparticle /PU	-	Layer-by-layer coating	16	-	7×10^5	10000	5%	-0.004	[177]
43	Au nanoparticle /PU	-	Vacuum assisted filtration	75	-	5×10^4	10000	5%	-0.003	[177]
44	F4TCNQ[l]-doped SWCNT	PDMS	Spray-coating and buckling	150	0.3	1×10^5	12500	25%	0	[321]

[a]Conductivity was calculated using Conductivity [S m^{-1}] = 1/(sheet resistance [ohm sq^{-1}] × thickness [m]) where sq is unitless; [b]PDAC: poly(diallyldimethylammonium chloride); [c]PDMS: poly(dimethylsiloxane); [d]PET: poly(ethylene terephthalate); [e]CVD: chemical vapor deposition; [f]PEDOT:PSS: poly(3,4-ethylenedioxythiophene):polystyrene sulfonate; [g]PUA: polyurethane acrylate; [h]MWCNT: multi-walled carbon nanotubes; [i]SWCNT: single-walled carbon nanotubes; [j]SEBS: styrene-ethylene-butadiene-styrene; [k]NBR: nitrile butadiene rubber; and [l]F4TCNQ: 2,3,5,6-tetrafluoro-7,7,8,8-tetracyanoquinodimethane.

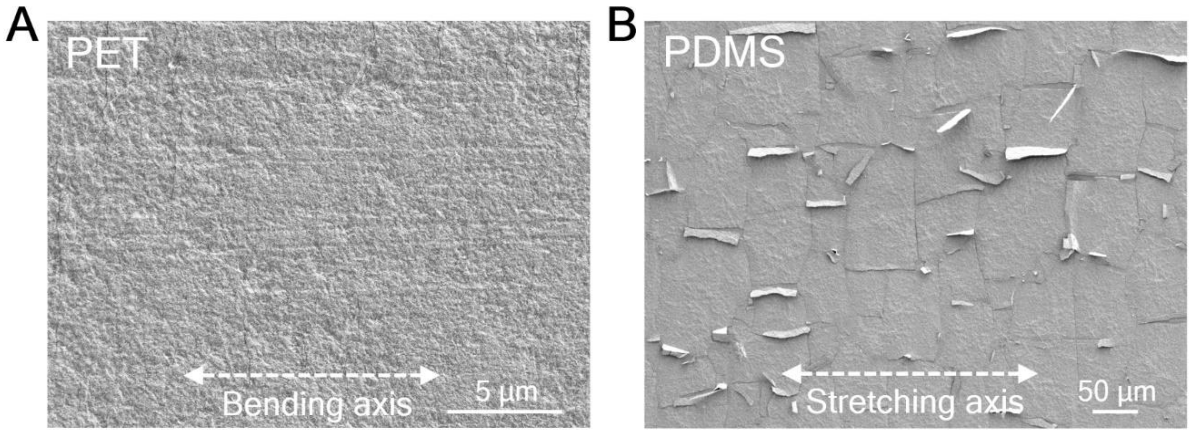

Figure 5.17 Low-magnification SEM images of deformed MXene multilayers on (a) PET and (b) PDMS after bending (r = 4.4 mm) and stretching (ε = 20 %), respectively.

To understand the underlying mechanism of the electro-mechanical coupling, we monitored structural changes in the MXene multilayer coating before and after bending and stretching (Figure 5.12e-f and Figure 5.17). As-prepared the MXene multilayer exhibited no cracks or defects by SEM. Upon initial bending or stretching, micro-cracks and gaps irreversibly formed, explaining the initial increase in the normalized resistance in Figure 5.12c-d. The gaps and cracks are not so large as to completely destroy the conductive network; rather, this lengthens the pathway for electron conduction. Upon release, the cracks and gaps close and recover and the conductive pathway is reformed.

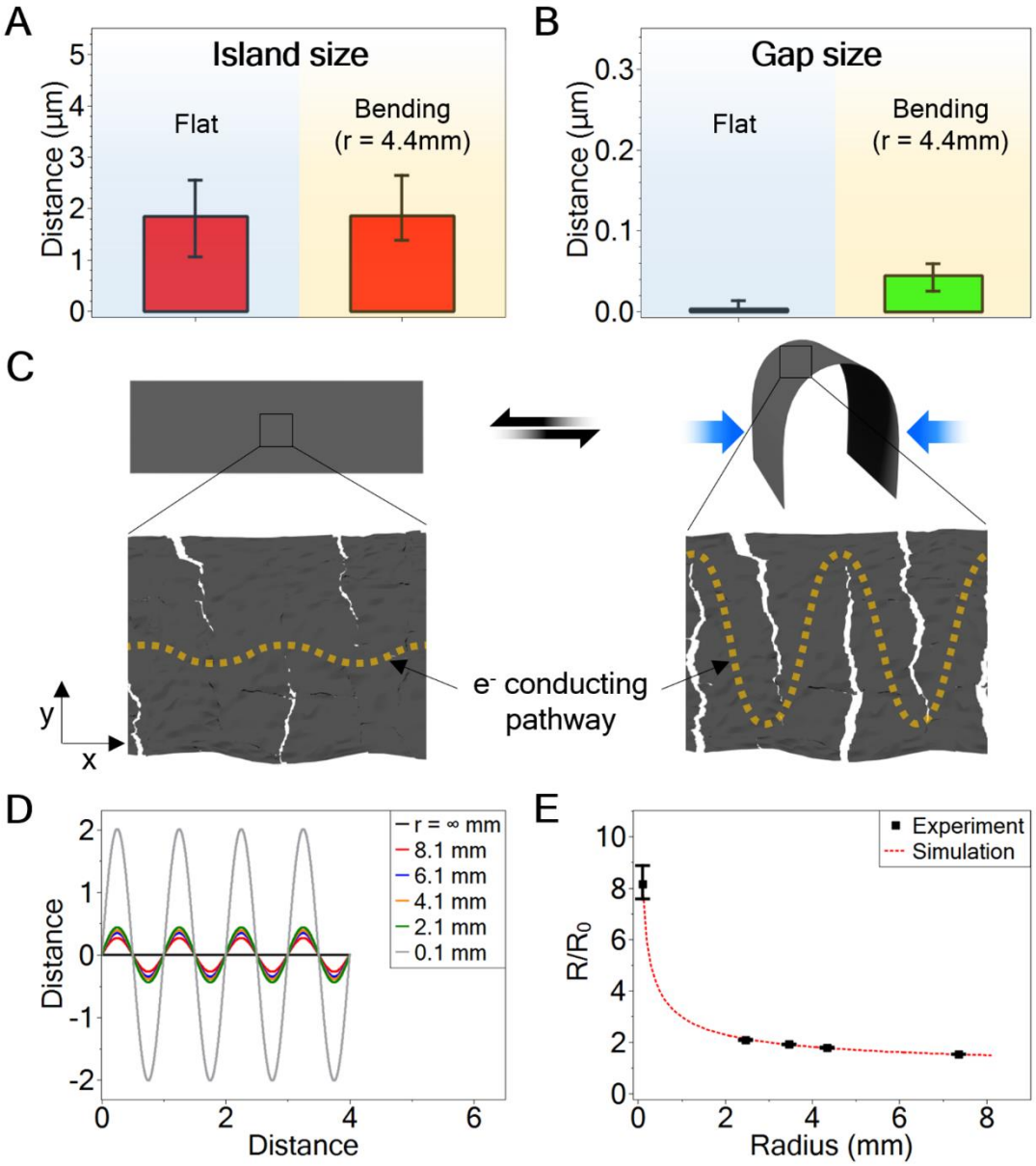

Figure 5.18 Average size of (a) islands and (b) gaps. (c) Schematic illustrations showing the mechanism of electromechanical behavior under bending. (d) Simulation results of the sinusoidal model. (e) Response of the multilayer to the applied bending by experimental measurement and numerical model.

A geometric analysis[322] revealed that an electron conduction path becomes more tortuous with strain because of the gap creations. We assume that the gaps are created periodically, the length of the gaps increase with bending, and the tortuous path resembles a sine wave. Thus, with assumption that resistivity (ρ) and cross-sectional area (a) are constant, resistance can be expressed by:

$$R = \frac{\rho l}{a} \propto l(r) = \int \sqrt{1 + \left(\frac{dx}{dy}\right)^2}\, dx$$

$$y = A\sin(Bx)$$

where ε is strain; x is variable; A is an amplitude which is a function of bending radius, $f(r)$; and B is a constant (i.e., 2π). Physically, an amplitude should increase with bending. A can be determined by fitting to experimental data (Figure 5.18d).

$$A = 0.6854\, r^{0.4661}$$

Thus, by knowing A, equation y is shown to follow a power-law:

$$y = A\sin(Bx) = 0.6854\, r^{0.4661}\sin(2\pi x)$$

Because equation (a) does not have an analytical solution, it should be solved numerically. The numerical solution of l and relative resistance are below:

$$l = l_o 3.0537 r^{0.365}$$

$$\frac{R}{R_o} = \frac{l}{l_o} = 3.0537 r^{0.365}$$

where l_o is the initial length of the film, and R_o is the initial resistance. The excellent agreement between the model and experiment (Figure 5.18e) allows us to gauge the resistance dependence on bending radius.

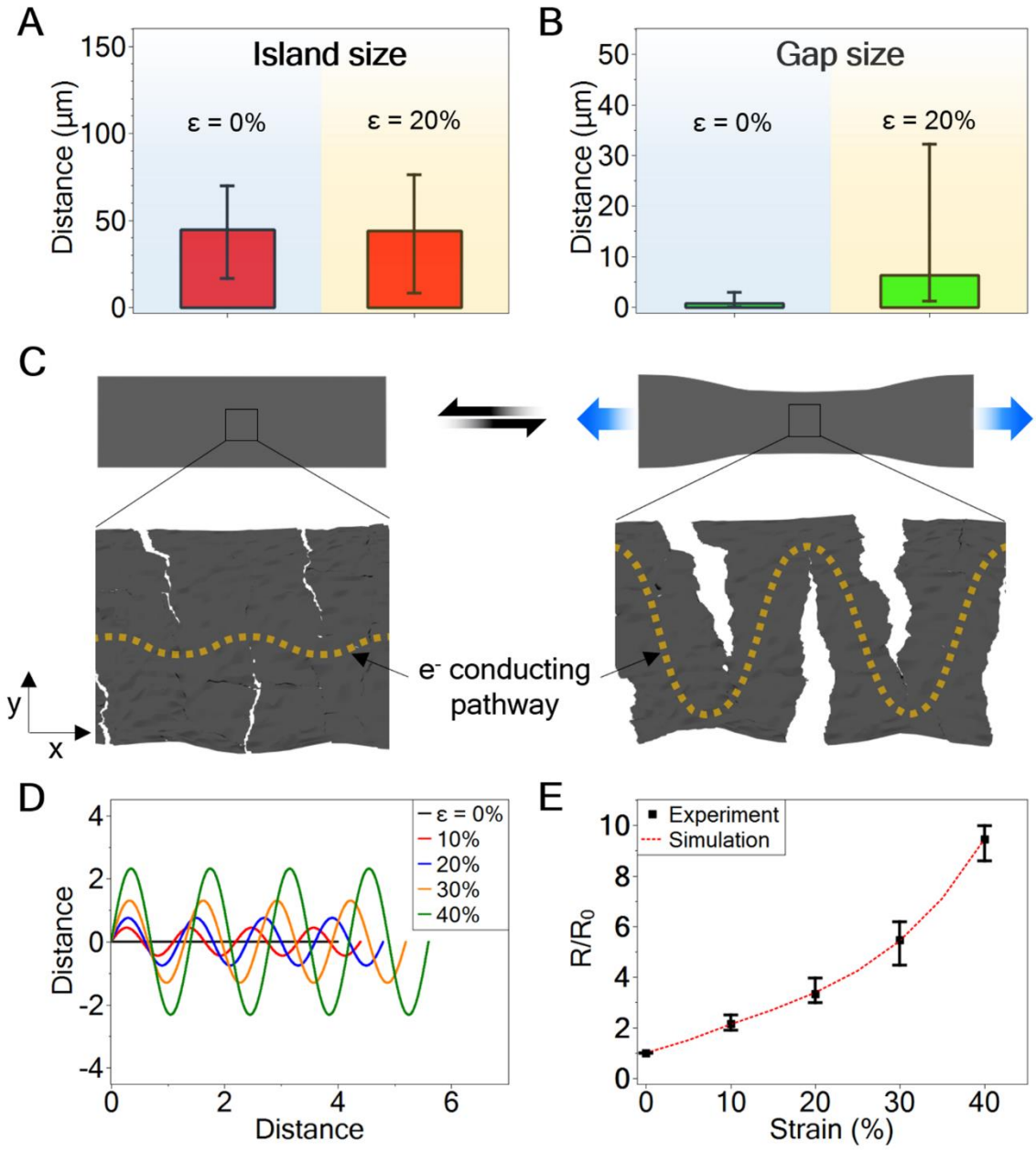

Figure 5.19 Average size of (a) islands and (b) gaps. (c) Schematic illustrations showing the mechanism of electromechanical behaviors under tensile strain (stretching). (d) Simulation results of the sinusoidal model. (e) Response of the multilayer to the applied strain by experimental measurement and numerical model.

A geometric analysis[322] reveals that the conductive path becomes more tortuous with strain because of the creation of gaps and islands. We assume that the gaps are created periodically, the length of the gaps increase with strain, and the tortuous path resembles a sine wave. Thus, with assumption that resistivity (ρ) and cross-sectional area (a) are constant, resistance can be expressed by

$$R = \frac{\rho l}{a} \propto l(\varepsilon) = \int \sqrt{1 + \left(\frac{dx}{dy}\right)^2}\, dx$$

$$y = A\sin(Bx)$$

where ε is strain; x is variable; A is an amplitude which is a function of strain, $f(\varepsilon)$; and B is a function of strain, $f(\varepsilon) = 2\pi/(1+\varepsilon)$. The amplitude and a period should increase with strain. A can be determined by fitting to experimental data (Figure 5.19).

$$A = 49.7\varepsilon^3 - 20.0\varepsilon^2 + 5.8\varepsilon$$

Thus, by knowing A, equation y is shown to increase with strain:

$$y = A\sin(Bx) = (49.7\varepsilon^3 - 20.0\varepsilon^2 + 5.8\varepsilon)\sin((\frac{2\pi}{1+\varepsilon})x)$$

Because equation (g) does not have an analytical solution, it should be solved numerically. The numerical solution of l and relative resistance are below:

$$l = l_o 1.1032\exp(5.4223\varepsilon)$$

$$\frac{R}{R_o} = \frac{l}{l_o} = 1.1032\exp(5.4223\varepsilon)$$

where l_o is the initial length of film, and R_o is an initial resistance. The excellent agreement between the model and experiment (Figure 5.19e) allows us to gauge the resistance dependence on strain. This is confirmed by a geometric analysis that accounts for the average island and gap size under deformed and released states as well as the tortuous conduction path that results (Figure 5.18 and

5.19 and analysis shown in Supporting Information). This mechanism has been observed elsewhere for carbon nanotube strain sensors [322, 323], a crack-based Pt sensor [324] and a microcracked organic semiconductor [325].

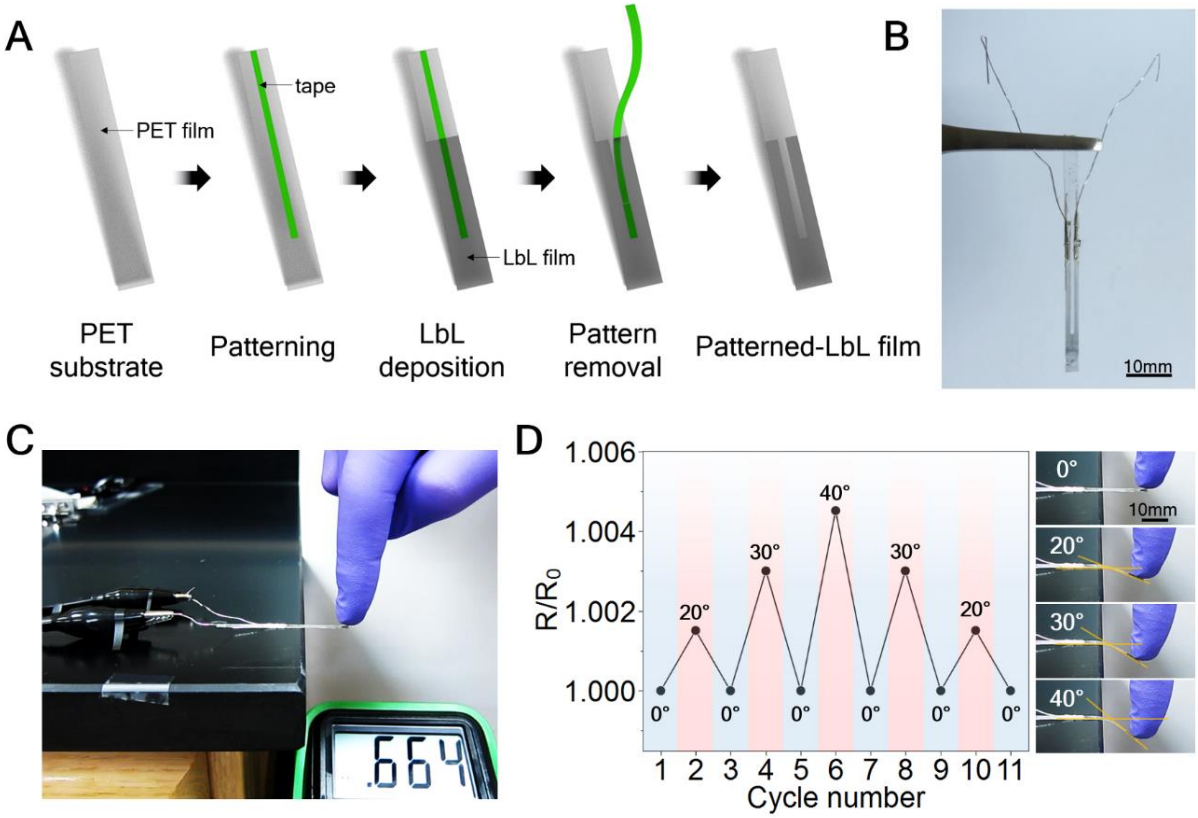

Figure 5.20 (a) An illustration showing the fabrication of a patterned MXene multilayer strain sensor. (b) A digital image of the patterned MXene multilayer strain sensor with copper wire connections and silver paste. (c) A digital image of electromechanical testing. (d) Normalized resistance (R/R_0) *vs.* bending angle. R_0 = 664 kΩ.

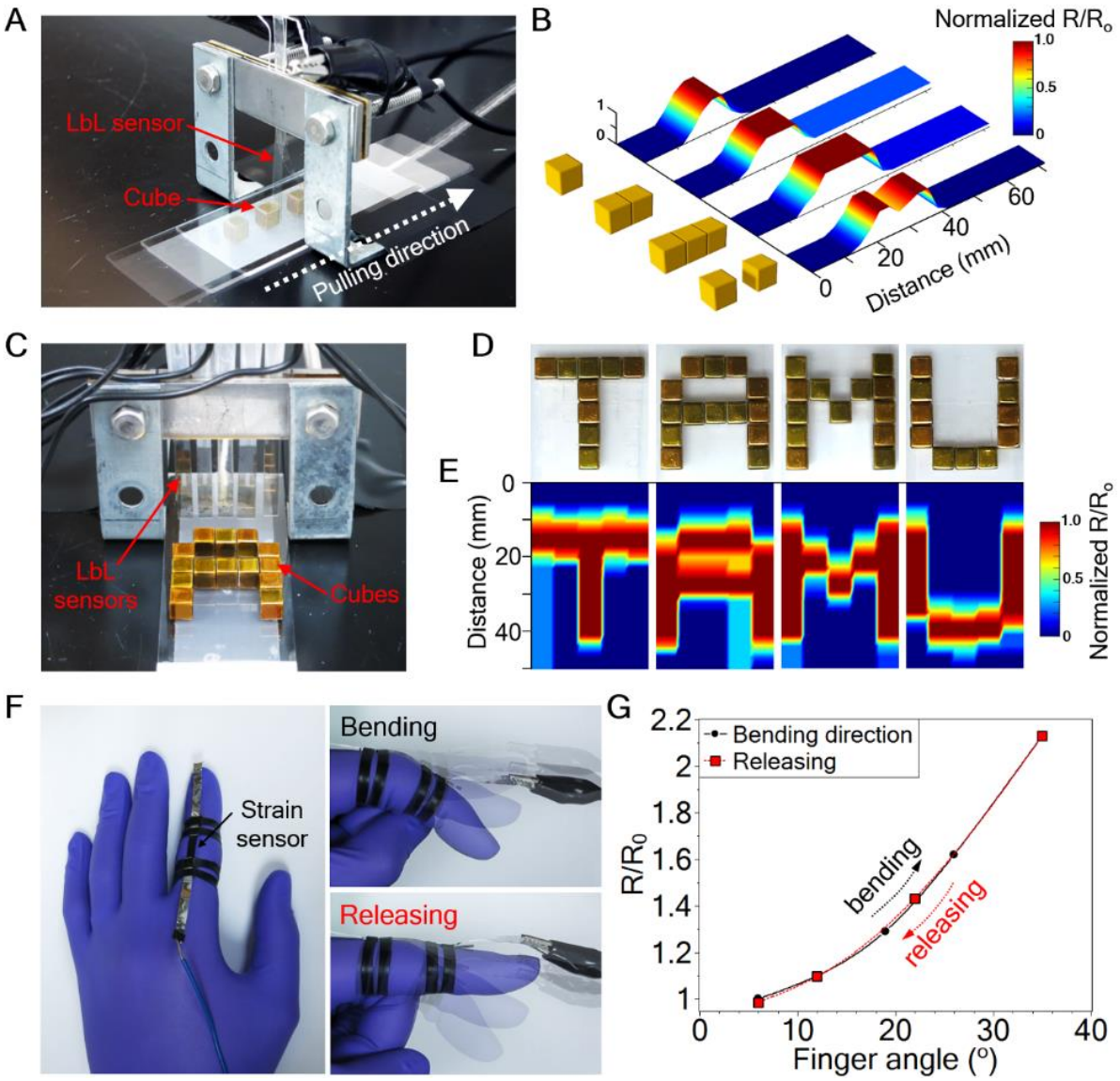

Figure 5.21 An object scanner and human motion sensor. (a) Digital image of a topographical scanner using the MXene multilayer-coated PET (LbL sensor). (b) The topographical map by normalized resistance variations with various cube patterns. (c) Topographical scanner with the five MXene-multilayer-coated PET sensors; and (d) T, A, M, and U patterns using cubes. (e) Topographical maps of normalized resistance variations for the T, A, M, and U patterns. (f) Digital image of the human motion strain sensor. (g) Response to finger motion.

These results suggest that the MXene multilayer films could be used as strain sensors to topographically sense objects or materials deformation. For demonstration, a topographic scanner was fabricated using a patterned MXene multilayer-coated PET film (Figure 5.20 and 5.21a). The MXene-coated PET bent and deformed as small objects passed through the scanner, resulting in a change in normalized resistance R/R_0 (Figure 5.21a-b). The topographic scanner (Figure 5.21c) was even able to map complex shapes such T, A, M, and U letters (Figure 5.21d-e). A soft human motion sensor was fabricated using MXene-coated PDMS (Figure 5.21f). The sensor detected the angle of a bent index finger with little hysteresis (Figure 5.21g and 5.22). As the bending angle increased to 35°, the normalized resistance R/R_0 more than doubled, showing a large gauge factor (GF, the sensitivity to bending) defined as GF = $(\Delta R/R)/\varepsilon$: 11.5; in comparison, common metal-foil gauges have a GF of 2.0 (5% maximum strain).[326] In sum, these results demonstrate that MXene nanosheets can form mechanically responsive conductive coatings, having implications for soft, flexible, and stretchable conductors that could enable organic electronics or biometric sensing on a variety of surfaces and interfaces.

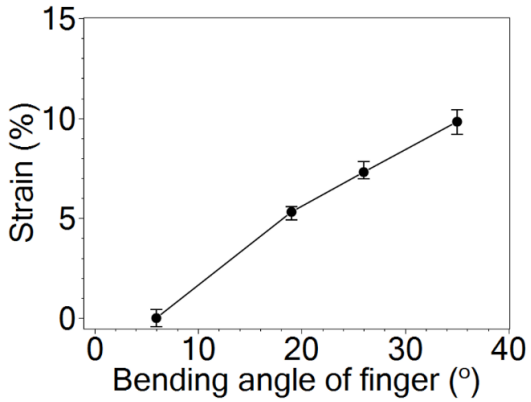

Figure 5.22 Strain versus the angle at the index finger. The strain sensor was attached to an index finger and bent at various angles.

5.4 CONCLUSIONS

We report on conductive and conformal MXene multilayer coatings that can undergo large-scale mechanical deformation while maintaining a conductivity as high as 2000 S/m. MXene multilayers are successfully deposited onto flexible polymer sheet, stretchable poly(dimethylsiloxane), nylon fiber, glass, and silicon. The coating shows a recoverable resistance response to bending (up to 2.5 mm bending radius) and stretching (up to 40% tensile strain), which was leveraged for detecting human motion and topographical scanning. We anticipate that this discovery will allow for the implementation of MXene-based coatings onto mechanically deformable objects.

CHAPTER VI

SUMMARY

A conductive block copolymer binder P3HT-b-PEO was studied to form a flexible, tough, carbon-free hybrid battery cathode (Chapter II). We present the water-based self-assembly approach to incorporate electron- and ion-conducting P3HT-*b*-PEO block copolymer binders into V_2O_5. Our approach led to a unique electrode structure consisting of interlocking V_2O_5 layers held together by the block copolymer binder in a brick-and mortar-like fashion. This structure resulted in robust mechanical properties, far exceeding the those obtained from conventional fluoropolymer binders. Only 5 wt % polymer was required to triple the flexibility of V_2O_5, and electrodes comprised of 10 wt % polymer had unusually high toughness (293 kJ/m3) and specific energy (530 Wh/kg), both higher than reduced graphene oxide paper electrodes. Hybridizing also roughly doubled the lithium-ion diffusion (0.85×10^{-11} cm^2/s for pure V_2O_5 *vs.* 2.09×10^{-11} cm^2/s for 10 wt% polymer), eliminated cracking during charging and discharging, and slowed the loss of capacity over time.

We investigated how P3HT-*b*-PEO interacts with V_2O_5 in the context of carbon-free hybrid electrodes as compared to P3HT, PEO, and a P3HT/PEO homopolymer blend (Chapter III). The use of block copolymer binders produced superior electrodes by providing the enhanced mixing between V_2O_5 and the polymeric binder. For a cathode containing 10 wt % P3HT-*b*-PEO discharged at a 0.1 C rate, the capacity after 200 cycling was 190 mAh/g, whereas that of V_2O_5 was 77 mAh/g (a 2.5-fold difference). Also, P3HT, PEO, and the blend exhibited low capacities (139, 130, and 70 mAh/g, respectively) due to macroscopic phase segregation and the presence of

the nonconducting polymer. The block copolymer architecture of P3HT-*b*-PEO, wherein P3HT and PEO blocks are connected by covalent bonding, enhanced the uniform distribution of the conductive binders within the V_2O_5 electrode, whereas the analogous P3HT/PEO showed large-scale phase separation.

We presented the strong effects of regioregularity and molecular weight of the P3HT block in P3HT-*b*-PEO on molecular conformation and electrochemical properties (Chapter IV) by comparing four different P3HT-*b*-PEO block copolymers—different regioregularity (86-97%) and molecular weight (8-19 kDa) of P3HT block while the PEO block was kept the same (7 kDa). It was found that the regioregularity and molecular weight of P3HT block strongly affected its backbone conformation and chain packing structure. The redox potential increased with decreasing molecular weight and the redox current response decreased with decreasing regioregularity. The specific capacity of P3HT-*b*-PEOs significantly increased with increasing regioregularity. This strong effect of regioregularity on capacity is because, in lower regioregularity P3HT, twisted chain conformations leads to charge localization and charge carrier trapping,[280] resulting in poor doping efficiency and low capacity. Conversely, in higher regioregularity P3HT, planar backbone conformations delocalize polarons along P3HT backbones and minimize charge carrier trapping,[280] resulting in high doping efficiency and high capacity.

We investigated conductive and conformal MXene multilayer coatings (Chapter V). The coatings can undergo large-scale mechanical deformation while maintaining a conductivity as high as 2,000 S/m. The conductive, stretchable, bendable, surface-agnostic MXene coatings were produced through the sequential adsorption of negatively charged MXene sheets and positively charged polyelectrolytes using a layer-by-layer assembly. MXene multilayers were successfully fabricated onto flexible polymer sheet, stretchable poly(dimethylsiloxane), nylon fiber, and glass.

The coating showed a recoverable resistance response to bending (up to 2.5 mm bending radius) and stretching (up to 40% tensile strain). Over the course of 2,000 cycles of bending, the resistance was fairly stable (increasing by 0.05% R/R_0 per cycle). MXene-coated PDMS showed similar stability with repeated stretching (0.03% R/R_0 per cycle). These MXene-based coatings endured other types of deformations, such as twisting and kirigami-stretching, reversibly responding to strain without forming large-scale visible cracks. This excellent electrical-mechanical coupling results from reversible structural changes in the MXene multilayer coatings. Upon initial bending or stretching, micro-cracks and gaps irreversibly formed. Upon release, the cracks and gaps close and recover and the conductive pathway is reformed. The islands and gaps changed negligibly over 2000 cycles of bending and 2000 cycles of strectching. The MXene multilayer coatings were leveraged for detecting human motion and topographical scanning.

REFERENCES

1. Patel, S. N.; Javier, A. E.; Balsara, N. P. Electrochemically Oxidized Electronic and Ionic Conducting Nanostructured Block Copolymers for Lithium Battery Electrodes. *ACS Nano* **2013**, 7, 6056-6068.

2. Chen, Z.; Christensen, L.; Dahn, J. Large-volume-change electrodes for Li-ion batteries of amorphous alloy particles held by elastomeric tethers. *Electrochemistry Communications* **2003**, 5, 919-923.

3. Wang, Z.; Dupré, N.; Gaillot, A.-C.; Lestriez, B.; Martin, J.-F.; Daniel, L.; Patoux, S.; Guyomard, D. CMC as a binder in $LiNi_{0.4}Mn_{1.6}O_4$ 5 V cathodes and their electrochemical performance for Li-ion batteries. *Electrochimica Acta* **2012**, 62, 77-83.

4. Sekitani, T.; Noguchi, Y.; Hata, K.; Fukushima, T.; Aida, T.; Someya, T. A rubberlike stretchable active matrix using elastic conductors. *Science* **2008**, 321, 1468-1472.

5. Rogers, J. A.; Someya, T.; Huang, Y. Materials and mechanics for stretchable electronics. *Science* **2010**, 327, 1603-1607.

6. White, M. S.; Kaltenbrunner, M.; Głowacki, E. D.; Gutnichenko, K.; Kettlgruber, G.; Graz, I.; Aazou, S.; Ulbricht, C.; Egbe, D. A.; Miron, M. C. Ultrathin, highly flexible and stretchable PLEDs. *Nature Photonics* **2013**, 7, 811.

7. Larson, C.; Peele, B.; Li, S.; Robinson, S.; Totaro, M.; Beccai, L.; Mazzolai, B.; Shepherd, R. Highly stretchable electroluminescent skin for optical signaling and tactile sensing. *Science* **2016**, 351, 1071-1074.

8. Takei, K.; Takahashi, T.; Ho, J. C.; Ko, H.; Gillies, A. G.; Leu, P. W.; Fearing, R. S.; Javey, A. Nanowire active-matrix circuitry for low-voltage macroscale artificial skin. *Nature Materials* **2010**, 9, 821.

9. Volta, A.; Banks, J. I. On the electricity excited by the mere contact of conducting substances of different kinds. *The Philosophical Magazine* **1800**, 7, 289-311.

10. Faraday, M. VI. Experimental researches in electricity.—Sixth series. *Philosophical Transactions of the Royal Society of London* **1834**, 124, 77-122.

11. Whittingham, M. S. The role of ternary phases in cathode reactions. *Journal of the Electrochemical Society* **1976**, 123, 315-320.

12. Mizushima, K.; Jones, P.; Wiseman, P.; Goodenough, J. Li_xCoO_2 ($0< x\leqslant 1$): a new cathode material for batteries of high energy density. *Solid State Ionics* **1981**, 3, 171-174.

13. Mizushima, K.; Jones, P.; Wiseman, P.; Goodenough, J. B. Li_xCoO_2 (0< x<-1): a new cathode material for batteries of high energy density. *Materials Research Bulletin* **1980**, 15, 783-789.

14. Nagaura, T.; Tozawa, K. Progress in batteries and solar cells. *JEC Press* **1990**, 9, 209.

15. Roy, P.; Srivastava, S. K. Nanostructured anode materials for lithium ion batteries. *Journal of Materials Chemistry A* **2015**, 3, 2454-2484.

16. Tarascon, J. M.; Armand, M. Issues and challenges facing rechargeable lithium batteries. *Nature* **2001**, 414, 359.

17. Fu, L.; Liu, H.; Li, C.; Wu, Y.; Rahm, E.; Holze, R.; Wu, H. Electrode materials for lithium secondary batteries prepared by sol–gel methods. *Progress in Materials Science* **2005**, 50, 881-928.

18. Yang, S.; Song, Y.; Zavalij, P. Y.; Whittingham, M. S. Reactivity, stability and electrochemical behavior of lithium iron phosphates. *Electrochemistry Communications* **2002**, 4, 239-244.

19. Xiao, X.; Lu, P.; Ahn, D. Ultrathin multifunctional oxide coatings for lithium ion batteries. *Advanced Materials* **2011**, 23, 3911-3915.

20. Shao, L.; Jeon, J.-W.; Lutkenhaus, J. L. Polyaniline/vanadium pentoxide layer-by-layer electrodes for energy storage. *Chemistry of Materials* **2011**, 24, 181-189.

21. Chan, C. K.; Peng, H.; Liu, G.; McIlwrath, K.; Zhang, X. F.; Huggins, R. A.; Cui, Y. High-performance lithium battery anodes using silicon nanowires. *Nature Nanotechnology* **2008**, 3, 31.

22. Landi, B. J.; Ganter, M. J.; Cress, C. D.; DiLeo, R. A.; Raffaelle, R. P. Carbon nanotubes for lithium ion batteries. *Energy & Environmental Science* **2009**, 2, 638-654.

23. Wang, Y.; He, P.; Zhou, H. Olivine $LiFePO_4$: development and future. *Energy & Environmental Science* **2011**, 4, 805-817.

24. Mazouzi, D.; Karkar, Z.; Hernandez, C. R.; Manero, P. J.; Guyomard, D.; Roué, L.; Lestriez, B. Critical roles of binders and formulation at multiscales of silicon-based composite electrodes. *Journal of Power Sources* **2015**, 280, 533-549.

25. Liu, G.; Zheng, H.; Simens, A. S.; Minor, A. M.; Song, X.; Battaglia, V. S. Optimization of acetylene black conductive additive and PVDF composition for high-power rechargeable lithium-ion cells. *Journal of the Electrochemical Society* **2007**, 154, A1129-A1134.

26. Soo, P. P.; Huang, B.; Jang, Y. I.; Chiang, Y. M.; Sadoway, D. R.; Mayes, A. M. Rubbery block copolymer electrolytes for solid-state rechargeable lithium batteries. *Journal of the Electrochemical Society* **1999**, 146, 32-37.

27. Mike, J. F.; Lutkenhaus, J. L. Electrochemically active polymers for electrochemical energy storage: opportunities and challenges. *ACS Macro Letters* **2013**, 2, 839-844.

28. Kim, J.-M.; Park, H.-S.; Park, J.-H.; Kim, T.-H.; Song, H.-K.; Lee, S.-Y. Conducting polymer-skinned electroactive materials of lithium-ion batteries: ready for monocomponent electrodes without additional binders and conductive agents. *ACS Applied Materials & Interfaces* **2014**, 6, 12789-12797.

29. Das, P. R.; Komsiyska, L.; Osters, O.; Wittstock, G. PEDOT:PSS as a functional binder for cathodes in lithium ion batteries. *Journal of the Electrochemical Society* **2015**, 162, A674-A678.

30. Wu, H.; Yu, G.; Pan, L.; Liu, N.; McDowell, M. T.; Bao, Z.; Cui, Y. Stable Li-ion battery anodes by in-situ polymerization of conducting hydrogel to conformally coat silicon nanoparticles. *Nature Communications* **2013**, 4, 1943.

31. Zhao, H.; Wang, Z.; Lu, P.; Jiang, M.; Shi, F.; Song, X.; Zheng, Z.; Zhou, X.; Fu, Y.; Abdelbast, G. Toward practical application of functional conductive polymer binder for a high-energy lithium-ion battery design. *Nano Letters* **2014**, 14, 6704-6710.

32. Huguenin, F.; Torresi, R. M. Investigation of the electrical and electrochemical properties of nanocomposites from V_2O_5, polypyrrole, and polyaniline. *The Journal of Physical Chemistry C* **2008**, 112, 2202-2209.

33. Kundu, S.; Satpati, B.; Mukherjee, M.; Kar, T.; Pradhan, S. K. Hydrothermal synthesis of polyaniline intercalated vanadium oxide xerogel hybrid nanocomposites: effective control of morphology and structural characterization. *New Journal of Chemistry* **2017**, 41, 3634-3645.

34. Wu, Q.; Xu, Y.; Yao, Z.; Liu, A.; Shi, G. Supercapacitors based on flexible graphene/polyaniline nanofiber composite films. *ACS Nano* **2010**, 4, 1963-1970.

35. Mao, L.; Zhang, K.; Chan, H. S. O.; Wu, J. Surfactant-stabilized graphene/polyaniline nanofiber composites for high performance supercapacitor electrode. *Journal of Materials Chemistry* **2012**, 22, 80-85.

36. Xu, J.; Wang, K.; Zu, S.-Z.; Han, B.-H.; Wei, Z. Hierarchical nanocomposites of polyaniline nanowire arrays on graphene oxide sheets with synergistic effect for energy storage. *ACS Nano* **2010**, 4, 5019-5026.

37. Kumar, N. A.; Choi, H.-J.; Shin, Y. R.; Chang, D. W.; Dai, L.; Baek, J.-B. Polyaniline-grafted reduced graphene oxide for efficient electrochemical supercapacitors. *ACS Nano* **2012**, 6, 1715-1723.

38. Xue, M.; Li, F.; Zhu, J.; Song, H.; Zhang, M.; Cao, T. Structure-based enhanced capacitance: in situ growth of highly ordered polyaniline nanorods on reduced graphene oxide patterns. *Advanced Functional Materials* **2012**, 22, 1284-1290.

39. Shao, L.; Jeon, J.-W.; Lutkenhaus, J. L. Porous polyaniline nanofiber/vanadium pentoxide layer-by-layer electrodes for energy storage. *Journal of Materials Chemistry A* **2013**, 1, 7648-7656.

40. Shao, L.; Jeon, J.-W.; Lutkenhaus, J. L. Polyaniline nanofiber/vanadium pentoxide sprayed layer-by-layer electrodes for energy storage. *Journal of Materials Chemistry A* **2014**, 2, 14421-14428.

41. Wong, H. P.; Dave, B. C.; Leroux, F.; Harreld, J.; Dunn, B.; Nazar, L. F. Synthesis and characterization of polypyrrole/vanadium pentoxide nanocomposite aerogels. *Journal of Materials Chemistry* **1998**, 8, 1019-1027.

42. Yang, Y.; Wang, C.; Yue, B.; Gambhir, S.; Too, C. O.; Wallace, G. G. Electrochemically synthesized polypyrrole/graphene composite film for lithium batteries. *Advanced Energy Materials* **2012**, 2, 266-272.

43. Kim, J.; Lee, J.; You, J.; Park, M.-S.; Al Hossain, M. S.; Yamauchi, Y.; Kim, J. H. Conductive polymers for next-generation energy storage systems: recent progress and new functions. *Materials Horizons* **2016**, 3, 517-535.

44. Cíntora-Juárez, D.; Pérez-Vicente, C.; Kazim, S.; Ahmad, S.; Tirado, J. L. Judicious design of lithium iron phosphate electrodes using poly(3, 4-ethylenedioxythiophene) for high performance batteries. *Journal of Materials Chemistry A* **2015**, 3, 14254-14262.

45. Lee, J. I.; Kang, H.; Park, K. H.; Shin, M.; Hong, D.; Cho, H. J.; Kang, N. R.; Lee, J.; Lee, S. M.; Kim, J. Y. Amphiphilic graft copolymers as a versatile binder for various electrodes of high-performance lithium-ion batteries. *Small* **2016**, 12, 3119-3127.

46. Yang, C.; Zhang, Z.; Tian, Z.; Zhang, K.; Li, J.; Lai, Y. Polydopamine-coated nano-ZnO for high-performance rechargeable Zn–Ni battery. *Materials Letters* **2017**, 197, 163-166.

47. Bie, Y.; Yang, J.; Liu, X.; Wang, J.; Nuli, Y.; Lu, W. Polydopamine wrapping silicon cross-linked with polyacrylic acid as high-performance anode for lithium-ion batteries. *ACS Applied Materials & Interfaces* **2016**, 8, 2899-2904.

48. Ryou, M. H.; Kim, J.; Lee, I.; Kim, S.; Jeong, Y. K.; Hong, S.; Ryu, J. H.; Kim, T. S.; Park, J. K.; Lee, H. Mussel-inspired adhesive binders for high-performance silicon nanoparticle anodes in lithium-ion batteries. *Advanced Materials* **2013**, 25, 1571-1576.

49. Salem, N.; Lavrisa, M.; Abu-Lebdeh, Y. Ionically-functionalized poly(thiophene) conductive polymers as binders for silicon and graphite anodes for li-ion batteries. *Energy Technology* **2016**, 4, 331-340.

50. Kwon, Y. H.; Minnici, K.; Huie, M. M.; Takeuchi, K. J.; Takeuchi, E. S.; Marschilok, A. C.; Reichmanis, E. Electron/ion transport enhancer in high capacity Li-ion battery anodes. *Chemistry of Materials* **2016**, 28, 6689-6697.

51. Yao, C.-F.; Wang, K.-L.; Huang, H.-K.; Lin, Y.-J.; Lee, Y.-Y.; Yu, C.-W.; Tsai, C.-J.; Horie, M. Cyclopentadithiophene–terephthalic acid copolymers: synthesis via direct arylation and saponification and applications in Si-based lithium-ion batteries. *Macromolecules* **2017**, 50, 6924-6934.

52. Wei, L.; Chen, C.; Hou, Z.; Wei, H. Poly(acrylic acid sodium) grafted carboxymethyl cellulose as a high performance polymer binder for silicon anode in lithium ion batteries. *Scientific Reports* **2016**, 6, 19583.

53. Javier, A. E.; Patel, S. N.; Hallinan, D. T.; Srinivasan, V.; Balsara, N. P. Simultaneous electronic and ionic conduction in a block copolymer: application in lithium battery electrodes. *Angewandte Chemie International Edition* **2011**, 50, 9848-9851.

54. Aurbach, D.; Talyosef, Y.; Markovsky, B.; Markevich, E.; Zinigrad, E.; Asraf, L.; Gnanaraj, J. S.; Kim, H.-J. Design of electrolyte solutions for Li and Li-ion batteries: a review. *Electrochimica Acta* **2004**, 50, 247-254.

55. Xu, K. Nonaqueous liquid electrolytes for lithium-based rechargeable batteries. *Chemical Reviews* **2004**, 104, 4303-4418.

56. Matsumoto, H.; Sakaebe, H.; Tatsumi, K.; Kikuta, M.; Ishiko, E.; Kono, M. Fast cycling of Li/$LiCoO_2$ cell with low-viscosity ionic liquids based on bis(fluorosulfonyl)imide $[FSI]^-$. *Journal of Power Sources* **2006**, 160, 1308-1313.

57. Suo, L.; Hu, Y.-S.; Li, H.; Armand, M.; Chen, L. A new class of solvent-in-salt electrolyte for high-energy rechargeable metallic lithium batteries. *Nature Communications* **2013**, 4, 1481.

58. Lewandowski, A.; Świderska-Mocek, A. Ionic liquids as electrolytes for Li-ion batteries—an overview of electrochemical studies. *Journal of Power Sources* **2009**, 194, 601-609.

59. Xu, K.; Angell, C. A. Sulfone-based electrolytes for lithium-ion batteries. *Journal of the Electrochemical Society* **2002**, 149, A920-A926.

60. Arora, P.; White, R. E.; Doyle, M. Capacity fade mechanisms and side reactions in lithium-ion batteries. *Journal of the Electrochemical Society* **1998**, 145, 3647-3667.

61. Aravindan, V.; Gnanaraj, J.; Madhavi, S.; Liu, H. K. Lithium-ion conducting electrolyte salts for lithium batteries. *Chemistry-A European Journal* **2011**, 17, 14326-14346.

62. Zhang, S. S. An unique lithium salt for the improved electrolyte of Li-ion battery. *Electrochemistry Communications* **2006**, 8, 1423-1428.

63. Chernova, N. A.; Roppolo, M.; Dillon, A. C.; Whittingham, M. S. Layered vanadium and molybdenum oxides: batteries and electrochromics. *Journal of Materials Chemistry* **2009**, 19, 2526-2552.

64. An, Q.; Wei, Q.; Mai, L.; Fei, J.; Xu, X.; Zhao, Y.; Yan, M.; Zhang, P.; Huang, S. Supercritically exfoliated ultrathin vanadium pentoxide nanosheets with high rate capability for lithium batteries. *Physical Chemistry Chemical Physics* **2013**, 15, 16828-16833.

65. Whittingham, M. S. Lithium batteries and cathode materials. *Chemical Reviews* **2004**, 104, 4271-4302.

66. Huang, X.; Rui, X.; Hng, H. H.; Yan, Q. Vanadium pentoxide-based cathode materials for lithium-ion batteries: morphology control, carbon hybridization, and cation doping. *Particle & Particle Systems Characterization* **2015**, 32, 276-294.

67. Wang, Y.; Takahashi, K.; Lee, K. H.; Cao, G. Nanostructured vanadium oxide electrodes for enhanced lithium-ion intercalation. *Advanced Functional Materials* **2006**, 16, 1133-1144.

68. Winter, M.; Besenhard, J. O.; Spahr, M. E.; Novak, P. Insertion electrode materials for rechargeable lithium batteries. *Advanced Materials* **1998**, 10, 725-763.

69. West, K.; Zachau-Christiansen, B.; Jacobsen, T.; Skaarup, S. Vanadium oxide xerogels as electrodes for lithium batteries. *Electrochimica Acta* **1993**, 38, 1215-1220.

70. Yue, Y.; Liang, H. Micro-and Nano-Structured Vanadium Pentoxide (V_2O_5) for Electrodes of Lithium-Ion Batteries. *Advanced Energy Materials* **2017**.

71. Chae, O. B.; Kim, J.; Park, I.; Jeong, H.; Ku, J. H.; Ryu, J. H.; Kang, K.; Oh, S. M. Reversible lithium storage at highly populated vacant sites in an amorphous vanadium pentoxide electrode. *Chemistry of Materials* **2014**, 26, 5874-5881.

72. Braithwaite, J.; Catlow, C.; Gale, J.; Harding, J. Lithium intercalation into vanadium pentoxide: a theoretical study. *Chemistry of Materials* **1999**, 11, 1990-1998.

73. Li, Y.; Yao, J.; Uchaker, E.; Zhang, M.; Tian, J.; Liu, X.; Cao, G. Sn-doped V_2O_5 film with enhanced lithium-ion storage performance. *The Journal of Physical Chemistry C* **2013**, 117, 23507-23514.

74. Liu, Y.; Clark, M.; Zhang, Q.; Yu, D.; Liu, D.; Liu, J.; Cao, G. V_2O_5 nano-electrodes with high power and energy densities for thin film li-ion batteries. *Advanced Energy Materials* **2011**, 1, 194-202.

75. Dewangan, K.; Sinha, N. N.; Chavan, P. G.; Sharma, P. K.; Pandey, A. C.; More, M.; Joag, D.; Munichandraiah, N.; Gajbhiye, N. Synthesis and characterization of self-assembled nanofiber-bundles of V_2O_5: their electrochemical and field emission properties. *Nanoscale* **2012**, 4, 645-651.

76. Delmas, C.; Cognac-Auradou, H.; Cocciantelli, J.; Menetrier, M.; Doumerc, J. The $Li_xV_2O_5$ system: an overview of the structure modifications induced by the lithium intercalation. *Solid State Ionics* **1994**, 69, 257-264.

77. Salloux, K.; Chaput, F.; Wong, H.; Dunn, B.; Breiter, M. Lithium intercalation in vanadium pentoxide aerogels. *Journal of the Electrochemical Society* **1995**, 142, L191-L192.

78. Le, D.; Passerini, S.; Guo, J.; Ressler, J.; Owens, B.; Smyrl, W. High surface area V_2O_5 aerogel intercalation electrodes. *Journal of the Electrochemical Society* **1996**, 143, 2099-2104.

79. Passerini, S.; Le, D. B.; Smyrl, W. H.; Berrettoni, M.; Tossici, R.; Marassi, R.; Giorgetti, M. XAS and electrochemical characterization of lithiated high surface area V_2O_5 aerogels. *Solid State Ionics* **1997**, 104, 195-204.

80. Rolison, D. R.; Dunn, B. Electrically conductive oxide aerogels: new materials in electrochemistry. *Journal of Materials Chemistry* **2001**, 11, 963-980.

81. Aldebert, P.; Baffier, N.; Gharbi, N.; Livage, J. Layered structure of vanadium pentoxide gels. *Materials Research Bulletin* **1981**, 16, 669-676.

82. Owens, B. B.; Passerini, S.; Smyrl, W. H. Lithium ion insertion in porous metal oxides. *Electrochimica Acta* **1999**, 45, 215-224.

83. Le, D.; Passerini, S.; Tipton, A.; Owens, B.; Smyrl, W. Aerogels and xerogels of V_2O_5 as intercalation hosts. *Journal of the Electrochemical Society* **1995**, 142, L102-L103.

84. Lantelme, F.; Mantoux, A.; Groult, H.; Lincot, D. Electrochemical study of phase transition processes in lithium insertion in V_2O_5 electrodes. *Journal of the Electrochemical Society* **2003**, 150, A1202-A1208.

85. An, H.; Mike, J.; Smith, K. A.; Swank, L.; Lin, Y.-H.; Pesek, S. L.; Verduzco, R.; Lutkenhaus, J. L. Highly flexible self-assembled V_2O_5 cathodes enabled by conducting diblock copolymers. *Scientific Reports* **2015**, 5, 14166.

86. Zhang, C.; Chen, Z.; Guo, Z.; Lou, X. W. D. Additive-free synthesis of 3D porous V_2O_5 hierarchical microspheres with enhanced lithium storage properties. *Energy & Environmental Science* **2013**, 6, 974-978.

87. Gao, X.-W.; Wang, J.-Z.; Chou, S.-L.; Liu, H.-K. Synthesis and electrochemical performance of LiV_3O_8/polyaniline as cathode material for the lithium battery. *Journal of Power Sources* **2012**, 220, 47-53.

88. Liu, J.; Lu, P.-J.; Liang, S.; Wang, W.; Lei, M.; Tang, S.; Yang, Q. Ultrathin Li_3VO_4 nanoribbon/graphene sandwich-like nanostructures with ultrahigh lithium ion storage properties. *Nano Energy* **2015**, 12, 709-724.

89. Wang, Y.; Shang, H.; Chou, T.; Cao, G. Effects of thermal annealing on the Li^+ intercalation properties of $V_2O_5 \cdot nH_2O$ xerogel films. *The Journal of Physical Chemistry B* **2005**, 109, 11361-11366.

90. Wang, Y.; Cao, G. Li^+-intercalation electrochemical/electrochromic properties of vanadium pentoxide films by sol electrophoretic deposition. *Electrochimica Acta* **2006**, 51, 4865-4872.

91. Wang, S.; Lu, Z.; Wang, D.; Li, C.; Chen, C.; Yin, Y. Porous monodisperse V_2O_5 microspheres as cathode materials for lithium-ion batteries. *Journal of Materials Chemistry* **2011**, 21, 6365-6369.

92. Goward, G.; Leroux, F.; Nazar, L. Poly(pyrrole) and poly(thiophene)/vanadium oxide interleaved nanocomposites: positive electrodes for lithium batteries. *Electrochimica Acta* **1998**, 43, 1307-1313.

93. Leroux, F.; Goward, G.; Power, W.; Nazar, L. Electrochemical Li insertion into conductive polymer/V_2O_5 nanocomposites. *Journal of the Electrochemical Society* **1997**, 144, 3886-3895.

94. Olivetti, E. A.; Kim, J. H.; Sadoway, D. R.; Asatekin, A.; Mayes, A. M. Sol-gel synthesis of vanadium oxide within a block copolymer matrix. *Chemistry of Materials* **2006**, 18, 2828-2833.

95. Kim, Y.; Cook, S.; Tuladhar, S. M.; Choulis, S. A.; Nelson, J.; Durrant, J. R.; Bradley, D. D.; Giles, M.; McCulloch, I.; Ha, C.-S. A strong regioregularity effect in self-organizing conjugated polymer films and high-efficiency polythiophene: fullerene solar cells. *Nature Materials* **2006**, 5, 197.

96. Agostinelli, T.; Lilliu, S.; Labram, J. G.; Campoy-Quiles, M.; Hampton, M.; Pires, E.; Rawle, J.; Bikondoa, O.; Bradley, D. D.; Anthopoulos, T. D. Real-time investigation of crystallization and phase-segregation dynamics in P3HT: PCBM solar cells during thermal annealing. *Advanced Functional Materials* **2011**, 21, 1701-1708.

97. Chen, H.; Peet, J.; Hsiao, Y.-C.; Hu, B.; Dadmun, M. The impact of fullerene structure on its miscibility with P3HT and its correlation of performance in organic photovoltaics. *Chemistry of Materials* **2014**, 26, 3993-4003.

98. Ballantyne, A. M.; Chen, L.; Dane, J.; Hammant, T.; Braun, F. M.; Heeney, M.; Duffy, W.; McCulloch, I.; Bradley, D. D.; Nelson, J. The effect of poly(3-hexylthiophene) molecular weight on charge transport and the performance of polymer: fullerene solar cells. *Advanced Functional Materials* **2008**, 18, 2373-2380.

99. Sirringhaus, H.; Brown, P.; Friend, R.; Nielsen, M. M.; Bechgaard, K.; Langeveld-Voss, B.; Spiering, A.; Janssen, R. A.; Meijer, E.; Herwig, P. Two-dimensional charge transport in self-organized, high-mobility conjugated polymers. *Nature* **1999**, 401, 685.

100. Lee, S.; Moon, G. D.; Jeong, U. Continuous production of uniform poly(3-hexylthiophene)(P3HT) nanofibers by electrospinning and their electrical properties. *Journal of Materials Chemistry* **2009**, 19, 743-748.

101. Wang, S.; Ha, M.; Manno, M.; Frisbie, C. D.; Leighton, C. Hopping transport and the Hall effect near the insulator–metal transition in electrochemically gated poly(3-hexylthiophene) transistors. *Nature Communications* **2012**, 3, 1210.

102. Chang, J.-F.; Clark, J.; Zhao, N.; Sirringhaus, H.; Breiby, D. W.; Andreasen, J. W.; Nielsen, M. M.; Giles, M.; Heeney, M.; McCulloch, I. Molecular-weight dependence of interchain polaron delocalization and exciton bandwidth in high-mobility conjugated polymers. *Physical Review B* **2006**, 74, 115318.

103. McCullough, R. D. The chemistry of conducting polythiophenes. *Advanced Materials* **1998**, 10, 93-116.

104. Aiyar, A. R.; Hong, J.-I.; Reichmanis, E. Regioregularity and intrachain ordering: impact on the nanostructure and charge transport in two-dimensional assemblies of poly(3-hexylthiophene). *Chemistry of Materials* **2012**, 24, 2845-2853.

105. Poelking, C.; Andrienko, D. Effect of polymorphism, regioregularity and paracrystallinity on charge transport in poly(3-hexylthiophene)(P3HT) nanofibers. *Macromolecules* **2013**, 46, 8941-8956.

106. Guo, J.; Ohkita, H.; Benten, H.; Ito, S. Charge generation and recombination dynamics in poly(3-hexylthiophene)/fullerene blend films with different regioregularities and morphologies. *Journal of the American Chemical Society* **2010**, 132, 6154-6164.

107. Woo, C. H.; Thompson, B. C.; Kim, B. J.; Toney, M. F.; Fréchet, J. M. The influence of poly(3-hexylthiophene) regioregularity on fullerene-composite solar cell performance. *Journal of the American Chemical Society* **2008**, 130, 16324-16329.

108. Kajiya, D.; Ozawa, S.; Koganezawa, T.; Saitow, K.-i. Enhancement of out-of-plane mobility in P3HT film by rubbing: aggregation and planarity enhanced with low regioregularity. *The Journal of Physical Chemistry C* **2015**, 119, 7987-7995.

109. Lee, M.; Jeon, H.; Jang, M.; Yang, H. A physicochemical approach toward extending conjugation and the ordering of solution-processable semiconducting polymers. *ACS Applied Materials & Interfaces* **2016**, 8, 4819-4827.

110. Mazzio, K. A.; Rice, A. H.; Durban, M. M.; Luscombe, C. K. Effect of regioregularity on charge transport and structural and excitonic coherence in poly(3-hexylthiophene) nanowires. *The Journal of Physical Chemistry C* **2015**, 119, 14911-14918.

111. Kim, J.-S.; Kim, J.-H.; Lee, W.; Yu, H.; Kim, H. J.; Song, I.; Shin, M.; Oh, J. H.; Jeong, U.; Kim, T.-S. Tuning mechanical and optoelectrical properties of poly(3-hexylthiophene) through systematic regioregularity control. *Macromolecules* **2015**, 48, 4339-4346.

112. Mao, H.; Xu, B.; Holdcroft, S. Synthesis and structure-property relationships of regioirregular poly(3-hexylthiophenes). *Macromolecules* **1993**, 26, 1163-1169.

113. McCullough, R. D.; Tristram-Nagle, S.; Williams, S. P.; Lowe, R. D.; Jayaraman, M. Self-orienting head-to-tail poly(3-alkylthiophenes): new insights on structure-property relationships in conducting polymers. *Journal of the American Chemical Society* **1993**, 115, 4910-4911.

114. Bondarev, D.; Zedník, J.; Šloufová, I.; Sharf, A.; Procházka, M.; Pfleger, J.; Vohlídal, J. Synthesis and properties of cationic polyelectrolyte with regioregular polyalkylthiophene backbone and ionic-liquid like side groups. *Journal of Polymer Science Part A: Polymer Chemistry* **2010**, 48, 3073-3081.

115. Chen, T.-A.; Wu, X.; Rieke, R. D. Regiocontrolled synthesis of poly(3-alkylthiophenes) mediated by Rieke zinc: their characterization and solid-state properties. *Journal of the American Chemical Society* **1995**, 117, 233-244.

116. Kuila, B. K.; Malik, S.; Batabyal, S. K.; Nandi, A. K. In-situ synthesis of soluble poly(3-hexylthiophene)/multiwalled carbon nanotube composite: morphology, structure, and conductivity. *Macromolecules* **2007**, 40, 278-287.

117. Liu, C.; Oshima, K.; Shimomura, M.; Miyauchi, S. Anisotropic conductivity–temperature characteristic of solution-cast poly(3-hexylthiophene) films. *Synthetic metals* **2006**, 156, 1362-1367.

118. Obrzut, J.; Page, K. A. Electrical conductivity and relaxation in poly(3-hexylthiophene). *Physical Review B* **2009**, 80, 195211.

119. Pal, S.; Roy, S.; Nandi, A. K. Temperature variation of DC conductivity of poly(3-alkyl thiophenes) and their cocrystals. *The Journal of Physical Chemistry B* **2005**, 109, 18332-18341.

120. Heeger, A. J. Semiconducting and metallic polymers: the fourth generation of polymeric materials (Nobel lecture). *Angewandte Chemie International Edition* **2001**, 40, 2591-2611.

121. Fuzell, J.; Jacobs, I. E.; Ackling, S.; Harrelson, T. F.; Huang, D. M.; Larsen, D.; Moulé, A. J. Optical dedoping mechanism for P3HT:F4TCNQ mixtures. *The Journal of Physical Chemistry Letters* **2016**, 7, 4297-4303.

122. Scholes, D. T.; Hawks, S. A.; Yee, P. Y.; Wu, H.; Lindemuth, J. R.; Tolbert, S. H.; Schwartz, B. J. Overcoming film quality issues for conjugated polymers doped with F4TCNQ by solution sequential processing: hall effect, structural, and optical measurements. *The Journal of Physical Chemistry Letters* **2015**, 6, 4786-4793.

123. Pingel, P.; Neher, D. Comprehensive picture of p-type doping of P3HT with the molecular acceptor F4TCNQ. *Physical Review B* **2013**, 87, 115209.

124. Wang, C.; Duong, D. T.; Vandewal, K.; Rivnay, J.; Salleo, A. Optical measurement of doping efficiency in poly(3-hexylthiophene) solutions and thin films. *Physical Review B* **2015**, 91, 085205.

125. Chung, T.-C.; Kaufman, J.; Heeger, A.; Wudl, F. Charge storage in doped poly(thiophene): optical and electrochemical studies. *Physical Review B* **1984**, 30, 702.

126. Chen, G.; Thomas-Alyea, K. E.; Newman, J.; Richardson, T. J. Characterization of an electroactive polymer for overcharge protection in secondary lithium batteries. *Electrochimica Acta* **2005**, 50, 4666-4673.

127. Jiang, X.; Harima, Y.; Yamashita, K.; Tada, Y.; Ohshita, J.; Kunai, A. Doping-induced change of carrier mobilities in poly(3-hexylthiophene) films with different stacking structures. *Chemical Physics Letters* **2002**, 364, 616-620.

128. Kline, R. J.; Frechet, J. M.; Toney, M. F.; Liu, J.; Kadnikova, E. N.; McGehee, M. D. The Dependence of regioregular poly(3-hexylthiphene) film morphology and field effect mobility on molecular weight. *Macromolecules* **2004**, 38, 3312.

129. Pingel, P.; Zen, A.; Abellón, R. D.; Grozema, F. C.; Siebbeles, L. D.; Neher, D. Temperature-resolved local and macroscopic charge carrier transport in thin P3HT layers. *Advanced Functional Materials* **2010**, 20, 2286-2295.

130. Zen, A.; Pflaum, J.; Hirschmann, S.; Zhuang, W.; Jaiser, F.; Asawapirom, U.; Rabe, J. P.; Scherf, U.; Neher, D. Effect of molecular weight and annealing of poly(3-hexylthiophene)s on the performance of organic field-effect transistors. *Advanced Functional Materials* **2004**, 14, 757-764.

131. Kline, R. J.; McGehee, M. D.; Kadnikova, E. N.; Liu, J.; Frechet, J. M. Controlling the field-effect mobility of regioregular polythiophene by changing the molecular weight. *Advanced Materials* **2003**, 15, 1519-1522.

132. Brinkmann, M.; Rannou, P. Molecular weight dependence of chain packing and semicrystalline structure in oriented films of regioregular poly(3-hexylthiophene) revealed by high-resolution transmission electron microscopy. *Macromolecules* **2009**, 42, 1125-1130.

133. Zen, A.; Saphiannikova, M.; Neher, D.; Grenzer, J.; Grigorian, S.; Pietsch, U.; Asawapirom, U.; Janietz, S.; Scherf, U.; Lieberwirth, I. Effect of molecular weight on the structure and crystallinity of poly(3-hexylthiophene). *Macromolecules* **2006**, 39, 2162-2171.

134. Sivaraman, P.; Mishra, S. P.; Bhattacharrya, A. R.; Thakur, A.; Shashidhara, K.; Samui, A. B. Effect of regioregularity on specific capacitance of poly(3-hexylthiophene). *Electrochimica Acta* **2012**, 69, 134-138.

135. Naguib, M.; Mochalin, V. N.; Barsoum, M. W.; Gogotsi, Y. 25th anniversary article: MXenes: a new family of two-dimensional materials. *Advanced Materials* **2013**, 26, 992-1005.

136. Naguib, M.; Kurtoglu, M.; Presser, V.; Lu, J.; Niu, J.; Heon, M.; Hultman, L.; Gogotsi, Y.; Barsoum, M. W. Two-dimensional nanocrystals produced by exfoliation of Ti_3AlC_2. *Advanced Materials* **2011**, 23, 4248-4253.

137. Seh, Z. W.; Fredrickson, K. D.; Anasori, B.; Kibsgaard, J.; Strickler, A. L.; Lukatskaya, M. R.; Gogotsi, Y.; Jaramillo, T. F.; Vojvodic, A. Two-dimensional molybdenum carbide (MXene) as an efficient electrocatalyst for hydrogen evolution. *ACS Energy Letters* **2016**, 1, 589-594.

138. Ma, T. Y.; Cao, J. L.; Jaroniec, M.; Qiao, S. Z. Interacting carbon nitride and titanium carbide nanosheets for high-performance oxygen evolution. *Angewandte Chemie International Edition* **2016**, 55, 1138-1142.

139. Zhao, Y.; Watanabe, K.; Hashimoto, K. Self-supporting oxygen reduction electrocatalysts made from a nitrogen-rich network polymer. *Journal of the American Chemical Society* **2012**, 134, 19528-19531.

140. Ghidiu, M.; Lukatskaya, M. R.; Zhao, M.-Q.; Gogotsi, Y.; Barsoum, M. W. Conductive two-dimensional titanium carbide 'clay' with high volumetric capacitance. *Nature* **2014**, 516, 78-81.

141. Khazaei, M.; Arai, M.; Sasaki, T.; Estili, M.; Sakka, Y. Two-dimensional molybdenum carbides: potential thermoelectric materials of the MXene family. *Physical Chemistry Chemical Physics* **2014**, 16, 7841-7849.

142. Naguib, M.; Halim, J.; Lu, J.; Cook, K. M.; Hultman, L.; Gogotsi, Y.; Barsoum, M. W. New two-dimensional niobium and vanadium carbides as promising materials for Li-ion batteries. *Journal of the American Chemical Society* **2013**, 135, 15966-15969.

143. Anasori, B.; Lukatskaya, M. R.; Gogotsi, Y. 2D metal carbides and nitrides (MXenes) for energy storage. *Nature Reviews Materials* **2017**, 2, 16098.

144. Dillon, A. D.; Ghidiu, M. J.; Krick, A. L.; Griggs, J.; May, S. J.; Gogotsi, Y.; Barsoum, M. W.; Fafarman, A. T. Highly conductive optical quality solution-processed films of 2D titanium carbide. *Advanced Functional Materials* **2016**, 26, 4162-4168.

145. Sang, X.; Xie, Y.; Lin, M.-W.; Alhabeb, M.; Van Aken, K. L.; Gogotsi, Y.; Kent, P. R.; Xiao, K.; Unocic, R. R. Atomic defects in monolayer titanium carbide ($Ti_3C_2T_x$) MXene. *ACS Nano* **2016**, 10, 9193-9200.

146. Lukatskaya, M. R.; Mashtalir, O.; Ren, C. E.; Dall'Agnese, Y.; Rozier, P.; Taberna, P. L.; Naguib, M.; Simon, P.; Barsoum, M. W.; Gogotsi, Y. Cation intercalation and high volumetric capacitance of two-dimensional titanium carbide. *Science* **2013**, 341, 1502-1505.

147. Wang, X.; Kajiyama, S.; Iinuma, H.; Hosono, E.; Oro, S.; Moriguchi, I.; Okubo, M.; Yamada, A. Pseudocapacitance of MXene nanosheets for high-power sodium-ion hybrid capacitors. *Nature Communications* **2015**, 6, 6544.

148. Liang, X.; Garsuch, A.; Nazar, L. F. Sulfur cathodes based on conductive mxene nanosheets for high-performance lithium–sulfur batteries. *Angewandte Chemie International Edition* **2015**, 54, 3907-3911.

149. Shahzad, F.; Alhabeb, M.; Hatter, C. B.; Anasori, B.; Hong, S. M.; Koo, C. M.; Gogotsi, Y. Electromagnetic interference shielding with 2D transition metal carbides (MXenes). *Science* **2016**, 353, 1137-1140.

150. Halim, J.; Lukatskaya, M. R.; Cook, K. M.; Lu, J.; Smith, C. R.; Näslund, L.-Å.; May, S. J.; Hultman, L.; Gogotsi, Y.; Eklund, P. Transparent conductive two-dimensional titanium carbide epitaxial thin films. *Chemistry of Materials* **2014**, 26, 2374-2381.

151. Hantanasirisakul, K.; Zhao, M. Q.; Urbankowski, P.; Halim, J.; Anasori, B.; Kota, S.; Ren, C. E.; Barsoum, M. W.; Gogotsi, Y. Fabrication of $Ti_3C_2T_x$ MXene transparent thin films with tunable optoelectronic properties. *Advanced Electronic Materials* **2016**, 2, 1600050.

152. Ren, C. E.; Hatzell, K. B.; Alhabeb, M.; Ling, Z.; Mahmoud, K. A.; Gogotsi, Y. Charge- and size-selective ion sieving through $Ti_3C_2T_x$ MXene membranes. *The Journal of Physical Chemistry Letters* **2015**, 6, 4026-4031.

153. Ling, Z.; Ren, C. E.; Zhao, M.-Q.; Yang, J.; Giammarco, J. M.; Qiu, J.; Barsoum, M. W.; Gogotsi, Y. Flexible and conductive MXene films and nanocomposites with high capacitance. *Proceedings of the National Academy of Sciences* **2014**, 111, 16676-16681.

154. Naguib, M.; Saito, T.; Lai, S.; Rager, M. S.; Aytug, T.; Paranthaman, M. P.; Zhao, M.-Q.; Gogotsi, Y. $Ti_3C_2T_x$ (MXene)–polyacrylamide nanocomposite films. *RSC Advances* **2016**, 6, 72069-72073.

155. Zhang, H.; Wang, L.; Chen, Q.; Li, P.; Zhou, A.; Cao, X.; Hu, Q. Preparation, mechanical and anti-friction performance of MXene/polymer composites. *Materials & Design* **2016**, 92, 682-689.

156. Iler, R. Multilayers of colloidal particles. *Journal of Colloid and Interface Science* **1966**, 21, 569-594.

157. Decher, G. Fuzzy nanoassemblies: toward layered polymeric multicomposites. *Science* **1997**, 277, 1232-1237.

158. Lutkenhaus, J. L.; McEnnis, K.; Hammond, P. T. Tuning the glass transition of and ion transport within hydrogen-bonded layer-by-layer assemblies. *Macromolecules* **2007**, 40, 8367-8373.

159. Shimazaki, Y.; Mitsuishi, M.; Ito, S.; Yamamoto, M. Preparation of the layer-by-layer deposited ultrathin film based on the charge-transfer interaction. *Langmuir* **1997**, 13, 1385-1387.

160. Lojou, É.; Bianco, P. Buildup of polyelectrolyte−protein multilayer assemblies on gold electrodes. Role of the hydrophobic effect. *Langmuir* **2004**, 20, 748-755.

161. Tang, Z.; Wang, Y.; Podsiadlo, P.; Kotov, N. A. Biomedical applications of layer-by-layer assembly: from biomimetics to tissue engineering. *Advanced Materials* **2006**, 18, 3203-3224.

162. Fu, J.; Schlenoff, J. B. Driving forces for oppositely charged polyion association in aqueous solutions: enthalpic, entropic, but not electrostatic. *Journal of the American Chemical Society* **2016**, 138, 980-990.

163. Xiang, Y.; Lu, S.; Jiang, S. P. Layer-by-layer self-assembly in the development of electrochemical energy conversion and storage devices from fuel cells to supercapacitors. *Chemical Society Reviews* **2012**, 41, 7291-7321.

164. Ho, B. C.; Lee, Y. D.; Chin, W. K. Thermal degradation of polymethacrylic acid. *Journal of Polymer Science Part A: Polymer Chemistry* **1992**, 30, 2389-2397.

165. Lazzari, M.; Kitayama, T.; Hatada, K.; Chiantore, O. Effect of stereoregularity on the thermal behavior of poly(methacrylic acid)s. 2. Decomposition at low temperatures. *Macromolecules* **1998**, 31, 8075-8082.

166. Mark, J. E. *Physical properties of polymers handbook*. Springer: **2007**; Vol. 1076.

167. Wunderlich, B. *Thermal analysis of polymeric materials*. Springer Science & Business Media: **2005**.

168. Tate, R. S.; Fryer, D. S.; Pasqualini, S.; Montague, M. F.; de Pablo, J. J.; Nealey, P. F. Extraordinary elevation of the glass transition temperature of thin polymer films grafted to silicon oxide substrates. *The Journal of Chemical Physics* **2001**, 115, 9982-9990.

169. Dubin, P.; Bock, J.; Davis, R.; Schulz, D. N.; Thies, C. *Macromolecular complexes in chemistry and biology*. Springer Science & Business Media: **2012**.

170. Ikawa, T.; Abe, K.; Honda, K.; Tsuchida, E. Interpolymer complex between poly(ethylene oxide) and poly(carboxylic acid). *Journal of Polymer Science Part A: Polymer Chemistry* **1975**, 13, 1505-1514.

171. Cimmino, S.; Di Pace, E.; Martuscelli, E.; Silvestre, C. Evaluation of the equilibrium melting temperature and structure analysis of poly(ethylene oxide)/poly(methyl methacrylate) blends. *Macromolecular Chemistry and Physics* **1990**, 191, 2447-2454.

172. DeMaggio, G.; Frieze, W.; Gidley, D.; Zhu, M.; Hristov, H.; Yee, A. Interface and surface effects on the glass transition in thin polystyrene films. *Physical Review Letters* **1997**, 78, 1524.

173. Li, X.; Hu, D.; Huang, K.; Yang, C. Hierarchical rough surfaces formed by LBL self-assembly for oil–water separation. *Journal of Materials Chemistry A* **2014**, 2, 11830-11838.

174. Joseph, N.; Ahmadiannamini, P.; Hoogenboom, R.; Vankelecom, I. F. Layer-by-layer preparation of polyelectrolyte multilayer membranes for separation. *Polymer Chemistry* **2014**, 5, 1817-1831.

175. Onitsuka, O.; Fou, A.; Ferreira, M.; Hsieh, B.; Rubner, M. Enhancement of light emitting diodes based on self-assembled heterostructures of poly(p-phenylene vinylene). *Journal of Applied Physics* **1996**, 80, 4067-4071.

176. Seo, J.; Lutkenhaus, J. L.; Kim, J.; Hammond, P. T.; Char, K. Effect of the layer-by-layer (LbL) deposition method on the surface morphology and wetting behavior of hydrophobically modified PEO and PAA LbL films. *Langmuir* **2008**, 24, 7995-8000.

177. Kim, Y.; Zhu, J.; Yeom, B.; Di Prima, M.; Su, X.; Kim, J.-G.; Yoo, S. J.; Uher, C.; Kotov, N. A. Stretchable nanoparticle conductors with self-organized conductive pathways. *Nature* **2013**, 500, 59.

178. Lee, S. W.; Kim, J.; Chen, S.; Hammond, P. T.; Shao-Horn, Y. Carbon nanotube/manganese oxide ultrathin film electrodes for electrochemical capacitors. *ACS Nano* **2010**, 4, 3889-3896.

179. Lee, S. W.; Kim, B.-S.; Chen, S.; Shao-Horn, Y.; Hammond, P. T. Layer-by-layer assembly of all carbon nanotube ultrathin films for electrochemical applications. *Journal of the American Chemical Society* **2008**, 131, 671-679.

180. Hyder, M. N.; Lee, S. W.; Cebeci, F. Ç.; Schmidt, D. J.; Shao-Horn, Y.; Hammond, P. T. Layer-by-layer assembled polyaniline nanofiber/multiwall carbon nanotube thin film electrodes for high-power and high-energy storage applications. *ACS Nano* **2011**, 5, 8552-8561.

181. Kim, S. Y.; Hong, J.; Kavian, R.; Lee, S. W.; Hyder, M. N.; Shao-Horn, Y.; Hammond, P. T. Rapid fabrication of thick spray-layer-by-layer carbon nanotube electrodes for high power and energy devices. *Energy & Environmental Science* **2013**, 6, 888-897.

182. Lee, S. W.; Yabuuchi, N.; Gallant, B. M.; Chen, S.; Kim, B.-S.; Hammond, P. T.; Shao-Horn, Y. High-power lithium batteries from functionalized carbon-nanotube electrodes. *Nature Nanotechnology* **2010**, 5, 531.

183. Zheludkevich, M. L.; Shchukin, D. G.; Yasakau, K. A.; Möhwald, H.; Ferreira, M. G. Anticorrosion coatings with self-healing effect based on nanocontainers impregnated with corrosion inhibitor. *Chemistry of Materials* **2007**, 19, 402-411.

184. Raoufi, N.; Surre, F.; Sun, T.; Rajarajan, M.; Grattan, K. T. Wavelength dependent pH optical sensor using the layer-by-layer technique. *Sensors and Actuators B: Chemical* **2012**, 169, 374-381.

185. Zhang, B.; Cui, T. An ultrasensitive and low-cost graphene sensor based on layer-by-layer nano self-assembly. *Applied Physics Letters* **2011**, 98, 073116.

186. Hsu, B. B.; Hagerman, S. R.; Jamieson, K.; Veselinovic, J.; O'Neill, N.; Holler, E.; Ljubimova, J. Y.; Hammond, P. T. Multilayer films assembled from naturally-derived materials for controlled protein release. *Biomacromolecules* **2014**, 15, 2049-2057.

187. Wood, K. C.; Boedicker, J. Q.; Lynn, D. M.; Hammond, P. T. Tunable drug release from hydrolytically degradable layer-by-layer thin films. *Langmuir* **2005**, 21, 1603-1609.

188. Nyholm, L.; Nyström, G.; Mihranyan, A.; Strømme, M. Toward flexible polymer and paper-based energy storage devices. *Advanced Materials* **2011**, 23, 3751-3769.

189. Shirshova, N.; Qian, H.; Houllé, M.; Steinke, J. H.; Kucernak, A. R.; Fontana, Q. P.; Greenhalgh, E. S.; Bismarck, A.; Shaffer, M. S. Multifunctional structural energy storage composite supercapacitors. *Faraday Discussions* **2014**, 172, 81-103.

190. Snyder, J. F.; Carter, R. H.; Wetzel, E. D. Electrochemical and mechanical behavior in mechanically robust solid polymer electrolytes for use in multifunctional structural batteries. *Chemistry of Materials* **2007**, 19, 3793-3801.

191. Ng, S.; Wang, J.; Guo, Z.; Chen, J.; Wang, G.; Liu, H. K. Single wall carbon nanotube paper as anode for lithium-ion battery. *Electrochimica Acta* **2005**, 51, 23-28.

192. Whitten, P. G.; Spinks, G. M.; Wallace, G. G. Mechanical properties of carbon nanotube paper in ionic liquid and aqueous electrolytes. *Carbon* **2005**, 43, 1891-1896.

193. Rigueur, J. L.; Hasan, S. A.; Mahajan, S. V.; Dickerson, J. H. Buckypaper fabrication by liberation of electrophoretically deposited carbon nanotubes. *Carbon* **2010**, 48, 4090-4099.

194. Yang, X.; Zhu, J.; Qiu, L.; Li, D. Bioinspired effective prevention of restacking in multilayered graphene films: towards the next generation of high-performance supercapacitors. *Advanced Materials* **2011**, 23, 2833-2838.

195. Dikin, D. A.; Stankovich, S.; Zimney, E. J.; Piner, R. D.; Dommett, G. H.; Evmenenko, G.; Nguyen, S. T.; Ruoff, R. S. Preparation and characterization of graphene oxide paper. *Nature* **2007**, 448, 457-460.

196. Liu, S.; Wang, Z.; Yu, C.; Wu, H. B.; Wang, G.; Dong, Q.; Qiu, J.; Eychmüller, A. A flexible TiO_2(B)-based battery electrode with superior power rate and ultralong cycle life. *Advanced Materials* **2013**, 25, 3462-3467.

197. Noerochim, L.; Wang, J.-Z.; Wexler, D.; Rahman, M. M.; Chen, J.; Liu, H.-K. Impact of mechanical bending on the electrochemical performance of bendable lithium batteries with paper-like free-standing V_2O_5–polypyrrole cathodes. *Journal of Materials Chemistry* **2012**, 22, 11159-11165.

198. Goward, G. R.; Leroux, F.; Nazar, L. F. Poly(pyrrole) and poly(thiophene)/vanadium oxide interleaved nanocomposites: positive electrodes for lithium batteries. *Electrochimica Acta* **1998**, 43, 1307-1313.

199. Bates, F. S.; Fredrickson, G. H. Block copolymer thermodynamics: theory and experiment. *Annual Review of Physical Chemistry* **1990**, 41, 525-557.

200. Park, N.-G.; Ryu, K. S.; Park, Y. J.; Kang, M. G.; Kim, D.-K.; Kang, S.-G.; Kim, K. M.; Chang, S.-H. Synthesis and electrochemical properties of V_2O_5 intercalated with binary polymers. *Journal of power sources* **2002**, 103, 273-279.

201. Kempf, C. N.; Smith, K. A.; Pesek, S. L.; Li, X.; Verduzco, R. Amphiphilic poly(alkylthiophene) block copolymers prepared via externally initiated GRIM and click coupling. *Polymer Chemistry* **2013**, 4, 2158-2163.

202. Jiang, Z.; Li, X.; Strzalka, J.; Sprung, M.; Sun, T.; Sandy, A. R.; Narayanan, S.; Lee, D. R.; Wang, J. The dedicated high-resolution grazing-incidence X-ray scattering beamline 8-ID-E at the Advanced Photon Source. *Journal of Synchrotron Radiation* **2012**, 19, 627-636.

203. Jiang, Z. GIXSGUI software. Available at: https://www1.aps.anl.gov/Sector-8/8-ID/Operations-and-Schedules/Useful-Links/Sector-8-GIXSGUI. (Accessed: 23th July 2015).

204. Bronstein, H. A.; Luscombe, C. K. Externally initiated regioregular P3HT with controlled molecular weight and narrow polydispersity. *Journal of the American Chemical Society* **2009**, 131, 12894-12895.

205. Huguenin, F.; Giz, M. J.; Ticianelli, E. A.; Torresi, R. M. Structure and properties of a nanocomposite formed by vanadium pentoxide containing poly(N-propane sulfonic acid aniline). *Journal of Power Sources* **2001**, 103, 113-119.

206. Lira-Cantú, M.; Gómez-Romero, P. The organic-inorganic polyaniline/V_2O_5 system. application as a high-capacity hybrid cathode for rechargeable lithium batteries. *Journal of the Electrochemical Society* **1999**, 146, 2029-2033.

207. Wanakule, N. S.; Panday, A.; Mullin, S. A.; Gann, E.; Hexemer, A.; Balsara, N. P. Ionic conductivity of block copolymer electrolytes in the vicinity of order− disorder and order− order transitions. *Macromolecules* **2009**, 42, 5642-5651.

208. Patel, S. N.; Javier, A. E.; Stone, G. M.; Mullin, S. A.; Balsara, N. P. Simultaneous conduction of electronic charge and lithium ions in block copolymers. *ACS Nano* **2012**, 6, 1589-1600.

209. Kamps, A. C.; Fryd, M.; Park, S.-J. Hierarchical self-assembly of amphiphilic semiconducting polymers into isolated, bundled, and branched nanofibers. *ACS Nano* **2012**, 6, 2844-2852.

210. Park, S.-J.; Kang, S.-G.; Fryd, M.; Saven, J. G.; Park, S.-J. Highly tunable photoluminescent properties of amphiphilic conjugated block copolymers. *Journal of the American Chemical Society* **2010**, 132, 9931-9933.

211. Yang, H.; Xia, H.; Wang, G.; Peng, J.; Qiu, F. Insights into poly(3-hexylthiophene)-*b*-poly(ethylene oxide) block copolymer: synthesis and solvent-induced structure formation in thin films. *Journal of Polymer Science Part A: Polymer Chemistry* **2012**, 50, 5060-5067.

212. Kline, R. J.; McGehee, M. D.; Kadnikova, E. N.; Liu, J.; Fréchet, J. M.; Toney, M. F. Dependence of regioregular poly(3-hexylthiophene) film morphology and field-effect mobility on molecular weight. *Macromolecules* **2005**, 38, 3312-3319.

213. Petkov, V.; Trikalitis, P. N.; Bozin, E. S.; Billinge, S. J.; Vogt, T.; Kanatzidis, M. G. Structure of $V_2O_5 \cdot nH_2O$ xerogel solved by the atomic pair distribution function technique. *Journal of the American Chemical Society* **2002**, 124, 10157-10162.

214. Coleman, J. N.; Blau, W. J.; Dalton, A. B.; Munoz, E.; Collins, S.; Kim, B. G.; Razal, J.; Selvidge, M.; Vieiro, G.; Baughman, R. H. Improving the mechanical properties of single-walled carbon nanotube sheets by intercalation of polymeric adhesives. *Applied Physics Letters* **2003**, 82, 1682-1684.

215. Park, S.; Lee, K.-S.; Bozoklu, G.; Cai, W.; Nguyen, S. T.; Ruoff, R. S. Graphene oxide papers modified by divalent ions—enhancing mechanical properties via chemical cross-linking. *ACS Nano* **2008**, 2, 572-578.

216. Timoshenko, S. P.; Goodier, J. N.; Abramson, H. N. Theory of elasticity (3rd ed.). *Journal of Applied Mechanics* **1970**, 37, 888-888.

217. Hibino, M.; Ugaji, M.; Kishimoto, A.; Kudo, T. Preparation and lithium intercalation of a new vanadium oxide with a two-dimensional structure. *Solid State Ionics* **1995**, 79, 239-244.

218. Galiote, N. A.; Camargo, M. N.; Iost, R. M.; Crespilho, F.; Huguenin, F. Effects of self-assembled materials prepared from V_2O_5 for lithium ion electroinsertion. *Langmuir* **2011**, 27, 12209-12217.

219. Giorgetti, M.; Passerini, S.; Smyrl, W. H.; Mukerjee, S.; Yang, X.; McBreen, J. In situ X-ray absorption spectroscopy characterization of V_2O_5 xerogel cathodes upon lithium intercalation. *Journal of the Electrochemical Society* **1999**, 146, 2387-2392.

220. Tipton, A.; Passerini, S.; Owens, B.; Smyrl, W. Performance of lithium/V_2O_5 xerogel coin cells. *Journal of the Electrochemical Society* **1996**, 143, 3473-3477.

221. Sathiya, M.; Prakash, A.; Ramesha, K.; Tarascon, J. M.; Shukla, A. V_2O_5-anchored carbon nanotubes for enhanced electrochemical energy storage. *Journal of the American Chemical Society* **2011**, 133, 16291-16299.

222. Levi, M.; Lu, Z.; Aurbach, D. Li-insertion into thin monolithic V_2O_5 films electrodes characterized by a variety of electroanalytical techniques. *Journal of power sources* **2001**, 97, 482-485.

223. Navone, C.; Baddour-Hadjean, R.; Pereira-Ramos, J.; Salot, R. A kinetic study of electrochemical lithium insertion into oriented V_2O_5 thin films prepared by rf sputtering. *Electrochimica Acta* **2008**, 53, 3329-3336.

224. Ha, S. H.; Jeong, Y. S.; Lee, Y. J. Free standing reduced graphene oxide film cathodes for lithium ion batteries. *ACS Applied Materials & Interfaces* **2013**, 5, 12295-12303.

225. Klavetter, K. C.; Snider, J. L.; de Souza, J. P.; Tu, H.; Cell, T. H.; Cho, J. H.; Ellison, C. J.; Heller, A.; Mullins, C. B. A free-standing, flexible lithium-ion anode formed from an air-dried slurry cast of high tap density SnO_2, CMC polymer binder and Super-P Li. *Journal of Materials Chemistry A* **2014**, 2, 14459-14467.

226. Mike, J. F.; Lutkenhaus, J. L. Recent advances in conjugated polymer energy storage. *Journal of Polymer Science Part B: Polymer Physics* **2013**, 51, 468-480.

227. Wu, M.; Xiao, X.; Vukmirovic, N.; Xun, S.; Das, P. K.; Song, X.; Olalde-Velasco, P.; Wang, D.; Weber, A. Z.; Wang, L.-W. Toward an ideal polymer binder design for high-capacity battery anodes. *Journal of the American Chemical Society* **2013**, 135, 12048-12056.

228. Liu, P.; Lee, S.-H.; Tracy, C. E.; Yan, Y.; Turner, J. A. Preparation and lithium insertion properties of mesoporous vanadium oxide. *Advanced Materials* **2002**, 14, 27-30.

229. Strelcov, E.; Cothren, J.; Leonard, D.; Borisevich, A. Y.; Kolmakov, A. In situ SEM study of lithium intercalation in individual V_2O_5 nanowires. *Nanoscale* **2015**, 7, 3022-3027.

230. Liu, Q.; Li, Z.-F.; Liu, Y.; Zhang, H.; Ren, Y.; Sun, C.-J.; Lu, W.; Zhou, Y.; Stanciu, L.; Stach, E. A. Graphene-modified nanostructured vanadium pentoxide hybrids with extraordinary electrochemical performance for Li-ion batteries. *Nature Communications* **2015**, 6, 6127.

231. ShengáHu, Y.; QiangáMai, L.; YaoáZhu, Q. Effect of modification by poly(ethylene oxide) on the reversibility of insertion/extraction of Li^+ ion in V_2O_5 xerogel films. *Journal of Materials Chemistry* **2002**, 12, 1926-1929.

232. Ruiz-Hitzky, E. Conducting polymers intercalated in layered solids. *Advanced Materials* **1993**, 5, 334-340.

233. Pandey, G. P.; Liu, T.; Brown, E.; Yang, Y.; Li, Y.; Sun, X. S.; Fang, Y.; Li, J. Mesoporous hybrids of reduced graphene oxide and vanadium pentoxide for enhanced performance in lithium-ion batteries and electrochemical capacitors. *ACS Applied Materials & Interfaces* **2016**, 8, 9200-9210.

234. Chen, Y.; Yang, G.; Zhang, Z.; Yang, X.; Hou, W.; Zhu, J.-J. Polyaniline-intercalated layered vanadium oxide nanocomposites—one-pot hydrothermal synthesis and application in lithium battery. *Nanoscale* **2010**, 2, 2131-2138.

235. Lu, Y.-C.; Crumlin, E. J.; Veith, G. M.; Harding, J. R.; Mutoro, E.; Baggetto, L.; Dudney, N. J.; Liu, Z.; Shao-Horn, Y. In situ ambient pressure X-ray photoelectron spectroscopy studies of lithium-oxygen redox reactions. *Scientific Reports* **2012**, 2, 715.

236. Du, G.; Seng, K. H.; Guo, Z.; Liu, J.; Li, W.; Jia, D.; Cook, C.; Liu, Z.; Liu, H. Graphene–$V_2O_5 \cdot nH_2O$ xerogel composite cathodes for lithium ion batteries. *RSC Advances* **2011**, 1, 690-697.

237. Oliveira, H.; Graeff, C.; Zanta, C.; Galina, A.; Gonçalves, P. Synthesis, characterization and properties of a melanin-like/vanadium pentoxide hybrid compound. *Journal of Materials Chemistry* **2000**, 10, 371-375.

238. Jeon, J.-W.; Ma, Y.; Mike, J. F.; Shao, L.; Balbuena, P. B.; Lutkenhaus, J. L. Oxidatively stable polyaniline:polyacid electrodes for electrochemical energy storage. *Physical Chemistry Chemical Physics* **2013**, 15, 9654-9662.

239. Dreyer, W.; Jamnik, J.; Guhlke, C.; Huth, R.; Moškon, J.; Gaberšček, M. The thermodynamic origin of hysteresis in insertion batteries. *Nature Materials* **2010**, 9, 448-453.

240. Yang, Y.; Li, L.; Fei, H.; Peng, Z.; Ruan, G.; Tour, J. M. Graphene nanoribbon/V_2O_5 cathodes in lithium-ion batteries. *ACS Applied Materials & Interfaces* **2014**, 6, 9590-9594.

241. Zhong, K.; Xia, X.; Zhang, B.; Li, H.; Wang, Z.; Chen, L. MnO powder as anode active materials for lithium ion batteries. *Journal of Power Sources* **2010**, 195, 3300-3308.

242. Ligneel, E.; Lestriez, B.; Hudhomme, A.; Guyomard, D. Shaping of advanced ceramics: the case of composite electrodes for lithium batteries. *Journal of the European Ceramic Society* **2009**, 29, 925-929.

243. Zhu, M.; Park, J.; Sastry, A. Particle interaction and aggregation in cathode material of Li-ion batteries: a numerical study. *Journal of the Electrochemical Society* **2011**, 158, A1155-A1159.

244. Kwon, Y. H.; Huie, M.; Choi, D.; Chang, M.; Marschilok, A. C.; Takeuchi, K. J.; Takeuchi, E. S.; Reichmanis, E. Towards uniformly dispersed battery electrode composite materials: characteristics and performance. *ACS Applied Materials & Interfaces* **2016**, 8, 3452–3463.

245. Tao, T.; Glushenkov, A. M.; Zhang, C.; Zhang, H.; Zhou, D.; Guo, Z.; Liu, H. K.; Chen, Q.; Hu, H.; Chen, Y. MoO_3 nanoparticles dispersed uniformly in carbon matrix: a high capacity composite anode for Li-ion batteries. *Journal of Materials Chemistry* **2011**, 21, 9350-9355.

246. Huguenin, F.; dos Santos, D.; Bassi, A.; Nart, F. C.; Oliveira, O. Charge storage capability in nanoarchitectures of V_2O_5/chitosan/poly(ethylene oxide) produced using the layer-by-layer technique. *Advanced Functional Materials* **2004**, 14, 985-991.

247. Guo, H.; Liu, L.; Shu, H.; Yang, X.; Yang, Z.; Zhou, M.; Tan, J.; Yan, Z.; Hu, H.; Wang, X. Synthesis and electrochemical performance of LiV_3O_8/polythiophene composite as cathode materials for lithium ion batteries. *Journal of Power Sources* **2014**, 247, 117-126.

248. Geng, Y.; Wang, G.; Cong, Y.; Bai, L.; Li, L.; Yang, C. Surface adsorption-induced conformational ordering and crystallization of polyethylene oxide. *Journal of Polymer Science Part B: Polymer Physics* **2010**, 48, 106-112.

249. Tamanai, A.; Beck, S.; Pucci, A. Mid-infrared characterization of thiophene-based thin polymer films. *Displays* **2013**, 34, 399-405.

250. Guo, Y.; Jin, Y.; Su, Z. Spectroscopic study of side-chain melting and crystallization of regioregular poly(3-dodecylthiophene). *Polymer Chemistry* **2012**, 3, 861-864.

251. Zhou, G.; Wang, D.-W.; Yin, L.-C.; Li, N.; Li, F.; Cheng, H.-M. Oxygen bridges between NiO nanosheets and graphene for improvement of lithium storage. *ACS Nano* **2012**, 6, 3214-3223.

252. Sun, J.; Zheng, G.; Lee, H.-W.; Liu, N.; Wang, H.; Yao, H.; Yang, W.; Cui, Y. Formation of stable phosphorus–carbon bond for enhanced performance in black phosphorus nanoparticle–graphite composite battery anodes. *Nano Letters* **2014**, 14, 4573-4580.

253. Lindström, H.; Södergren, S.; Solbrand, A.; Rensmo, H.; Hjelm, J.; Hagfeldt, A.; Lindquist, S.-E. Li^+ ion insertion in TiO_2 (Anatase). 2. voltammetry on nanoporous films. *The Journal of Physical Chemistry B* **1997**, 101, 7717-7722.

254. Wang, J.; Polleux, J.; Lim, J.; Dunn, B. Pseudocapacitive contributions to electrochemical energy storage in TiO_2 (Anatase) nanoparticles. *The Journal of Physical Chemistry C* **2007**, 111, 14925-14931.

255. Bates, J.; Dudney, N.; Lubben, D.; Gruzalski, G.; Kwak, B.; Yu, X.; Zuhr, R. Thin-film rechargeable lithium batteries. *Journal of Power Sources* **1995**, 54, 58-62.

256. Rao, K.; Pecquenard, B.; Gies, A.; Levasseur, A.; Etourneau, J. Structural and electrochemical behaviour of sputtered vanadium oxide films: oxygen non-stoichiometry and lithium ion sequestration. *Bulletin of Materials Science* **2006**, 29, 535-546.

257. Noriega, R.; Rivnay, J.; Vandewal, K.; Koch, F. P.; Stingelin, N.; Smith, P.; Toney, M. F.; Salleo, A. A general relationship between disorder, aggregation and charge transport in conjugated polymers. *Nature Materials* **2013**.

258. Tu, G.; Li, H.; Forster, M.; Heiderhoff, R.; Balk, L. J.; Sigel, R.; Scherf, U. Amphiphilic conjugated block copolymers: synthesis and solvent-selective photoluminescence quenching. *Small* **2007**, 3, 1001-1006.

259. Gu, Z.; Tan, Y.; Tsuchiya, K.; Shimomura, T.; Ogino, K. Synthesis and characterization of poly(3-hexylthiophene)-*b*-polystyrene for photovoltaic application. *Polymers* **2011**, 3, 558-570.

260. He, M.; Qiu, F.; Lin, Z. Conjugated rod–coil and rod–rod block copolymers for photovoltaic applications. *Journal of Materials Chemistry* **2011**, 21, 17039-17048.

261. Vohra, A.; Imin, P.; Imit, M.; Carmichael, R. S.; Meena, J. S.; Adronov, A.; Carmichael, T. B. Transparent, stretchable, and conductive SWNT films using supramolecular functionalization and layer-by-layer self-assembly. *RSC Advances* **2016**, 6, 29254-29263.

262. Kim, J.-S.; Kim, Y.; Kim, H.-J.; Kim, H. J.; Yang, H.; Jung, Y. S.; Stein, G. E.; Kim, B. J. Regioregularity-driven morphological transition of poly(3-hexylthiophene)-based block copolymers. *Macromolecules* **2017**, 50, 1902-1908.

263. Liu, F.; Chen, D.; Wang, C.; Luo, K.; Gu, W.; Briseno, A. L.; Hsu, J. W.; Russell, T. P. Molecular weight dependence of the morphology in P3HT: PCBM solar cells. *ACS Applied Materials & Interfaces* **2014**, 6, 19876-19887.

264. Malik, S.; Nandi, A. K. Crystallization mechanism of regioregular poly(3-alkyl thiophene)s. *Journal of Polymer Science Part B: Polymer Physics* **2002**, 40, 2073-2085.

265. Ying, L.; Huang, F.; Bazan, G. C. Regioregular narrow-bandgap-conjugated polymers for plastic electronics. *Nature Communications* **2017**, 8.

266. Yamagata, H.; Spano, F. C. Interplay between intrachain and interchain interactions in semiconducting polymer assemblies: the HJ-aggregate model. *The Journal of Chemical Physics* **2012**, 136, 184901.

267. Spano, F. C.; Silva, C. H-and J-aggregate behavior in polymeric semiconductors. *Annual Review of Physical Chemistry* **2014**, 65, 477-500.

268. Martin, T. P.; Wise, A. J.; Busby, E.; Gao, J.; Roehling, J. D.; Ford, M. J.; Larsen, D. S.; Moulé, A. J.; Grey, J. K. Packing dependent electronic coupling in single poly(3-hexylthiophene) H-and J-aggregate nanofibers. *The Journal of Physical Chemistry B* **2012**, 117, 4478-4487.

269. Jimison, L. H.; Toney, M. F.; McCulloch, I.; Heeney, M.; Salleo, A. Charge-transport anisotropy due to grain boundaries in directionally crystallized thin films of regioregular poly(3-hexylthiophene). *Advanced Materials* **2009**, 21, 1568-1572.

270. Österbacka, R.; An, C. P.; Jiang, X.; Vardeny, Z. V. Two-dimensional electronic excitations in self-assembled conjugated polymer nanocrystals. *Science* **2000**, 287, 839-842.

271. Wu, P.-T.; Xin, H.; Kim, F. S.; Ren, G.; Jenekhe, S. A. Regioregular poly(3-pentylthiophene): synthesis, self-assembly of nanowires, high-mobility field-effect transistors, and efficient photovoltaic cells. *Macromolecules* **2009**, 42, 8817-8826.

272. Zheng, F.; Yang, X.-Y.; Bi, P.-Q.; Niu, M.-S.; Lv, C.-K.; Feng, L.; Hao, X.-T.; Ghiggino, K. P. Improved compatibility of DDAB-functionalized graphene oxide with a conjugated polymer by isocyanate treatment. *RSC Advances* **2017**, 7, 17633-17639.

273. Brown, P. J.; Thomas, D. S.; Köhler, A.; Wilson, J. S.; Kim, J.-S.; Ramsdale, C. M.; Sirringhaus, H.; Friend, R. H. Effect of interchain interactions on the absorption and emission of poly(3-hexylthiophene). *Physical Review B* **2003**, 67, 064203.

274. Ehrenreich, P.; Birkhold, S. T.; Zimmermann, E.; Hu, H.; Kim, K.-D.; Weickert, J.; Pfadler, T.; Schmidt-Mende, L. H-aggregate analysis of P3HT thin films-Capability and limitation of photoluminescence and UV/Vis spectroscopy. *Scientific Reports* **2016**, 6, 32434.

275. Niles, E. T.; Roehling, J. D.; Yamagata, H.; Wise, A. J.; Spano, F. C.; Moulé, A. J.; Grey, J. K. J-aggregate behavior in poly-3-hexylthiophene nanofibers. *The Journal of Physical Chemistry Letters* **2012**, 3, 259-263.

276. Clark, J.; Silva, C.; Friend, R. H.; Spano, F. C. Role of intermolecular coupling in the photophysics of disordered organic semiconductors: aggregate emission in regioregular polythiophene. *Physical Review Letters* **2007**, 98, 206406.

277. Turner, S. T.; Pingel, P.; Steyrleuthner, R.; Crossland, E. J.; Ludwigs, S.; Neher, D. Quantitative analysis of bulk heterojunction films using linear absorption spectroscopy and solar cell performance. *Advanced Functional Materials* **2011**, 21, 4640-4652.

278. Bartelt, J. A.; Beiley, Z. M.; Hoke, E. T.; Mateker, W. R.; Douglas, J. D.; Collins, B. A.; Tumbleston, J. R.; Graham, K. R.; Amassian, A.; Ade, H. The importance of fullerene percolation in the mixed regions of polymer–fullerene bulk heterojunction solar cells. *Advanced Energy Materials* **2013**, 3, 364-374.

279. Rivnay, J.; Noriega, R.; Kline, R. J.; Salleo, A.; Toney, M. F. Quantitative analysis of lattice disorder and crystallite size in organic semiconductor thin films. *Physical Review B* **2011**, 84, 045203.

280. Gao, J.; Stein, B. W.; Thomas, A. K.; Garcia, J. A.; Yang, J.; Kirk, M. L.; Grey, J. K. Enhanced charge transfer doping efficiency in J-Aggregate poly(3-hexylthiophene) nanofibers. *The Journal of Physical Chemistry C* **2015**, 119, 16396-16402.

281. Ciprelli, J.-L.; Clarisse, C.; Delabouglise, D. Enhanced stability of conducting poly(3-octylthiophene) thin films using organic nitrosyl compounds. *Synthetic Metals* **1995**, 74, 217-222.

282. Chen, J.; Wang, J.; Wang, C.; Too, C.; Wallace, G. Lithium–polymer battery based on polybithiophene as cathode material. *Journal of Power Sources* **2006**, 159, 708-711.

283. Kaneto, K.; Yoshino, K.; Inuishi, Y. Characteristics of polythiophene battery. *Japanese Journal of Applied Physics* **1983**, 22, L567.

284. Naguib, M.; Mashtalir, O.; Carle, J.; Presser, V.; Lu, J.; Hultman, L.; Gogotsi, Y.; Barsoum, M. W. Two-dimensional transition metal carbides. *ACS Nano* **2012**, 6, 1322-1331.

285. Gao, H.; Benitez, R.; Son, W.; Arroyave, R.; Radovic, M. Structural, physical and mechanical properties of $Ti_3(Al_{1-x}Si_x)C_2$ solid solution with x=0–1. *Materials Science and Engineering: A* **2016**, 676, 197-208.

286. Richardson, J. J.; Björnmalm, M.; Caruso, F. Technology-driven layer-by-layer assembly of nanofilms. *Science* **2015**, 348, aaa2491.

287. Yeom, B.; Char, K. Nanostructured $CaCO_3$ thin films formed on the urease multilayers prepared by the layer-by-layer deposition. *Chemistry of Materials* **2009**, 22, 101-107.

288. Radovic, M.; Barsoum, M. W. MAX phases: bridging the gap between metals and ceramics. *American Ceramics Society Bulletin* **2013**, 92, 20-27.

289. Chen, J.; Bi, H.; Sun, S.; Tang, Y.; Zhao, W.; Lin, T.; Wan, D.; Huang, F.; Zhou, X.; Xie, X. Highly conductive and flexible paper of 1D silver-nanowire-doped graphene. *ACS Applied Materials & Interfaces* **2013**, 5, 1408-1413.

290. Xie, X.; Xue, Y.; Li, L.; Chen, S.; Nie, Y.; Ding, W.; Wei, Z. Surface Al leached Ti_3AlC_2 as a substitute for carbon for use as a catalyst support in a harsh corrosive electrochemical system. *Nanoscale* **2014**, 6, 11035-11040.

291. Shah, S.; Habib, T.; Gao, H.; Gao, P.; Sun, W.; Green, M.; Radovic, M. Template-free 3D titanium carbide ($Ti_3C_2T_x$) MXene particles crumpled by capillary forces. *Chemical Communications* **2017**, 53, 400-403.

292. Wang, X.; Shen, X.; Gao, Y.; Wang, Z.; Yu, R.; Chen, L. Atomic-scale recognition of surface structure and intercalation mechanism of Ti_3C_2X. *Journal of the American Chemical Society* **2015**, 137, 2715-2721.

293. Zhao, M. Q.; Ren, C. E.; Ling, Z.; Lukatskaya, M. R.; Zhang, C.; Van Aken, K. L.; Barsoum, M. W.; Gogotsi, Y. Flexible MXene/carbon nanotube composite paper with high volumetric capacitance. *Advanced Materials* **2015**, 27, 339-345.

294. Chen, Z.; Ren, W.; Gao, L.; Liu, B.; Pei, S.; Cheng, H.-M. Three-dimensional flexible and conductive interconnected graphene networks grown by chemical vapour deposition. *Nature Materials* **2011**, 10, 424-428.

295. Li, X.; Zhu, Y.; Cai, W.; Borysiak, M.; Han, B.; Chen, D.; Piner, R. D.; Colombo, L.; Ruoff, R. S. Transfer of large-area graphene films for high-performance transparent conductive electrodes. *Nano Letters* **2009**, 9, 4359-4363.

296. Zeng, X. Y.; Zhang, Q. K.; Yu, R. M.; Lu, C. Z. A new transparent conductor: silver nanowire film buried at the surface of a transparent polymer. *Advanced Materials* **2010**, 22, 4484-4488.

297. Dai, X.; Wu, J.; Qian, Z.; Wang, H.; Jian, J.; Cao, Y.; Rummeli, M. H.; Yi, Q.; Liu, H.; Zou, G. Ultra-smooth glassy graphene thin films for flexible transparent circuits. *Science Advances* **2016**, 2, e1601574.

298. Wu, X.; Liu, J.; Wu, D.; Zhao, Y.; Shi, X.; Wang, J.; Huang, S.; He, G. Highly conductive and uniform graphene oxide modified PEDOT:PSS electrodes for ITO-free organic light emitting diodes. *Journal of Materials Chemistry C* **2014**, 2, 4044-4050.

299. Chang, H.; Wang, G.; Yang, A.; Tao, X.; Liu, X.; Shen, Y.; Zheng, Z. A transparent, flexible, low-temperature, and solution-processible graphene composite electrode. *Advanced Functional Materials* **2010**, 20, 2893-2902.

300. Cho, C.-K.; Hwang, W.-J.; Eun, K.; Choa, S.-H.; Na, S.-I.; Kim, H.-K. Mechanical flexibility of transparent PEDOT:PSS electrodes prepared by gravure printing for flexible organic solar cells. *Solar Energy Materials and Solar Cells* **2011**, 95, 3269-3275.

301. De, S.; Higgins, T. M.; Lyons, P. E.; Doherty, E. M.; Nirmalraj, P. N.; Blau, W. J.; Boland, J. J.; Coleman, J. N. Silver nanowire networks as flexible, transparent, conducting films: extremely high DC to optical conductivity ratios. *ACS Nano* **2009**, 3, 1767-1774.

302. Na, S. I.; Kim, S. S.; Jo, J.; Kim, D. Y. Efficient and flexible ITO-free organic solar cells using highly conductive polymer anodes. *Advanced Materials* **2008**, 20, 4061-4067.

303. Ma, R.; Kwon, S.; Zheng, Q.; Kwon, H. Y.; Kim, J. I.; Choi, H. R.; Baik, S. Carbon-nanotube/silver networks in nitrile butadiene rubber for highly conductive flexible adhesives. *Advanced Materials* **2012**, 24, 3344-3349.

304. Moon, I. K.; Kim, J. I.; Lee, H.; Hur, K.; Kim, W. C.; Lee, H. 2D graphene oxide nanosheets as an adhesive over-coating layer for flexible transparent conductive electrodes. *Scientific Reports* **2013**, 3.

305. Kim, K. S.; Zhao, Y.; Jang, H.; Lee, S. Y.; Kim, J. M.; Kim, K. S.; Ahn, J.-H.; Kim, P.; Choi, J.-Y.; Hong, B. H. Large-scale pattern growth of graphene films for stretchable transparent electrodes. *Nature* **2009**, 457, 706-710.

306. Yu, Z.; Niu, X.; Liu, Z.; Pei, Q. Intrinsically stretchable polymer light-emitting devices using carbon nanotube-polymer composite electrodes. *Advanced Materials* **2011**, 23, 3989-3994.

307. Teng, C.; Lu, X.; Zhu, Y.; Wan, M.; Jiang, L. Polymer in situ embedding for highly flexible, stretchable and water stable PEDOT:PSS composite conductors. *RSC Advances* **2013**, 3, 7219-7223.

308. Liu, H.; Li, Y.; Dai, K.; Zheng, G.; Liu, C.; Shen, C.; Yan, X.; Guo, J.; Guo, Z. Electrically conductive thermoplastic elastomer nanocomposites at ultralow graphene loading levels for strain sensor applications. *Journal of Materials Chemistry C* **2016**, 4, 157-166.

309. Mates, J. E.; Bayer, I. S.; Palumbo, J. M.; Carroll, P. J.; Megaridis, C. M. Extremely stretchable and conductive water-repellent coatings for low-cost ultra-flexible electronics. *Nature Communications* **2015**, 6, 8874.

310. Wang, X.; Hu, H.; Shen, Y.; Zhou, X.; Zheng, Z. Stretchable conductors with ultrahigh tensile strain and stable metallic conductance enabled by prestrained polyelectrolyte nanoplatforms. *Advanced Materials* **2011**, 23, 3090-3094.

311. Liang, J.; Li, L.; Tong, K.; Ren, Z.; Hu, W.; Niu, X.; Chen, Y.; Pei, Q. Silver nanowire percolation network soldered with graphene oxide at room temperature and its application for fully stretchable polymer light-emitting diodes. *ACS Nano* **2014**, 8, 1590-1600.

312. Zahid, M.; Papadopoulou, E. L.; Athanassiou, A.; Bayer, I. S. Strain-responsive mercerized conductive cotton fabrics based on PEDOT:PSS/graphene. *Materials & Design* **2017**, 135, 213-222.

313. Shin, M. K.; Oh, J.; Lima, M.; Kozlov, M. E.; Kim, S. J.; Baughman, R. H. Elastomeric conductive composites based on carbon nanotube forests. *Advanced Materials* **2010**, 22, 2663-2667.

314. Zhao, N.; Yang, M.; Zhao, Q.; Gao, W.; Xie, T.; Bai, H. Superstretchable nacre-mimetic graphene/poly(vinyl alcohol) composite film based on interfacial architectural engineering. *ACS Nano* **2017**, 11, 4777-4784.

315. Liu, K.; Sun, Y.; Liu, P.; Lin, X.; Fan, S.; Jiang, K. Cross-stacked superaligned carbon nanotube films for transparent and stretchable conductors. *Advanced Functional Materials* **2011**, 21, 2721-2728.

316. Boland, C. S.; Khan, U.; Backes, C.; O'Neill, A.; McCauley, J.; Duane, S.; Shanker, R.; Liu, Y.; Jurewicz, I.; Dalton, A. B. Sensitive, high-strain, high-rate bodily motion sensors based on graphene–rubber composites. *ACS Nano* **2014**, 8, 8819-8830.

317. Liu, N.; Chortos, A.; Lei, T.; Jin, L.; Kim, T. R.; Bae, W.-G.; Zhu, C.; Wang, S.; Pfattner, R.; Chen, X. Ultratransparent and stretchable graphene electrodes. *Science Advances* **2017**, 3, e1700159.

318. Liang, J.; Li, L.; Chen, D.; Hajagos, T.; Ren, Z.; Chou, S.-Y.; Hu, W.; Pei, Q. Intrinsically stretchable and transparent thin-film transistors based on printable silver nanowires, carbon nanotubes and an elastomeric dielectric. *Nature Communications* **2015**, 6.

319. Yu, Y.; Luo, Y.; Guo, A.; Yan, L.; Wu, Y.; Jiang, K.; Li, Q.; Fan, S.; Wang, J. Flexible and transparent strain sensors based on super-aligned carbon nanotube films. *Nanoscale* **2017**, 9, 6716-6723.

320. Chun, K.-Y.; Oh, Y.; Rho, J.; Ahn, J.-H.; Kim, Y.-J.; Choi, H. R.; Baik, S. Highly conductive, printable and stretchable composite films of carbon nanotubes and silver. *Nature Nanotechnology* **2010**, 5, 853-857.

321. Lipomi, D. J.; Vosgueritchian, M.; Tee, B. C.; Hellstrom, S. L.; Lee, J. A.; Fox, C. H.; Bao, Z. Skin-like pressure and strain sensors based on transparent elastic films of carbon nanotubes. *Nature Nanotechnology* **2011**, 6, 788-792.

322. Yamada, T.; Hayamizu, Y.; Yamamoto, Y.; Yomogida, Y.; Izadi-Najafabadi, A.; Futaba, D. N.; Hata, K. A stretchable carbon nanotube strain sensor for human-motion detection. *Nature Nanotechnology* **2011**, 6, 296-301.

323. Li, C.; Cui, Y.-L.; Tian, G.-L.; Shu, Y.; Wang, X.-F.; Tian, H.; Yang, Y.; Wei, F.; Ren, T.-L. Flexible CNT-array double helices Strain Sensor with high stretchability for motion capture. *Scientific Reports* **2015**, 5.

324. Kang, D.; Pikhitsa, P. V.; Choi, Y. W.; Lee, C.; Shin, S. S.; Piao, L.; Park, B.; Suh, K.-Y.; Kim, T.-i.; Choi, M. Ultrasensitive mechanical crack-based sensor inspired by the spider sensory system. *Nature* **2014**, 516, 222-226.

325. Chortos, A.; Lim, J.; To, J. W.; Vosgueritchian, M.; Dusseault, T. J.; Kim, T. H.; Hwang, S.; Bao, Z. Highly stretchable transistors using a microcracked organic semiconductor. *Advanced Materials* **2014**, 26, 4253-4259.

326. Beeby, S.; Ensel, G.; Kraft, M. *MEMS mechanical sensors*. Artech House: **2004**.